THÈSE

Pour l'obtention du titre de :
Docteur de l'Université de Lorraine
Spécialité : Physique

Présentée par :

Héloïse Damas

Spin current generation and self-induced spin-orbit torque in quasi-isolated GdFeCo ferrimagnet

---

Thèse soutenue publiquement le 9 Novembre 2023 à Nancy, devant le jury composé de :

Alexandra Mougin	Directrice de recherche	Rapportrice
Pietro Gambardella	Professeur	Rapporteur
Stefania Pizzini	Directrice de recherche	Examinatrice *(Présidente du jury)*
Andrew Kent	Professeur	Examinateur
Michel Hehn	Professeur	Invité
Vincent Cros	Directeur de recherche	Invité
Juan-Carlos Rojas-Sanchez	Chargé de recherche	Directeur de thèse
Sébastien Petit-Watelot	Maître de conférence	Co-directeur de thèse

Institut Jean Lamour
UMR 7198 - Université de Lorraine - CNRS
Equipe 101 : Nanomagnétisme et Electronique de Spin

"When I think about everything we've been through together,
maybe it's not the destination that matters,
maybe it's the journey,
and if that journey takes a little longer, so we can do something we all believe in,
I can't think of any place I'd rather be or any people I'd rather be with."

Harry Kim, Star Trek: Voyager

Acknowledgement

First of all, I would like to thank all the members of the jury who evaluated my defense and my thesis manuscript, and with whom I had great scientific discussions about my research. Je remercie également Sébastien G. d'avoir enregistré et diffusé ma soutenance en ligne.

Ce manuscrit de thèse est le résultat de 3 années de recherche dans l'équipe de Spintronique et Nanomagnétisme à l'Institut Jean Lamour. Ce travail ne serait jamais né sans l'aide précieuse de nombreuses personnes que je souhaite remercier chaleureusement.

Je remercie Juan-Carlos Rojas-Sánchez et Sébastien Petit-Watelot pour votre encadrement et votre énorme soutien. Je suis vraiment très heureuse de vous avoir eu tous les deux comme encadrants.

Carlos, je te remercie de m'avoir appris à faire les mesures de transport (de la seconde harmonique à la ST-FMR) et pour tes conseils en fabrication en salle blanche. Je te remercie aussi de m'avoir poussée à m'impliquer dans le métier de chercheur, en m'initiant au peer-review d'articles et en me poussant à vaincre ma timidité en présentant nos travaux à des conférences.

Sébastien, Seb, je te remercie de m'avoir poussée à mettre le nez dans le modèle analytique et d'avoir corrigé tant de fois des erreurs de calcul. Merci de t'être tant impliqué dans l'interprétation de mes résultats, et de m'avoir poussée à réfléchir à la physique qui pouvait se cacher derrière (tout ça autour d'un bon thé). Tu m'as aussi appris à être critique quant à nos méthodes et nos résultats, et je pense que cela m'aidera dans le futur à produire la meilleure recherche possible.

Je remercie Michel Hehn, tout d'abord pour la croissance de très nombreux échantillons de qualité supérieure, mais aussi pour ton implication dans mes travaux. Vive la Moselle.

Je remercie également les membres des différents des centres de compétences qui m'ont beaucoup appris: Laurent Badie, Gwladys Lengaine, Demba Ba du CC Minalor pour m'avoir

formée et/ou aidée à la lithographie optique. Je vous remercie d'avoir passé du temps avec moi pour essayer de régler mes problèmes de résine qui ne part pas après le lift-off. Promis Laurent, je te laisse tranquille. Sylvie Migot et Jafaar Ghanbaja du CC 3M, pour m'avoir respectivement appris à faire les lames FIB et pour la caractérisation TEM de mes échantillons. Stéphane Suire du CC Cryo, pour m'avoir formé à la manipulation et aux transferts de liquides cryogéniques et de m'avoir aidé ici et là pour d'autres projets techniques, toujours dans l'humour et la bonne humeur. J'ai énormément d'estime pour le temps que j'ai passé avec vous tous. Je vous souhaite à tous bonne continuation et de beaux projets.

The members of Team 101 have also contributed to the success of this thesis, whether for their help with my work[1], the scientific discussions[2], the card and board game sessions[3] or their good humor[4] :
1 and 2) Alberto A., I'd like to thank you for the help you provided me here and there for the parterning of devices and for transport measurements. Junta I., it was a pleasure discussing with you about our respective work and about orange cats. You both are very inspiring people and I hope to be as good postdoc researcher as you are. Je remercie également Emeric R. et Arthur H. avec qui j'ai pu travailler lors de leur stage et qui ont contribué à des résultats expérimentaux se trouvant dans cette thèse.
3) Valentin D., Sandrine L., Yann LG., merci de m'avoir appris à jouer au Tarot, à la Couinche et à la Belote. Valentin D., Sandrine L., Yann LG., Maxime V., Jude CS., Jon G. and Seb PW., thank you for playing Tarot, Couinche, Belote almost every day. These card games were my favorite moment of the day I have to say. Alberto A., thank you for bringing the tradition of board games to the team. Destroying the queen in Nemesis is still my favorite memory.
4) Anna M F., tant de choses à dire ... merci pour tout. Je te souhaite le meilleur. Yi P., one of the best parts of my thesis was sharing the office with you. Thank you for teaching me about the Chinese culture and especially food. See you ASAP at conferences ! Valentin D., la rédaction de thèse n'est pas forcément le moment le plus drôle de la thèse, mais j'en garderai un bon souvenir grâce aux sessions d'écriture que nous avons fait ensemble. Maxime V., merci pour ta gentillesse et ton soutien lors de ma rédaction de thèse. Tes mèmes sont les meilleurs. My sincere regards to everyone I've met : Eva D., Po-Wei L. (my "self-torque bro"), Jean-Loïs B., Victor P., Jérémy L., Wei Y., Wei Z., Mingming T., Hangtian W., Tianxun H., Jun-Xiao L., Corentin P., Mariam M., Junior A., Melissa Y., Magherlly D., Rodrigo M.,... I wish the best to the new students in our team : Akilan K., Hyacinthe C., Harjinder S., Léo P., Théo C., Corentin A., Boonthum K.. The PhD is a great journey, I hope it will be as fun and inspiring as mine. Pour finir, j'exprime mes remerciements aux membres permanents de l'équipe 101 qui font au mieux pour permettre aux étudiants de se former et d'évoluer dans un cadre encourageant et sain.

During my Ph.D., I had the opportunity to spend a month at the Magnetic Resonance Laboratory in San Carlos de Bariloche, Argentina, thanks to the Ultimate I. program. I'd like to thank the program for this opportunity, and the people of the laboratory for making this visit unforgettable : Luis AF., Mara G., Marcello VM., Jose Luis AT., Ana S., Florencia L., and Daniela PV.. Je remercie également particulièrement Isabelle Fournelle sans qui

aucun de mes déplacements en France ou à l'étranger n'aurait été possible. Tout le chocolat du monde ne suffirait pas pour te remercier à la hauteur de ton aide.

J'aimerais remercier mes amies pour leur soutien, et pour m'avoir toujours tendu une oreille dans les moments les plus difficiles : Julie J., Eva M., et Aurélie G-H.. Aurélie, je te souhaite beaucoup de succès pour ta thèse.

Je tiens à remercier Guillaume (aka mon Doudou) avec qui j'ai partagé ces 5 dernières années. Merci de m'avoir plus ou moins écouté quand je me plaignais de ma thèse, merci de m'avoir fait à manger quasiment tous les jours, et merci de me faire tant rire. Et pour finir, un énorme merci à mes parents et mes frères pour leur soutien depuis toujours et d'avoir organisé (je cite) "le meilleur pot de thèse que l'équipe 101 ait connu". Je vous aime tous infiniment.

Abstract

Spintronics has emerged as a revolutionary science for innovative information processing and storage technologies. Based on the fundamental law of conservation of angular momentum, spintronics uses spin currents to manipulate the orientation of the magnetization of a magnetic film to write and store information. Because data is encoded in the magnetic state, spintronic-based memory devices offer non-volatile storage capabilities, ensuring data persistence even without power. To meet the challenges posed by the ever-increasing amount of digital data, spintronics is dedicated to developing sustainable and effective solutions by continuously exploring new materials and spin current generation mechanisms. The research work presented in this thesis is in line with these efforts and presents GdFeCo ferrimagnet as an interesting material for the generation of spin currents with different symmetries and for the generation of self-torque, i.e. the spin-orbit torque generated in a single magnetic layer. Due to the presence of two magnetic sublattices whose relative dominance can be tuned by temperature, GdFeCo can be used as a platform to better understand the generation of spin currents and self-torque in this material. We first report the study of the spin current generated by GdFeCo and absorbed by NiFe, carried out at different temperatures using the spin-torque ferromagnetic resonance technique. We show that the spin current responsible for the generation of the self-torque has the same sign independently of the magnetic state of the ferrimagnet, which can be tuned by temperature. We then report the study of the spin-orbit torque and the self-torque using the second harmonic technique. While the sign of the damping-like spin-orbit torque induced by a Pt layer is unchanged over the magnetization compensation of GdFeCo, we report that the sign of the self-torque in a quasi-isolated GdFeCo changes over the compensation. Finally, we present different structures that allow to increase the efficiency of the self-torque by allowing the electrical switching of the magnetization, paving the way for the use of self-torque in applications.

Résumé

La spintronique s'est imposée comme une science révolutionnaire pour les technologies innovantes de traitement et de stockage de l'information. Fondée sur la loi fondamentale de la conservation du moment cinétique, la spintronique utilise les courants de spin pour manipuler l'orientation de l'aimantation d'un film magnétique afin d'écrire et de stocker de l'information. Les données étant encodées dans l'état magnétique, les dispositifs de mémoire basés sur la spintronique offrent des capacités de stockage non volatiles, garantissant la persistance des données même en l'absence d'alimentation. Pour relever les défis posés par la quantité toujours croissante de données numériques, la spintronique se consacre au développement de solutions durables et efficaces en explorant continuellement de nouveaux matériaux et mécanismes de génération de courant de spin. Les travaux de recherche présentés dans cette thèse s'inscrivent dans la continuité de ces efforts et présentent le matériau ferrimagnétique GdFeCo comme un matériau intéressant pour la génération de courants de spin avec différentes symétries et pour la génération de *self-torque*, c'est-à-dire de couple de spin-orbite généré dans une seule couche magnétique. Grâce à la présence de ses deux sous-réseaux magnétiques dont la dominance peut être contrôlée par la température, GdFeCo peut être utilisé comme une plateforme pour pousser notre compréhension sur la génération de courants de spin et de *self-torque* dans ce matériau. Nous rapportons tout d'abord l'étude du courant de spin généré par GdFeCo et absorbé par NiFe, réalisée à différentes températures par la technique de résonance ferromagnétique du couple de spin. Nous montrons que le courant de spin responsable de la génération de *self-torque* a le même signe indépendamment du sous-réseau magnétique dominant du ferrimagnétique, qui peut être contrôlé par la température. Nous présentons ensuite l'étude du couple spin-orbite et du *self-torque* à l'aide de la technique de la seconde harmonique. Alors que le signe du couple spin-orbite induit par une couche de Pt reste inchangé lors de la compensation de l'aimantation du GdFeCo, nous rapportons que le signe du *self-torque* dans un GdFeCo quasi-isolé change lors de la compensation magnétique du ferrimagnétique. Enfin, nous présentons différentes structures qui permettent d'augmenter l'efficacité du *self-torque* en permettant le renversement électrique de l'aimantation, ouvrant la voie à des applications pour les *self-torques*.

Contents

Introduction

With the proliferation of connected devices, the exponential growth of the Internet and the rapid development of various technologies, our world is witnessing a flood of digital data that needs to be manipulated and stored, putting immense pressure on our existing data storage infrastructure. It is estimated that global storage consumption, which stood at 286 TWh in 2016, will rise to 321 TWh by 2030 [1], equivalent to 1.15 times the energy produced by the entire nuclear power plant of France in 2022 [2]. In response to the escalating data challenge, research efforts must focus on developing of effective and sustainable solutions. In this context, today's electronics face certain constraints: the miniaturization of electronic elements is approaching its physical limits, and the corresponding need for heat dissipation results in an additional energy consumption for cooling mechanisms [3]. For example, random access memory (RAM) requires a continuous power supply to prevent data loss. Unlike electronics, which rely solely on the motion of electron charges, spintronics exploits the interplay between the quantum properties of electron spin and magnetism. A spin current, consisting of electrons with identical spins, becomes a tool for manipulating the orientation of the magnetization of a magnetic material, which correlates with the binary values of 0 and 1. Because data is encoded within a magnetic state, spintronics-based memory devices offer non-volatile storage capabilities - meaning that information persists even without a power supply. Thanks to this fundamental change, spintronics has emerged in recent decades as a key discipline for the development of innovative technologies for information processing and storage.

The birth of spintronics can be traced back to the discovery of giant magnetoresistance (GMR) in 1988 by A. Fert [4] and one year later by P. Grünberg [5], for which they were awarded the Nobel Prize in 2007. This discovery contributed significantly to the development of more efficient and compact read heads within hard disk drives (HDD) [6], thereby significantly increasing storage capacity. The transfer of angular momentum between a spin current and a magnetization was later predicted by J.C. Slonczewski [7] and L. Berger [8] in 1996 and led to the electrical manipulation of magnetization. These major revolutions paved the way for the creation of magnetic random access memory (MRAM) devices, which combine the advantages of traditional semiconductor memory with non-volatile magnetic

storage. Continuing along this path, the discovery of spin-orbit torque (SOT) in 2010 [9] introduced an alternative method of generating spin currents and writing information in a power-efficient manner, and has attracted considerable attention for its potential to drive the development of high-density memory and logic devices.

Conventional SOT-MRAM relies on a multilayer configuration that includes magnetic layers and non-magnetic heavy metals. These elements serve different purposes: the magnetic layers store information, while the heavy metals are responsible for writing the information. However, due to this complex structure, the scalability of such devices presents challenges, such as maintaining efficient spin manipulation, which requires innovative fabrication techniques. Therefore, new materials, new structures and new spin current generation mechanisms are being explored. In this context, SOT within a single layer (called bulk SOT, or mainly self-torque in this thesis) has emerged as a promising approach to simplify device architectures.

Self-torque was first observed in crystalline materials in 2014 [10] and 2016 [11]. However, the first observation of self-torque in a polycrystalline ferromagnetic material -preferred for practical applications- occurred only in 2019 [12]. My research journey started in 2020, focusing on GdFeCo amorphous ferrimagnet as the main material for efficient self-torque generation. During my research, it seems that GdFeCo also provides a unique platform to study the origins of self-torque mechanisms, especially thanks to the temperature-dependent ferrimagnetic properties.

The primary objective of this thesis is to present the main results of my research on self-torque in a quasi-isolated layer of GdFeCo without relying on external heavy metals known to generate spin currents. My thesis also highlights ways to improve the self-torque with respect to its potential integration into practical spintronic applications. This thesis is organized as follows:

- Chapter 1 provides a textbook description of the various mechanisms involved in spin currents, from their generation to their transport to their absorption, and provides a definition of self-torque.

- Chapter 2 introduces the GdFeCo ferrimagnet. Its structural and magnetic properties are described, as well as new phenomena observed in this material. Emphasis is placed on properties that make the material a good candidate for the study of self-torque.

- Chapter 3 presents the nuanced magnetotransport properties of GdFeCo. The idea is to present an up-to-date view of the magnetotransport properties of this type of ferrimagnet.

- Chapter 4 presents a model to describe the magnetization dynamics. This model is the starting point for the calculation of the analytical expressions for the voltages for the study of the spin current generation of GdFeCo as well as for the study of the self-torque.

- Chapter 5 investigates the spin current generation in GdFeCo using the spin transfer ferromagnetic resonance (ST-FMR) technique at different temperatures.
- Chapter 6 explores the sign of the spin-orbit torque and self-torque in GdFeCo using the second harmonic technique.
- Chapter 7 focuses on various structures that can be used to increase the self-torque, which is critical to their viability in applications.
- The conclusion gives a synthesis of the results of my research.

CHAPTER 1

From spin current to self-induced spin-orbit torque

The motivation of this chapter is to present the life cycle of a spin current, from its generation to its absorption, and to describe the effect this process has on the magnetization of a magnetic material. To this end, we first introduce the different types of currents encountered throughout this thesis. We then focus on the charge-to-spin conversion effects that generate spin currents in spin-orbit coupled materials. Spin currents propagate through matter but are subject to relaxation effects that tend to randomize the spins. While the total angular momentum of the system is a conserved quantity, a spin current is not. As a consequence, in certain configurations that we will describe, it is possible to transfer the spin angular momentum carried by the spin current to a local magnetization. This process results in a torque on the magnetization, called spin-transfer torque or spin-orbit torque depending on the source of the spin current. The dynamics of the magnetization without and with the action of a spin torque is presented. The concept of the *self-induced* spin-orbit torque, which is at the heart of this thesis, is then explained.

1.1 Charge current, spin current and spin accumulation

The concepts of charge and spin current densities are essential in spintronics. Although both current densities represent the displacement of charges or spins, they are still different mathematical objects. On the one hand, the charge current density $\vec{J}_c$ is a vectorial quantity representing the density of electrons n of charge e flowing along a direction given by their velocity $\vec{v}$. On the other hand, the spin current density $\overline{J}_s$ is a tensorial quantity and takes into account not only the flow direction, but also the spin direction, i.e. the spin polarization $\vec{\sigma} = \hbar/2\hat{\sigma}$ [13, 14]. Their general expressions are:

$$\vec{J}_c = -ne\vec{v} \qquad \text{and} \qquad \overline{J}_s = \vec{v} \otimes \vec{\sigma}, \tag{1.1}$$

with the charge current density expressed in $\mathrm{A/m^3}$, and the spin current density expressed in units of $\hbar$.

The electronic transport can essentially be deduced from the shape of the conduction band at the Fermi energy level [15, 16]. The associated surface separates the filled states from the empty states, and only the electrons at the Fermi level can contribute to the conduction. For non-magnetic metals, the Fermi surfaces are identical regardless of the spin state. The situation is different for magnetic metals, such as transition metals, where the Fermi surfaces are different for spin-up $\uparrow$ and spin-down $\downarrow$ electrons [17]. As a consequence, magnetic materials show spin dependent conduction and we can consider that the transport is achieved through two spin channels; this is known as the two-channel Mott model [18]. As a consequence, we can express the spin currents $J_{\uparrow(\downarrow)}$ for the $\uparrow$ electrons and for the $\downarrow$ electrons and define the spin dependent electron density $n_{\uparrow(\downarrow)}$ and the spin dependent velocity $v_{\uparrow(\downarrow)}$:

$$\vec{J_{\uparrow}} = -n_{\uparrow} e \vec{v_{\uparrow}} \qquad \text{and} \qquad \vec{J_{\downarrow}} = -n_{\downarrow} e \vec{v_{\downarrow}}, \tag{1.2}$$

where we voluntarily omit the tensorial definition of the spin current and use the same units as for the charge current density to simplify the expressions. Hereafter, we describe the different contributions to the spin currents, namely the drift current and the diffusion current.

1.1.1 Drude model for the drift current density

In the presence of an electric field $\vec{E}$, the drift current density $\vec{J}^{\text{drift}}_{\uparrow(\downarrow)}$ is directly proportional to the spin dependent conductivity matrix $\overline{\sigma}_{\uparrow(\downarrow)}$, which has the following form in the framework of the Drude model [15]:

$$\vec{J}^{\text{drift}}_{\uparrow(\downarrow)} = \sigma_{\uparrow(\downarrow)} \vec{E} \quad \text{with} \quad \overline{\sigma}_{\uparrow(\downarrow)} = \frac{\rho_{\uparrow(\downarrow)}(E_F) e^2 \tau_{\uparrow(\downarrow)}}{m}, \tag{1.3}$$

where $\overline{\sigma}_{\uparrow(\downarrow)}$ is directly related to the Fermi surface by the electronic density of state at the Fermi energy E_F for each spin population $\rho_{\uparrow(\downarrow)}(E_F)$. It also depends on the spin dependent scattering rate $\tau_{\uparrow(\downarrow)} = l_{\uparrow(\downarrow)}/v_F$, where $l_{\uparrow(\downarrow)}$ is the mean free path and v_F is the Fermi velocity.

1.1.2 Fick law for the diffusive current density

Let us consider an interface between a non-magnetic material and a magnetic material. Because of the change in conductivity for the two spin populations across the interface, one spin population can be locally in excess. This is called a spin accumulation, which is expressed as the gradient of the carrier density $\vec{\nabla} n_{\uparrow(\downarrow)}$. The imbalance then relaxes to equilibrate the population. The diffusive spin current $\vec{J}^{\text{diffusion}}_{\uparrow(\downarrow)}$ associated with this diffusion mechanism is governed by the Fick law:

$$\vec{J}^{\text{diffusion}}_{\uparrow(\downarrow)} = e \overline{D}_{\uparrow(\downarrow)} \vec{\nabla} n_{\uparrow(\downarrow)}, \tag{1.4}$$

where the spin-dependent diffusion tensor $\overline{D}_{\uparrow(\downarrow)}$ is directly related to the spin-dependent conductivity tensor and to the Fermi energy by the Einstein relation [19]:

$$\overline{D}_{\uparrow(\downarrow)} = \frac{\overline{\sigma}_{\uparrow(\downarrow)}}{e^2 \rho_{\uparrow(\downarrow)}(E_F)}. \tag{1.5}$$

This expression highlights that the driving force of a diffusive spin current density is the gradient of the carrier density $\vec{\nabla} n_{\uparrow(\downarrow)}$.

1.1.3 Generalized Ohm law for the total current density

The two aforementioned contributions to the electronic transport can be summarized in the generalized Ohm's law [19]:

$$\vec{J}_{\uparrow(\downarrow)} = \overline{\sigma}_{\uparrow(\downarrow)} \vec{E} + e\overline{D}_{\uparrow(\downarrow)} \vec{\nabla} n_{\uparrow(\downarrow)}. \tag{1.6}$$

We can introduce another parameter: the spin-dependent electrochemical potential $\mu_{\uparrow(\downarrow)}$ which is the sum of the chemical potential $\nu_{\uparrow(\downarrow)} = \dfrac{n_{\uparrow(\downarrow)}}{\rho_{\uparrow(\downarrow)}}$ and electrostatic potential $-eV$, i.e. $\mu_{\uparrow(\downarrow)} = \nu_{\uparrow(\downarrow)} - eV$. Thus, the spin dependent conduction takes the final form:

$$\vec{J}_{\uparrow(\downarrow)} = \frac{\overline{\sigma}_{\uparrow(\downarrow)}}{e} \vec{\nabla} \mu_{\uparrow(\downarrow)}, \tag{1.7}$$

where the gradient of the spin-dependent electrochemical potential $\vec{\nabla} \mu_{\uparrow(\downarrow)}$ is the driving force of the spin current here.

1.1.4 Charge current, spin-polarized current and pure spin current

Knowing the expression for the spin dependent conduction, we can define the total charge current $\vec{J}_c = \vec{J}_\uparrow + \vec{J}_\downarrow$ and the total spin current densities $\vec{J}_s = \vec{J}_\uparrow - \vec{J}_\downarrow$ as:

$$\vec{J}_c = \frac{1}{e} \vec{\nabla} (\overline{\sigma}_\uparrow \mu_\uparrow + \overline{\sigma}_\downarrow \mu_\downarrow) \qquad \text{and} \qquad \vec{J}_s = \frac{1}{e} \vec{\nabla} (\overline{\sigma}_\uparrow \mu_\uparrow - \overline{\sigma}_\downarrow \mu_\downarrow), \tag{1.8}$$

and several scenarios can occur depending on the material:

- In non-magnetic metals, $\overline{\sigma}_\uparrow = \overline{\sigma}_\downarrow$. If there is no spin accumulation such that $\mu_\uparrow = \mu_\downarrow$, then the transport consists of a *charge current* with no net spin current flow, as shown in Figure 1.1(a).
- In non-magnetic metals, $\overline{\sigma}_\uparrow = \overline{\sigma}_\downarrow$. If there is a spin accumulation such that $\nabla(\mu_\uparrow - \mu_\downarrow) \neq 0$, then two diffusive spin currents of opposite polarities flow in opposite directions. The result is a *pure spin current* that carries angular momentum without being carried by a net charge current, as shown in Figure 1.1(b).
- In magnetic metals, $\overline{\sigma}_\uparrow \neq \overline{\sigma}_\downarrow$. As a result, the charge current is said to be *spin-polarized*, as illustrated in Figure 1.1(c). The direction of the spin polarization is then given by the orientation of the magnetization of the magnetic layer.

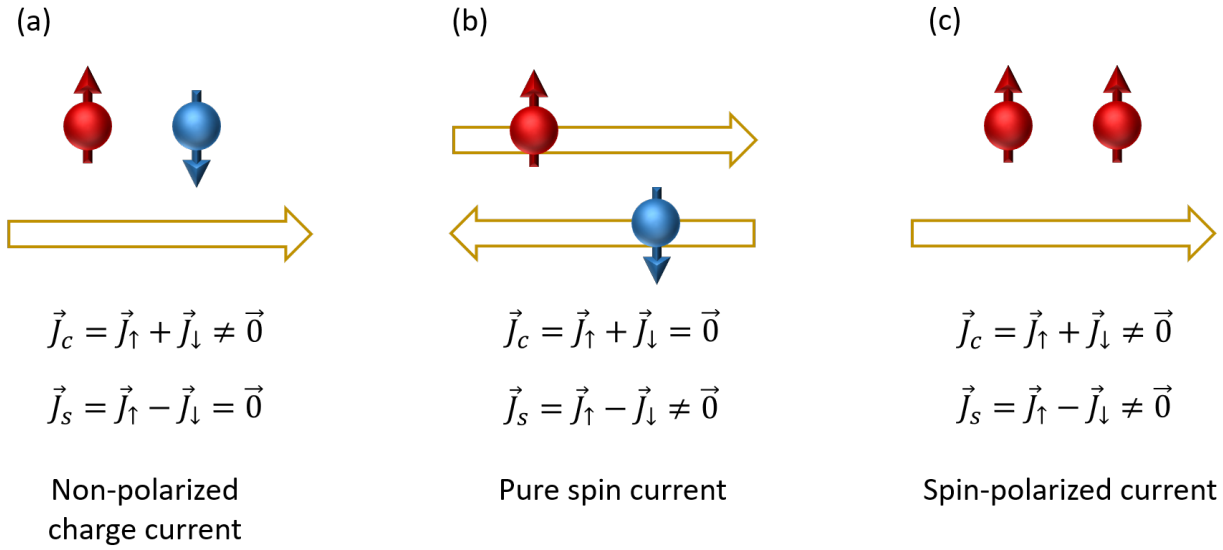

Figure 1.1: Illustration of the different types of currents. (a) Pure charge current, (b) pure spin current and (c) spin-polarized current.

We define the polarization of the spin-polarized current as the difference in the spin population at the Fermi level:

$$P = \frac{J_\uparrow - J_\downarrow}{J_\uparrow + J_\downarrow} = \frac{n_\uparrow v_\uparrow - n_\downarrow v_\downarrow}{n_\uparrow v_\uparrow + n_\downarrow v_\downarrow}. \tag{1.9}$$

Various excitations can lead to the generation of spin currents, such as thermal gradient [20], spin pumping [21, 22], mechanical rotation [23], electric current [24, 25] and so on [26]. We will now focus on mechanisms that transform a charge current into a spin current which is catalyzed by the spin-orbit interactions.

1.2 Spin current generation by spin-orbit coupling

The spin-orbit interaction is a relativistic effect that links the trajectory of a particle to its spin angular momentum [27]. Materials that exhibit this effect, mainly 4d and 5d heavy metals, also exhibit exotic transport phenomena. In particular, it is at the origin of several mechanisms of conversion of a charge current into a spin current. The coupling between the spin and the trajectory of an electron is first derived mathematically. Then we consider spin Hall effects, which occur in the volume of the material and the Rashba effect (RE), which usually occurs at interfaces.

1.2.1 Origin of spin-orbit coupling

Spin-orbit coupling (SOC) is a fundamental component for the conversion of a charge current into a spin current and vice versa. This relativistic effect takes place in heavy atoms where the electrons can be treated as relativistic particles. Let us consider an isolated atom and one of its electrons. The latter moves in the electric field $\vec{E}$ generated by the nucleus, which

can be expressed as the gradient of a spherical potential $V(r)$:

$$\vec{E} = -\frac{dV(r)}{dr}\hat{r}. \tag{1.10}$$

Due to relativistic effects, the electron sees the electric field in its frame as an effective magnetic field $\vec{B}_{SO}$ as a consequence of the Lorentz transformation:

$$\vec{B}_{SO} = -\frac{\vec{v} \times \vec{E}}{c^2}, \tag{1.11}$$

where $\vec{v}$ is the velocity of the nucleus in the electron frame and c is the speed of light. Considering the definition of the angular momentum $\vec{L} = \hat{r} \times \vec{p}$, we can see that the effective magnetic field is related to the angular momentum:

$$\vec{B}_{SO} = \frac{1}{mc^2}\frac{1}{r}\frac{dV}{dr}\vec{L}. \tag{1.12}$$

As a result, the spin angular momentum of the electron $\vec{\mu}_s = \frac{g_s e}{2m}\vec{S}$ is aligned with the effective magnetic field by a Zeeman interaction described by the following Hamiltonian $\mathcal{H}_{SO}$:

$$\mathcal{H}_{SO} = -\vec{\mu_s} \cdot \vec{B}_{SO} = \frac{1}{2m^2c^2}\frac{1}{r}\frac{dV}{dr}\vec{S} \cdot \vec{L} = \lambda_{SO}\vec{S} \cdot \vec{L},$$

where λ_{SO} is the spin-orbit coupling constant which depends on the atomic number Z. The effect of the spin-orbit coupling can be seen from the previous equation: the orbital angular momentum tends to align with the spin of the electron. In other words, a change in the trajectory of the electron induces a change in the spin, and vice versa.

We have derived the equations for an isolated atom, but the reasoning can be extended without loss of generality to a conducting electron in a metal. Any kind of electric field that the electron encounters (crystalline field, electric field radiated by an impurity) can be seen as an effective magnetic field that couples the spin to the electron trajectory. We will see in the next subsection that this results in a spin-dependent transverse velocity for the electron, which generates a spin current or spin accumulation in the material.

1.2.2 Spin Hall effects

Hall effects are mechanisms that convert an electric current into a transverse current. They are named after E. H. Hall, who demonstrated in 1879 that a normal metal exposed to a magnetic field generates a transverse voltage [28]. This ordinary Hall effect (HE) is explained by the deflection of the trajectory of the charge carriers influenced by the Lorentz force (see Figure 1.2(a)). As a result, carriers of opposite charge accumulate at opposite edges of the material, creating a voltage known as the Hall voltage. The name *spin Hall effect* was later given by J. E. Hirsch in 1999, in analogy to the HE, to new effects that transform a charge current into a transverse spin current. Here we consider two central effects:

- The anomalous Hall effect (AHE):

After the discovery of the HE, E. H. Hall discovered a similar effect in magnetic materials in 1881 [29]. In addition to the HE, he highlighted a contribution related to the magnetization known as the anomalous Hall effect (AHE). Electrons flowing in magnetic materials develop a spin-dependent velocity that is transverse to the current flow, as shown in Figure 1.2(b). The AHE produces both spin and charge accumulations at the edges, allowing the measurement of a Hall voltage that contains information about the magnetization. The quality of the conversion from a charge current to a transverse charge accumulation is defined by the Anomalous Hall angle θ_{AHE}, which is the ratio between the generated transverse electric field E_y and the applied longitudinal electric field E_x [30]. It can also be expressed in terms of the corresponding voltages V_Y and V_X considering the width w and the length L of the current line:

$$\boxed{\theta_{AHE} = \frac{E_y}{E_x} = \frac{V_Y}{V_X}\frac{L}{w}.} \tag{1.13}$$

Nowadays, the spin accumulation generated by the AHE is exploited to induce a spin transfer torque on another magnetic layer [31]. The notion of spin torque will be introduced in Section 1.4.2. In this case, the AHE is often referred to as the spin anomalous Hall effect (SAHE) [32], and the efficiency of the conversion from the longitudinal charge current to the transverse spin-polarized current is given by the dimensionless parameter θ_{SAHE} so that:

$$\boxed{\vec{J}_s = -\frac{\hbar}{2e}\,\theta_{SAHE}\,(\hat{m} \times \vec{J}_c) \otimes \hat{\sigma}_{SAHE}, \qquad \text{with} \qquad \hat{\sigma}_{SAHE} \parallel \hat{m}.} \tag{1.14}$$

- The spin Hall effect (SHE):
  M. I. Dyakonov and V. I. Perel predicted in 1971 that the same spin-dependent transverse velocity can take place in a non-magnetic material with spin-orbit coupling [33]. Since there is no magnetization, an equal number of electrons with opposite spins are deflected in opposite directions and no electric voltage is generated. The spin polarization is transverse to both the initial charge current and the final pure spin current, as shown in Figure 1.2(c). The quality of the conversion from a longitudinal charge current to a transverse pure spin current is given by the Spin Hall angle θ_{SHE} which is the ratio of the transverse conductivity to the longitudinal conductivity:

$$\boxed{\theta_{SHE} = \frac{\sigma_{XY}}{\sigma_{XX}} \qquad \text{and} \qquad \vec{J}_s = -\frac{\hbar}{2e}\,\theta_{SHE}\,(\hat{\sigma}_{SHE} \times \vec{J}_c) \otimes \hat{\sigma}_{SHE}.} \tag{1.15}$$

  The SHE has aroused great interest and opened up new perspectives for the development of magnetic memories, as it allows the magnetization of a magnetic layer to be electrically manipulated by a spin-orbit torque. The latter concept is introduced in Section 1.4.3.

The microscopic mechanisms behind the generation of transverse spin currents are now essentially described by two main contributions: an intrinsic one and an extrinsic one [30, 34], which arise from the spin-orbit interaction:

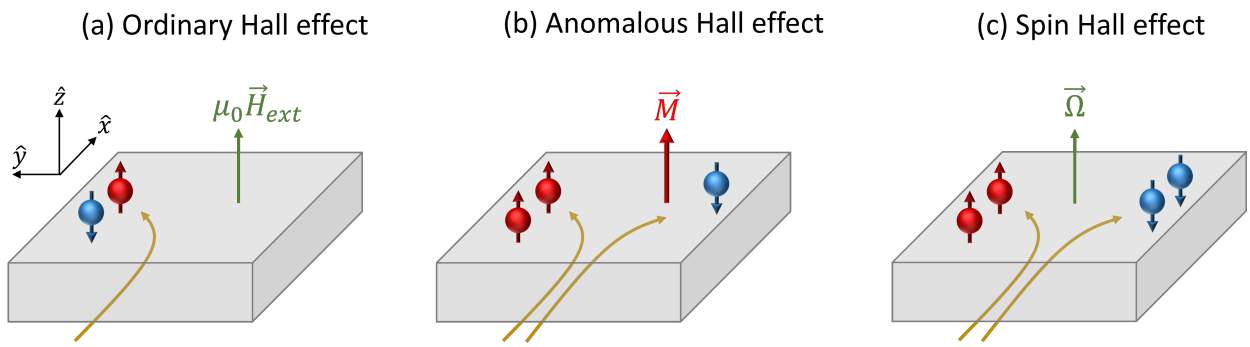

Figure 1.2: Illustration of different Hall effects. (a) Ordinary Hall effect resulting from an external magnetic field $\mu_0\vec{H}_{ext}$, (b) anomalous Hall effect in a magnetic layer with magnetization $\vec{M}$, and (c) spin Hall effect in a non-magnetic material with Berry curvature $\vec{\Omega}$.

- The intrinsic contribution (Figure 1.3(a)):
  The transverse spin-dependent velocity arises only from the effect of spin-orbit coupling on the band structure [35] and thus evolves between scattering events [34]. This anomalous velocity is now explained by the concept of Berry curvature $\vec{\Omega}$, which can be seen as a pseudomagnetic field in the momentum space that affects the trajectories of the conduction electrons [36]. The intrinsic spin Hall conductivity is directly related to the Berry curvature as:

$$\sigma_{xy}^{\text{intrinsic}} = \frac{e^2}{\hbar}\sum_{\vec{k}}\Omega_n^z(\vec{k}) \propto \rho_{xx}^{-2}. \tag{1.16}$$

- The extrinsic side-jump contribution (Figure 1.3(b)):
  During scattering events with impurities with spin-orbit coupling, the conduction electron is accelerated and decelerated differently depending on its spin [34]. This results in a spin dependent velocity for repeated scattering events. This contribution is therefore directly proportional to the impurity concentration. The relevance of this contribution is questioned as it may be weak compared to the skew scattering contribution, even for very dirty materials [37, 38]. The Hall resistivity is therefore directly proportional to the square of the longitudinal resistivity:

$$\rho_{xy}^{\text{side-jump}} \propto \rho_{xx}^2 \tag{1.17}$$

- The extrinsic skew scattering contribution (Figure 1.3(c)):
  This contribution comes from the effective magnetic field generated by the impurity with spin-orbit coupling. The spin of the conduction electrons interacts with this magnetic field and the trajectory of the electron is therefore affected [34]. The result is a transverse spin dependent velocity. This effect is independent of the impurity concentration and the Hall resistivity evolves with the longitudinal resistivity:

$$\rho_{xy}^{\text{skew}} \propto \rho_{xx} \tag{1.18}$$

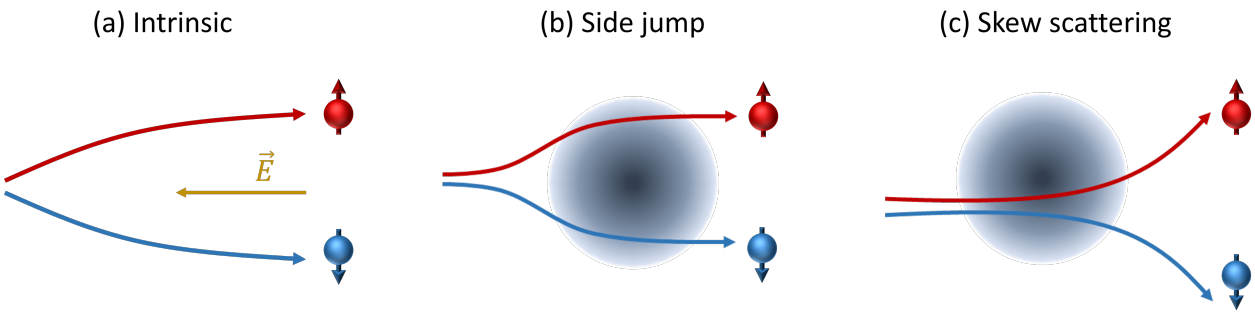

Figure 1.3: Illustration of the different mechanisms that produce a transverse spin dependent velocity. (a) The intrinsic mechanism, (b) the side jump mechanism, and (c) the skew scattering mechanism.

The SHE and the (S)AHE are bulk effects. At the interface, the intrinsic contribution gives rise to the Rashba effect.

1.2.3 Rashba effect

Volumes and interfaces have very unique properties because the atoms in the bulk experience a different environment than those at the interface. In fact, the interface breaks the continuity of the crystal electric field, and the atoms in the vicinity experience an electric field, called the Rashba field $\vec{E}_R$, normal to the interface. For the electrons at the interface, the Rashba field is experienced as an effective magnetic field $\vec{H}_R$ perpendicular to both the Rashba field and the direction of the current. As a consequence, the spin of the conduction electrons interacts with this magnetic field through a Zeeman interaction, so that:

$$H_{SO} \propto (\vec{E}_R \times \vec{k}) \cdot \vec{S}, \tag{1.19}$$

where $\vec{k}$ is the electron momentum and $\vec{S}$ is the Pauli matrix that account for the spin of the electron. This expression emphasizes the connection between the motion of the electron and its spin. The energy eignevalue of the electron is therefore the sum of its kinetic energy and its spin-orbit interaction:

$$\epsilon_{\pm,k} = \frac{\hbar^2 k^2}{2m_e^*} \pm \alpha_R |k|. \tag{1.20}$$

This energy dispersion equation accounts for a constant shift $+\alpha_R$ for $\uparrow$ spins and $-\alpha_R$ for $\downarrow$ spins. In other words, the spin-orbit coupling at the interface lifts the spin degeneracy, as illustrated in Figure 1.4(a). The Fermi surface and the spin texture associated with the bands are shown in Figure 1.4(b).

When an electric field is applied, or when a charge current is injected, the Fermi surfaces are both shifted by a value δk, as illustrated in Figure 1.4(c). This shift induces a spin accumulation transverse to the charge current, since the opposite contributions no longer compensate each other.

In summary, the Rashba effect allows to convert a charge current into a spin accumulation.

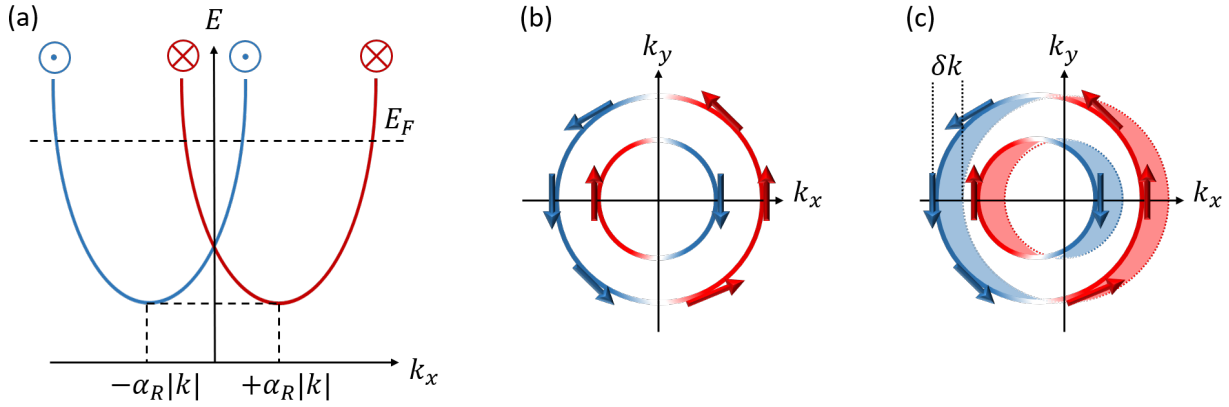

Figure 1.4: (a) Bands with a spin degeneracy lifted by the Rashba interaction. (b) Fermi surface of the (a) band. (c) Fermi surface when an electric field is applied. The Fermi surfaces for both bands are shifted and are not symmetric in $\vec{k}$. A spin accumulation is generated at the interface.

1.2.4 Other spin-orbit induced spin currents

In addition to the traditional spin Hall and Rashba effects, other spin current generation effects have been highlighted. In 2009, M. B. Lifshits *et al.* have introduced a new mechanism for the transformation of spin currents called the spin swapping. This occurs during scattering events in spin-orbit coupled materials [39]. As a result, the spin direction and the flow direction are interchanged. In 2018, effects at spin-orbit coupled interfaces were highlighted by V. P. Amin *et al.*, such as the spin filtering and the spin precession effects [40]. At non-magnetic interfaces, the interfacial spin-orbit field scatterers spin differently depending on their orientation. This leads to filtering, where reflected and transmitted carriers become polarized even if they were not before reaching the interface. At magnetic interfaces, the spins of a polarized current precess around the interfacial spin-orbit field.

We have described different charge-to-spin conversion effects arising from the spin-orbit interaction. After the generation, the spin current can flow in an adjacent metallic material, which can be non-magnetic or magnetic. The spin, as opposed to the charge, is a non-conservative quantity. Consequently, a spin current decays as it flows spatially in matter.

1.3 Spin current relaxation

When we have defined the notion of spin current in section 1.1, we introduced the spin dependent scattering rate $\tau_{\uparrow(\downarrow)} = l_{\uparrow(\downarrow)}/v_F$, where $l_{\uparrow(\downarrow)}$ is the spin dependent mean free path. It represents the time between two scattering events with the associated length for each spin, and the spin information is assumed to be preserved during the scattering. In reality, however, the spin information can be changed and lost during multiple scattering events, and the spin current can be destroyed. The characteristic length on which the spin information is conserved is the spin diffusion length l_{sf} and the associated scattering rate is τ_{sf}. Different mechanisms lead to the decay of the spin current, and we consider here three contributions: the Elliot-Yafet mechanism, the Dyakonov-Perel mechanism, and the spin dephasing

mechanism.

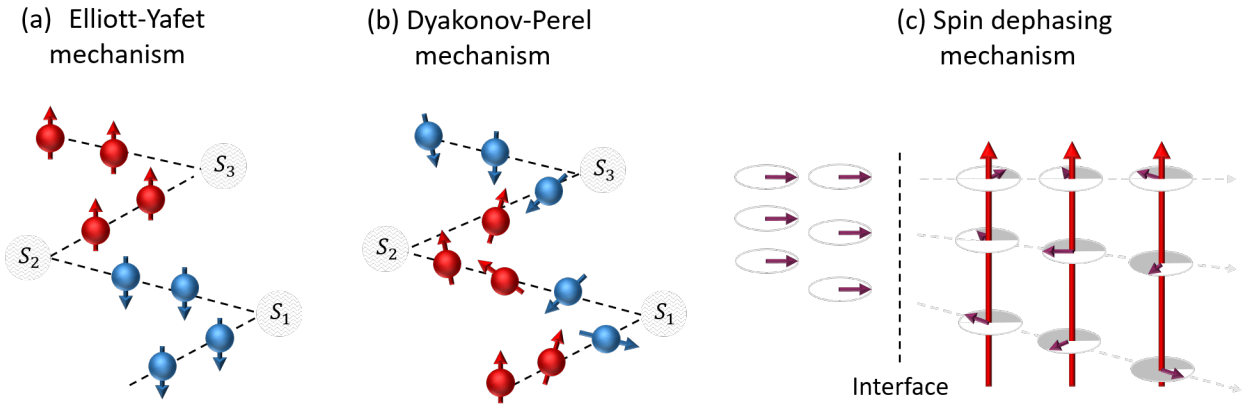

Figure 1.5: Illustration of the different types of spin relaxation mechanisms. (a) The Elliot-Yafet mechanism, (b) the Dyakonov-Perel mechanism, and (c) the spin dephasing mechanism in a magnetic layer.

1.3.1 The Elliot-Yafet mechanism

The Elliot-Yafet (EY) spin relaxation mechanism describes the change in the spin information of conduction electrons during scattering events with impurities and phonons [41, 42] in centrosymmetric systems. With the spin-orbit coupling, the $\uparrow$ and $\downarrow$ eigenstates are mixed, and any spin independent scattering allows the spin to flip from one state to the other. Therefore, the spin current carried by the electrons decays and the information is lost (see Figure 1.5(a)). We expect the scattering rate to increase with the temperature and the phonon population. This spin relaxation mechanism leads to a spin relaxation rate τ_{SO}^{EY} proportional to the elastic scattering rate τ. When the EY effect dominates, the spin-flip length is linearly proportional to the mean free path l.

1.3.2 Dyakonov-Perel mechanism

The Dyakonov-Perel (DP) spin relaxation mechanism describes the fluctuations of the spin between scattering events [43, 44] in systems without inversion symmetry. The spin-orbit coupling induces a $\vec{k}$-dependent effective magnetic field that interacts with the spin and induces its precession. This random walk like precession leads to spin relaxation, as shown in Figure 1.5(b)). In contrast to the EY mechanism, the DP spin relaxation rate τ_{SO}^{DP} is inversely proportional to the elastic scattering rate τ.

1.3.3 Spin dephasing mechanism

When a spin current is injected into a magnetic layer, and if the spin polarization is transverse to the magnetization, the spin polarization decoheres by dephasing (see Figure 1.5(c)). The electrons enter the magnetic layer at different angles with respect to the normal of the interface, and in the magnetic layer, the spins precess around the magnetic exchange field. On the same plan colinear to the interface, the electrons have precess at different rates and,

on average, the spin polarization transverse to the magnetization is lost. This process is similar to the destructive interference of light. In a typical ferromagnet, the spin dephasing length has been estimated to be $\lambda_{dp} \approx 1$ nm [13] due to the rapid dephasing around a strong exchange field of 100T. The spin coherence length is inversely proportional to the exchange field strength. We will see in Chapter 2 that the spin dephasing length is longer in ferrimagnets.

1.4 Spin transfer torque

The spin current carries spin angular momentum. The spin information can be lost, but the total angular momentum of the system must be conserved to satisfy the conservation of angular momentum law. We will see how this law can be observed in magnetic materials and show how angular momentum transfer is possible.

1.4.1 Conservation of the total angular momentum in magnetic materials

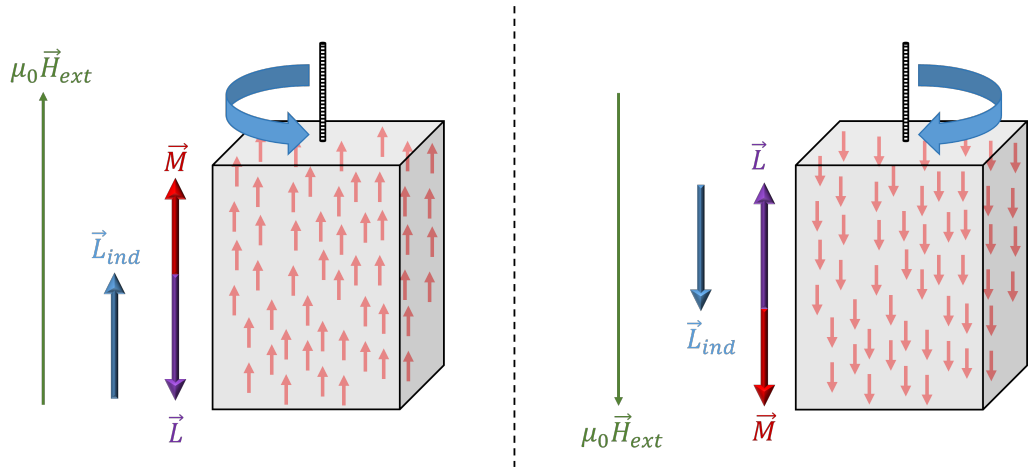

Figure 1.6: Illustration of the Einstein-de Haas effect. A magnetic material is suspended by a rope. The application of a vertical magnetic field $\mu_0\vec{H}_{ext}$ induces a change in the orientation of the magnetization $\vec{M}$ and of the associated orbital angular momentum $\vec{L}$. As a consequence of the conservation of angular momentum, an opposite orbital angular momentum $\vec{L}_{ind}$ is induced by the application of the magnetic field and the material rotates under its influence.

At the beginning of the 20th century, the origin of magnetism in materials was unclear. Immediately after H. C. Oersted's discovery that a magnetic field is created by the circulation of a current in a conductor, A-M. Ampere stated in 1820 that the magnetic properties of a material could be caused by loops of current in the materials, also called molecular currents. In 1915, A. Einstein and W. J. de Haas reported the experimental proof of molecular currents [45] based on the fundamental law of conservation of total angular momentum. In fact, Ampere's molecular loops correspond to an electron orbiting a nucleus. A magnetic dipole momentum can be associated with this current loop, and just as in classical mechanics, we

can associate an angular momentum with this rotating electron. A simple calculation shows:

$$\mu_l = -\frac{|e|}{2m}\vec{l}, \tag{1.21}$$

where μ_l is the orbital magnetic dipole moment and $\vec{l}$ is the orbital angular momentum. Both quantities are antiparallel to each other. We define the total angular momentum $\vec{L}$ and the magnetization $\vec{M}$ as:

$$\vec{L} = \sum_i^{\infty} \vec{l}_i \qquad \text{and} \qquad \vec{M} = \frac{\sum_i^{\infty} \vec{\mu}_i}{V}. \tag{1.22}$$

Thus, the magnetization and the total angular momentum are directly related. The magnetization can be controlled by an external magnetic field and the orbital angular momentum is indirectly controlled. Owing to the law of conservation of the total angular momentum, a change in the magnetization, i.e. a change in the orbital angular momentum, will result in the generation of an opposite and counterbalancing change. This is exactly what A. Einstein and W. J. de Haas demonstrated. The experiment consists of a magnetic cylinder suspended by a rope. At the beginning of the experiment, the material is demagnetized. Therefore, both the magnetization and the angular momentum of the cylinder are zero. When the external magnetic field is applied along the vertical axis, the cylinder begins to rotate counterclockwise. If the magnetic field is applied in the opposite direction, the cylinder rotates clockwise. The rotation of the material is the evidence of an induced angular momentum which counterbalances the one associated with the magnetization, as shown in Figure 1.6.

Angular momentum is conserved in magnetic materials. The spin current carries angular momentum that is associated with the magnetization. Because of the conservation of angular momentum, it is possible to transfer angular momentum from the spin current to the magnetization. Such a process is called spin transfer and allows the manipulation of the magnetization.

1.4.2 Physical idea behind the spin transfer torque

The idea that a transfer of angular momentum between a spin current and a magnetization is possible was introduced by J. Slonczewski in 1996 [7]. For this process to occur, the polarization of the spin current must be non-colinear to the magnetization. In Figure 1.7(a), we consider a spin current polarized along the $\hat{z}$ axis. When the spin-polarized current travels through a magnetic layer whose magnetization is rotated by an angle θ with respect to $\hat{z}$, the spin angular momentum of the electrons precesses and aligns with the magnetization by spin dephasing, which we introduced in section 1.3.3. We can see that the transverse component has been absorbed between the initial and final spin polarizations. By the law of conservation of total angular momentum, the absorbed component has been transferred to the magnetization, and the latter undergoes a torque $\vec{T}$. The effect of this torque is to rotate the magnetization, and for a strong torque it can also reverse the magnetization.

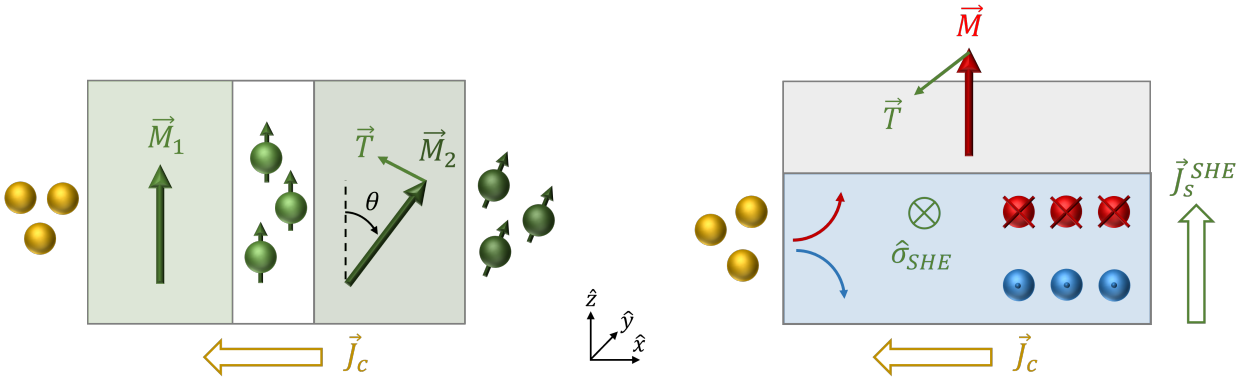

(a) Spin Transfer Torque (STT) (b) Spin-Orbit Torque (SOT)

Figure 1.7: Illustration of the spin transfer torque (STT) and the spin-orbit torque (SOT). (a) A STT acts on the magnetization $\vec{M}_2$ when a $\hat{z}$ spin-polarized current flows through it. The transverse component of the spin polarization is transferred to the magnetization.

1.4.3 Spin-orbit torque

The spin-polarized current or spin accumulation generated by the Rashba effect or the Spin Hall effect can also be exploited to manipulate the magnetization of an adjacent magnetic layer. The reversal of the magnetization under the action of such a torque was experimentally demonstrated in 2010 [9]. This effect is seen as an alternative to STT-MRAM technologies, as the current used to write the information does not flow through the memory cell, leading to an expected better lifetime of the device.

1.5 Effect of a spin torque on the magnetization dynamics

In this section, we first introduce the macrospin equation of motion of the magnetization without a spin torque. Then, we discuss the effect of a spin torque.

1.5.1 Landau-Lifshitz-Gilbert equation

The dynamics of the magnetization $\vec{M}(\hat{r},t)$ is described phenomenologically by the Landau-Lifshitz-Gilbert (LLG) equation [46, 47, 48]:

$$\frac{d\vec{M}}{dt} = -\gamma_0 \vec{M} \wedge \vec{H}_{eff} + \frac{\alpha}{M_S} \vec{M} \wedge \frac{d\vec{M}}{dt}, \tag{1.23}$$

where $\gamma_0 = \mu_0|\gamma|$, and $\alpha > 0$ is the Gilbert damping parameter. $\vec{H}_{eff}$ is the effective magnetic field felt by the magnetization and is derived from the total magnetic energy density ε so that:

$$\vec{H}_{eff}(\vec{M},\hat{r},t) = -\frac{1}{\mu_0} \vec{\nabla}_{\vec{M}} \left[\varepsilon(\vec{M},\hat{r},t) \right]. \tag{1.24}$$

The first term on the right hand side of Equation (1.23) describes the precessional motion of the magnetization around $\vec{H}_{eff}$. The second term is a damping term perpendicular to

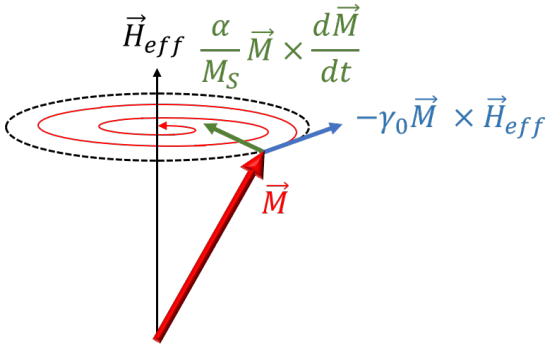

Figure 1.8: The trajectory of the magnetization $\vec{M}$ follows a damped spiral towards the effective field $\vec{H}_{eff}$ as described by the precession term and the damping term.

both the precession term and the magnetization. It translates the energy dissipation and the return of the magnetization to a low energy configuration along the effective field. These two terms are illustrated in Figure 1.9.

1.5.2 Transfer of angular momentum

The consideration of angular momentum transfer and spin torque is not straightforward and has subtleties that need to be addressed. If we consider spin angular momentum transfer as described in Section 1.4.2, the spin current does not actually transfer its momentum to the magnetization, but acts on the local spin density. Given the conservation of angular momentum, the time variation of the spin density $\vec{S}$ - the transfer of angular momentum - can be expressed as the net flux of the non-equilibrium spin current $\overline{Q}$ through the magnetic material [13, 49, 14]:

$$\boxed{\frac{d\vec{S}}{dt} \propto -\vec{\nabla}\cdot\overline{J}_s \equiv \vec{\Gamma}_{ext},} \tag{1.25}$$

with S in $\hbar/\mathrm{m}^3$ and J_s in $\hbar/\mathrm{sm}^2$. The conversion from spin density to magnetization is only direct if the magnetism is solely due to the spin angular momentum. This is the case for example in transition metals, where the orbital angular momentum is quenched, or in S-ions such as Gd. In this case, the spin angular momentum is colinear with the magnetization and related to it by $\gamma < 0$, the electron gyromagnetic ratio, such that $\vec{M} = \gamma\vec{S}$. Thus, in this case the spin transfer is described phenomenologically by a *add hoc* term added to the LLG equation.

1.5.3 Dynamics of the magnetization with spin torque

The action of a spin torque $\vec{\Gamma}_{ext}$ on the magnetization is described by the Landau-Lifshitz-Gilbert-Slonczewski (LLGS) equation [50, 25]:

$$\boxed{\frac{d\vec{M}}{dt} = -\gamma_0\vec{M}\wedge\vec{H}_{eff} + \frac{\alpha}{M_S}\vec{M}\wedge\frac{d\vec{M}}{dt} + \gamma_0\vec{\Gamma}_{ext}.} \tag{1.26}$$

Regardless of its origin, the torque can be decomposed into plans orthogonal to $\vec{M}$:

$$\vec{\Gamma}_{ext} = \frac{a_j}{M_S^2}\vec{M}\times(\vec{M}\times\hat{\sigma}) + \frac{b_j}{M_S}\vec{M}\times\hat{\sigma}, \tag{1.27}$$

where $\hat{\sigma}$ is the spin polarization direction of the spin current, a_j is the amplitude of the *damping-like* term, or Slonczweski-Berger term [7, 8] and b_j is the amplitude of the *field-like* term [51, 52]. In fact, the *damping-like* term has the same form as the damping term and its role is to align the magnetization along the spin polarization, while the *field-like* term makes the magnetization precess around the spin polarization in the same way as a magnetic field. The parameters a_j and b_j depend only on the material parameters and the charge current density, but not on the magnetization direction $\vec{M}$.

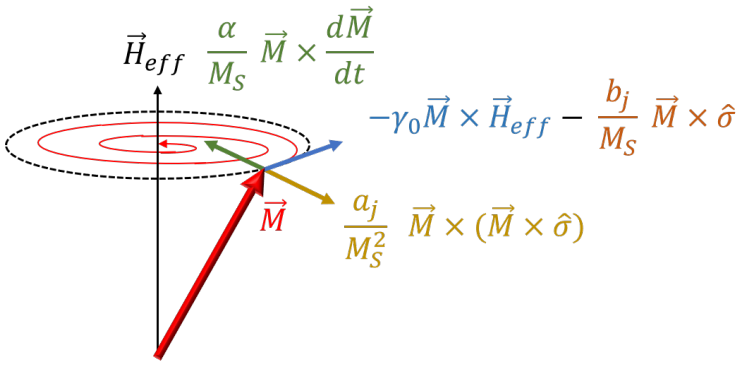

Figure 1.9: The effect of the spin torque on the magnetization can be described by two orthogonal terms, and in the case where the spin polarization is aligned with the effective field, the field-like torque is aligned with the precession term, and the damping-like torque is opposite to the damping term.

Therefore, the effect of the spin torque is twofold: it can participate in the precession of the magnetization, or it can oppose the damped motion of the magnetization. If the torque exactly compensates the damping, then the magnetization presents a sustained precession which allows to create nano-oscillators [53], or if the torque counterbalances the damping, the magnetization can be reversed and the spin torque can be a tool to write the information in magnetic memories [54].

1.5.4 Efficiency of spin-orbit torque

The efficiency of the spin-orbit torque ξ^j corresponds to the ratio of the spin current injected into the magnetic material (J_s^{inj}) and the charge current density, which can also be described by θ_{SHE} and the spin transmissivity T_{int} at the interface [55, 56]:

$$\xi^j \equiv \frac{2e}{\hbar}\frac{J_s^{inj}}{J_c} = T_{int}\theta_{SHE}, \tag{1.28}$$

with $T_{int} = \dfrac{J_s^{inj}}{J_s^{SHE}}$ [57]. To achieve a high efficiency, a combination of a high charge-to-spin conversion and high interfacial transmissivity are required. The spin transmissivity is affected by spin backflow (SBF) and spin memory loss (SML) such that $T_{int} = T_{int}^{SBF} \times T_{int}^{SML}$ and includes the spin mixing conductance [58, 59]. Reference [56] provides detailed explanations on the parameters to obtain a high efficiency SOT.

The efficiency of the damping-like torque ξ_{DL} and the efficiency of the field-like torque ξ_{FL} can be calculated by combining Equation (1.28) and Equation (1.25) and are directly related to the torque coefficient:

$$\boxed{\xi_{DL,FL} = \frac{2e}{\hbar} t_{FM} \frac{a_j, b_j}{J_c}.} \tag{1.29}$$

1.6 Towards self-induced spin-orbit torques

As explained in the previous sections, a torque can act on a magnetization. In the case of STT and SOT, this is only possible in heterostructures where a specific layer generates the spin current (the reference layer for STT and the HM for SOT) and another layer absorbs the spin current (FM for STT and SOT). To simplify the heterostructures, fabrication and lithography steps, we wondered if it was possible to create a torque on the magnetization in a single magnetic layer. We call this torque *self-induced torque* or *self-torque* because the material is both the source of the spin current and the spin absorber that ensures the generation of a torque. At first glance, it seems impossible to generate self-torque in a single magnetic layer because the spin-polarized current generated by a magnetic layer has its spin polarization aligned with the magnetization. Consequently, no transverse component can be transferred to the magnetization by the dephasing process. The only remaining possibility remaining is to use the spin-polarized AHE current to induce a torque on another magnetic layer whose magnetization is not aligned with the spin polarization.

The first record of bulk SOT, or torque in single layers, involved intrinsic origins. In 2014, Kurebayashi *et al.* reported a torque of purely intrinsic origin in a single ferromagnetic semiconductor (Ga,Mn)As with broken inversion symmetry in the bulk [10]. They attributed the origin of the SOT to a Berry phase in the material. They concluded that this phenomenon should be generic and appear in any spin-orbit coupled magnetic system with broken space symmetry and even in ferromagnet-paramagnet bilayers, where a Rashba-like SOT should appear. In 2016, C. Ciccarelli *et al.* demonstrated the bulk SOT in NiMnSb [11]. This Heusler ferromagnet has the same crystal symmetry as zinc-blende (Ga,Mn)As and they show that the measured SOT is similar to that reported for (Ga,Mn)As.

In 2018, C. O. Pauyac *et al.* derived a set of drift-diffusion equations to describe the transport of charges and spins in ferromagnets with extrinsic spin-orbit coupling [60]. In these magnetic materials, the exchange magnetic field tends to randomize the spins through the dephasing mechanism, but at the same time the SOC constructively generates spin accumulation or spin currents. Therefore, the overall generation of a spin current here depends on the competition between the aforementioned effects and their characteristic lengths: the spin dephasing length and the spin diffusion length. When the exchange coupling is strong, the spin dephasing mechanism dominates the spin relaxation over the spin flip mechanism. As a result, spin Hall effects quickly disappear, and when a spin current is generated, its spin polarization eventually aligns with the magnetization. In the case of weak exchange, the spin dephasing length is much larger and spin-coupled phenomena can dominate. As a consequence, spin currents with polarization transverse to the magnetization can exist in this material and offer the possibility to manipulate the magnetization even in centrosymmetric systems. This *spin Hall effect-like* spin current has been identified as the origin of an *anomalous SOT* in a single layer of $Ni_{80}Fe_{20}$ by W. Wang *et al.* in 2019 [12].

Manipulation of magnetization with spin-orbit torque is of great interest for the application of magnetic memory, called SOT-MRAM. Unlike typical D-RAM found in conventional

computers, magnetic memories are non-volatile and more energy efficient. By moving towards self-induced spin-orbit torque, we can simplify the structure, along with a better scalability of the memory cell. Extrinsic origins are preferred over intrinsic ones because they can generate torque even in non-crystalline materials. Such materials can be grown by sputtering, a technique preferred by the industry.

In the following chapter, we will explain the interesting properties of GdFeCo. The idea is to explain and convince the reader that the chosen material, GdFeCo, is a good candidate for the study of self-torque.

CHAPTER 2

GdFeCo ferrimagnet, a promising candidate for self-torque

All the samples presented in this thesis were deposited by Prof. Michel Hehn using DC magnetron sputtering. GdFeCo is co-deposited using separate Gd, Co and Fe targets. The cross sections of the samples for transmission electron microscopy (TEM) characterization were prepared by focused ion beam (FIB) milling either by Sylvie Migot or by myself using an FEI Helios Nanolab dual beam 600i. The TEM characterization was performed at IJL by Jaafar Ghanbaja on a JEM-ARM 200F Cold FEG microscope, with an acceleration voltage of 200 kV and coupled to a GIF Quantum 965 ER. The resolution is 0.12 nm in TEM mode and 0.078 nm in Scanning TEM mode.

GdFeCo is a ferrimagnetic (FiM) alloy belonging to the family of rare earth (RE) and transition metal (TM) FiMs. These materials, and in particular the GdFe and GdCo binaries, attracted great interest in the 1980s and 1990s due to their magneto-optical properties and the possibility of using the material as a medium for thermomagnetooptical recording [61, 62]. In the 2000s, the discovery of fast magnetization reversal by femtosecond laser pulses [63] opened the study of all-optical switching and ultrafast dynamics and highlighted the role of magnetic and angular momentum compensation [64]. The 2010s marked the beginning of studies on current-induced effects, such as the spin-orbit torque [65], and again highlighted the peculiar spin dynamics at angular compensation, with fast domain wall motion [66] or the vanishing of the skyrmionic Hall effect [67]. Our work on the self-induced spin-orbit torque is part of this renewed interest in this material. The aim of this chapter is to enlighten the properties and effects in GdFeCo that make the material a good candidate for the study of self-torque. In this regard, we first present the specific chemical, structural and magnetic properties of GdFeCo. We then discuss the evolution of the magnetic and angular momenta with temperature. Due to the spin-orbit coupling and the magnetism of GdFeCo, the material is the source of spin currents with different symmetries. We will describe how these spin currents can be exploited to generate self-torque.

2.1 A brief introduction on ferrimagnetism

The macroscopic magnetic state of a material is determined by the exchange interactions between magnetic moments at the atomic scale. As a result of these interactions, the moments can exhibit a parallel or antiparallel order, which are referred to as the ferromagnetic (FM) and antiferromagnetic (AFM) orders [17]. Ferrimagnets (FiM) are another type of magnetic materials that exhibit both FM and AFM properties. On the one hand, a ferrimagnet has two or more magnetic populations (called sublattices[1]) with antiparallel coupling like an AFM. On the other hand, the magnetic sublattices have different magnetic properties, resulting in a net magnetization, which allows us to probe and manipulate them like an FM. The corresponding magnetic orders are shown in Figure 2.1.

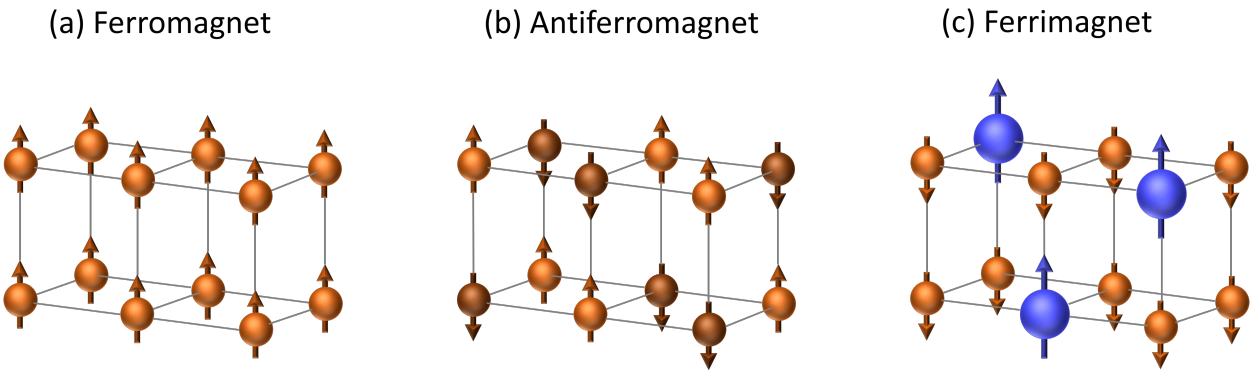

Figure 2.1: Illustration of the different magnetic orders. (a) In a ferromagnet, the magnetic moments are mostly aligned in the same direction. (b) In an antiferromagnet, neighboring moments are antiparallel and the magnetization . (c) In a ferrimagnet, two populations of moments (sublattice) coexist and are coupled antiparallel. Because the magnetic properties of the sublattices are different, a weak magnetization results from this particular magnetic order.

Thus, the magnetic properties such as the magnetic order or the magnetic anisotropy are closely related to the atomic environment of the magnetic moments. For this reason, we discuss the structure and the chemical composition of GdFeCo and describe its main magnetic properties.

2.2 Structure and chemical composition of GdFeCo

2.2.1 Lack of long-range order

The samples of GdFeCo presented in this thesis are grown by co-sputtering and show amorphous structures, i.e. a lack of long-range structural order, as observed by transmission electron microscopy (TEM). Figure 2.2(a) shows a high-resolution TEM micrograph (HRTEM) of a SiO_2//$Gd_{24}Fe_{68}Co_8$(10)/Cu(5)/Pt(6) thin film, where textures can be observed in the Cu

[1]Magnetic sublattices are not necessarily associated with a structural order.

and Pt layers, while none are observed in GdFeCo and in the SiO_2 substrate. A fast Fourier transformation (FFT) of specific areas in the layers (represented by the colored squares) shows their diffraction pattern, where bright diffraction spots observed in Figure 2.2(b-c) show the crystallinity in Cu and Pt. The diffuse background associated with the diffraction peaks indicates that Cu and Pt are polycrystalline. The FFTs of SiO_2 and GdFeCo shown in Figure 2.2(d-e) do not show any diffraction peaks. The diffuse ring pattern therefore highlights that there is no long range order and that GdFeCo is amorphous. This has also been confirmed in the literature by other techniques such as X-ray diffraction [68] where no diffraction peaks are obtained.

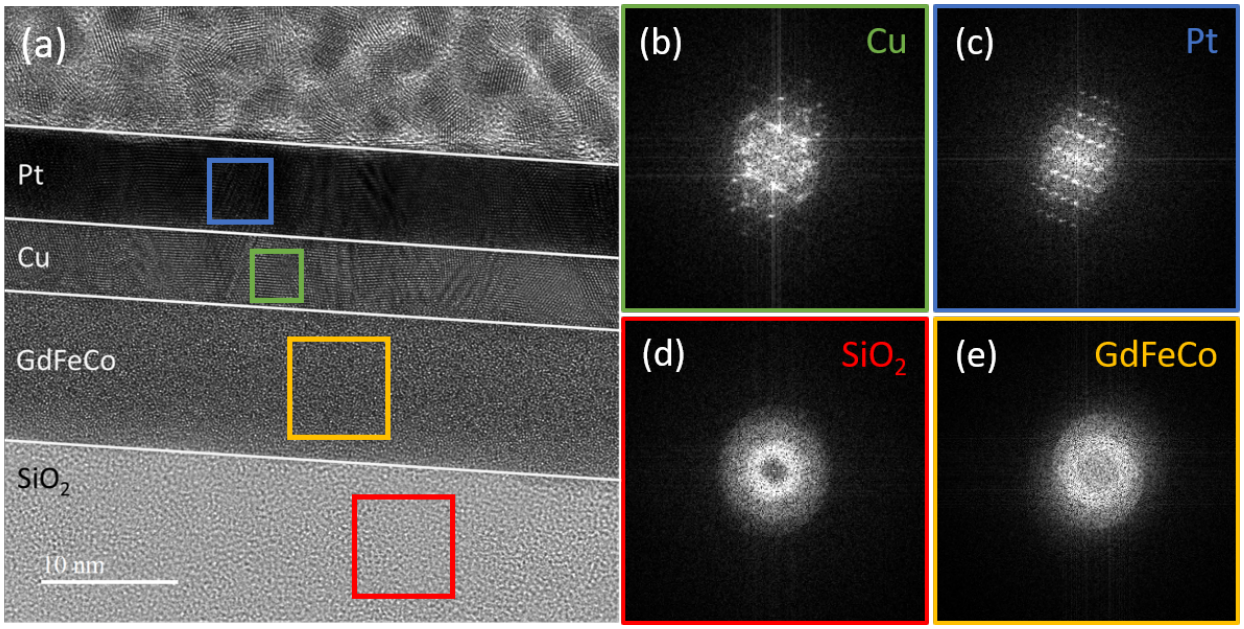

Figure 2.2: TEM characterization of SiO_2//$Gd_{24}Fe_{68}Co_8$(10)/Cu(5)/Pt(6). (a) High resolution TEM micrograph of the deposited layers. The different squares indicates where the fast Fourier transform (FFT) analysis was performed (respectively in red for the SiO_2 substrate, in yellow for GdFeCo, in green for Cu and in blue for Pt). The corresponding FFT highlight that (b-c) Cu and Pt are polycrystalline, while (d-e) SiO_2 and GdFeCo show no long-range structural order.

2.2.2 Chemical composition

The chemical composition can be studied by scanning TEM (STEM) using energy dispersive X-ray spectroscopy (EDS) or electron energy loss spectroscopy (EELS). Figure 2.3 shows the EELS maps of a SiO_2//$Gd_{24}Fe_{68}Co_8$(10)/Cu(5)/Pt(6) thin film where interdiffusion of Gd and O at the bottom of the FiM layer is highlighted. It indicates the formation of an oxide of Gd in the layer, which is non-magnetic and insulating. Overall, the maps show a homogeneous distribution of each element in their respective layers and a reduced interdiffusion at the interface of Cu and GdFeCo.

Since GdFeCo is amorphous, the composition of the different elements in the layer can be expected to be perfectly homogeneous. Using STEM-EDS in the GdFeCo layer, we can quantify the concentration of each element as well as the concentration of oxygen. Figure

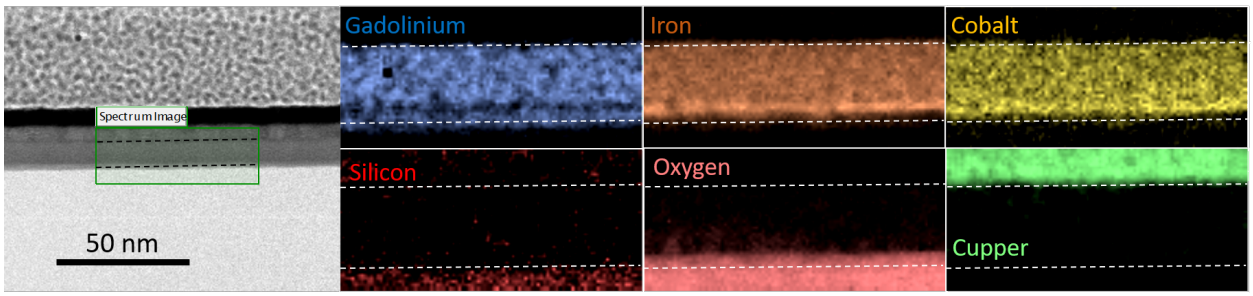

Figure 2.3: STEM micrograph of $SiO_2//Gd_{24}Fe_{68}Co_8(10)/Cu(5)/Pt(6)$. The corresponding EELS elemental maps show the distribution of the different elements, where we can see for example the interdiffusion of Gd and O in the lower part of the GdFeCo layer.

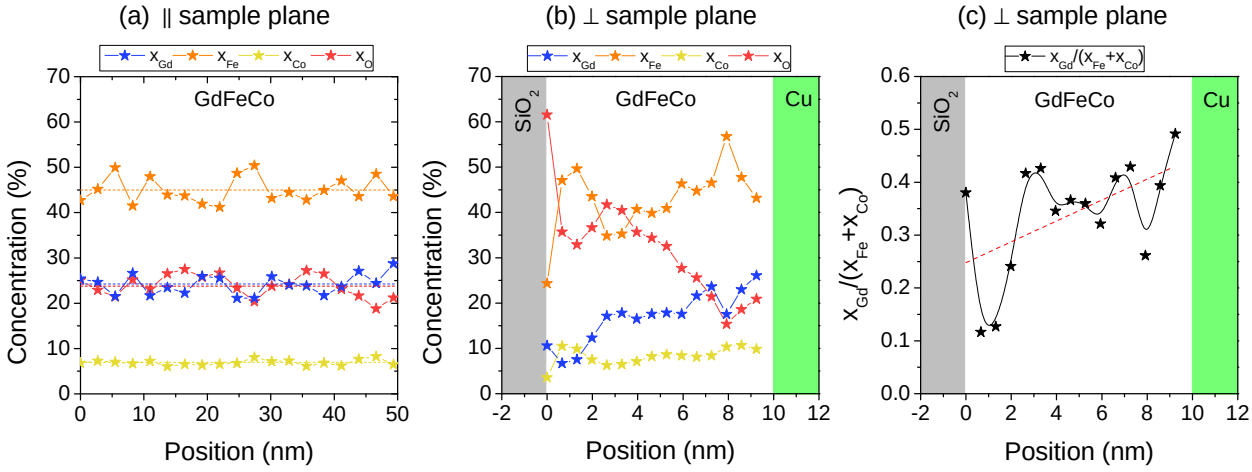

Figure 2.4: STEM-EDS analysis of $SiO_2//Gd_{24}Fe_{68}Co_8(10)/Cu(5)/Pt(6)$. Evolution of the concentrations of Gd, Fe, Co and O in the GdFeCo layer (a) along the film plane and (b) along the thickness. (c) Evolution of the ratio of Gd concentration to Fe and Co concentration $x_{Gd}/(x_{Fe}+x_{Co})$ in the GdFeCo layer. This ratio increases in the upper layers, indicating an inhomogeneity in the Gd content.

2.4(a) shows the concentration of the different elements on 50 nm in the direction parallel to the interface and verifies that the concentration is relatively homogeneous. However, the situation is very different in the thickness direction where the EDS scan of Figure 2.4(b) shows a variation of the O and Gd concentrations. Plotting the variation of the Gd concentration against that of FeCo, we can see in Figure 2.4(c) a clear gradient of Gd concentration.

An inhomogeneous distribution of the elements in the film thickness of RE-TM FiM is naturally present and is commonly reported, such as in Tb-based ferrimagnets [69, 70, 71], or in Gd-based ferrimagnets [72, 73, 74], but the origin of such a composition gradient is not clear and can be explained by different chemical mechanisms. For example, because the RE atom is much larger than the TM atom, it may have a different diffusion rate [75] leading to different chemical phases with distinct compositions within the materials. Another hypothesis is that RE and TM have different surface energies, leading to different segregation of the atoms towards the surface [76, 77]. Therefore, the concentration gradients are highly dependent on the growth process and its parameters, as well as on the interfaces surrounding

the ferrimagnet. We can also highlight that amorphous alloys are metastable, meaning that they tend to transform into stable crystalline phases with time and thermal treatment [78, 79].

Thus, GdFeCo is amorphous and has a non-homogeneous distribution of the elements. Since magnetism is closely related to structural and environmental environment, FiM can exhibit a distribution of the magnetic moments, of exchange interaction, or of magnetocrystalline anisotropy. In the following section, we discuss the main magnetic properties considered for GdFeCo.

2.3 Magnetic properties of GdFeCo

The magnetism of GdFeCo arises from the interaction between the Gd and FeCo magnetic sublattices and from their distinct electronic structure:

- Gd ([Xe] $4f^7$ $5d^1$ $6s^2$)
- Fe ([Ar] $3d^6 4s^2$)
- Co ([Ar] $3d^7 4s^2$)

The magnetism of Gd comes mainly from its half-filled localized 4f band, which is preserved from the environment. On the other hand, the magnetic moment of FeCo comes from the 3d delocalized band.

2.3.1 Exchange interactions

In the Gd atom there is an intraatomic ferromagnetic exchange interaction between the 4f and 5d electrons. This ferromagnetic exchange $J_{4f-5d} > 0$ allows the 5d electrons to be polarized. Thus, the 4f electrons of Gd atoms can interact with each other via the 5d electrons, but this indirect exchange interaction J_{4f-4f} is usually neglected.
In FeCo, due to the overlap of the 3d bands, the corresponding electrons are coupled by an intraatomic ferromagnetic exchange $J_{3d-3d} > 0$.
In GdFeCo alloy, Gd and FeCo moments are additionally coupled together by an interatomic antiferromagnetic exchange $J_{5d-3d} < 0$, allowing the antiparallel alignment between Gd and FeCo magnetic moments [80, 81]. So, we have $|J_{4f-4f}| \ll |J_{5d-3d}| < |J_{3d-3d}| < |J_{4f-5d}|$. Figure 2.5 shows the electronic structure of Gd and FeCo and the main exchange interactions.

2.3.2 Magnetization and angular compensation points

GdFeCo consists of two magnetic sublattices that are antiferromagnetically coupled. Depending on the relative concentration x of Gd compared to FeCo, or depending on the temperature T of the system, the magnetic properties of the alloy can change. The spontaneous magnetization is therefore defined as:

$$M_S(x,T) = M_{FeCo}(T) - M_{Gd}(T). \tag{2.1}$$

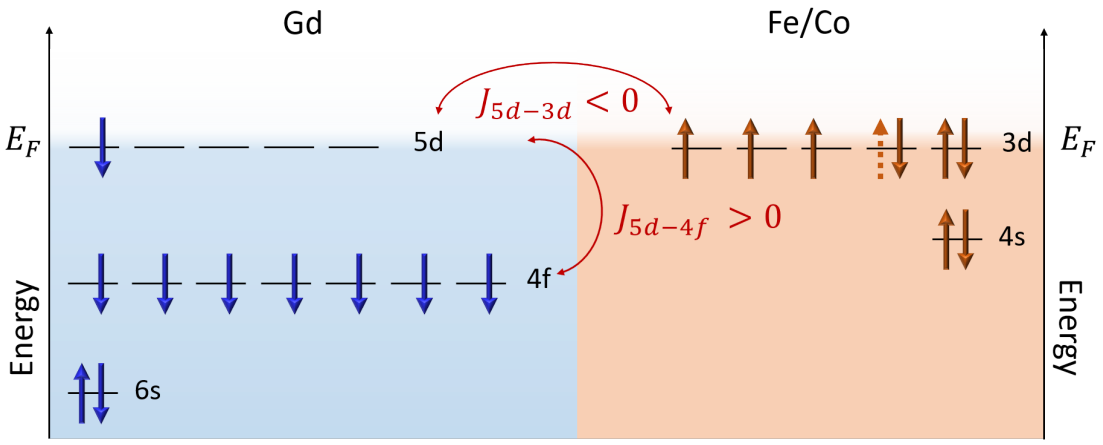

Figure 2.5: Illustration of the electronic states of Gd and FeCo and of the exchange interactions between the different electrons (adapted from [82]). J_{5d-3d} is the antiparallel exchange between the delocalized 5d and 3d electrons, and J_{5d-4f} is the parallel intraatomic exchange between the delocalized and localized electrons of Gd.

For a given concentration x, the material is Gd-dominant at very low temperatures (see Figure 2.6(a)). As the temperature increases, both Gd and FeCo magnetic moments decrease in amplitude due to thermal fluctuations. The Gd magnetization decays faster than the FeCo magnetization due to its relatively weak 4f-4f coupling. As a consequence, there is a specific temperature at which both sublattices are equal, and $M_S = 0$. This temperature is called the magnetization compensation temperature T_M, where $M_{FeCo} = -M_{Gd}$ (see Figure 2.6(c)). After this temperature, the material is FeCo-dominant (see Figure 2.6(b)).

In addition to a spontaneous magnetization, GdFeCo has a total angular momentum L, defined as:

$$L(x,T) = \frac{-M_{FeCo}}{\gamma_{FeCo}}(T) + \frac{-M_{Gd}}{\gamma_{Gd}}(T), \tag{2.2}$$

where γ_{FeCo} and γ_{Gd} are the gyromagnetic ratios of Gd and FeCo, respectively. Since $\gamma_{FeCo} \neq \gamma_{Gd}$, the total angular momentum L vanishes at the angular compensation temperature $T_A > T_M$ (see Figure 2.6(c)). Finally, at very high temperatures, the fluctuations completely randomize the magnetic and angular moments and the material becomes paramagnetic. This transition corresponds to the Curie temperature T_C.

Thus, GdFeCo and RE-TM FiM show a distinct evolution of their spontaneous magnetization and angular momentum with the temperature. Three temperature ranges defined by the two compensations are described in Table 2.1.

2.3.3 Perpendicular magnetic anisotropy

In a solid, the magnetic moments are oriented in preferred orientations to minimize interactions with the environment [17]. On the one hand, the magnetic moments interact with the dipolar magnetic field produced by neighboring moments, which depends on the shape of the magnetic sample. This is called shape anisotropy and in a thin film geometry, it results

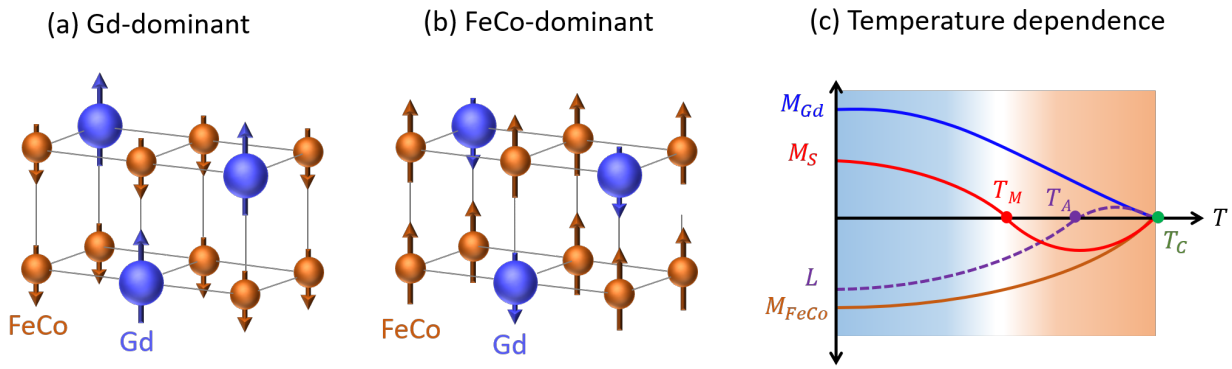

Figure 2.6: (a) Illustration of the GdFeCo magnetic order when the material is Gd-dominant and when it is (b) FeCo-dominant. (c) Schematic evolution of the magnetization of the Gd sublattice M_{Gd} and the FeCo sublattice M_{FeCo} as a function of the temperature. At low temperatures, M_{Gd} dominates over M_{FeCo} and the material is Gd-dominant (blue background). The spontaneous magnetization of GdFeCo M_S vanishes first at the magnetization compensation temperature T_M and finally at the Curie temperature T_C. The material then becomes FeCo-dominant (orange background) after T_M. The schematic also shows the evolution of the total angular momentum L with the temperature. It vanishes at the angular compensation temperature $T_A > T_M$.

$T < T_M$	$T = T_M$	$T_M < T < T_A$	$T = T_A$	$T > T_A$
$M_{Gd} > M_{FeCo}$	$M_{Gd} = M_{FeCo}$	$M_{FeCo} > M_{Gd}$	$M_{FeCo} > M_{Gd}$	$M_{FeCo} > M_{Gd}$
$\frac{M_{Gd}}{\gamma_{Gd}} > \frac{M_{FeCo}}{\gamma_{FeCo}}$	$\frac{M_{Gd}}{\gamma_{Gd}} > \frac{M_{FeCo}}{\gamma_{FeCo}}$	$\frac{M_{Gd}}{\gamma_{Gd}} > \frac{M_{FeCo}}{\gamma_{FeCo}}$	$\frac{M_{Gd}}{\gamma_{Gd}} = \frac{M_{FeCo}}{\gamma_{FeCo}}$	$\frac{M_{FeCo}}{\gamma_{FeCo}} > \frac{M_{Gd}}{\gamma_{Gd}}$
$M_S \uparrow\downarrow L$	$M_S = 0$ $L \neq 0$	$M_S \uparrow\uparrow L$	$L = 0$ $M_S \neq 0$	$M_S \uparrow\downarrow L$

Table 2.1: Table summarizing the dominant magnetic sublattice and dominant angular momentum over the magnetization compensation temperature T_M and the angular compensation temperature T_A. The last row summarizes the relative orientation between M_S and L.

in the moments lying in the plane of the film. On the other hand, the magnetic moments interact with the electrostatic environment of the material via the spin-orbit interactions, and the moments orient themselves to reduce the Coulomb interaction with the surrounding atoms. This is called magnetocrystalline anisotropy, and as a result of this anisotropy the magnetization lies along a preferred axis. In an amorphous solid, an isotropic distribution of atoms and moments would result in the absence of magnetocrystalline anisotropy. However, several RE-TM alloys exhibit uniaxial anisotropy oriented out of the sample plane. This perpendicular magnetic anisotropy (PMA) is also present in GdFeCo and its origin is still under investigation. It is proposed that the PMA arises from the inhomogeneous distribution of elements along the thickness of the material [68, 77] or even from the columnar structure in the out-of-plane direction [83]. In addition to a bulk origin of the PMA, a study at IJL by J-L. Bello *et al.* highlights the influence of interfaces on the PMA of GdFeCo [84]. They showed that the PMA of 5 nm of Gd_xFeCo is promoted when it is associated with (111) tex-

tured Cu, while the use of Pt reduces the concentration range in which the PMA is observed. The origin of this improved or reduced PMA by the interface is not fully understood, but the clear promotion of PMA with Cu shown in this study explains why GdFeCo is always associated with Cu in the samples presented in this work.

2.3.4 Sperimagnetism

The structural and chemical disorder in GdFeCo is at the origin of a distribution of its magnetic properties. This distribution is modeled by a competition between the locally varying exchange interaction and a random anisotropy [85], which can lead to non-collinear magnetic order. Since Fe atoms are very sensitive to the structural environment, the exchange interaction between Fe atoms is reduced in an amorphous alloy [86]. In contrast to Fe, Co atoms are less sensitive to the environment and there is a strong ferromagnetic coupling between Co atoms. A dispersion in the orientation of the magnetic moments of Gd has also been suggested [87]. The distribution of magnetic moments of Gd, Fe and Co in an amorphous structure is illustrated in Figure 2.7(a). As a result, GdFeCo exhibits a non-colinear magnetic order known as sperimagnetism when the composition ratio of Co is less than 30% [88, 89, 78]. The non-colinear magnetic order of GdFeCo is shown in Figure 2.7(b), and Figure 2.7(c) shows the influence of a magnetic field on the dispersion of the magnetic moments.

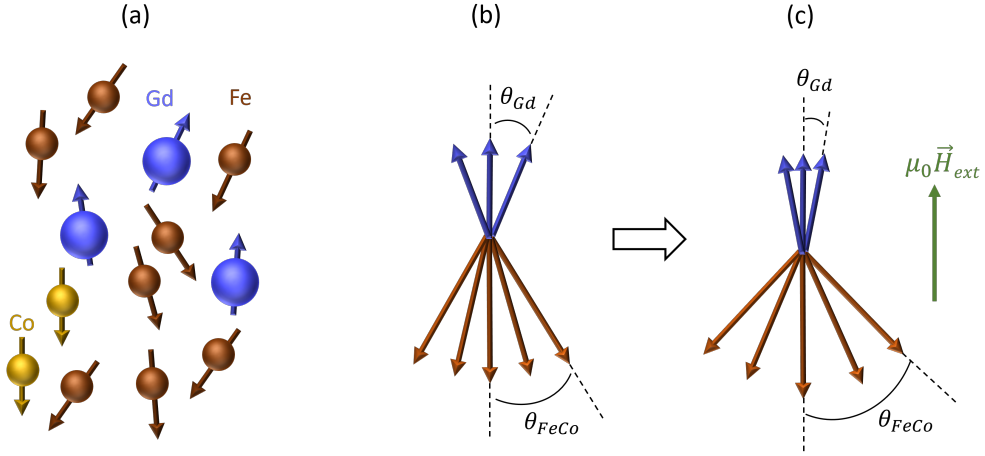

Figure 2.7: Schematic of the sperimagnetic order in GdFeCo, adapted from [87]. (a) Distribution of the magnetic moments in amorphous GdFeCo, with Gd in blue, Fe in orange and Co in yellow. (b) We can assume that the Gd and FeCo magnetic sublattices are distributed with a cone angle θ_{Gd} and θ_{FeCo}, respectively. (c) The cone angles are increased or decreased by the external magnetic field.

2.4 Spin current generation and propagation in GdFeCo

In Chapter 1, we discussed several mechanisms that lead to the conversion of a charge current into a spin current. The main component driving this conversion is the spin-orbit coupling (SOC). For GdFeCo we consider that the spin-orbit coupling comes from the 5d

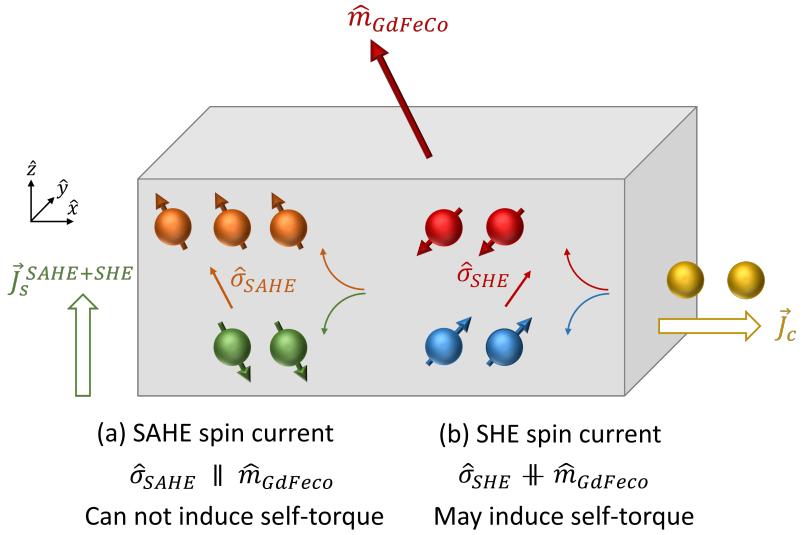

Figure 2.8: Spin current generation in GdFeCo. (a) The SAHE spin current has its spin polarization $\hat{\sigma}_{SAHE}$ parallel to the GdFeCo magnetization $\hat{m}_{GdFeCo}$. Therefore, this spin current cannot induce a self-torque. (b) The SHE spin current has a spin polarization $\hat{\sigma}_{SHE}$ which is not necessarily parallel to the magnetization, so it has the possibility to induce a self-torque on the magnetization.

electron of Gd. Indeed, the Rashba splitting reported in the majority spin surface state of Gd(0001) [90] correlates with the presence of SOC. In addition, bulk Dzyaloshinskii-Moriya interaction (DMI) has been reported in GdFeCo [72] as a result of composition gradient induced symmetry breaking and SOC. Thus, the GdFeCo ferrimagnet could interconvert charge and spin currents due to its SOC.

2.4.1 Spin current symmetries in GdFeCo

Due to the combination of SOC and magnetism, GdFeCo can generate spin currents with different symmetries as a result of different effects:

- The spin anomalous Hall effect (SAHE) symmetry:
  This effect produces a spin-polarized current with a spin polarization aligned with the ferrimagnet magnetization $\hat{\sigma}_{SAHE} \parallel \hat{m}_{GdFeCo}$ (see section 1.2.2). Since a spin torque results from the absorption of the transverse component of the spin current by the magnetization, the SAHE spin current cannot induce a torque in a GdFeCo single layer, i.e. it cannot induce a self-torque. Instead, this SAHE spin current can be used to generate a spin torque on another magnetic layer [31, 32].

- The spin Hall effet-like (SHE) symmetry:
  As discussed in Section 1.6, a magnetic material with SOC can generate a spin current with the same symmetries as the SHE in typical heavy metals [60], i.e. with the spin polarization $\hat{\sigma}_{SHE} \perp \vec{J}_c \perp \vec{J}_s$. If the magnetization is not aligned with the spin polarization, a self-torque can be generated on the magnetization, provided that there is an imbalance between the generated spin current and the absorbed spin current

as described in section 1.5.2. Ways to create the imbalance in the spin current are discussed in Section 2.5.

Once generated, the spin currents can propagate and eventually relax in the material by the various mechanisms described in Section 1.3. In ferromagnetic materials, the spin dephasing mechanism dominates the spin relaxation. In the following, we discuss this mechanism in a ferrimagnet such as GdFeCo.

2.4.2 Large spin dephasing length in FiM

When a spin current flows in a magnetic material, the spins rapidely precess around the magnetization, resulting in a decay of the transverse spin current over a very short dephasing length of less than 1 nm [13]. However, in an antiferromagnetically coupled system such as a FiM, the spins encounter different moments with alternating orientations. In a simple picture, the effects of each sublattice on the incoming spins are almost compensating, resulting in a spin dephasing length that is longer than in a typical FM, as shown in Figure 2.9(a). In fact, a spin diffusion length of about 4 nm has been reported in the GdCo alloy [91]. This dephasing length can be tuned by the temperature or concentration, and is maximal at the magnetization compensation temperature where the FiM appears like an AFM.

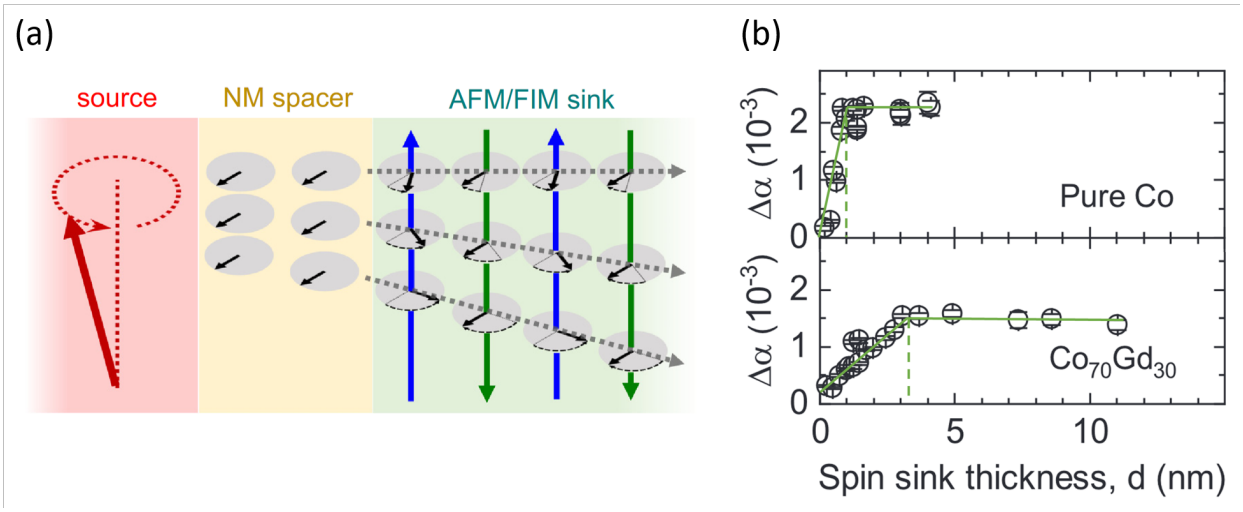

Figure 2.9: (a) Illustration of the spin dephasing mechanism in an antiferromagnetic or ferrimagnetic sink. The spins enter the sink with different dispersion and precess around the exchange field. Due to the antiferromagnetic coupling between the magnetic sublattices, the exchange field is opposite for each magnetic population. As a result, the spins experience an alternative precession, and the spins travel a longer distance before being completely dephased. (b) In $Gd_{30}Co_{70}$, the spin dephasing length is estimated to be about 4 nm, while it is 1 nm for pure Co. Figure adapted from [91].

In conclusion, spin currents with the SAHE and the SHE symmetries can be generated in GdFeCo. However, only the SHE spin current can be exploited to generate a self-torque on GdFeCo magnetization. Since the torque is the result of an imbalance between the generated spin current and the absorbed spin current, a spin torque cannot occur in a centrosymmetric

system. For this reason, we need to design the layer or the structure. In the following section, we discuss two cases to exploit the self-torque.

2.5 Versality of GdFeCo for the generation of self-torque

By exploiting the compositional gradient of GdFeCo and taking advantage of its relatively long spin dephasing length, self-torque can be generated in various types of structures.

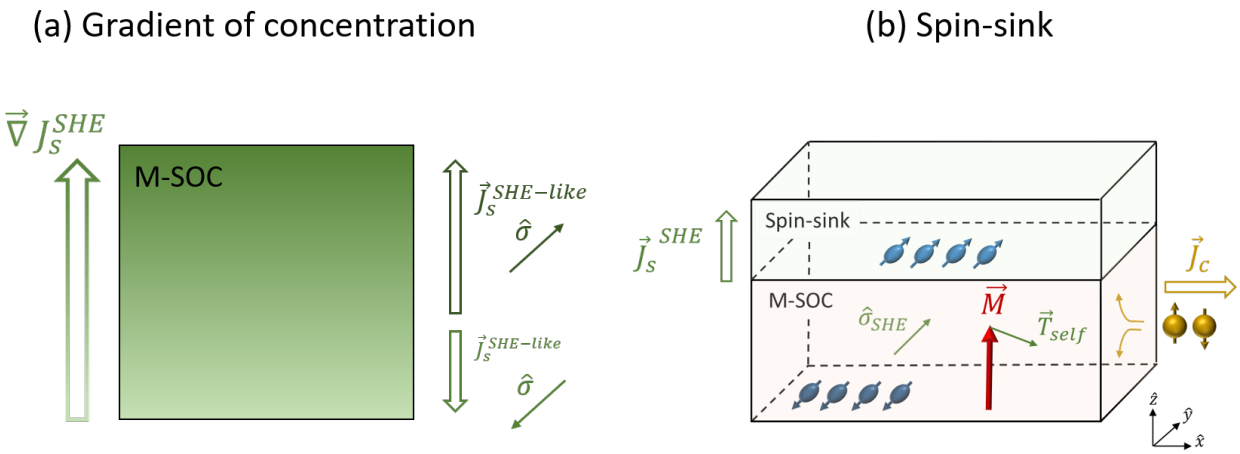

Figure 2.10: GdFeCo can be used in different structures for self-torque generation. (a) Self-torque can be generated in a single layer of GdFeCo where the gradient of Gd concentration is used to break the inversion symmetry. The layer thickness must be longer than the spin diffusion and spin dephasing lengths to ensure proper absorption, while the gradient ensures an imbalance of spin current absorption in the thickness. (b) Self-torque can be exploited with a spin sink. The spin current emitted from GdFeCo is absorbed outside by a spin sink. We can then exploit the large spin dephasing length of GdFeCo (this layer can then be quite thin), and the spin sink needs its spin diffusion length to be shorter than the layer thickness.

- Exploiting the gradient of composition (see Figure 2.10(a)):
  We can use the natural composition gradient, or we can create an intentional gradient to break the inversion symmetry. Our intuition suggests that this gradient leads to an inhomogeneous distribution of magnetization, resulting in an imbalance of spin current absorption in the film thickness. A study of self-torque in amorphous FePt published in 2021 [92] rather suggests that the composition gradient is related to a strain gradient that induces an imbalance in the generation and relaxation of spin currents, further demonstrating the importance of the composition gradient. Thus, self-torque can be generated in a single layer of GdFeCo only if a composition gradient induces an imbalance in spin current generation or absorption. In this case, the GdFeCo layer must be thicker than its spin diffusion and spin dephasing length to ensure that the spin current is absorbed in the layer.

- Exploiting the large spin dephasing length and using a spin-sink (see Figure 2.10(b)):
  A spin sink is an additional layer whose purpose is to absorb an incoming spin current. It can be either a magnetic layer (with a magnetization not aligned with the spin

polarization), a heavy metal (which absorbs the spin current through the ISHE), or a highly resistive layer that can absorb the spin current through a spin flip mechanism. If the thickness of GdFeCo is less than or equal to its spin dephasing length, the spin current can propagate outside the layer without being absorbed, the spin sink can absorb the spin current, resulting in a self-torque. To absorb the spin current, the spin sink must have a thickness larger than the spin diffusion and spin dephasing length if it is magnetic.

2.6 Conclusion

To conclude this chapter, we have shown that GdFeCo has the necessary properties for self-torque generation. The 5d electron of Gd carries the spin-orbit coupling, potentially allowing the generation of a spin current with spin Hall effect symmetry. Since the spin polarization of such a current is independent of the magnetization, the absorption of this current can lead to self-torque if the magnetization is not aligned with the spin polarization. We explained that GdFeCo is a versatile material for the generation of self-torque due to its natural composition gradient and large spin dephasing length, which allows to study self-torque in a variety of structures and to tune the efficiency of self-torque.

CHAPTER 3

Magnetotransport and spin-flop in GdFeCo

The measurements presented in this chapter were mainly performed in 2023, in the context of the master internship of Hyacinthe Cabrel Tadaha, working under the supervision of Dr. Juan-Carlos Rojas-Sanchez, Dr. Sébastien Petit-Watelot and myself. In particular, Hyacinthe carried out the spin-flop measurements. The devices were patterned by myself using UV-lithoraphy in CC-Minalor facilities at IJL. Dr. Sébastien Petit-Watelot, Prof. Michel Hehn, Prof. Stéphane Mangin and myself contributed to the interpretation of the magnetoresistance and spin-flop measurements.

The transport properties of RE-TM ferrimagnetic alloys were intensively studied in the 1980s, in particular to determine the role of each magnetic sublattice in transport. For magnetoresistive effects, such as the anomalous Hall effect, a dominant role was sometimes assigned to the RE sublattice [93], others assigned a dominant role to the TM sublattice [94, 95, 96], while others assigned the role of both sublattices [97]. However, for spin polarized transport phenomena such as the giant magnetoresistance, the dominant role is clearly assigned to the TM sublattice [98, 99]. The lack of consensus for the anomalous Hall effect, and the consensus for the giant magnetoresistance have since led to the preconceived idea that only the TM sublattice dominates all ferrimagnetic transport. This common belief has recently been challenged [87, 100] and the role of both the RE and TM sublattices in the magnetotransport of RE-TM ferrimagnets has been brought back into focus.

The idea of this chapter is to present the transport in GdFeCo, and to make a distinction between the spin-polarized transport and the magnetotransport. We first discuss the spin-polarized transport based on the observations reported in the literature. Then we focus on the magnetotransport. For this purpose, we introduce the concept of magnetotransport in a thin film, and discuss the sign of the magnetoresistive effects in Gd, FeCo and GdFeCo. We then discuss the nuances of the role of each magnetic sublattice in GdFeCo magnetotransport using spin-flop measurements.

3.1 Spin-polarized transport in Gd-based ferrimagnet

In Chapter 1, we introduced the notion of spin-polarized current, which arises in magnetic metals as a result of the spin-dependent conductivities of electrons at the Fermi level. In this section, we first review the spin-polarized transport in Gd, Fe, Co before moving on to the Gd-based ferrimagnet. Then, the giant magnetoresistance in spin valves using Gd-based ferrimagnet is discussed.

3.1.1 Spin-polarized transport in Gd, Fe and Co

The spin polarization of a spin-polarized current, as defined by Equation (1.9), can be probed by superconducting electron tunneling [101]. In essence, the technique consists of measuring the conductivity of a tunnel junction where one of the electrodes is the material of interest and the other electrode is a superconductor. Using a large magnetic field in the plane of the film, the superconductor acts as an analyzer for the spin-polarized current and the sign and amplitude of the polarization can be determined from asymmetries in the conductance.

The spin polarization in metallic Gd, Fe, and Co has all been reported to be positive [102, 103, 104] (see Figure 3.1(a)). In Gd, the 4f electrons which are responsible for the magnetism are in a core orbital and do not contribute to the transport. Instead, the spin polarized transport is associated with the 6s and 5d electrons that are polarized by the 4f electrons. In the case of Fe and Co, the spin-polarized transport is driven by the s and d conduction electrons, with the 3d electrons also responsible for the magnetism.

3.1.2 Spin polarization of Gd-based ferrimagnets

We report here the results published by C. Kaiser *et al.*. They studied the spin polarization of Gd_xCo_{1-x} amorphous alloy by superconducting electron tunneling, where they are sensitive to the sign and amplitude of the spin polarization. By varying the concentration of Gd, they show that the spin polarization can have a positive and negative values depending on the relative concentrations of Gd and Co [105]. The evolution of the spin polarization as a function of Gd concentration is shown in Figure 3.1(b). The sign of the spin polarization is defined with respect to the orientation of the net magnetization. The spin polarization is positive when the ferrimagnet is Co-dominant for $x \in [0,0.2]$, then its sign is reversed over the magnetization compensation concentration at $x = 0.2$. At the compensation, when the net magnetization vanishes, a finite and large spin polarization still remains (a finite spin polarization at the compensation of GdCo has also been observed using another technique [106]). For Gd concentrations $x > 0.75$, the spin polarization is positive again.

They qualitatively explain the sign changes of the polarization of GdCo by considering that both Gd and Co contribute to the total polarization. They showed that the spin polarization of pure Co is positive and that the spin polarization of Gd is also positive. In addition, the spin polarization of pure Co is higher than that of pure Gd. In both cases, the positive spin polarization is obtained when the magnetic sublattice is aligned with the external magnetic field. To explain the case of GdCo, they assumed that due to the anti-

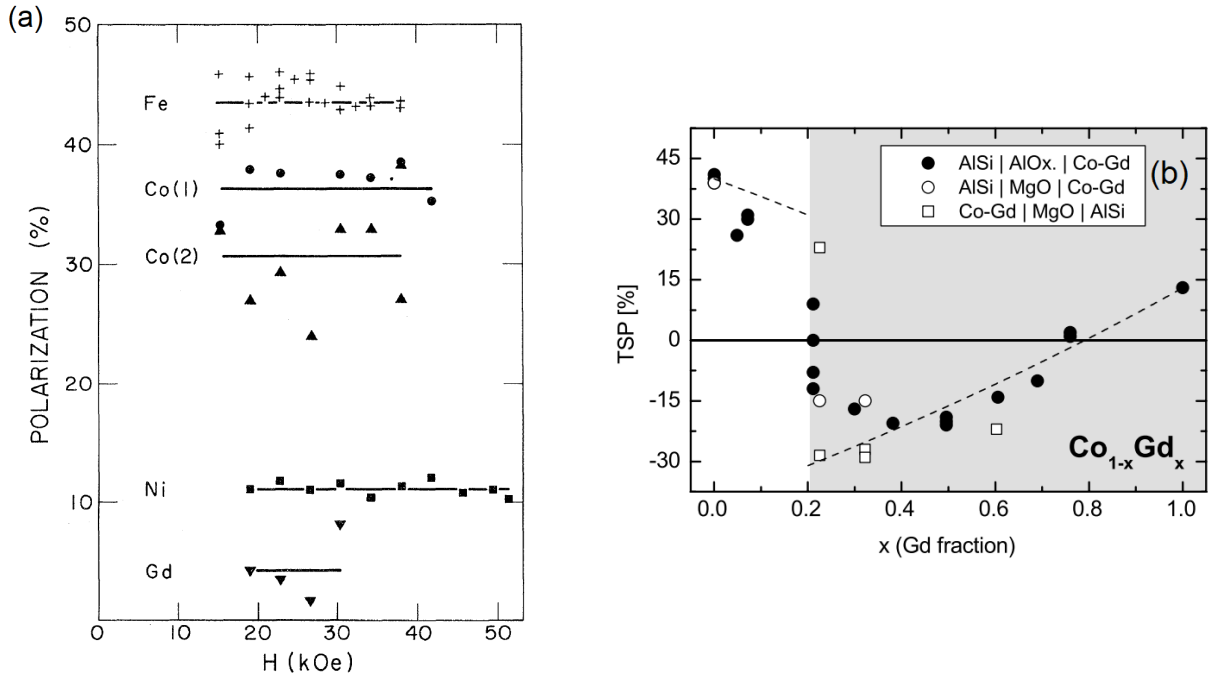

Figure 3.1: (a) Spin polarization of different metals as a function of the applied magnetic field. Gd, Fe and Co all have a positive spin polarization. Results from [102]. (b) Tunneling spin polarization (TSP) of the Gd_xCo_{1-x} ferrimagnet as a function of Gd concentration. The TSP changes its sign over the magnetization compensation concentration at $x = 0.2$ and changes its sign again for higher Gd concentrations $x > 0.75$. Results from [105].

ferromagnetic coupling between the sublattices, the non-dominant sublattice gives rise to a negatively spin-polarized current. In addition, the net contribution of the two species depends on their relative concentration, i.e. Co dominates the spin-polarized transport at high Co concentrations and Gd dominates the spin-polarized transport at higher Gd concentrations. Therefore, for low concentrations of Gd, Co dominates the spin-polarized transport. When the material is Co-dominant ($x < 0.2$), the Co magnetic sublattice is aligned with the external magnetic field and the resulting spin polarization is positive. When the magnetization compensation point is crossed, the material is Gd-dominant in terms of magnetism and the Co sublattice is antiparallel to the field. Co still dominates the spin-polarized transport, resulting in negative spin polarization. By adding more Gd in the ferrimagnet up to $x > 0.75$, Gd starts to dominate the spin-polarized transport. Since this sublattice is aligned with the magnetic field, the resulting spin polarization becomes positive.

In conclusion, the spin-polarized transport in ferrimagnets seems to depend on the relative concentrations of the different species. **From this study on Gd-based ferrimagnets, in the typical concentrations of Gd used to overcome the magnetization compensation (between 22-26%), the transition metal sublattice dominates the spin-polarized transport**. Let us now discuss the case of the giant magnetoresistance in Gd-based ferrimagnets, which is also related to the spin-polarized transport in the ferrimagnet.

3.1.3 Giant magnetoresistance over the magnetic compensation of Gd-based ferrimagnets

Let us consider a trilayer system consisting of two magnetic layers separated by a conductive material. The giant magnetoresistance (GMR) corresponds to the change in resistance of the trilayer when the relative orientation of the two magnetizations is changed. The GMR is typically minimal when the magnetizations are parallel, because the spin-polarized current is subject to fewer spin-dependent scattering events, while the GMR is maximal when the magnetizations are transverse or antiparallel to each other, because of more spin-dependent scattering events. Therefore, this effect originates from the spin-polarized transport in the system and only exists in a structure with multiple magnetic layers. In this sense, GMR is different from the magnetoresistive effects that we will introduce in the next section, where the magnetoresistive effect occurs in the magnetic layer itself.

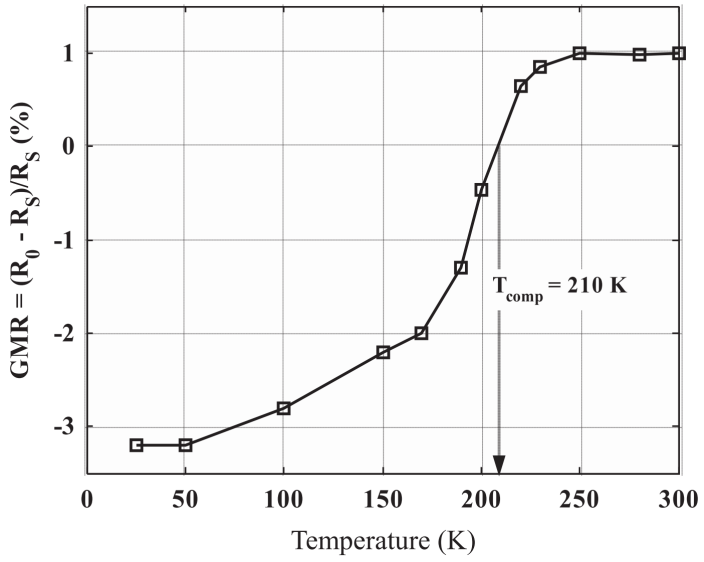

Figure 3.2: Evolution of the giant magnetoresistance (GMR) in $Fe_{20}Ni_{80}(10)/Cu(2)/Gd_{20}Co_{80}(15)$ with the temperature. The measurements are performed in a current-in-plane geometry. The sign of the GMR changes over the magnetization compensation temperature of GdCo at $T_M = 210$K. Results from [99].

We present here the study of GMR using GdCo ferrimagnet published by N.T. Nam *et al.* [99]. They studied the GMR of $Fe_{20}Ni_{80}(10)/Cu(2)/Gd_{20}Co_{80}(15)$ as a function of temperature. GdCo exhibits PMA and NiFe has a small in-plane anisotropy. An external magnetic field applied in the plane allows to orient the GdCo magnetization towards the direction of the NiFe magnetization, and the GMR is defined as the difference in resistance between the transverse configuration at low magnetic field and the parallel configuration at high magnetic field, normalized by the value of the resistance in the parallel configuration. The evolution of the GMR with temperature is shown in Figure 3.2. It can be seen that the sign of the GMR changes over the magnetization compensation temperature of GdCo. For all temperatures, the GMR is measured with parallel alignment of NiFe and GdCo magnetization at high magnetic field, therefore the sign change of the GMR suggests that the effect is not related to the magnetization of GdCo, but rather to one of the magnetic sublattices. We recall that both Co and Gd sublattices have positive spin polarization. Therefore, a positive GMR when the material is Co-dominant and when the Co sublattice is parallel to the NiFe magnetization suggests that the Co sublattice dominates the spin-polarized transport. Similarly, a negative GMR when the material is Gd-dominant and when the Co sublattice is antiparallel to the NiFe magnetization further confirms the dominant role of the Co sub-

lattice in the spin-polarized transport.

In this section, we have presented the spin-polarized transport of Gd-based ferrimagnets by presenting work from the literature. The spin polarization of Gd, Fe and Co are all positive, and the polarization of the transition metals is higher than that of Gd. In a GdCo ferrimagnet, it has been shown that the spin polarization can be positive or negative depending on the relative concentration of the species and the magnetic sublattice that dominates the magnetization. **For 20% of Gd, the Co sublattice dominates the spin-polarized transport as shown by the superconducting electron tunneling technique [105] and also by GMR measurements [99]**. The Gd sublattice also seems to dominate the spin-polarized transport in ferrimagnets with a high Gd concentration. Finally, we emphasize that the results presented in this section have been explained using a phenomenological approach where the contribution of each sublattice is considered independently. This model does not explain the microscopic phenomena associated with spin polarized transport. In fact, the spin polarization of the conduction electrons is determined by the s-electrons, which are polarized by the d-states at the Fermi level. The Fermi level of the alloy is different for each composition, therefore the spin polarization mechanism cannot be considered as the sum of the effect of two independent sublattices [106].

3.2 Magnetoresistive effects in thin films

The resistance of a non-magnetic metal changes under the influence of a magnetic field due to the Lorentz force acting on the electrons. Similarly, the spontaneous magnetization in a magnetic material affects electronic transport and a change in resistance is observed depending on the orientation of the magnetization with respect to the applied charge current. The response of the electric field $\vec{E}$ to the current density $\vec{J_c}$ can be written in the form of the generalized Ohm's law [107], where the direction of the magnetization $\hat{m}$ appears explicitly as:

$$\vec{E} = \rho\vec{J_c} + \Delta\rho\left(\vec{J_c}.\hat{m}\right)\hat{m} + \rho^{AHE}\,\hat{m}\times\vec{J_c}, \tag{3.1}$$

where ρ is the electrical resistivity independent of the magnetization, $\Delta\rho$ is the anisotropic magnetoresistance, and ρ^{AHE} is the anomalous Hall effect (AHE) contribution, all expressed in Ω.m.

Let us consider a current density flowing in the current line of a Hall cross of width w, length L, and thickness t, as shown in Figure 4.3. Using the geometric parameters of the cross, we can express Eq.(3.1) in terms of the longitudinal voltage V_X, the transverse voltage V_Y, and the current I_X:

$$\frac{V_X}{L} = \frac{I_X}{wt}\left[\rho + \Delta\rho^{AMR}\,m_x^2\right], \quad \text{and} \tag{3.2a}$$

$$\frac{V_Y}{w} = \frac{I_X}{wt}\left[\rho^{AHE}m_z + 2\Delta\rho^{PHE}m_x m_y\right], \tag{3.2b}$$

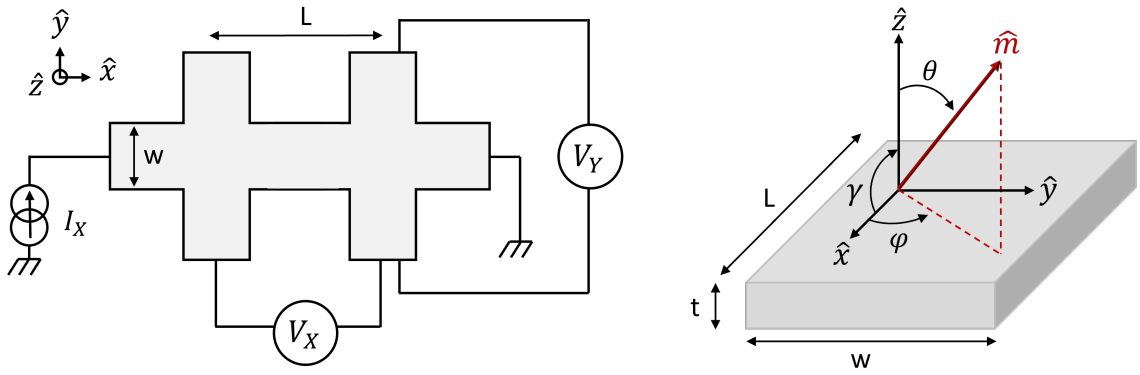

Figure 3.3: Schematic of an integrated Hall cross. The length of the current line is L, the width is w and the thickness is t. This geometry allows to inject the current along $\hat{x}$ and to measure either the longitudinal voltage V_X or the transverse voltage V_Y. The magnetization direction is described by the angles θ and φ.

which can be written in terms of the resistances:

$$V_X = I_X \left[R_0 + \Delta R^{AMR} m_x^2\right], \quad \text{and} \tag{3.3a}$$

$$V_Y = I_X \left[\Delta R^{AHE} m_z + 2\Delta R^{PHE} m_x m_y\right], \tag{3.3b}$$

considering for the resistances in the longitudinal voltage $R = \dfrac{\rho L}{wt}$ and for the resistances in the transverse voltage $R = \dfrac{\rho}{t}$. It follows that a change in the magnetization position in the $(\hat{x},\hat{y})$ plane can be sense in the longitudinal and transverse voltages. These effects are referred to as the anisotropic magnetoresistance (AMR) and the planar Hall effect (PHE) respectively. When the magnetization is in motion in the $\hat{z}$ plane, the AHE contributes to the transverse voltage. $\Delta R^{AMR,PHE,AHE}$ are expressed in Ω and are the amplitudes of the different magnetoresistive effects. In spherical coordinates, the equations (3.3a) and (3.3b) are transformed to:

$$V_X = I_X \left[R_0 + \Delta R^{AMR} \sin^2(\theta) \cos^2(\varphi)\right], \tag{3.4a}$$

$$V_Y = I_X \left[\Delta R^{AHE} \cos(\theta) + \Delta R^{PHE} \sin^2(\theta) \sin(2\varphi)\right]. \tag{3.4b}$$

In this way, electrical measurements allow direct probing of the magnetization direction and are used as a tool to probe the magnetization dynamics, for example to characterize the spin torque. The idea for the following is to characterize the magnetoresistive effects in GdFeCo, which is the material of interest in this thesis.

3.3 Magnetotransport in Gd, FeCo and GdFeCo

The GdFeCo ferrimagnet consists of two magnetic sublattices: Gd and FeCo. As discussed in the introduction of this chapter, each sublattice can participate in the magnetic transport. To determine the individual contributions of the Gd and FeCo sublattices, we present

magnetoresistive measurements in pure Gd and pure FeCo and compare them with GdFeCo, all grown by sputtering. The following structures are investigated:

- SiO_2//Gd(10)/Cu(2)/Al(3)
- SiO_2//FeCo(10)/Cu(2)/Al(3)
- SiO_2//$Gd_{24.1}$FeCo(10)/Cu(2)/Al(3)

Gd and FeCo are polycrystalline and GdFeCo is amorphous. The Cu layer is associated with GdFeCo to promote perpendicular magnetic anisotropy (see Section 2.3.3), so we add the same Cu layer on top of Gd and FeCo to be able to compare the structures together. We assume that the 3 nm thick Al layer is completely oxidized and therefore insulating. Therefore, the current flows in a 12 nm conductive bilayer, which can be modeled as an equivalent circuit with two resistors connected in parallel [108]. Knowing the resistivity of Cu, the resistivity of the magnetic layer can be directly calculated. Since the resistivity of 2 nm of Cu is unknown, we describe here the overall effect of the structure.

3.3.1 Evolution of the resitivity with temperature

We first report the resistivity evolution with the temperature of the aforementionned structures. The total longitudinal resistivity ρ_{XX} is determined from the longitudinal resistance measured by a 4-probe method in a patterned Hall cross ($L = 80\mu$m and $w = 20\mu$m). Two lockin amplifiers are used for these measurements. The first lockin applies a low-frequency AC voltage to the device and a 1 kΩ resistance connected in series. The same lockin synchronously measures the longitudinal voltage voltage V_X across the double Hall cross. The second lockin synchronously measures the voltage across the 1 kΩ resistance to determine the current flowing in the resistance, which is the same as the current flowing in the Hall cross. The measurements are performed without an external magnetic field and by lowering the temperature from 300K to 5K.

For Gd(10)/Cu(2) (see Figure 3.4 (a)), the resistivity decreases with decreasing temperature before increasing abruptly from 100K to 5K. This increase is associated with the appearance of magnetism in Gd. Since no external magnetic field is applied during the measurement, magnetic domains may appear. The resistivity of FeCo(10)/Cu(2) (see Figure 3.4 (b)) follows the typical Matthiessen rule for a metal. Its resistivity decreases with decreasing temperature as the thermal fluctuations and phonon scattering are reduced. The resistivity then reaches a plateau which is explained by the temperature independent scattering with impurities or defects in the material. Finally, the resistivity of $Gd_{24.1}$FeCo(10)/Cu(2) (see Figure 3.4 (c)) increases with decreasing temperature. This is a common feature in magnetic amorphous alloys, which is described by a coherent exchange scattering [109, 110].

The resistivity for each structure is about $10^{-6} - 10^{-7}\,\Omega$.m, i.e. the conductivity is about $10^4 - 10^6\,\Omega^{-1}.\text{m}^{-1}$. For these conductivity values, the materials are considered to be dirty or moderately dirty [34], and the skew scattering and side-jump mechanisms can be dominant mechanisms at the origin of the AHE.

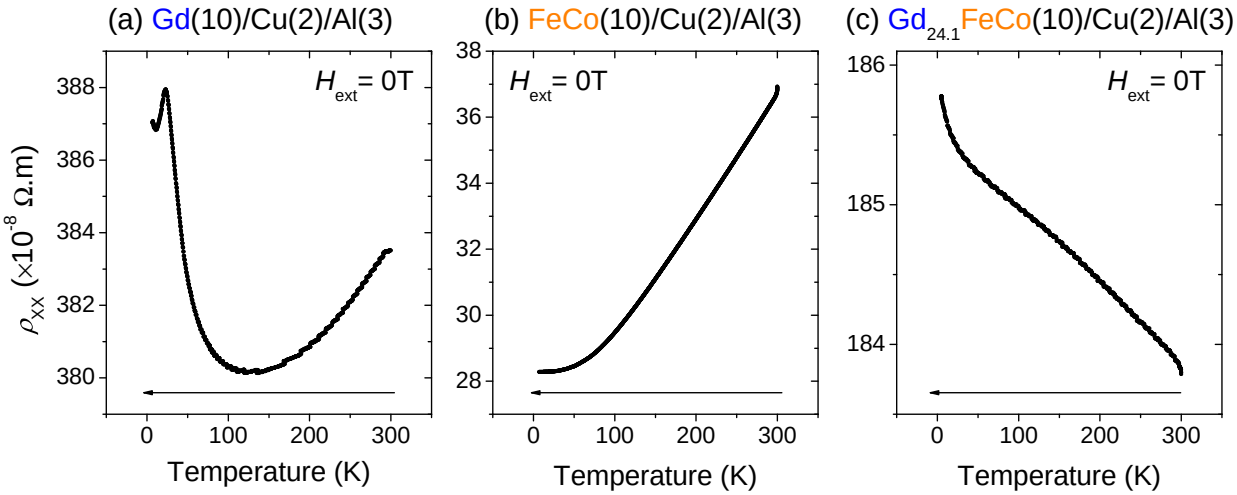

Figure 3.4: Evolution of the longitudinal resitivity of (a) Gd(10)/Cu(2), (b) FeCo(10)/Cu(2) and (c) $Gd_{24.1}$FeCo(10)/Cu(2) as a function of the temperature. (a) The increase in the resistivity of Gd from 100K to 5K marks the transition from paramagnetism to ferromagnetism. (b) The curve shows a typical evolution of the resistivity with temperature, indicating that FeCo is a metal. (c) In amorphous compounds, the resistivity decreases with increasing temperature.

3.3.2 Anisotropic magnetoresistance

We investigated the AMR by applying a DC current along the $\hat{x}$ axis ($i_{DC} = 1$mA) and by rotating a constant field along the angle $\gamma \in [0,360°]$, where the 0 angle corresponds to the alignment of the magnetic field with the current line (see Figure 4.3). We report the evolution of the longitudinal resistance R_{XX} and normalize by the value of the resistance when the magnetization is aligned along $\hat{z}$ i.e. $R^{\perp}$. The AMR for the different materials can be seen in Figure 3.5, where the data have been fitted by $R_{XX}/R^{\perp} = R_0 + \Delta R^{AMR}/R^{\perp} \cos(\gamma + \gamma_0)^2$. The data deviates from the fit near the hard axis because the magnetization is not fully saturated along the magnetic field.

It turns out that Gd(10)/Cu(2) has a negative AMR with a resistance change of -0.3%, while FeCo(10)/Cu(2) has a positive AMR and a resistance change of 0.4% (see Figure 3.5(a) and (b)). The AMR is positive for $Gd_{24.1}$FeCo(10)/Cu(2) and has the same sign over the magnetization compensation temperature, with a small change in resistance of 0.1% and of 0.07% when the material is Gd-dominant and FeCo-dominant, respectively (see Figure 3.5(c) and (d)). The different values are summarized in Table 3.1.

The AMR of GdFeCo can be phenomenologically modeled as the sum of the Gd and FeCo contributions [87]:

$$R_{XX}^{AMR} = A(m_x^{FeCo})^2 + B(m_x^{Gd})^2, \tag{3.5}$$

where A and B are the magnitude and sign of the AMR for both magnetic sublattices, and $m_x^{Gd(FeCo)}$ is the projection of the Gd (FeCo) sublattice along the current (along $\hat{x}$). According to our experimental results and the literature [87] $A > 0$ and $B < 0$. Thus, the AMR results from the destructive contributions of the Gd and FeCo sublattices. This

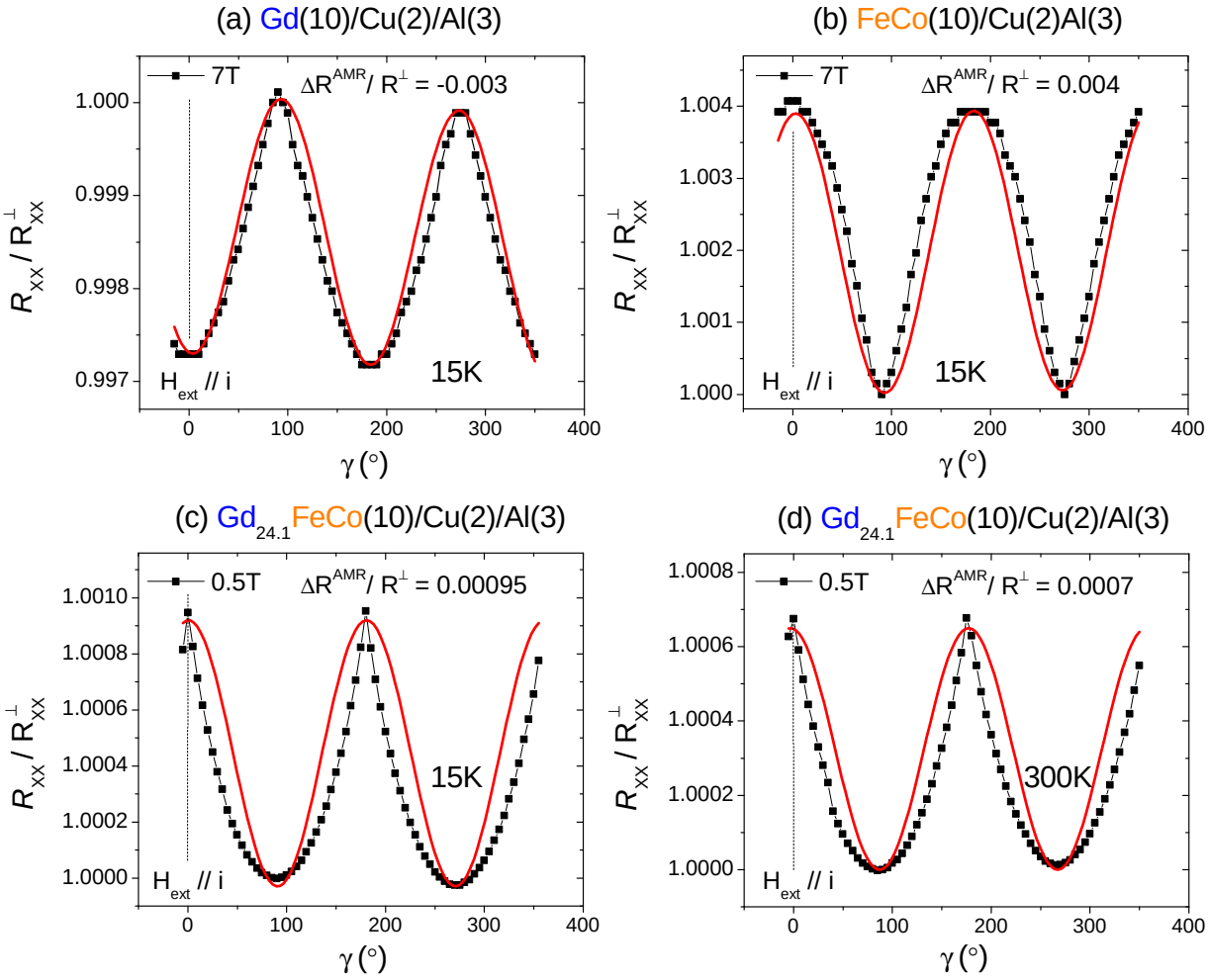

Figure 3.5: Evolution of the longitudinal resistance R_{XX} as a function of the angle γ. The signal is normalized to the resistance when the field is perpendicular to the current at $\gamma = 90°$, called $R^{\perp}_{XX}$. (a) For Gd(10)/Cu(2) at 15K, the AMR amplitude is negative. (b) For FeCo(10)/Cu(2) at 15K, the AMR amplitude is positive. (c) For $Gd_{24.1}$FeCo(10) at 15K when the material is Gd-dominant, the AMR amplitude is positive. (d) For $Gd_{24.1}$FeCo(10) at 300K when the material is FeCo-dominant, the AMR amplitude is positive.

	Gd(10)/Cu(2)	FeCo(10)/Cu(2)	$Gd_{24.1}$FeCo(10)/Cu(2)	$Gd_{24.1}$FeCo(10)/Cu(2)
T (K)	15K	15K	15K (Gd-dominant)	300K (FeCo-dominant)
ΔR^{AMR} (Ω)	-2.4	+0.26	+0.57	+0.4
$\frac{\Delta R^{AMR}}{R^{\perp}}$	-0.3%	$+0.4\%$	$+0.095\%$	$+0.07\%$

Table 3.1: Sign and amplitude of the anisotropic magnetoresistance effect for pure Gd, pure FeCo and GdFeCo over its magnetization compensation temperature.

explains the low AMR amplitude of GdFeCo compared to that of Gd and FeCo. The sign of the AMR of GdFeCo, which is positive even over the magnetic compensation, indicates that the FeCo sublattice dominates over the Gd effect in the AMR.

3.3.3 Anomalous Hall Effect

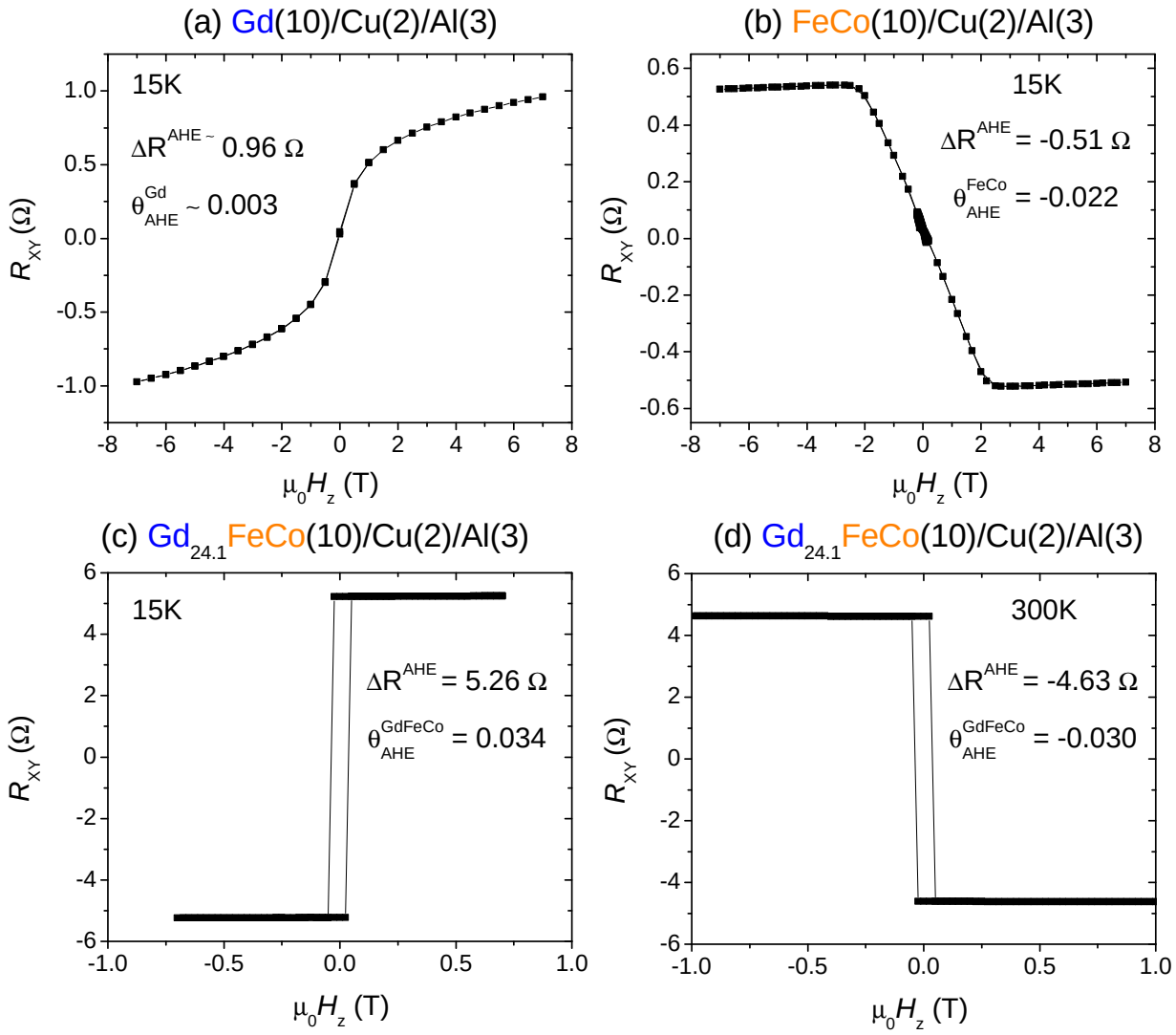

Figure 3.6: Transverse resistance R_{XY} as a function of the magnetic field amplitude along the $\hat{z}$ axis. (a) For Gd(10)/Cu(2) at 15K, the AHE amplitude is positive. The magnetization is naturally in the plane. (b) For FeCo(10)/Cu(2) at 15K, the AHE amplitude is negative. The magnetization is naturally in the plane. (c) For $Gd_{24.1}$FeCo(10)/Cu(2) at 15K, when the material is Gd-dominant, the AHE amplitude is positive. (d) For $Gd_{24.1}$FeCo(10)/Cu(2) at 300K, when the material is FeCo-dominant, the AHE amplitude is negative. The magnetization of GdFeCo is out of plane for the different temperatures.

The AHE is first measured for the different materials using a DC current $i_{DC} = 1$mA and by recording the DC transverse voltage while the external magnetic field is swept along $\hat{z}$. The data are shown in Figure 3.6. Gd(10)/Cu(2) shows a positive amplitude of AHE and the shape of the signal shows that the magnetization spontaneously lies in the plane of the

sample. FeCo(10)/Cu(2) shows a negative value of AHE and also an in-plane magnetization. For the case of $Gd_{24.1}$FeCo(10)/Cu(2), which has perpendicular magnetic anisotropy as shown by the square hysteresis loops, the sign of the AHE changes over the magnetization compensation temperature, being positive when the material is Gd-dominant and negative when the material is FeCo-dominant. Thus, the sign of the AHE over the magnetization compensation corresponds to the sign of the AHE in Gd and FeCo materials.

In the case of Gd and FeCo, the magnetization is naturally in the plane of the sample in an unknown direction. Therefore, if the magnetization is not along the $\hat{x}$ or $\hat{y}$ axis, the planar Hall effect can contribute to the transverse signal before the saturation of the magnetization along the out-of-plane magnetic field. To avoid the PHE contribution, we measure the transverse voltage while rotating the magnetic field in the ($\hat{x}$,$\hat{z}$) plane where the PHE vanishes. We obtain the same sign and the same amplitudes for the AHE for the different materials. The AHE efficiency, characterized by θ_{AHE} (see section 1.2.2) in GdFeCo is $\theta_{AHE}^{GdFeCo} = +0.034$ and -0.03 when the material is Gd-dominant and FeCo-dominant, respectively, and is higher than the AHE efficiencies of Gd and FeCo, which are $\theta_{AHE}^{Gd} = +0.003$ and $\theta_{AHE}^{FeCo} = -0.022$, respectively. The different values are summarized in Table 3.2.

The AHE signal of GdFeCo can therefore be phenomenologically modeled by the sum of the contributions of Gd and FeCo [87] such that:

$$R_{XY}^{AHE} = Cm_z^{FeCo} + Dm_z^{Gd}, \tag{3.6}$$

where C and D are the amplitude and sign of the AHE of Gd and FeCo, and $m_z^{Gd(FeCo)}$ is the projection of the Gd (FeCo) sublattice along the $\hat{z}$ axis. From our experimental data and from the literature we can see that $C < 0$ and $D > 0$ and that both contributions add up constructively when the sublattices are antiferromagnetically coupled. This leads to a higher value of AHE in GdFeCo than in Gd or FeCo.

The AHE arises from different mechanisms that we have described in Chapter 1 (Section 1.2.2). By looking at the dependence of the transverse conductivity as a function of the longitudinal conductivity, it is possible to identify the mechanism at the origin of the AHE for the different materials studied here. For Gd(10)/Cu(2) (see Figure 3.8(a)), no clear dependence between the transverse and longitudinal resistivity is observed, probably because the measurements were made at temperatures close to the Curie temperature. Further measurements should be performed to investigate the origin of the AHE. Longitudinal resistivity measurements should be made at different magnetic fields to saturate the magnetization below the Curie temperature, and transverse resistivity measurements should be performed with higher magnetic fields to saturate the magnetization along the magnetic field and for different temperatures. In the literature, the AHE of Gd is attributed to both the skew scattering and the side-jump mechanisms [111, 112]. For FeCo(10)/Cu(2) (see Figure 3.8(b)), the linear evolution of the transverse resistivity appears as a function of the longitudinal resistivity. This suggests that the skew scattering is at the origin of the AHE in FeCo. Finally, for $Gd_{24.1}$FeCo(10)/Cu(2) (see Figure 3.8(c)), we can see that the transverse resistivity does

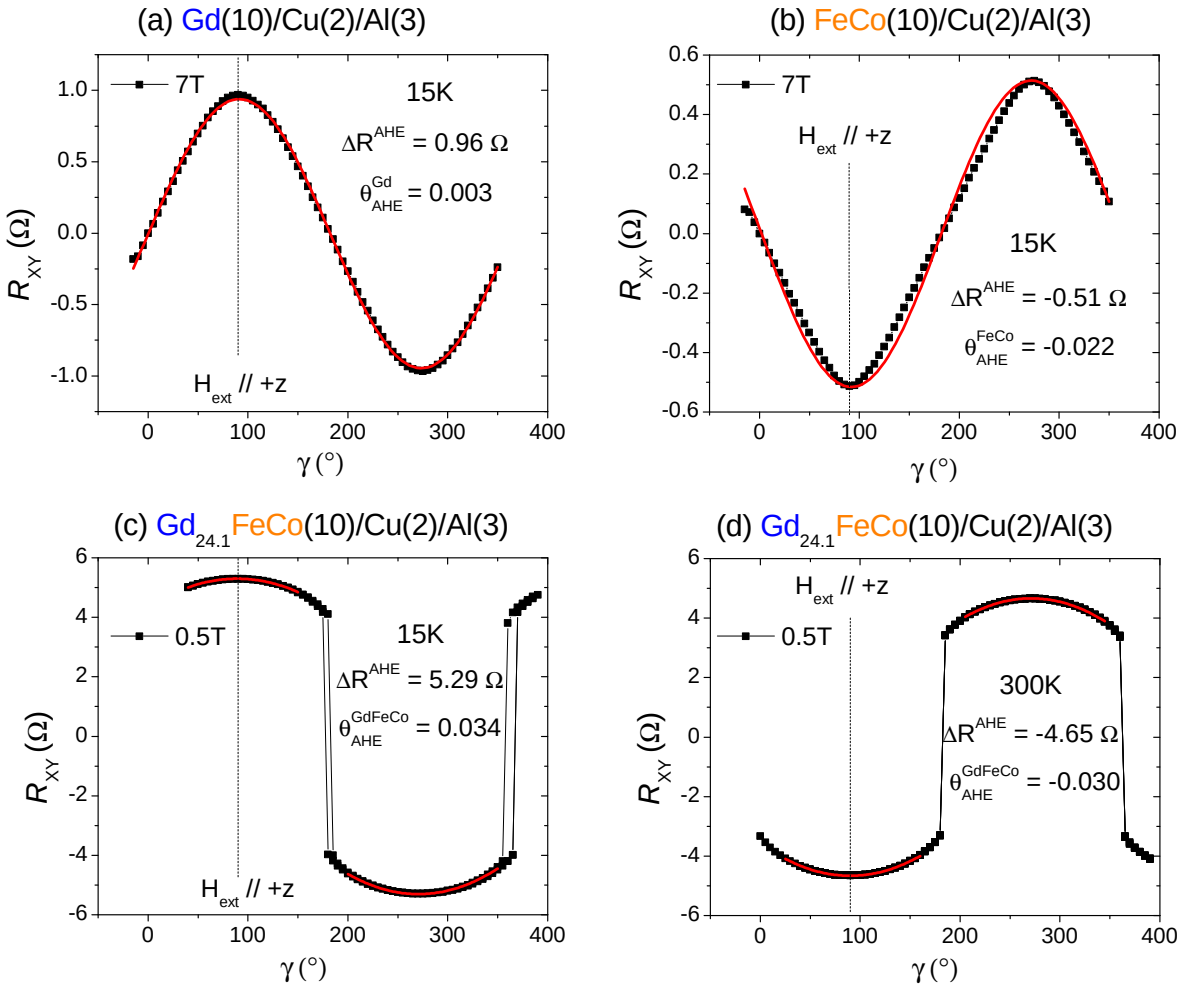

Figure 3.7: Evolution of the transverse resistance R_{XY} as a function of the angle γ. (a) For Gd(10)/Cu(2) at 15K, the AHE amplitude is positive. (b) For FeCo(10)/Cu(2) at 15K, the AHE amplitude is negative. (c) For $Gd_{24.1}$FeCo(10)/Cu(2) at 15K when the material is Gd-dominant, the AHE amplitude is positive. (d) For $Gd_{24.1}$FeCo(10)/Cu(2) at 300K when the material is FeCo-dominant, the AHE amplitude is negative.

	Gd(10)/Cu(2)	FeCo(10)/Cu(2)	$Gd_{24.1}$FeCo(10)/Cu(2)	$Gd_{24.1}$FeCo(10)/Cu(2)
T	15K	15K	15K (Gd-dominant)	300K (FeCo-dominant)
$\Delta R^{AHE}(\Omega)$	+0.96	−0.51	+5.29	−4.65
θ_{AHE}	+0.003	−0.022	+0.034	−0.030

Table 3.2: Sign and amplitude of the anomalous Hall effect in Gd, FeCo and GdFeCo over its magnetic compensation temperature.

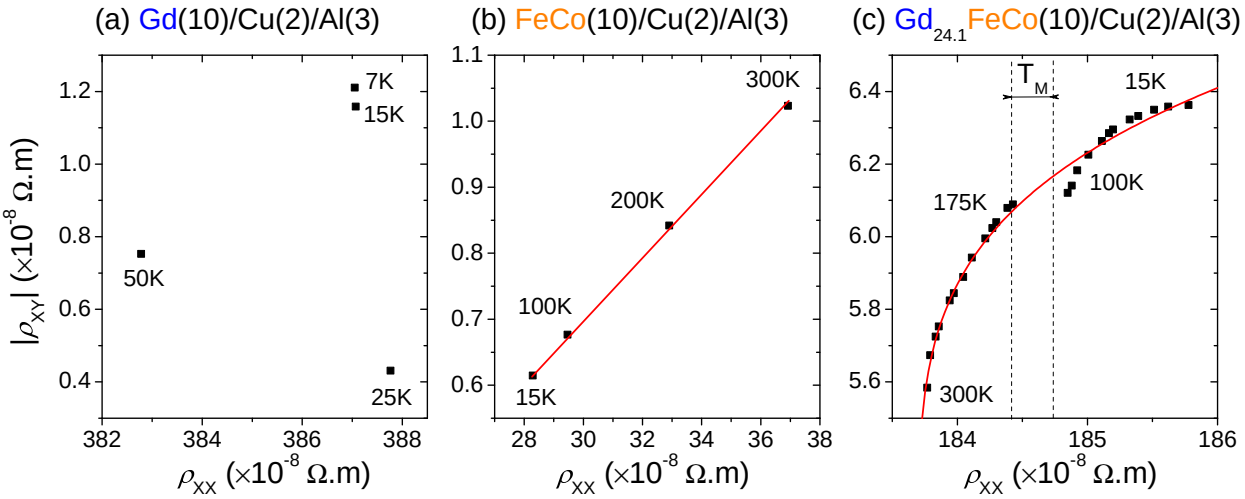

Figure 3.8: Transverse resistivity ρ_{XY} as a function of the longitudinal resistivity ρ_{XX} for different temperatures. (a) In Gd(10)/Cu(2), no clear behavior can be observed. (b) In FeCo(10)/Cu(2), a linear evolution suggests that the skew scattering mechanism is at the origin of the AHE. (c) In GdFeCo(10)/Cu(2), the transverse resistivity is neither linear nor parabolic with the longitudinal resistivity. It evolves in $\rho_{XX} \propto (\rho_{XX})^{0.2}$.

not evolve in $\rho_{XY} \propto (\rho_{XX})^{\alpha}$ with $\alpha = 1$ or 2. Instead, it evolves in $\rho_{XY} \propto (\rho_{XX})^{0.2}$. In GdFeCo, the mechanisms behind the conduction of the material are not solely related to the scattering of the electrons with impurities and phonons, but also involve other complex effects that depend, for example, on the exchange interaction [109, 110]. Therefore, the resistivities of GdFeCo do not capture the scattering rate in a simple way, and the evolution of the transverse resistivity with the longitudinal resistivity may not be a good indicator to access the anomalous Hall effect mechanisms as it is usually done.

To conclude this section, we have studied the AMR and AHE in Gd, FeCo, and GdFeCo. **Comparing the sign of the effects for the different materials, it turns out that the magnetotransport in the GdFeCo ferrimagnet, when the sublattices are antiferromagnetically coupled, can be described phenomenologically by the constructive contributions of the sublattices for the AMR and by the constructive contributions of the sublattices for the AHE.** Since the contributions of Gd and FeCo to the AHE have the same sign in the presence of a ferrimagnetic order, the AHE loop alone does not allow to infer the dominance of one sublattice over the other. One way to distinguish these contributions is to break the ferrimagnetic order with a strong magnetic field. When a ferromagnetic order is reached between Gd and FeCo (called spin-flop transition), their contribution to the AHE can add destructively, and the sign of the AHE can indicate which sublattice dominates the transport.

3.4 Spin-flop to determine the dominant sublattice

GdFeCo naturally exhibits a ferrimagnetic ordering, with the Gd sublattice being anticolinear to the FeCo sublattice. When the magnetic field reaches the spin-flop threashold H_{sf}, the Zeeman interaction starts to compete with the exchange interaction and the two sublattices get tilted as shown in the Figure 3.9. For very a strong magnetic fields, the Zeeman

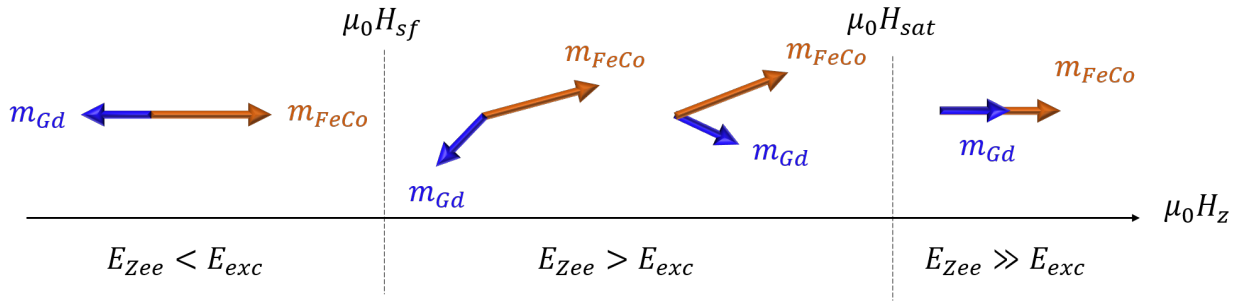

Figure 3.9: Illustration of the spin-flop mechanism. For a small magnetic field amplitude, such that the exchange interaction dominates over the Zeeman interaction, the two magnetic sublattices are antiferromagnetically coupled. The canting of the two sublattices starts at the spin-flop field H_{sf}, when the magnetic field dominates the exchange interaction, and the sublattices saturate in a parallel alignment for a very high magnetic field, defined as the saturation field H_{sat}.

interaction can dominate over the interatomic exchange, and the two magnetic sublattices tend to align with the magnetic field, forming a ferromagnetic order.

Figure 3.10 shows the spin-flop observed by SQUID-VSM. The evolution of the saturation magnetization of $Gd_{26}FeCo(10)/Cu(2)/Al(3)$ as a function of the magnetic field is shown in Figure 3.10(a). The increase in spontaneous magnetization at high magnetic field, indicated by the red stars, corresponds to the spin-flop transition. We define the spin-flop field H_{sf} as the field at which the spin-flop starts. In our experiment, 7T is not enough to achieve full saturation of the two sublattices along the magnetic field, since the magnetization signal does not saturate. We can see that the spin-flop field depends on the magnetization, in fact it reaches a minimum value at the magnetization compensation temperature of GdFeCo.

If the projection of the sublattices is positive for both species, the sublattices contribute destructively to the AHE, and the sign of the effect at the saturation in the ferromagnetic order can indicate the dominant sublattice for the AHE transport.

3.4.1 Spin-flop in the AHE and AMR signals

We present here the observation of the spin-flop mechanism by magnetotransport measurements. The idea is to compare the AHE and AMR signals in the absence of spin-flop with the signals obtained with spin-flop. The presented sample is FeCo-dominant for the whole temperature range between 2K and 300K. Figure 3.11 shows the evolution of the transverse and longitudinal resistances as a function of the amplitude of the magnetic field applied along the $\hat{z}$ axis.

Let us first look at the AHE and AMR signals as a function of the magnetic field amplitude at 200K, where no spin-flop is observed (see Figure 3.11(a) and (b)). The AHE signal shows a typical square loop, indicating that GdFeCo has perpendicular magnetic anisotropy. The sign of the negative amplitude loop of the AHE is consistent with the signs extracted in the previous section. The AMR is measured simultaneously and we can see a slight de-

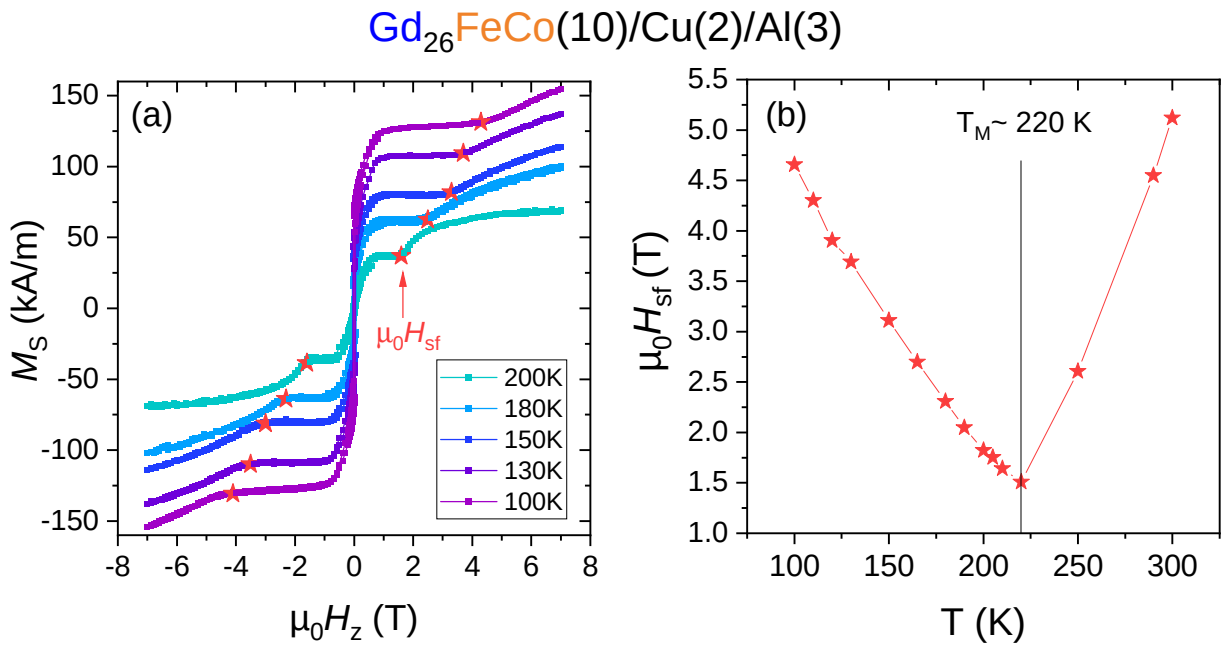

Figure 3.10: Spin-flop measurements performed by SQUID-VSM in $Gd_{26}FeCo(10)/Cu(2)/Al(3)$. (a) Evolution of the saturation magnetization as a function of the magnetic field amplitude along $\hat{z}$. The red stars correspond to the spin-flop field H_{sf}. (b) Evolution of the spin-flop field as a function of the temperature. This field has a minimum near to the magnetization compensation temperature of GdFeCo.

crease of the AMR signal compared to the full amplitude with increasing magnetic field. This change in the AMR can be explained by the sperimagnetism of GdFeCo [87]. In fact, Gd and FeCo are distributed on a cone whose dispersion can be decreased or increased depending on the sign of the magnetic field. Since the AMR in FeCo is positive, the decrease in AMR with increasing magnetic field suggests that the dispersion of the FeCo cone is decreased by the magnetic field. Similarly, the magnetic field can increase the dispersion cone of Gd, whose AMR is negative, which also results in a decrease of the total AMR.

Let us now look at the AHE and AMR signals near the compensation temperature where spin-flop occurs (see Figure 3.11(c) and (d)). We discuss the three magnetic regions described by the color change of the background.

- I. Between 0T and 2T:
  The transverse resistance shows a typical behavior with the out-of-plane magnetic field. However, the associated AMR signal cannot be simply understood by the sperimagnetism as for the measurement at 200K. The increase in AMR this time suggests that the dispersion cone of FeCo is increased by the magnetic field and the dispersion cone of Gd is decreased.

- II. Between 2T and 3.7T:
  The transverse signal decreases, indicating the onset of spin-flop mechanisms. It can be explained by the rotation of the Gd sublattice with respect to the magnetic field, which also drives the rotation of the FeCo sublattice. As the total projection along the $\hat{z}$ axis

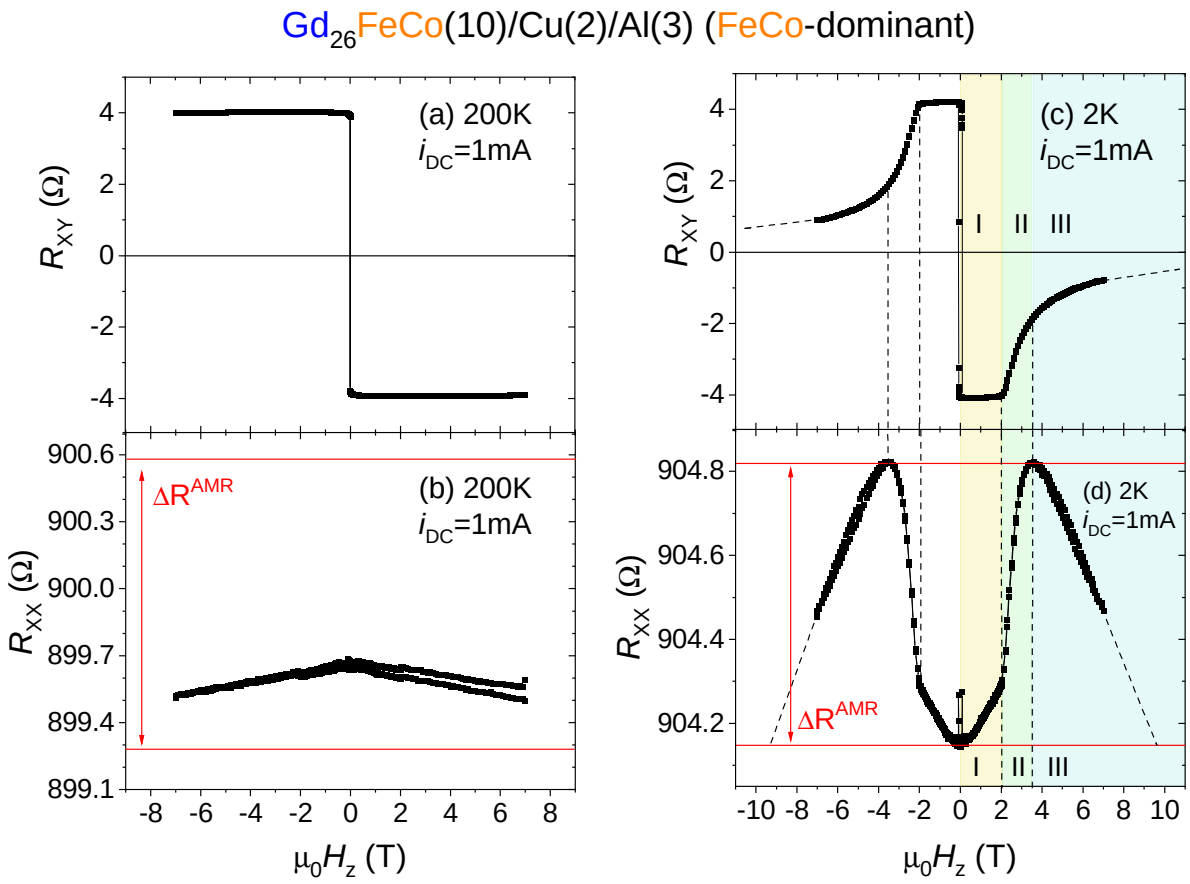

Figure 3.11: Spin-flop in FeCo-dominant $Gd_{26}FeCo(10)/Cu(2)/Al(3)$. Evolution of the transverse resistance R_{XY} (a) and the longitudinal resistance R_{XX} (b) as a function of the intensity of the external magnetic field applied along the $\hat{z}$ axis at 200K when there is no spin-flop. Evolution of the transverse resistance (c) and longitudinal resistance (d) as a function of the intensity of the external magnetic field applied along the $\hat{z}$ axis at 2K when spin-flop is observed.

decreases, the transverse signal decreases. The rotation of one or both sublattices is confirmed by the AMR signal, which increases as the AHE decreases. The increase of the AMR corresponds to an increase of the projections of the sublattices along the $\hat{x}$ axis, which supports the rotation of the sublattices during the spin-flop process. The AMR shows a maximum at 3.7T, corresponding to the highest projection of the sublattices along the $\hat{x}$ axis, perhaps indicating that the Gd sublattice is aligned along $\hat{x}$. The amplitude of the AMR ΔR^{AMR} was measured independently by rotating the magnetic field in the $(\hat{x},\hat{z})$ plane with a constant field of 2T. However, 2T was not enough to fully manipulate the magnetization along the hard axis, so the value for the amplitude of the AMR represented by the red lines in Figure 3.11(d) may be underestimated.

- III. Above 3.7T:
  After 3.7 T, the longitudinal signal decreases, indicating that the sublattices are moving toward the colinear state. Extrapolating the longitudinal signal to higher magnetic

field amplitudes, we expect the field at which ferromagnetic order is obtained to be 10 T. The longitudinal resistance value is expected to be the same as the value with antiferromagnetic order at zero magnetic field. Extrapolating the transverse signal, it appears that the signal would be negative at 10T when ferromagnetic order is reached. This means that the FeCo contribution to the AHE is higher than the Gd contribution.

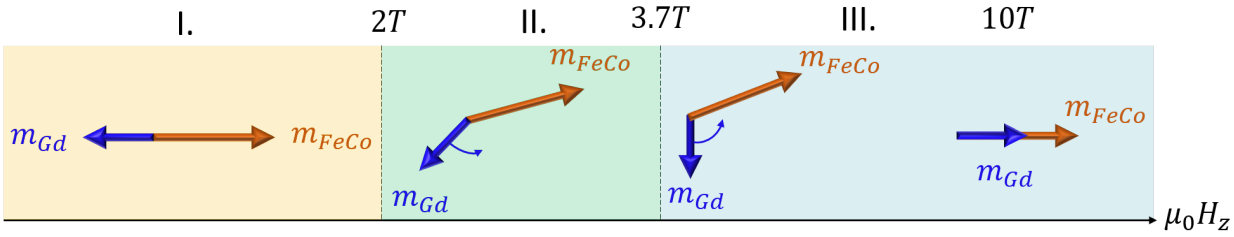

Figure 3.12: Interpretation of the spin-flop mechanism based on the longitudinal and transverse signals in FeCo-dominant Gd_{26}FeCo(10)/Cu(2)/Al(3).

The spin-flop mechanism and the way the sublattices rotate is illustrated in Figure 3.12 from our interpretation of the longitudinal and transverse signals with the magnetic fields.

Therefore, we have shown in this sample how the dominant sublattice contributing to the AHE can be determined by spin-flop measurements. In this sample, the FeCo sublattice appears to dominate the AHE transport. We will now show a case where the Gd sublattice dominates the AHE effect over the FeCo sublattice.

3.4.2 Case of Gd-sublattice dominating the AHE

We then present the case of Gd_{30}FeCo(10)/Cu(2)/Al(3), which requires a surprisingly low magnetic field to initiate the spin-flop. The evolution of the transverse and longitudinal resistance as a function of the magnetic field is shown in Figure 3.13 when the material is Gd-dominant at 70K (a) and when it is FeCo-dominant at 100K (b).

We first discuss the case of the transverse signals Figure3.13(a) and (c). The sign reversal of the AHE amplitude at low magnetic field confirms that the magnetic compensation temperature has been crossed between 70K and 100K. The spin-flop is observed at a very low magnetic field, $0.3T$. At 70K, the transverse signal decreases with increasing magnetic field, as discussed for the previous sample. Since the signal does not saturate with the magnetic field, we cannot conclude which sublattice might dominate the effect. However, at 100K, when GdFeCo is FeCo-dominant, the signal becomes positive for 2T and saturates at a positive value of the transverse resistance. This saturation indicates that at 100K the two sublattices have reached parallel alignment with the magnetic field. Since the AHE amplitude does not change much with temperature, we would expect the transverse resistance at 70K to saturate at the same value of R_{XY} as at 100K (shown by the red dashed lines). Extrapolating the signal at 70K, it appears that the transverse resistance saturates at a positive value for a positive magnetic field. **The positive sign of the saturated transverse resistances indicates that, in this particular sample, the Gd sublattice dominates the signal over the**

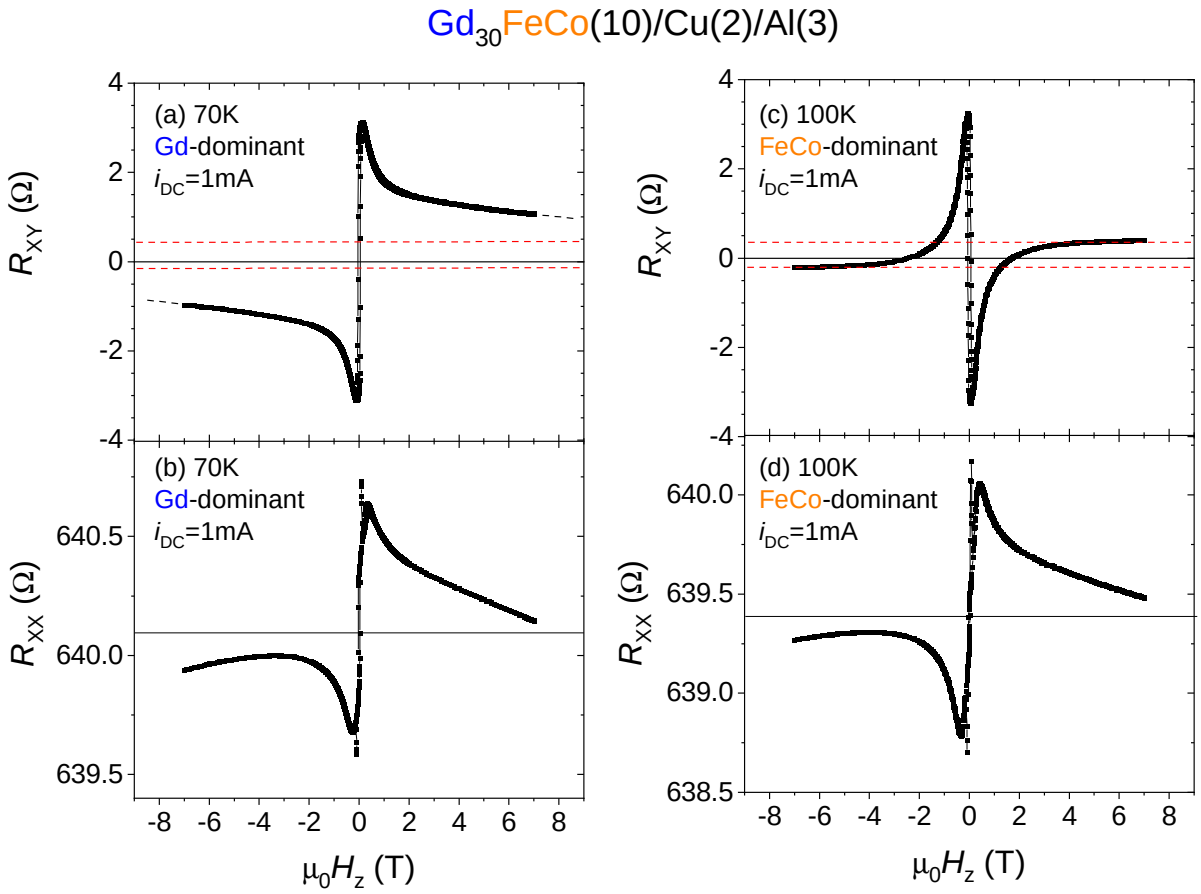

Figure 3.13: Evolution of the transverse signal as a function of the intensity of the external magnetic field applied along the $\hat{z}$ axis for $Gd_{30}FeCo(10)$ when the material is Gd-dominant at 70K (a,b) and when it is FeCo-dominant at 100K (c,d). We can see that the transverse resistance saturates at a positive value at high positive magnetic field, indicating that in this particular sample the Gd sublattice dominates the AHE signal.

FeCo sublattice over the magnetization compensation temperature.

The case of the longitudinal signals is very unusual (see Figure 3.13(b) and (d)), since the signal is antisymmetric with respect to the applied magnetic field. However, if we look at the signal for positive magnetic fields, we can see that it follows the same trend as the signal discussed in Section 3.4.1, i.e. it increases during the spin-flop up to a maximum corresponding to the alignment of Gd along the $\hat{x}$ axis and then decreases towards the value at zero magnetic field when the ferromagnetic order is reached. We also emphasize that the longitudinal signals obtained far from the compensation, where there is no or little spin-flop, are usual and symmetric with respect to the magnetic field. Thus, the feature shown here seems to be correlated with the spin-flop. Therefore, we will try to provide some idea to explain the antisymmetric behavior of the longitudinal signal with the magnetic field. We recall that the longitudinal signal is described phenomenologically by [87]:

$$R_{XX}^{AMR} = R_0 + A(m_x^{FeCo})^2 + B(m_x^{Gd})^2, \tag{3.7}$$

where $A > 0$ is the contribution of FeCo sublattice and $B < 0$ is the contribution of Gd sublattice. Considering that this equation is correct to fully describe the longitudinal signal, the antisymmetric behavior can only be explained if $A(m_x^{FeCo})^2 > B(m_x^{Gd})^2$ for positive magnetic fields and $B(m_x^{Gd})^2 > A(m_x^{FeCo})^2$ for negative magnetic fields and both when GdFeCo is Gd-dominant (70K) and when it is FeCo-dominant (100K). The sperimagnetic nature of GdFeCo may explain this behavior.

3.5 Conclusion

In this chapter we have introduced transport phenomena in GdFeCo.
First, we discussed the spin-polarized transport of the Gd-based ferrimagnet. This discussion is based solely on results from the literature. The spin-polarized transport is mainly attributed to the 3d electrons of the transition metal. It has been shown that the polarization of the Gd-based ferrimagnet has the same sign over the magnetization compensation temperature. The GMR using GdFeCo, which is related to the spin-polarized current of GdFeCo, changes its sign over the magnetization compensation temperature of the ferrimagnet. **These experiments confirm the dominant role of the 3d electrons of FeCo in the spin-polarized transport.**
We then presented magnetoresistive effects in GdFeCo such as AMR and AHE based on our results and literature. We determined the sign of AMR and AHE for Gd, FeCo and then compared with GdFeCo. From our results, which are consistent with the literature, **the AHE and AMR of GdFeCo result from the contributions of the Gd and FeCo sublattices**. In the case of AMR, the contributions add up destructively, and in the case of AHE, the contributions add up constructively. Therefore, there is no direct way to determine which sublattice dominates the AHE effect. **We propose to break the ferrimagnetic order to reveal which sublattice dominates the transport. We report the case of Gd_{30}FeCo(10)/Cu(2), where it appears that the Gd sublattice dominates the AHE transport** in contrast to the conventional wisdom that the FeCo sublattice always dominates magnetotransport effects. Our intuition suggests that the relative contribution of the sublattices to the magnetoresistive effects depends on the concentration of the two populations, and therefore Gd dominates the transport at higher concentrations. A more complete study needs to be performed to answer this question with certainty.

CHAPTER 4

Magnetization dynamics and SOT methodology

Dr. Thibaud Fache first developed the model for the ST-FMR technique as part of his PhD thesis and under the supervision of Dr. Sébastien Petit-Watelot. Then, I then extended the model for the second harmonic technique, again with the help of Dr. Sébastien Petit-Watelot. An article related to this model is currently being written.

The absorption of a spin current in a magnetic layer results in a spin torque on the magnetization that drives its dynamics. As experimenters, our goal is to estimate the amplitude of these torques as reliably as possible in order to compare their strength between different materials. Many quantification techniques have been developed for this purpose [113]. In this thesis, we focus on electrical measurements and in particular on the second harmonic and spin torque ferromagnetic resonance (ST-FMR) techniques, which are actually equivalent and based on the same underlying physical framework.

The aim of this chapter is to describe in detail the model that takes into account the effect of the torque on the magnetization and that allows to derive the analytical expressions of the electric voltages. First, since we are dealing with a ferrimagnet in this thesis, we will show that the dynamics of the net magnetization of a ferrimagnet can be described by the same equation as for the magnetization of a ferromagnet. Thus, considering this equivalence, we will derive the effect of a harmonic excitation due to a spin torque and show that the magnetization dynamics equation can be linearized. The dynamics is thus directly related to the excitation by the dynamical susceptibility. Its full expression is obtained after deriving the expression for the total magnetic energy density for the case of a ferromagnetic layer with out-of-plane uniaxial anisotropy. Considering the magnetoresistive effects described in Chapter 3, we will derive the general equation for the voltage that includes the dynamics of the magnetization, and will include thermal effects.

This chapter contains many equations that may not be appealing to read, but we deliberately chose to keep most of the calculation steps because they may be useful to students

or novices. The most important equations are framed for ease of reading. These general expressions are used in the following chapters to derive the analytical expressions for voltages in the case of the second harmonic technique and the ST-FMR technique.

4.1 Ferromagnetic and ferrimagnetic dynamics with a spin torque

4.1.1 Ferromagnetic dynamics in the presence of a spin torque

Let us recall the Landau-Lifshitz-Gilbert-Slonczewski (LLGS) equation for the dynamics of the magnetization of a ferromagnet under the action of a spin torque:

$$\frac{d\vec{M}}{dt} = -\gamma_0 \vec{M} \wedge \vec{H}_{eff} + \frac{\alpha}{M_S}\vec{M} \wedge \frac{d\vec{M}}{dt} + \gamma_0 \vec{\Gamma}_{ext}. \tag{4.1}$$

We recall that $\hat{\sigma}$ is the spin polarization direction, a_j is the amplitude of the damping-like torque, and b_j is the amplitude of the field-like torque. The spin torque a_j and b_j can be positive or negative. Since the LLGS equation conserves the modulus of magnetization, we can consider the dynamics of the normalized magnetization $\hat{m}(t) = \vec{M}(t)/M_S$, where M_S is the value of the magnetization at saturation. The LLGS equation can be expressed as [50, 25]:

$$\boxed{\frac{d\hat{m}}{dt} = -\gamma_0 \hat{m} \times \vec{H}_{eff} + \alpha \hat{m} \times \frac{d\hat{m}}{dt} + \frac{\gamma_0}{M_S} a_j \hat{m} \times (\hat{m} \times \hat{\sigma}) + \frac{\gamma_0}{M_S} b_j \hat{m} \times \hat{\sigma}.} \tag{4.2}$$

We define the effective fields associated with these torques using the general expression for a torque $\vec{\Gamma} = -M_S \hat{m} \times \mu_0 \vec{h}$ [114]:

$$\boxed{\vec{h}_{DL} \equiv -\frac{a_j}{\mu_0 M_S} \hat{m} \times \hat{\sigma}, \quad \text{and} \quad \vec{h}_{FL} \equiv -\frac{b_j}{\mu_0 M_S} \hat{\sigma}.} \tag{4.3}$$

We define $h_{DL,FL} \equiv -\frac{a_j, b_j}{\mu_0 M_S}$, which is not the norm of the vector $\vec{h}_{DL,FL}$ and can be positive or negative. $\vec{h}_{FL}$ is mathematically analogous to the precessional torque induced by the effective field $\vec{H}_{eff}$ and thus can be described by an additional contribution to the effective field, while $\vec{h}_{DL}$ tends to align the magnetization along or against $\hat{\sigma}$. In addition, the field-like term is independent of $\hat{m}$ while the damping-like term depends on the magnetization direction. Changing the external torque by both effective fields transforms the LLGS equation given by Eq.(4.2) into:

$$\frac{d\hat{m}}{dt} = -\gamma_0 \hat{m} \times (\vec{H}_{eff} + \delta\vec{h}) + \alpha \hat{m} \times \frac{d\hat{m}}{dt}, \tag{4.4}$$

with $\delta\vec{h} = \vec{h}_{DL} + \vec{h}_{FL} + \vec{h}_{Oe}$. The magnetization equilibrium position is obtained by setting $\frac{\partial \hat{m}}{\partial t} = 0$, which results in $\hat{m}_0 \parallel (\vec{H}_{eff} + \delta\vec{h})$. Therefore, the equilibrium position of the magnetization can be changed and misaligned with $\vec{H}_{eff}$ if the spin polarization is not aligned with $\vec{H}_{eff}$ and if the time average of the excitation field is $< \delta h(t) > \neq 0$.

In the framework of this thesis, self-induced spin torques act on the magnetization of a ferrimagnet. In the following section we show that the dynamics of the net magnetization of a ferrimagnet is equivalent to the dynamics of the magnetization of a ferromagnet.

4.1.2 Equivalency between ferrimagnetic and ferromagnetic dynamics

In the case of a ferrimagnet, two magnetic sublattices play a role in the dynamics. In the case where the magnetism comes solely from the spin angular momentum, allowing to translate the spin angular momentum directly into a magnetization, we can write a LLGS equation for each spin sublattice $S_{1,2}$. It comes:

$$\frac{d\vec{S}_1}{dt} = -\gamma_1 \vec{S}_1 \times \vec{H}_{eff} + \frac{\alpha_1}{S_1}\vec{S}_1 \times \frac{d\vec{S}_1}{dt} + \frac{a_j^1}{S_1^2}\vec{S}_1 \times (\vec{S}_1 \times \hat{\sigma}) + \frac{b_j^1}{S_1}\vec{S}_1 \times \hat{\sigma}, \tag{4.5a}$$

$$\frac{d\vec{S}_2}{dt} = -\gamma_2 \vec{S}_2 \times \vec{H}_{eff} + \frac{\alpha_2}{S_2}\vec{S}_2 \times \frac{d\vec{S}_2}{dt} + \frac{a_j^2}{S_2^2}\vec{S}_2 \times (\vec{S}_2 \times \hat{\sigma}) + \frac{b_j^2}{S_2}\vec{S}_2 \times \hat{\sigma}. \tag{4.5b}$$

We can consider three cases depending on the temperature of the system:

$T < T_M$	$T \in [T_M, T_A]$	$T > T_A$
1-dominant	2-dominant	2-dominant
$\gamma_1 S_1 > \gamma_2 S_2$	$\gamma_2 S_2 > \gamma_1 S_1$	$\gamma_2 S_2 > \gamma_1 S_1$
$S_1 > S_2$	$S_1 > S_2$	$S_2 > S_1$
$\vec{S}_1 + \vec{S}_2 = (S_1 - S_2)\hat{s}_1$	$\vec{S}_1 + \vec{S}_2 = (S_2 - S_1)\hat{s}_2$	$\vec{S}_1 + \vec{S}_2 = (S_2 - S_1)\hat{s}_2$

We can add Eq.(4.5a) and Eq.(4.5b) and consider the spin sublattice direction $\hat{s}_1$ or $\hat{s}_2$ depending on the dominance of the sublattice. Replacing the spin sublattice by the magnetic sublattice with $M_{1,2} = \gamma_{1,2} S_{1,2}$, we can write the LLGS equation for the net magnetization of a ferrimagnet far from the spin angular compensation as:

$$\begin{aligned} \frac{d\hat{m}_{net}}{dt} =& -\gamma_{eff}\hat{m}_{net} \times \vec{H}_{eff} + \alpha_{eff}\hat{m}_{net} \times \frac{d\hat{m}_{net}}{dt} \\ &+ \frac{\gamma_{eff}}{M_{net}}\left[a_j^{eff}\hat{m}_{net} \times (\hat{m}_{net} \times \hat{\sigma}) + b_j^{eff}\hat{m}_{net} \times \hat{\sigma}\right]. \end{aligned} \tag{4.6}$$

Thus, the LLGS equation for the net magnetization of a ferrimagnet can be written in the same form as the LLGS equation for a ferromagnet (see Eq.4.2) if we consider effective quantities for the gyromagnetic ratio γ_{eff} and the Gilbert damping α_{eff} but also for the torques a_i^{eff} and b_j^{eff} or for the effective fields h_{DL}^{eff} and h_{FL}^{eff}. These effective quantities can be positive or negative depending on the temperature of the system, in contrast to the classical quantities in the case of a ferromagnet. The definition and the sign of the effective quantities are shown in Figure (4.1).

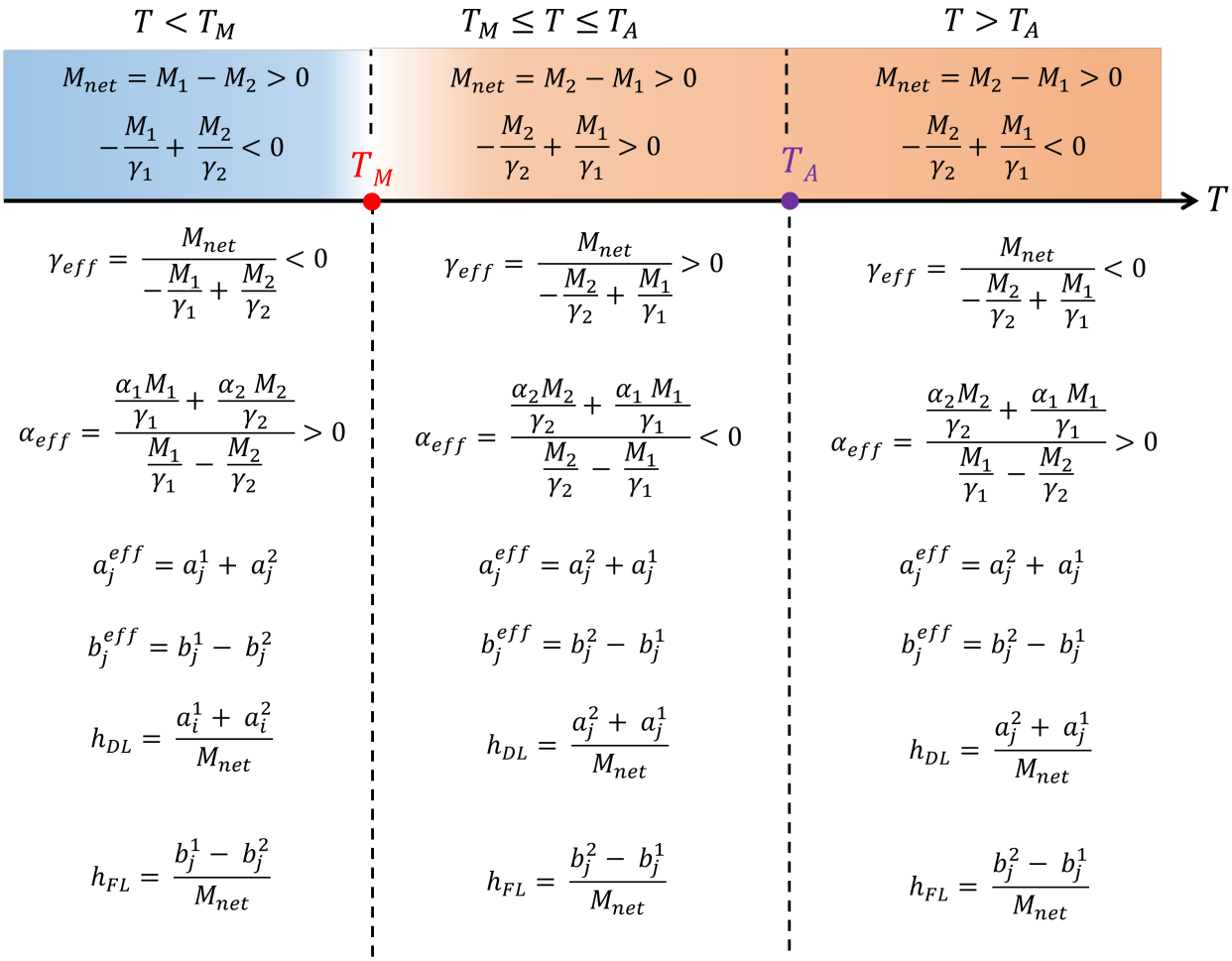

Figure 4.1: Definition and sign of the effective quantities appearing in the LLGS equation for a ferrimagnet (see Eq.(4.6)) in three different temperature ranges defined by T_M and T_A. The effective gyromagnetic ratio and the effective damping change their sign first over T_M and then over T_A. The DL effective spin torque a_j^{eff} and the associated effective field h_{DL} seems to have the same sign over the compensation temperatures.

It turns out that the effective gyromagnetic ratio is positive for $T < T_M$, then negative above T_M, and positive again for $T > T_A$. It can be seen that the precession of the magnetization around $\vec{H}_{eff}$ occurs in opposite directions (clockwise for $\gamma_{eff} > 0$, counterclockwise for $\gamma_{eff} < 0$). The effective damping also follows a double sign reversal at T_M and T_A in the same way as the gyromagnetic ratio. The sign changes of α_{eff} compensate the sign change of $d\hat{m}/dt$ related to γ_{eff}, and as a result the damping term in the LLGS equation still aligns the magnetization to $\vec{H}_{eff}$ for all temperature ranges.

It is interesting to note that the damping-like effective spin torque and the associated effective field have the same sign for all temperatures. For the field-like case, if we consider that $b_j^1 > b_j^2$ for all temperatures, the effective spin torque and the associated effective field changes its sign at T_M. These sign changes for the spin torque will be discussed in more details in the chapter focusing on the spin-orbit torque and self-torque in GdFeCo (Chapter 6).

Thus, the dynamics of the net magnetization of a ferrimagnet can be described by the LLGS equation for a ferromagnet. For this reason, in the following sections, we further developed the model by considering the magnetization of a ferromagnet and the associated LLGS equation.

4.1.3 Magnetization dynamics in spherical coordinates

The magnetization dynamics of a ferrimagnet can essentially be expressed and described by the LLGS equation of a ferromagnet:

$$\frac{d\hat{m}}{dt} = -\gamma_0 \hat{m} \times (\vec{H}_{eff} + \delta\vec{h}) + \alpha \hat{m} \times \frac{d\hat{m}}{dt}. \tag{4.7}$$

To further clarify the LLGS equation (see Eq.(4.4)), we project the various quantities in spherical coordinates in the frame $(\hat{e}_r,\hat{e}_\theta,\hat{e}_\varphi)$ linked to the position of the magnetization $\hat{m} = \hat{e}_r$. The equilibrium position of the magnetization is expressed with the polar and azimuthal angles (θ,φ) according to $\hat{m} = (\sin(\theta)\cos(\varphi), \sin(\theta)\sin(\varphi), \cos(\theta))$ and as shown in Figure 4.2. The different quantities in the LLGS equation are written in spherical coordinates:

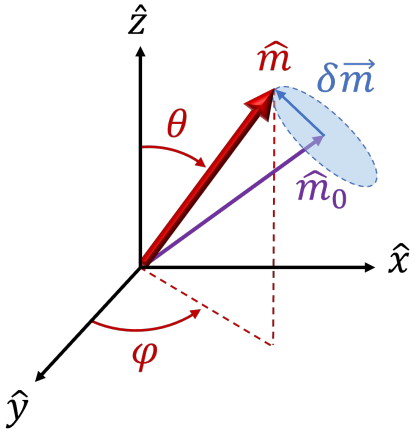

Figure 4.2: The magnetization $\hat{m}$ is described in spherical coordinates. It is aligned to $\hat{r}$ and is fully described by the polar and azimuthal angles (θ, φ). Under harmonic excitation, the motion of the magnetization is decomposed into oscillations $\delta\vec{m}(\delta\theta, \delta\varphi)$ around its equilibrium position $\hat{m}_0(\theta_0, \varphi_0)$.

$$\hat{m} = \begin{bmatrix} 1 \\ 0 \\ 0 \end{bmatrix}; \quad \frac{d\hat{m}}{dt} = \begin{bmatrix} 0 \\ \dot{\theta} \\ \dot{\varphi}\sin(\theta) \end{bmatrix}; \quad \vec{H}_{eff} = -\frac{1}{\mu_0 M_S} \begin{bmatrix} 0 \\ \varepsilon_\theta(\theta,\varphi) \\ \frac{1}{\sin(\theta)}\varepsilon_\varphi(\theta,\varphi) \end{bmatrix} \text{ and } \quad \delta\vec{h} = \begin{bmatrix} \delta h_r \\ \delta h_\theta \\ \delta h_\varphi \end{bmatrix},$$

so that LLGS is expressed in spherical coordinates:

$$\begin{bmatrix} 0 \\ \dot{\theta} \\ \dot{\varphi}\sin(\theta) \end{bmatrix} = -\gamma_0 \begin{bmatrix} 1 \\ 0 \\ 0 \end{bmatrix} \times \left(-\frac{1}{\mu_0 M_S} \begin{bmatrix} 0 \\ \varepsilon_\theta \\ \frac{1}{\sin(\theta)}\varepsilon_\varphi \end{bmatrix} + \begin{bmatrix} \delta h_r \\ \delta h_\theta \\ \delta h_\varphi \end{bmatrix} \right) + \alpha \begin{bmatrix} 1 \\ 0 \\ 0 \end{bmatrix} \times \begin{bmatrix} 0 \\ \dot{\theta} \\ \dot{\varphi}\sin(\theta) \end{bmatrix},$$

and can be reduced to a system of two coupled differential equations:

$$\begin{cases} \dot{\theta} = -\dfrac{\gamma_0}{\mu_0 M_S \sin(\theta)}\varepsilon_\varphi(\theta,\varphi) - \alpha\dot{\varphi}\sin(\theta) + \gamma_0\delta h_\varphi \\ \dot{\varphi}\sin(\theta) = \dfrac{\gamma_0}{\mu_0 M_S}\varepsilon_\theta(\theta,\varphi) + \alpha\dot{\theta} - \gamma_0\delta h_\theta \end{cases}. \tag{4.8}$$

The latter equations are nonlinear and analytical expressions can be found only for certain simple cases. One way to reduce the complexity of the equations is to linearize the system. To do this, we impose a harmonic excitation $\delta\vec{h}$ with pulsation ω.

4.2 Magnetization dynamics due to a harmonic excitation

Let us now consider a general periodic excitation $\delta\vec{h}(t)$ weak enough to excite the magnetization dynamics without changing its periodic equilibrium position. As a result, the magnetization precesses around a static equilibrium position $\hat{m}_0$ such that $\hat{m} = \hat{m}_0 + \delta\vec{m}(t)$ as shown in Figure 4.2. By considering a weak excitation, we describe the response of the magnetization in the general framework of the linear response theory, which allows to linearize LLGS by replacing the following terms in the LLGS equation Eq.(4.4):

$$\begin{cases} \hat{m}(t) \to \hat{m}_0 + \delta\vec{m}(t) \\ \vec{H}_{eff}(t) \to \vec{H}^0_{eff} + \delta\vec{H}_{eff}(t) + \delta\vec{h}(t). \end{cases}$$

Keeping the first-order terms in $\delta\vec{m}$ and $\delta\vec{H}_{eff}$, and considering that the equilibrium position is $\gamma_0\hat{m}_0 \times \vec{H}^0_{eff} = 0$, the linearized expression of LLGS is:

$$\frac{d\delta\vec{m}}{dt} - \alpha\hat{m}_0 \times \frac{d\delta\vec{m}}{dt} + \gamma_0\left(\hat{m}_0 \times \delta\vec{H}_{eff} + \delta\vec{m} \times \vec{H}^0_{eff}\right) = \gamma_0\hat{m}_0 \times \delta\vec{h}. \tag{4.9}$$

To express this linearized expression of the LLGS in spherical coordinates, we have to consider the following expressions for the magnetization position and the effective field:

$$\hat{m}(t) \to \hat{m}_0 + \delta\vec{m}(t) \Leftrightarrow \begin{cases} \theta(t) \to \theta_0 + \delta\theta(t) \\ \varphi(t) \to \varphi_0 + \delta\varphi(t) \end{cases} \quad \text{with } \delta\theta \text{ and } \delta\varphi \ll \pi,$$

$$\vec{H}_{eff}(t) \to \vec{H}^0_{eff} + \delta\vec{H}_{eff}(t) \Leftrightarrow \begin{cases} \varepsilon_\theta(\theta,\varphi) \to \varepsilon_\theta(\theta_0,\varphi_0) + \varepsilon_{\theta\theta}(\theta_0,\varphi_0)\delta\theta + \varepsilon_{\theta\varphi}(\theta_0,\varphi_0)\delta\varphi \\ \varepsilon_\varphi(\theta,\varphi) \to \varepsilon_\varphi(\theta_0,\varphi_0) + \varepsilon_{\theta\varphi}(\theta_0,\varphi_0)\delta\theta + \varepsilon_{\varphi\varphi}(\theta_0,\varphi_0)\delta\varphi \end{cases},$$

and considering the equilibrium position $\varepsilon_\theta(\theta_0,\varphi_0) = \varepsilon_\varphi(\theta_0,\varphi_0) = 0$, the system given by Eq.(4.8) can be reduced to the following matrix form of a coupled first-order differential equation:

$$\frac{1}{\gamma_0}\begin{bmatrix}\alpha & -1\\ 1 & \alpha\end{bmatrix}\cdot\begin{bmatrix}\dot{\delta\theta}\\ \sin(\theta_0)\dot{\delta\varphi}\end{bmatrix} + \frac{1}{\mu_0 M_S}\begin{bmatrix}\varepsilon_{\theta\theta} & \dfrac{\varepsilon_{\theta\varphi}}{\sin(\theta_0)}\\ \dfrac{\varepsilon_{\theta\varphi}}{\sin(\theta_0)} & \dfrac{\varepsilon_{\varphi\varphi}}{\sin^2(\theta_0)}\end{bmatrix}\cdot\begin{bmatrix}\delta\theta\\ \sin(\theta_0)\delta\varphi\end{bmatrix} = \begin{bmatrix}\delta h_\theta\\ \delta h_\varphi\end{bmatrix}. \quad (4.10)$$

In the linear response theory, the time-dependent variables can be written in terms of the pulsation-dependent variables using complex notation. For the excitation field $\delta\vec{h}(t) = \delta\vec{h}(t)\cos(\omega t) \to \delta\underline{\vec{h}}(\omega) = e^{i\omega t}\underline{\delta\vec{h}}$, for the magnetization $\delta\vec{m}(t) \to \delta\underline{\vec{m}}(\omega) = \delta\underline{\vec{m}}e^{i\omega t}$, and the response of the magnetization occurs at the same pulsation as the excitation, i.e. $d\underline{\delta\vec{m}}/dt = i\omega\underline{\delta\vec{m}}$. As a consequence, the magnetization is directly proportional to the excitation via the complex dynamical susceptibility matrix $\underline{\underline{\chi}}(\omega)$:

$$\boxed{M_S\underline{\delta\vec{m}}(\omega) = \underline{\underline{\chi}}(\omega)\cdot\underline{\delta\vec{h}}(\omega),} \quad (4.11)$$

The expression of the susceptibility matrix can be obtained from Eq.(4.10) and is:

$$\underline{\underline{\chi}}(\omega) = \frac{\gamma_0^2 M_S}{(1+\alpha^2)\left[(\omega_0^2-\omega^2)+i\Delta_\omega\omega\right]}\begin{bmatrix}\dfrac{\varepsilon_{\varphi\varphi}}{\mu_0 M_S\sin^2(\theta_0)} + i\alpha\dfrac{\omega}{\gamma_0} & -\dfrac{\varepsilon_{\theta\varphi}}{\mu_0 M_S\sin(\theta_0)} + i\dfrac{\omega}{\gamma_0}\\ -\dfrac{\varepsilon_{\theta\varphi}}{\mu_0 M_S\sin(\theta_0)} - i\dfrac{\omega}{\gamma_0} & \dfrac{\varepsilon_{\theta\theta}}{\mu_0 M_S} + i\alpha\dfrac{\omega}{\gamma_0}\end{bmatrix}, \quad (4.12)$$

where we define:

$$\boxed{\begin{aligned} &\text{- The resonance frequency:} \quad \omega_0 = \frac{\gamma_0}{\sqrt{1+\alpha^2}\mu_0 M_S\sin(\theta_0)}\sqrt{\varepsilon_{\theta\theta}\varepsilon_{\varphi\varphi} - (\varepsilon_{\theta\varphi})^2} \\ &\text{- The resonance linewidth:} \quad \Delta_\omega = \frac{\gamma_0\alpha}{(1+\alpha^2)\mu_0 M_S}\left(\varepsilon_{\theta\theta} + \frac{\varepsilon_{\varphi\varphi}}{\sin^2(\theta_0)}\right). \end{aligned}} \quad (4.13)$$

In addition, the susceptibility can be decomposed into a real part $\underline{\underline{\chi'}}$ and an imaginary part $\underline{\underline{\chi''}}$, which describe the ability of the magnetization to follow the excitation and to dissipate

energy, respectively:

$$\underline{\underline{\chi}}(\omega) = \begin{bmatrix} \underline{\chi}_{\theta\theta} & \underline{\chi}_{\theta\varphi} \\ \underline{\chi}_{\varphi\theta} & \underline{\chi}_{\varphi\varphi} \end{bmatrix} = \underline{\underline{\chi}}' + i\underline{\underline{\chi}}'' = \begin{bmatrix} \chi'_{\theta\theta} & \chi'_{\theta\varphi} \\ \chi'_{\varphi\theta} & \chi'_{\varphi\varphi} \end{bmatrix} + i \begin{bmatrix} \chi''_{\theta\theta} & \chi''_{\theta\varphi} \\ \chi''_{\varphi\theta} & \chi''_{\varphi\varphi} \end{bmatrix}, \tag{4.14}$$

with their respective forms:

$$\boxed{\underline{\underline{\chi}}'(\omega) = \frac{\gamma_0^2 M_S}{(1+\alpha^2)\left[(\omega_0^2-\omega^2)^2+(\Delta_\omega\omega)^2\right]} \begin{bmatrix} \dfrac{\varepsilon_{\varphi\varphi}(\omega_0^2-\omega^2)}{\mu_0 M_S \sin^2(\theta_0)} + \dfrac{\alpha\Delta_\omega\omega^2}{\gamma_0} & -\dfrac{\varepsilon_{\theta\varphi}(\omega_0^2-\omega^2)}{\mu_0 M_S \sin(\theta_0)} + \dfrac{\Delta_\omega\omega^2}{\gamma_0} \\ -\dfrac{\varepsilon_{\theta\varphi}(\omega_0^2-\omega^2)}{\mu_0 M_S \sin(\theta_0)} - \dfrac{\Delta_\omega\omega^2}{\gamma_0} & \dfrac{\varepsilon_{\theta\theta}(\omega_0^2-\omega^2)}{\mu_0 M_S} + \dfrac{\alpha\Delta_\omega\omega^2}{\gamma_0} \end{bmatrix}} \tag{4.15}$$

$$\boxed{\underline{\underline{\chi}}''(\omega) = \frac{\gamma_0^2 M_S \omega}{(1+\alpha^2)\left[(\omega_0^2-\omega^2)^2+(\Delta_\omega\omega)^2\right]} \begin{bmatrix} -\dfrac{\Delta_\omega\varepsilon_{\varphi\varphi}}{\mu_0 M_S \sin^2(\theta_0)} + \dfrac{\alpha(\omega_0^2-\omega^2)}{\gamma_0} & \dfrac{\omega_0^2-\omega^2}{\gamma_0} + \dfrac{\Delta_\omega\varepsilon_{\theta\varphi}}{\mu_0 M_S \sin(\theta_0)} \\ -\dfrac{\omega_0^2-\omega^2}{\gamma_0} + \dfrac{\Delta\varepsilon_{\theta\varphi}}{\mu_0 M_S \sin(\theta_0)} & -\dfrac{\Delta_\omega\varepsilon_{\theta\theta}}{\mu_0 M_S} + \dfrac{\alpha(\omega_0^2-\omega^2)}{\gamma_0} \end{bmatrix}}. \tag{4.16}$$

In summary, the response of the magnetization is directly proportional to the harmonic excitation through the dynamic susceptibility matrix:

$$\begin{bmatrix} \underline{\delta\theta_0} \\ \sin(\theta_0)\underline{\delta\varphi_0} \end{bmatrix} = \begin{bmatrix} \underline{\chi_{\theta\theta}} & \underline{\chi_{\theta\varphi}} \\ \underline{\chi_{\varphi\theta}} & \underline{\chi_{\varphi\varphi}} \end{bmatrix} \cdot \begin{bmatrix} \underline{\delta h_\theta} \\ \underline{\delta h_\varphi} \end{bmatrix}. \tag{4.17}$$

Therefore, to fully model the dynamics of the magnetization, we need to derive three main components: 1) the position of the magnetization dynamics, 2) the geometry of the excitation field, and 3) the components of the susceptibility matrix. The goal of the following sections is to derive these components. First, we derive the general expressions for the voltages that allow the position of the magnetization to be sensed.

4.3 Electrical readout effects

In Chapter 3, we introduced the notion of magnetoresistive effects and showed how the electrical voltages are directly related to the magnetization position. We recall the geometry of a Hall cross, where the current is applied along $\hat{x}$ and the longitudinal voltage V_X and the transverse voltage V_Y can be measured, as illustrated in Figure 4.3. The voltages have the form:

$$V_X = I_X\left[R_0 + \Delta R^{AMR}\sin^2(\theta)\cos^2(\varphi)\right], \tag{4.18a}$$

$$V_Y = I_X\left[\Delta R^{AHE}\cos(\theta) + \Delta R^{PHE}\sin^2(\theta)\sin(2\varphi)\right]. \tag{4.18b}$$

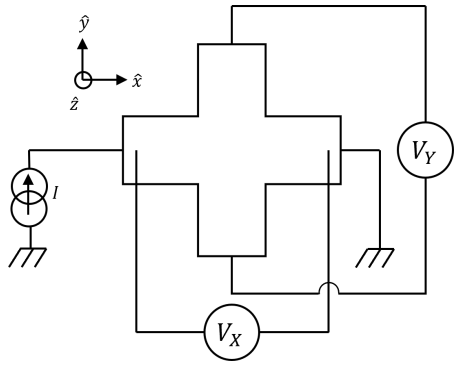

Figure 4.3: Schematic of an integrated Hall cross. This geometry allows to inject the current along $\hat{x}$ and to measure either the longitudinal voltage V_X or the transverse voltage V_Y.

where (θ,φ) describe the magnetization position in spherical coordinates (see Figure4.2). In the following, we derive these expressions further considering the case of a harmonic excitation driving the magnetization dynamics.

4.3.1 Harmonic response of the longitudinal and transverse voltages

Let us consider a sinusoidal current with a pulsation ω $I_X = I_X \cos(\omega t)$. The response of the longitudinal and transverse voltages occurs at the same pulsation as the excitation, but also at its harmonics:

$$V_X(\omega) = R_{XX}(\omega) I_X \cos(\omega t) \tag{4.19a}$$
$$\rightarrow \underline{V_X}(\omega) = \underline{V_X^0} + \underline{V_X^{1\omega}} + \underline{V_X^{2\omega}} = \frac{1}{2}\mathrm{Re}(\underline{R_{XX}^{2\omega}}) + \underline{R_{XX}^{1\omega}} I_X e^{i\omega t} + \frac{1}{2}\underline{R_{XX}^{2\omega}} I_X e^{2i\omega t},$$

$$V_Y(\omega) = R_{XY}(\omega) I_X \cos(\omega t) \tag{4.19b}$$
$$\rightarrow \underline{V_Y}(\omega) = \underline{V_Y^0} + \underline{V_Y^{1\omega}} + \underline{V_Y^{2\omega}} = \frac{1}{2}\mathrm{Re}(\underline{R_{XY}^{2\omega}}) + \underline{R_{XY}^{1\omega}} I_X e^{i\omega t} + \frac{1}{2}\underline{R_{XY}^{2\omega}} I_X e^{2i\omega t}.$$

We can now linearize the expressions for the voltages. Indeed, if I_X is weak enough, the magnetization precesses around its equilibrium position at the same frequency as the excitation in the framework of the linear response theory. The linearization consists in substituting in the expressions for the voltages:

$$\begin{cases} \theta(\omega) \rightarrow \theta_0 + \underline{\delta\theta} e^{i\omega t} \\ \varphi(\omega) \rightarrow \varphi_0 + \underline{\delta\varphi} e^{i\omega t} \end{cases}.$$

It turns out that the signal of the first harmonic depends on the static equilibrium of the magnetization (θ_0, φ_0):

$$\underline{V_X^{1\omega}} = I_X \left[R_0 + \Delta R^{AMR} \sin^2(\theta_0) \cos^2(\varphi_0) \right], \tag{4.20a}$$
$$\underline{V_Y^{1\omega}} = I_X \left[R^H H_{ext} \cos(\theta_H) + \Delta R^{AHE} \cos(\theta_0) + \Delta R^{PHE} \sin^2(\theta_0) \sin(2\varphi_0) \right]. \tag{4.20b}$$

while the second harmonic includes the dynamics of the magnetization given by $(\delta\theta, \delta\varphi)$

and induced by the Oersted field and the SOT effective fields:

$$\underline{V_X^{2\omega}} = \frac{I_X}{2}\left[\Delta R^{AMR}\left(\sin(2\theta_0)\cos^2(\varphi_0)\ \underline{\delta\theta} - \sin^2(\theta_0)\sin(2\varphi_0)\ \underline{\delta\varphi}\right)\right], \tag{4.21a}$$

$$\underline{V_Y^{2\omega}} = \frac{I_X}{2}\left[-\Delta R^{AHE}\sin(\theta_0)\ \underline{\delta\theta} + \Delta R^{PHE}\left(\sin(2\theta_0)\sin(2\varphi_0)\ \underline{\delta\theta} + 2\sin^2(\theta_0)\cos(2\varphi_0)\ \underline{\delta\varphi}\right)\right]. \tag{4.21b}$$

As explained in the previous sections, the magnetization dynamics is directly related to the excitation field through the dynamical susceptibility matrix (see Eq.(4.11)). Therefore, we can replace the angular terms related to the magnetization dynamics by the components of the susceptibility matrix and the excitation fields given by Eq.(4.17) in the expressions for the voltages. It comes:

$$\boxed{\begin{aligned}\underline{V_X^{2\omega}} = \frac{I_X}{2M_S}\Big[&\Delta R^{AMR}\left(\sin(2\theta_0)\cos^2(\varphi_0)\ \underline{\chi_{\theta\theta}} - \sin(\theta_0)\sin(2\varphi_0)\ \underline{\chi_{\varphi\theta}}\right)\underline{\delta h_\theta} \\ &+\Delta R^{AMR}\left(\sin(2\theta_0)\cos^2(\varphi_0)\ \underline{\chi_{\theta\varphi}} - \sin(\theta_0)\sin(2\varphi_0)\ \underline{\chi_{\varphi\varphi}}\right)\underline{\delta h_\varphi}\Big]\end{aligned}} \tag{4.22}$$

$$\boxed{\begin{aligned}\underline{V_Y^{2\omega}} = \frac{I_X}{2M_S}\Big[&\left(-\Delta R^{AHE}\sin(\theta_0) + \Delta R^{PHE}\sin(2\theta_0)\sin(2\varphi_0)\right)\underline{\chi_{\theta\theta}} \\ &+2\Delta R^{PHE}\sin(\theta_0)\cos(2\varphi_0)\ \underline{\chi_{\varphi\theta}}\Big]\underline{\delta h_\theta} \\ &+\frac{I_X}{2M_S}\Big[\left(-\Delta R^{AHE}\sin(\theta_0) + \Delta R^{PHE}\sin(2\theta_0)\sin(2\varphi_0)\right)\underline{\chi_{\theta\varphi}} \\ &+2\Delta R^{PHE}\sin(\theta_0)\cos(2\varphi_0)\underline{\chi_{\varphi\varphi}}\Big]\ \underline{\delta h_\varphi}.\end{aligned}} \tag{4.23}$$

Therefore, magnetoresistive effects are used as a tool to probe the magnetization dynamics. In addition to these effects, thermoelectric effects can lead to signals.

4.3.2 Thermoelectric and thermomagnetic phenomena

Joule heating and heat currents are inherent to electrical measurements due to the injection of a current density into a heterostructure. We describe here the Righi-Leduc (RL) effect [115], which is referred to as the thermal counterpart of the Hall effect, and the anomalous Nernst effect (ANE). These effects take into account the transverse temperature gradient produced by a charge current in a magnetic material. Under a heat current injection, an anisotropic temperature gradient is generated and imposed by the direction of magnetization. Considering the Onsager reciprocity relations in a magnetic system [116], it has been shown that the angular dependence of the thermal gradient takes the same form as the magnetoresistive effect such as the AMR, the PHE, and the AHE. In fact, as derived in Chapter 3, the anisotropic electronic transport can be written in the form of the generalized Ohm's law:

$$\vec{E} = \rho\vec{J}_c + \Delta\rho\left(\vec{J}_c.\hat{m}\right)\hat{m} + \rho^{AHE}\hat{m}\times\vec{J}_c, \tag{4.24}$$

where $\vec{E}$ is the electric field, $\hat{m}$ is the direction of the magnetization, ρ is the electrical resistivity, $\Delta\rho$ is the AMR, and ρ_{AHE} is the anomalous Hall resistivity. According to [116, 117, 118] , the temperature gradient $\vec{\nabla}T$ has a similar form:

$$\vec{\nabla}T = r\vec{J^Q} + \Delta r(\vec{J^Q}.\hat{m})\hat{m} + r_{ARL}\hat{m} \times \vec{J^Q}, \tag{4.25}$$

where $\vec{J^Q}$ is the heat current density, r is the magnetization independent thermal resistance, Δr is the anisotropic magnetothermal resistance, and β_{ARL} is the anomalous Righi-Leduc thermal resistance. The temperature difference at the contacts is converted into a potential variation by the Seebeck tensor [116]:

$$\Delta\vec{V}_{th} = S\Delta\vec{T} + \Delta S_{\parallel}(\Delta\vec{T}\cdot\hat{m})\hat{m} + S_{AN}\hat{m} \times \Delta\vec{T}, \tag{4.26}$$

where S is the Seebeck coefficient, $\Delta S_{\parallel}$ is the Nernst coefficient, and S_{AN} is the anomalous Nernst coefficient. Thus, the voltage related to the thermal gradient takes the general form:

$$\vec{\nabla}V^{th} = B_{th}\vec{J^Q} + \Delta B_{th\parallel}(\vec{J^Q}.\hat{m})\hat{m} + B_{AN/RL}\hat{m} \times \vec{J^Q}. \tag{4.27}$$

Let us consider an applied alternative current $I_X(t) = I_X\cos(\omega t)$. A heat flux density $\vec{J^Q} \propto I_X^2(t+\tau) = \frac{I_X^2}{2} + \frac{I_X^2}{2}\cos(2\omega t + 2\phi_0)$ is thus generated at DC and 2ω with a possible phase ϕ_0 resulting from the delay that thermal effects can take while propagating. Such a phase contributes to the imaginary voltage signal at 2ω. The magnetothermal signal is related to the position of the magnetization, which is the sum of its equilibrium position and its dynamics $\hat{m} = \hat{m}_0 + \delta\vec{m}(\omega)$. As a consequence, the magnetothermal effect related to $\hat{m}_0$ appears at DC and 2ω, and the one related to $\delta\vec{m}$ appears at ω and 3ω. The thermal contribution at ω is usually small compared to the thermal contribution at DC and is neglected here. Also, the thermal contribution at ω is negligible compared to the magnetoresistive signal at ω. Then we consider the thermal contribution in the second harmonic signal. It comes for the longitudinal and transverse voltages that:

$$\begin{aligned} V_X = {} & R_{th}I_X^2 + \Delta R_{\parallel th}\left[I_X^2\sin(\theta_0)\cos(\varphi_0) + I_X^2\sin(\theta_0)\sin(\varphi_0) + I_X^2\cos(\theta_0)\right]\sin(\theta_0)\cos(\varphi_0) \\ & + R_{ARLth}\left[I_X^2\sin(\theta_0)\sin(\varphi_0) - I_X^2\cos(\theta_0)\right] \end{aligned} \tag{4.28a}$$

$$\begin{aligned} V_Y = {} & R_{th}I_X^2 + \Delta R_{\parallel th}\left[I_X^2\sin(\theta_0)\cos(\varphi_0) + I_X^2\sin(\theta_0)\sin(\varphi_0) + I_X^2\cos(\theta_0)\right]\sin(\theta_0)\sin(\varphi_0) \\ & + R_{ARLth}\left[I_X^2\cos(\theta_0) - I_X^2\sin(\theta_0)\cos(\varphi_0)\right] \end{aligned} \tag{4.28b}$$

To obtain the full analytical expressions for the voltages, including the contribution of thermal effects, we need to know the exciting field expression and the component of the susceptibility matric. Let us first discuss the geometry of the excitation field.

4.4 Geometry of the exciting field

4.4.1 General expression

The harmonic excitation results from the periodic current density, which produces an Oersted field and SOT effective fields:

$$\delta\vec{h}(t) = \vec{h}_{Oe}(t) + \vec{h}_{SOT}(t) \rightarrow \underline{\delta\vec{h}}(\omega) = \underline{\vec{h}_{Oe}} + \underline{\vec{h}_{FL}} + \underline{\vec{h}_{DL}}.$$

The Oersted field is represented by a general vector, and the effective fields can be expressed according to Eq.(4.3):

$$\begin{aligned} \underline{\delta\vec{h}}(\omega) &= \left(\begin{bmatrix} \underline{h_{Oe_r}} \\ \underline{h_{Oe_\theta}} \\ \underline{h_{Oe_\varphi}} \end{bmatrix} + \underline{h_{FL}} \begin{bmatrix} \sigma_r \\ \sigma_\theta \\ \sigma_\varphi \end{bmatrix} + \underline{h_{DL}} \begin{bmatrix} 1 \\ 0 \\ 0 \end{bmatrix} \times \begin{bmatrix} \sigma_r \\ \sigma_\theta \\ \sigma_\varphi \end{bmatrix} \right) e^{i\omega t} \\ &= \begin{bmatrix} \underline{h_{Oe_r}} + \underline{h_{FL}}\sigma_r \\ \underline{h_{Oe_\theta}} + \underline{h_{FL}}\sigma_\theta - \underline{h_{DL}}\sigma_\varphi \\ \underline{h_{Oe_\varphi}} + \underline{h_{FL}}\sigma_\varphi + \underline{h_{DL}}\sigma_\theta \end{bmatrix} e^{i\omega t}, \end{aligned} \tag{4.29}$$

where the polarization direction $\hat{\sigma}$ is described by the angles $(\theta_\sigma, \varphi_\sigma)$ and its components are in spherical coordinates:

$$\begin{cases} \sigma_r = \sin(\theta_0)\sin(\theta_\sigma)\cos(\varphi_\sigma - \varphi_0) + \cos(\theta_\sigma)\cos(\theta_0) \\ \sigma_\theta = \cos(\theta_0)\sin(\theta_\sigma)\cos(\varphi_\sigma - \varphi_0) - \cos(\theta_\sigma)\sin(\theta_0) \\ \sigma_\varphi = \sin(\theta_\sigma)\sin(\varphi_\sigma - \varphi_0) \end{cases}. \tag{4.30}$$

And the motion of the magnetization is given by:

$$\begin{bmatrix} \underline{\delta\theta_0} \\ \sin(\theta_0)\underline{\delta\varphi_0} \end{bmatrix} = \begin{bmatrix} \underline{\chi_{\theta\theta}} & \underline{\chi_{\theta\varphi}} \\ \underline{\chi_{\varphi\theta}} & \underline{\chi_{\varphi\varphi}} \end{bmatrix} \cdot \begin{bmatrix} \underline{h_{Oe_\theta}} + \underline{h_{FL}}\sigma_\theta - \underline{h_{DL}}\sigma_\varphi \\ \underline{h_{Oe_\varphi}} + \underline{h_{FL}}\sigma_\varphi + \underline{h_{DL}}\sigma_\theta \end{bmatrix} e^{i\omega t}. \tag{4.31}$$

4.4.2 Case of the spin Hall effect

The spin Hall effect was introduced in Chapter 1 Section 1.2.2. The effect produces a pure spin current with a spin polarization along the $\hat{y}$ axis. The components of the spin polarization are expressed:

$$\begin{cases} \sigma_r = \sin(\theta_0)\sin(\varphi_0) \\ \sigma_\theta = \cos(\theta_0)\sin(\varphi_0) \\ \sigma_\varphi = \cos(\varphi_0) \end{cases}. \tag{4.32}$$

The excitation field driving the magnetization dynamics is the sum of the SOT effective fields and an Oersted field generated by the current. The SOT effective fields are considered to be in phase with the current because the mechanisms for the generating the spin current and spin torque occur on a very short time scale compared to the characteristic times of the magnetization dynamics. The Oersted field is also in phase with the current. Considering the current as the phase origin, it follows that the SOT effective fields and the Oersted are

real quantities, and we can express the components of the effective field in the case of the spin Hall effect:

$$\begin{aligned}\delta h_\theta &= h_{Oe\theta} + h_{FL}\cos(\theta_0)\sin(\varphi_0) - h_{DL}\cos(\varphi_0)\\ \delta h_\varphi &= h_{Oe\varphi} + h_{FL}\cos(\varphi_0) + h_{DL}\cos(\theta_0)\sin(\varphi_0)\end{aligned} \tag{4.33}$$

Let us discuss the geometry of the Oersted field in our systems. We consider a bilayer consisting of a ferromagnet FM and a non-magnetic material NM with respective thicknesses t_{FM} and t_{NM} as illustrated in Figure 4.4. We assume that the resistivity of NM is lower than that of FM, and a current density flowing along $\hat{x}$ will flow mainly in the NM layer. This results in an Oersted field on the FM layer with a spatial average along the $\hat{y}$ axis. When the bilayer is reversed, the Oersted field acting on FM is along $-\hat{y}$. Thus, the Oersted field in this geometry has the same symmetry as the field-like effective field. Therefore we write $h_{FL} + h_{Oe} = h_{FL'}$.

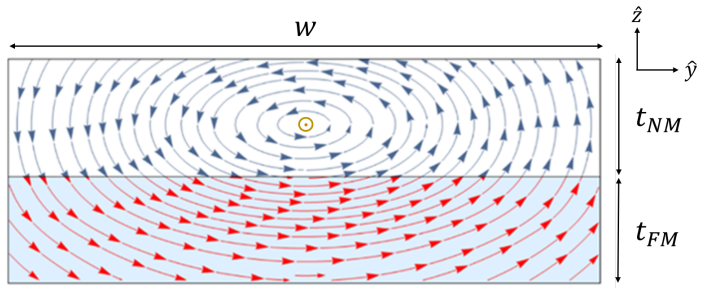

Figure 4.4: Schematic of a FM/NM bilayer section with a charge current applied along $\hat{x}$. Part of the current flows in the NM layer when its resistivity is lower than that of the FM layer. As a consequence, the current-induced Oersted field acting on the FM layer is along the $\hat{y}$ axis. If the stack is reversed, i.e. if we consider a NM/FM bilayer, the Oersted field is along $-\hat{y}$. Taken from [119].

After considering the symmetries of the spin Hall effect and the Oersted field in the typical geometry of a bilayer, the components of the excitation field that drives the magnetization dynamics are:

$$\begin{aligned}\delta h_\theta &= h'_{FL}\cos(\theta_0)\sin(\varphi_0) - h_{DL}\cos(\varphi_0)\\ \delta h_\varphi &= h'_{FL}\cos(\varphi_0) + h_{DL}\cos(\theta_0)\sin(\varphi_0).\end{aligned} \tag{4.34}$$

We have expressed the components of the excitation field in a general way, and then we have precise their expression in the case of the symmetry of the spin Hall effect. The last ingredient we need to derive is the components of the susceptibility matrix.

4.5 Magnetic properties of a magnetic thin film with perpendicular magnetic anisotropy

In this section we derive the expression of the total energy density which includes the magnetic properties of the studied magnetic materials. We will consider a magnetic thin film with perpendicular magnetic anisotropy to match the materials presented in the experimental part.

4.5.1 Total magnetic energy density and equilibrium position of the magentization

The total magnetic energy density ε, from which the effective magnetic field felt by the magnetization is derived, is composed of the following three terms:

- The Zeeman energy density, ε_Z, which describes the interaction between the magnetization and an external magnetic field $\vec{H}_{ext}$. It is expressed as:

$$\varepsilon_Z = -\mu_0 \vec{M}.\vec{H}_{ext}.$$

  The direction of the magnetic field of amplitude H_{ext} is given by the polar and azimuthal angles θ_H and φ_H. The Zeeman energy density is therefore given in polar coordinates:

$$\varepsilon_Z(\theta,\varphi) = -\mu_0 M_S H_{ext} \left[\cos(\theta_H)\cos(\theta) + \sin(\theta_H)\sin(\theta)\cos(\varphi-\varphi_H)\right].$$

- The dipolar energy density, ε_{dem}, describes the interaction between the magnetic field produced by the magnetization, called the demagnetization field, and the magnetization itself. This energy depends on the shape of the considered system, therefore it is also called shape anisotropy. It is given by:

$$\varepsilon_{dem} = \frac{\mu_0}{2}\vec{M}.(\underline{\underline{N}}\vec{M}),$$

  where $\underline{\underline{N}}$ is the demagnetization matrix. In the case of a thin film whose thickness is along the $\hat{z}$ axis, it is given by:

$$\underline{\underline{N}} = \begin{bmatrix} 0 & 0 & 0 \\ 0 & 0 & 0 \\ 0 & 0 & 1 \end{bmatrix}.$$

  The expression for the shape anisotropy energy density in polar coordinates is therefore:

$$\varepsilon_{dem}(\theta,\varphi) = \frac{\mu_0}{2} M_S^2 \cos^2(\theta).$$

- The magnetocrystalline anisotropy energy density, ε_{anis}, describes the interaction between the magnetization and the crystal lattice resulting in preferential directions for the magnetization. In the case of a single preferred spatial direction we speak of uniaxial anisotropy and the magnetocrystalline anisotropy energy density is given by:

$$\varepsilon_{anis} = -K(\hat{u}.\hat{m})^2,$$

  where $\vec{u}$ is the direction of the privileged axis and K (in J/m^3) is the amplitude of the interaction. When $K > 0$, $\hat{u}$ is said to be an easy axis since the magnetization tends to align along this direction. The system we consider as an easy axis along the out-of-plane direction $\hat{z}$, and the magnetocrystalline anisotropy energy density is:

$$\varepsilon_{anis}(\theta,\varphi) = -K\cos^2(\theta).$$

The total energy density is therefore written in spherical coordinates:

$$\varepsilon(\theta,\varphi) = -\mu_0 M_S H_{ext}\left[\cos(\theta_H)\cos(\theta) + \sin(\theta_H)\sin(\theta)\cos(\varphi-\varphi_H)\right] - K_{eff}\cos^2(\theta), \tag{4.35}$$

where $K_{eff} = K - \frac{\mu_0}{2}M_S^2$ is the effective anisotropy which includes the demagnetization field and the out-of-plane uniaxial anisotropy energy. When the magnetocrystalline anisotropy dominates over the shape anisotropy, i.e. when $K_{eff} > 0$, the magnetization naturally lies along the out-of-plane axis. If the demagnetization field dominates over the anisotropy, i.e. if $K_{eff} < 0$, then the magnetization lies in the plane of the sample. By looking at the solutions for which the derivative of ε is zero, we can obtain the expression for the equilibrium position of the magnetization (θ_0, φ_0) as a function of the external magnetic field:

$$\begin{cases} \varepsilon_\theta(\theta_0,\varphi_0) = \mu_0 M_S H_{ext}\left[\cos(\theta_H)\sin\theta_0 - \sin(\theta_H)\cos(\theta_0)\cos(\varphi_0-\varphi_H)\right] + K_{eff}\sin(2\theta_0) = 0 \\ \varepsilon_\varphi(\theta_0,\varphi_0) = \mu_0 M_S H_{ext}\sin(\theta_H)\sin(\theta_0)\sin(\varphi_0-\varphi_H) = 0 \end{cases},$$

where ε_θ and ε_φ are the first derivatives of ε with respect to the magnetization position. We obtain:

$$\begin{cases} \sin(2\theta_0) = \dfrac{\mu_0 M_S H_{ext}}{2K_{eff}}\sin(\theta_0-\theta_H), \\ \sin(\theta_0)\sin(\varphi_0-\varphi_H) = 0 \end{cases} \tag{4.36}$$

The stable solution is found by looking for the sign of the second derivatives of the free magnetic density energy evaluated over (θ_0, φ_0). Since $\theta_{0,H} \in [0,\pi]$, $\sin(\theta_{0,H}) > 0$, it follows that the only stable solution for φ_0 is $\varphi_0 = \varphi_H$. From this we can see that the in-plane component of the magnetization will always be aligned with the applied field, which is a consequence of the cylindrical symmetry of the system. Then only the equilibrium polar angle needs to be determined using the following set of equations:

$$\begin{cases} \sin 2\theta_0 = \dfrac{\mu_0 M_S H_{ext}}{2K_{eff}}\sin(\theta_0-\theta_H) \\ \varepsilon_{\theta\theta}(\theta_0,\varphi_0) = \mu_0 M_S H_{ext}\cos(\theta_0-\theta_H) + 2K_{eff}\cos(2\theta_0) \\ \varepsilon_{\varphi\varphi}(\theta_0,\varphi_0) = \mu_0 M_S H_{ext}\sin(\theta_H)\sin(\theta_0) \\ \varepsilon_{\theta\varphi}(\theta_0,\varphi_0) = 0 \end{cases} \tag{4.37}$$

The equilibrium position can be expressed analytically only for simple cases, such as when $\theta_H = 0[\pi]$ and $\theta_H = \pi/2[\pi]$. Let us consider different cases depending on the sign of K_{eff}:

- If $K_{eff} > 0$, then we define the positive anisotropic field $H_k = \dfrac{2K_{eff}}{\mu_0 M_S}$ as the magnetic field needed to orient the magnetization along the hard axis. In the absence of an external magnetic field, the magnetization naturally lies out of the plane of the sample and $\theta_0 = 0$ or π. By applying a magnetic field stronger than the coercive field, the magnetization can be directed to one or the other out-of-plane position. In the presence

of a magnetic field applied in the plane of the sample, i.e. $\theta_H = \pi/2$, we have:

$$\begin{cases} \sin\theta_0 = \dfrac{\mu_0 M_S H_{ext}}{2K_{eff}} = \dfrac{H_{ext}}{H_K} & \text{if } H_{ext} \leq H_K, \\ \theta_0 = \dfrac{\pi}{2} & \text{if } H_{ext} \geq H_K, \end{cases} \tag{4.38}$$

- If $K_{eff} < 0$, then we define the positive effective magnetization $M_{eff} = -\dfrac{2K_{eff}}{\mu_0 M_S}$, which is the magnetic field needed to align the magnetization along the hard axis. In the absence of an external magnetic field, we find that the magnetization naturally lies in the plane and $\theta_0 = \dfrac{\pi}{2}$. In the case where the magnetic field is applied along the hard axis, i.e. $\theta_H = 0$, the equilibrium position is given as a function of the magnetic field:

$$\begin{cases} \cos\theta_0 = \dfrac{-\mu_0 M_S H_{ext}}{2K_{eff}} = \dfrac{H_{ext}}{M_{eff}} & \text{if } H_{ext} \leq M_{eff}, \\ \theta_0 = 0 & \text{if } H_{ext} \geq M_{eff}, \end{cases} \tag{4.39}$$

In the following chapters we will present experimental results obtained with the spin torque ferromagnetic resonance (ST-FMR) technique and with the second harmonic technique. In both cases, an external magnetic field is applied in the plane of the sample so that $\theta_H = \pi/2[\pi]$. In the case of the ST-FMR technique, the dynamics of a NiFe thin film is studied. Its magnetization is naturally in the plane, so in this case we have $K_{eff} < 0$. In the case of the second harmonic technique, we study the dynamics of the GdFeCo magnetization, which is naturally out-of-plane, i.e. $K_{eff} > 0$. The idea now is to derive the susceptibility matrices for these two cases.

4.5.2 Magnetization dynamics in the ST-FMR technique

We want to derive the expression of the susceptibility matrix for the case of a magnetic material with in-plane magnetization to represent NiFe in our experimental part. The total energy density is given by Eq.(4.35). We need to derive the expression for the second derivative of the total energy density considering the position of the magnetic field. It comes:

$$\begin{cases} \epsilon_{\theta\theta}(\theta_0, \varphi_0) = \mu_0 M_S H_{ext} \sin(\theta_0) + 2K_{eff} \cos(2\theta_0) \\ \epsilon_{\varphi\varphi}(\theta_0, \varphi_0) = \mu_0 M_S H_{ext} \sin(\theta_0) \\ \epsilon_{\theta\varphi}(\theta_0, \varphi_0) = 0 \end{cases} . \tag{4.40}$$

Since $K_{eff} < 0$, we have $M_{eff} = \dfrac{-2K_{eff}}{\mu_0 M_S}$ and $\theta_0 = \pi/2$. The resonance frequency ω_0 and the linewidth Δ_ω are thus expressed according to Eq.(4.13):

$$\omega_0 = \gamma_0 \sqrt{H_{ext}(H_{ext} + M_{eff})} \qquad \text{and} \tag{4.41}$$

$$\Delta = \gamma_0 \alpha (2H_{ext} + M_{eff}), \tag{4.42}$$

where we made the assumption $\alpha^2 \ll 1$ because the damping of our samples is usually low (for instance $\alpha^{NiFe} = 0.012$ and $\alpha^{GdFeCo} = 0.08$).

The response of the magnetization is described by the real part of the susceptibility matrix given by Eq.(4.15) and is written as:

$$\underline{\underline{\chi}}'(\omega) = \frac{\gamma_0^2 M_S}{[(\omega_0^2-\omega^2)^2+(\Delta_\omega\omega)^2]} \begin{bmatrix} H_{ext}(\omega_0^2-\omega^2) & \dfrac{\Delta_\omega\omega^2}{\gamma_0} \\ -\dfrac{\Delta_\omega\omega^2}{\gamma_0} & (H_{ext}+M_{eff})(\omega_0^2-\omega^2) \end{bmatrix} \tag{4.43}$$

$$\underline{\underline{\chi}}''(\omega) = \frac{\gamma_0^2 M_S \omega}{[(\omega_0^2-\omega^2)^2+(\Delta_\omega\omega)^2]} \begin{bmatrix} -\Delta_\omega H_{ext} + \dfrac{\alpha(\omega_0^2-\omega^2)}{\gamma_0} & \dfrac{\omega_0^2-\omega^2}{\gamma_0} \\ -\dfrac{\omega_0^2-\omega^2}{\gamma_0} & -\Delta_\omega(H_{ext}+M_{eff}) + \dfrac{\alpha(\omega_0^2-\omega^2)}{\gamma_0} \end{bmatrix} \tag{4.44}$$

In the next Chapter 5, we will derive the full expression of the longitudinal voltage in the case of the ST-FMR technique.

4.5.3 Magnetization dynamics in the second harmonic technique

We want to derive the expression of the susceptibility matrix for the case of a magnetic material with out-of-plane magnetization to represent GdFeCo in our experimental part. Since $K_{eff} > 0$, we have $H_K = \dfrac{2K_{eff}}{\mu_0 M_S}$. The equilibrium position of the magnetization as a function of the magnetic field is given by Eq.(4.38). In the case where the excitation frequency is much lower than the resonance frequency, i.e. $\omega \ll \omega_0$, which is the case in the second harmonic technique, and the Gilbert damping is low, i.e. $\alpha \ll 1$, the expression for the real and imaginary parts of the susceptibility matrix can be simplified as follows:

$$\underline{\underline{\chi}}'(\omega) = \frac{\gamma_0^2}{\mu_0\omega_0^2} \begin{bmatrix} \dfrac{\varepsilon_{\varphi\varphi}}{\sin^2(\theta_0)} & -\dfrac{\varepsilon_{\theta\varphi}}{\sin(\theta_0)} \\ -\dfrac{\varepsilon_{\theta\varphi}}{\sin(\theta_0)} & \epsilon_{\theta\theta} \end{bmatrix}, \tag{4.45a}$$

and

$$\underline{\underline{\chi}}''(\omega) = \frac{\gamma_0 M_S \omega}{\omega_0^2} \begin{bmatrix} 0 & 1 \\ -1 & 0 \end{bmatrix} \approx 0 \tag{4.45b}$$

When $H_{ext} \leq H_K$:

$$\chi'(\omega) = \frac{M_S}{H_K(H_K^2-H_{ext}^2)} \begin{bmatrix} H_K^2 & 0 \\ 0 & H_K^2-H_{ext}^2 \end{bmatrix}, \tag{4.46a}$$

$$\chi''(\omega) = \frac{M_S\omega}{\gamma_0(H_K^2-H_{ext}^2)} \begin{bmatrix} 0 & 1 \\ -1 & 0 \end{bmatrix}, \tag{4.46b}$$

with

$$\omega_0 = \gamma_0 \sqrt{H_K^2 - H_{ext}^2}\,, \quad \text{and} \quad \Delta_\omega = \gamma_0 \alpha \left(2H_K - \frac{H_{ext}^2}{H_K}\right).$$

When $H_{ext} \geq H_K$:

$$\underline{\underline{\chi}}'(\omega) = \frac{M_S}{H_{ext}(H_{ext} - H_K)} \begin{bmatrix} H_{ext} & 0 \\ 0 & H_{ext} - H_K \end{bmatrix}, \tag{4.47a}$$

$$\underline{\underline{\chi}}''(\omega) = \frac{M_S \omega}{\gamma_0 H_{ext}(H_{ext} - H_K)} \begin{bmatrix} 0 & 1 \\ -1 & 0 \end{bmatrix}, \tag{4.47b}$$

with

$$\omega_0 = \gamma_0 \sqrt{H_{ext}(H_{ext} - H_K)}. \quad \text{and} \quad \Delta_\omega = \gamma_0 \alpha \left(2H_{ext} - H_K\right)$$

In Chapter 6, we will derive the full expression of the transverse voltage in the case of the second harmonic technique.

4.6 Conclusion

The goal of this chapter was to present a general model that contains all the ingredients to derive the analytical expressions for the voltages in a magnetic system whose dynamics is driven by a harmonic spin torque. First, since we are working with a ferrimagnet, we showed that the dynamics of the net magnetization in a ferrimagnet can be expressed in the same way as the dynamics of the magnetization of a ferromagnet. Then we developed the general model considering the magnetization of a ferromagnet. This model provides the general expression for i) the dynamics of the magnetization periodic spin-orbit torque, ii) the readout effects and thermal effects, and iii) the excitation field. All these are derived without considering the excitation frequency, the magnetic properties of the magnetic material and its geometry. Considering the magnetic energy density of a ferromagnet with out-of-plane anisotropy, and considering the specific geometries of the ST-FMR and second harmonic techniques, we have derived the expressions for the susceptibility matrices. The complete analytical expressions for the voltages are derived in the following chapters. Therefore, the model developed here with its formalism allows to consider the ST-FMR technique and the second harmonic technique as equivalent, since they are based on the same underlying physics given by the Landau-Lifshitz-Gilbert-Slonczeswki equation.

CHAPTER 5

Spin current generation by GdFeCo

The samples were grown by sputtering by Prof. Michel Hehn. The patterning of the device was done either by myself or by Dr. Juan-Carlos Rojas-Sanchez using CC Minalor equipments at IJL. The ST-FMR measurements on Pt/NiFe were performed and analyzed by Dr. Juan-Carlos Rojas-Sanchez, Dr. Alberto Anadon and by myself. The ST-FMR measurements on GdFeCo/Cu/NiFe were performed and analyzed by myself. The interpretation was discussed with Dr. Sébastien Petit-Watelot, Dr. Juan-Carlos Rojas-Sanchez and myself. The analytical expressions developed for the ST-FMR technique follow the model explained in Chapter 4. The model for the contribution of the different spin current symmetries of GdFeCo to the ST-FMR signal and part of the results of this chapter have been published in [120].

GdFeCo ferrimagnet is at the origin of coexisting spin currents with SHE and SAHE symmetries resulting from the spin Hall effect (SHE) and the spin anomalous Hall effect (SAHE), respectively. The aim of this chapter is to characterize the spin currents generated by GdFeCo over the magnetization compensation temperature T_M in order to find out whether their generation is related to its magnetic state. For this purpose, we study a GdFeCo/Cu/NiFe trilayer in which the spin currents are generated by GdFeCo and absorbed by NiFe, which is used as a detector. Since NiFe does not show any drastic change in its magnetic properties or magnetotransport effects in the temperature range of T_M (about 147K), a change in the spin torque acting on NiFe can be directly related to a change in the spin current generation occurring in GdFeCo.

We first introduce the spin torque ferromagnetic resonance (ST-FMR) technique in the case of a typical HM/FM bilayer, which allows the characterization of the SOT acting on the FM when the latter is at resonance. We apply the model derived in chapter 4 to our geometry to obtain the analytical expressions of the voltages of interest. We then consider the case of GdFeCo/Cu/NiFe, where two torques with different symmetries act on NiFe, and we derive the corresponding analytical voltages. We discuss different configurations for the

measurements and finally present the experimental results obtained over T_M.

5.1 Study of spin currents by spin torque ferromagnetic resonance

Magnetic fields, regardless of their origin, can excite magnetization dynamics. The precession of the magnetization is induced by the transverse component of the exciting magnetic field with respect to the equilibrium position of the magnetization, and the resonance of this precession is reached for a certain frequency (the Larmor frequency) of an oscillating magnetic field. This effect is known as ferromagnetic resonance (FMR) and has been widely used to determine magnetic properties of magnetic compounds such as the Gilbert damping, the effective magnetization, and the gyromagnetic ratio [121, 122], since the resonance frequency and the resonance linewidth (see Eq.(4.13)) are directly related to these different parameters. This well-established technique is now extended to study the changes in the magnetic properties of a magnet under the influence of a spin torque, and is called the spin torque ferromagnetic resonance (ST-FMR) technique [123, 124].

A radio frequency (RF) power is applied through an HM/FM bilayer so that the RF charge current is converted into a synchronous pure spin current in the HM layer via the SHE. The spin current is injected into the adjacent FM and results in a spin torque. As a result, both the RF spin torque and the RF Oersted field induced by the current flowing in the device drive the magnetization dynamics. At resonance of the FM, which can be achieved by changing the external magnetic field amplitude for a fixed excitation frequency (or reciprocally by changing the excitation frequency for a fixed field amplitude), the RF power is absorbed, the spin torque is maximum and the magnetization describes a sustained precession. The mixture of RF current and RF magnetoresistance effects results in a rectified DC voltage in the device. An external DC magnetic field is usually applied in the plane at 45° from the current line to maximize the AMR readout signal. Let us first derive the analytical expression for the voltage obtained at resonance in the case of the aforementioned HM/FM bilayer.

5.1.1 Analytical expression for the DC voltage

We can now derive the analytical expressions for the longitudinal voltage. According to Eq.(4.22), the DC and second harmonic longitudinal voltages when the magnetization is in the plane along the magnetic field ($\theta_0 = \frac{\pi}{2}$, $\varphi_0 = \varphi_H$) have the form [120] :

$$V_X^{DC,2\omega} = -\Delta R^{AMR} \sin(2\varphi_H) \left[\chi'_{\varphi\theta} \frac{\delta h_\theta}{M_S} + \chi'_{\varphi\varphi} \frac{\delta h_\varphi}{M_S} \right] \frac{I_X}{2}, \tag{5.1}$$

Finally, considering the components of the susceptibility defined in Eq.(4.16) and the expressions of the exciting fields in Eq.(4.34) in the expression of the DC voltage in Eq.(5.1), we obtain the analytical expression:

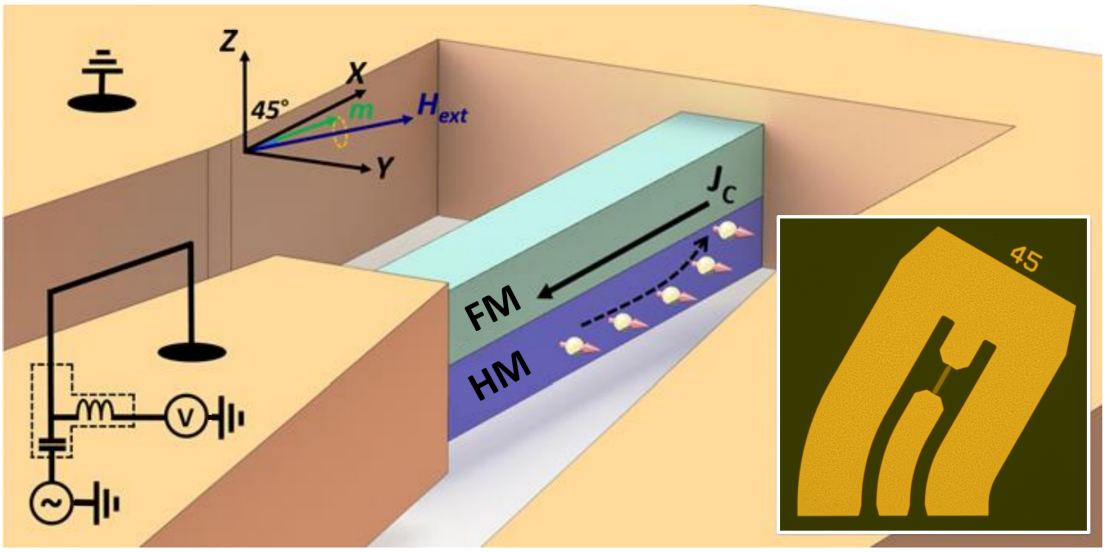

Figure 5.1: Schematic of a device used for the ST-FMR technique, adapted from [125]. An RF current flows in the HM/FM bilayer, resulting in both an RF spin torque and an RF Oersted field acting on the FM magnetization. By varying the amplitude of the external field, the resonant state of the FM can be reached, resulting in a DC voltage that can be measured through a bias tee. The inset shows an optical photograph of a typical device used in this thesis.

$$V_X^{DC,2\omega} = -\frac{I_X \Delta R^{AMR}}{2} \sin(2\varphi_H)\cos(\varphi_H) \times \frac{\gamma_0 \left[h_{DL}\Delta_\omega \omega^2 + h'_{FL}\left(\gamma_0(H_{ext}+M_{eff})(\omega_0^2-\omega^2)\right)\right]}{(\omega_0^2-\omega^2)^2+(\Delta_\omega\omega)^2}. \tag{5.2}$$

In our experiment, the excitation frequency is fixed and the external magnetic field is swept. Therefore, we can convert frequency-based quantities, such as the resonance frequency ω_0 and the linewidth Δ_ω, into magnetic-field-based quantities, such as the resonance field H_r and the linewidth Δ_H. The transition from one to the other is done by changing the following variables:

$$\begin{aligned} \Delta_\omega &= \gamma_0 \alpha (2H_{ext} + M_{eff}) \\ \omega^2 &= \gamma_0^2 H_r (H_r + M_{eff}) \\ \omega_0^2 &= \gamma_0^2 H_{ext}(H_{ext} + M_{eff}) \end{aligned} \tag{5.3}$$

and considering that the signal varies strongly only near the resonance, i.e. $\Delta_H \ll H_r$, the field linewidth is defined as $\Delta_H = \dfrac{\alpha\omega}{\gamma_0}$. It follows that the analytical expression for the DC voltage at resonance can be described by the sum of a symmetric Lorentzian function V_S and an antisymmetric Lorentzian function V_A, such that:

$$\boxed{V_X^{DC} = V_S \frac{\Delta_H^2}{\Delta_H^2 + (H_{ext}-H_r)^2} + V_A \frac{(H_{ext}-H_r)\Delta_H}{\Delta_H^2 + (H_{ext}-H_r)^2},} \tag{5.4}$$

with

$$\boxed{\begin{aligned} V_S &= -\frac{i_{rf}R^{AMR}}{2}\frac{\sin(2\varphi_H)\cos(\varphi_H)}{(2H_r+M_{eff})}\frac{1}{\alpha}h_{DL}, \\ V_A &= -\frac{i_{rf}R^{AMR}}{2}\frac{\sin(2\varphi_H)\cos(\varphi_H)}{(2H_r+M_{eff})}\frac{1}{\alpha}\sqrt{1+\frac{M_{eff}}{H_r}}h'_{FL}. \end{aligned}} \tag{5.5}$$

Figure 5.2(a) shows a typical ST-FMR signal as a function of the external magnetic field. The signal has two resonance peaks, both fitted by Eq.(5.4). The resonance field $\mu_0 H_r = \pm 0.05$T and linewidth $\mu_0 \Delta_H = 0.005$T are given in the figure.

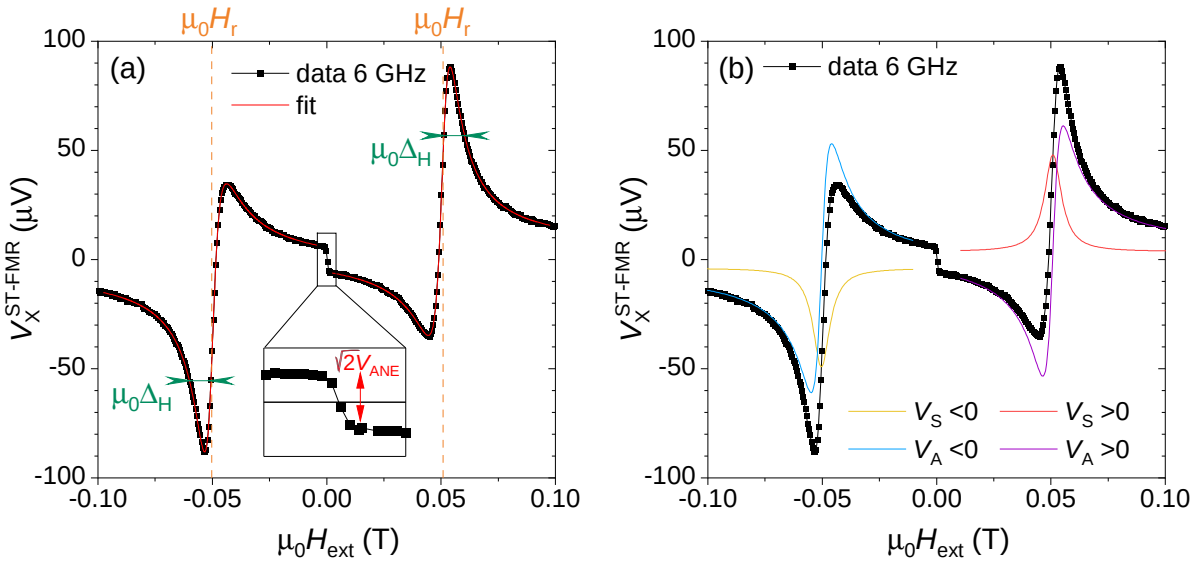

Figure 5.2: (a) ST-FMR signal as a function of the external magnetic field amplitude for Pt(5)/NiFe(4) at room temperature. The data at 6GHz are fitted according to Eq.(5.4), and the resonance field H_r and linewidth Δ_H are indicated. The jump at zero magnetic field is due to the anomalous Nernst effect. Since this jump is small compared to the resonance peak, we neglect this effect for this measurement. (b) The symmetric and antisymmetric parts of the resonance peak are plotted. In this case, for a positive magnetic field we have $V_{S,A} > 0$, while for a negative magnetic field we have $V_{S,A} < 0$, with an odd behavior with the magnetic field as expected from the SHE symmetry.

5.1.2 Lineshape analysis

From the above equations it follows that the amplitudes V_S and V_A are proportional to the damping-like and field-like effective fields, respectively. Knowing the direction of the applied magnetic field, the sign of the AMR, it is possible to extract the sign of h_{DL} and h'_{FL} considering the sign of V_S and V_A. The sign of $V_{S,A}$ for a typical ST-FMR signal is shown in Figure 5.2(b). The symmetric and antisymmetric parts of each peak are shown. In this case, the symmetric part is $V_S > 0\,(< 0)$ for positive (negative) magnetic field. Similarly, the antisymmetric part $V_A > 0\,(< 0)$ for a positive (negative) magnetic field. In our experiments, the positive magnetic field corresponds to an angle $\varphi_H = 135°$ from the cur-

rent line, and the negative field corresponds to $\varphi_H = 315°$, resulting in $h_{DL} < 0$ and $h_{FL'} < 0$.

The symmetric and antisymmetric amplitudes are also related to the RF current flowing in the sample, which is difficult to accurately determine without properly separating the contributions from the sample and the RF transmission line. To get around this problem, it is common practice to evaluate an effective efficiency ξ_{FMR} from the ratio of V_S and V_A. ξ_{FMR} is calculated considering that the effective field is [126] $h_{DL,FL} = \hbar J_{cHM} \xi_{DL(FL)} / 2eM_S t_{FM}$ and the Oersted field is [127] $h_{Oe} = J_{cHM} t_{HM}/2$:

$$\xi_{FMR} = \frac{V_S}{V_A} \frac{e\mu_0 M_S t_{HM} t_{FM}}{\hbar} \sqrt{1 + \frac{M_{eff}}{H_r}}, \tag{5.6}$$

and this parameter is related to the efficiencies of the torques according to:

$$\frac{1}{\xi_{FMR}} = \frac{1}{\xi_{DL}} \left(1 + \frac{\hbar}{e} \frac{\xi_{FL}}{\mu_0 M_S t_{HM} t_{FM}} \right), \tag{5.7}$$

where the different torques can be separated by a thickness dependence of the FM or HM layer.

At this point, we must emphasize an important point: the expression of the FMR efficiency as defined in Eq.(5.6) relies on the definition of the Oersted field, which requires knowledge on the distribution of the current in the different layers. However, RF current is not uniformly distributed in the structure due to skin effects and the device may be subject to inductive and capacitive effects, and the Oersted field is difficult to extract accurately. For this reason, we introduce here the total effective efficiency for the lineshape analysis (L-S), which considers the effect induced by the total current without separating the Oersted field:

$$\boxed{\xi_{FMR}^{tot-LS} = \frac{\xi_{DL}}{\xi_{FL'}} = \frac{V_S}{V_A} \sqrt{1 + \frac{M_{eff}}{H_r}}.} \tag{5.8}$$

5.1.3 DC bias technique

The DC bias technique is another way to access torque efficiency without relying on knowledge of magnetoresistance effects and RF current amplitude. It consists of an extended method in which a DC current is applied while the ST-FMR technique is being performed. The DC current induces a static torque on the oscillating magnetization, thus affecting the susceptibility of the magnetic material as well as its precession motion. The model to describe the dynamics under an additional DC torque is not discussed in this work. In essence, the applied DC current i_{DC} leads to a modulation of the linewidth Δ_H related to the DL torque and a shift of the resonance field H_r related to the FL torque [52, 128, 129]:

$$\boxed{\mu_0 \frac{\partial \Delta_H}{\partial i_{DC}} = -\frac{\omega \sin(\varphi_H)}{\gamma \mu_0 M_S (2H_r + M_{eff})} \frac{\hbar}{2et_{FM} w t_{tot}} \xi_{DL}} \tag{5.9}$$

$$\boxed{\mu_0 \frac{\partial H_r}{\partial i_{DC}} = \frac{\sin(\varphi_H)}{M_S} \frac{\hbar}{2et_{FM} w t_{tot}} \xi_{FL'}} \tag{5.10}$$

where t_{tot} is the total thickness of the conductive sample, w is the width of the current line, and t_{FM} is the thickness of the magnetic material. The main drawback of this technique has to do with the small effects to be detected. It therefore requires a signal with a good signal to noise ratio.

To compare the results between the lineshape analysis and the DC bias technique, we define the ratio between the damping-like and field-like efficiencies in a manner similar to the lineshape analysis:

$$\xi_{FMR}^{tot-DC} = \frac{\xi_{DL}}{\xi_{FL'}} = 2H_r + M_{eff}\frac{\gamma}{2\pi f}\frac{\dfrac{\partial \mu_0 \Delta_H}{\partial i_{DC}}}{\dfrac{\partial \mu_0 H_r}{\partial i_{DC}}}. \tag{5.11}$$

The total efficiencies obtained from the lineshape analysis and the DC bias technique should be the same. In the following section, we explain why the lineshape analysis is often inaccurate compared to the DC bias technique.

5.1.4 Accuracy of lineshape versus DC bias analysis

At the beginning of this chapter we derived the equation that describes the ST-FMR signal in the case of lineshape analysis. We made the strong assumption that the AMR is the only contributor to the signals, without considering any thermoelectric effects, additional effects that can generate a voltage, such as the inverse spin Hall effect or the spin pumping effect or GMR effects in more complex structures. In real systems, this assumption is not verified in most cases. In this sense, lineshape analysis can lead to inaccurate results.

We propose here a way to verifiy the validity of the model by comparing the value of the effective magnetization M_{eff} extracted from the ST-FMR signal with the value extracted by considering the dynamics of the magnetization. Indeed, the effective magnetization is unambiguously obtained from Kittel's law:

$$f = \frac{\gamma_0}{2\pi}\sqrt{H_r(H_r + M_{eff})}. \tag{5.12}$$

This expression related to the magnetization dynamics, is independent of the measurement technique, and does not rely on magnetoresistive effects. In the case where only the AMR contributes to the ST-FMR signal, our model predicts that:

$$\left(\frac{V_S}{V_A}\right)^2 = \left(\xi_{FMR}^{tot-LS}\right)^2 \frac{H_r}{H_r + M_{eff}}, \tag{5.13}$$

where M_{eff} has the same value as when using Kittel's law. If the value of M_{eff} differs from the value obtained from Kittel's law, it is a sign that the model is incomplete, that the macrospin approximation is inappropriate, or that other effects are contributing to the signal. By looking at the relative error between the values of M_{eff}, we can get an idea of

the deviation of our model. We define this as:

$$\delta^{model} = \frac{M_{eff}^{Kittel} - M_{eff}^{LS}}{M_{eff}^{Kittel}}, \tag{5.14}$$

where M_{eff}^{LS} is the effective magnetization extracted by lineshape analysis (see Eq.(5.13)) and M_{eff}^{Kittel} is the effective magnetization extracted by the Kittel law (see Eq.(5.12)).

In contrast to the lineshape analysis, the DC bias technique has the great advantage of not relying on magnetoresistive effects. The extraction of the spin torques is solely related to the modulation of the linewidth and the shift of the resonance peak, which does not require any knowledge of the magnetoresistive effects, but only the macrospin approximation to be fulfilled. In this way, the DC bias technique is unbiased and accurate even when other magnetoresistive effects contribute to the signal. Thermal effects can be detected by looking at the parabolic evolution of the modulations with the DC current.

To conclude this section, we present the data and analysis of an archetypal system : Pt/NiFe.

5.1.5 Reference case : Pt/NiFe

Before moving on to the case of GdFeCo(10)/Cu(4)/NiFe(4), let us discuss the case of an archetypal Pt(5)/NiFe(4) bilayer. This system has been studied by several groups using ST-FMR techniques [123, 130, 131] and the sign of the torques is well known. Therefore, the purpose of this section is twofold: first, to show how the analysis of the ST-FMR signals is performed, and second, to use the results from this bilayer as a reference for the study of GdFeCo/Cu/NiFe. In both systems, the layer that generates the spin current (Pt and GdFeCo) is located at the bottom of the structure and the layer that absorbs the spin current (NiFe) is located at the top of the structure and has the same thickness. Thus, the same placement of the layers allows a direct comparison of the sign of the torque [1]. In addition, both stacks have a similar longitudinal resistance (about 200 Ω for a 10μm wide current line), which allows to assume that the Oersted fields are aligned along $-\hat{y}$ and have about the same amplitude in both cases.

In our experimental setup, the positive magnetic field is applied at $\varphi_H = 135°$ from the current line, and negative values of the magnetic field correspond to $\varphi_H = 315°$. The lineshape analysis of Pt(5)/NiFe(4) at room temperature is shown in Figure 5.3. The ST-FMR signals are measured for different frequencies (Figure 5.3(a)) and both resonance peaks are fitted using Eq.(5.4). This gives the evolution of the symmetric and antisymmetric parts as a function of the frequency (Figure 5.3(b)). $V_{S,A} > 0\,(< 0)$ for positive (negative) magnetic field, which means $h_{DL} < 0$, $h'_{FL} < 0$, and that $\xi_{FMR} > 0$. The linewidth Δ_H varies linearly

[1] The sign of the torque induced by Pt is opposite in Pt/NiFe and NiFe/Pt due to the opposite spin polarizations generated by the SHE.

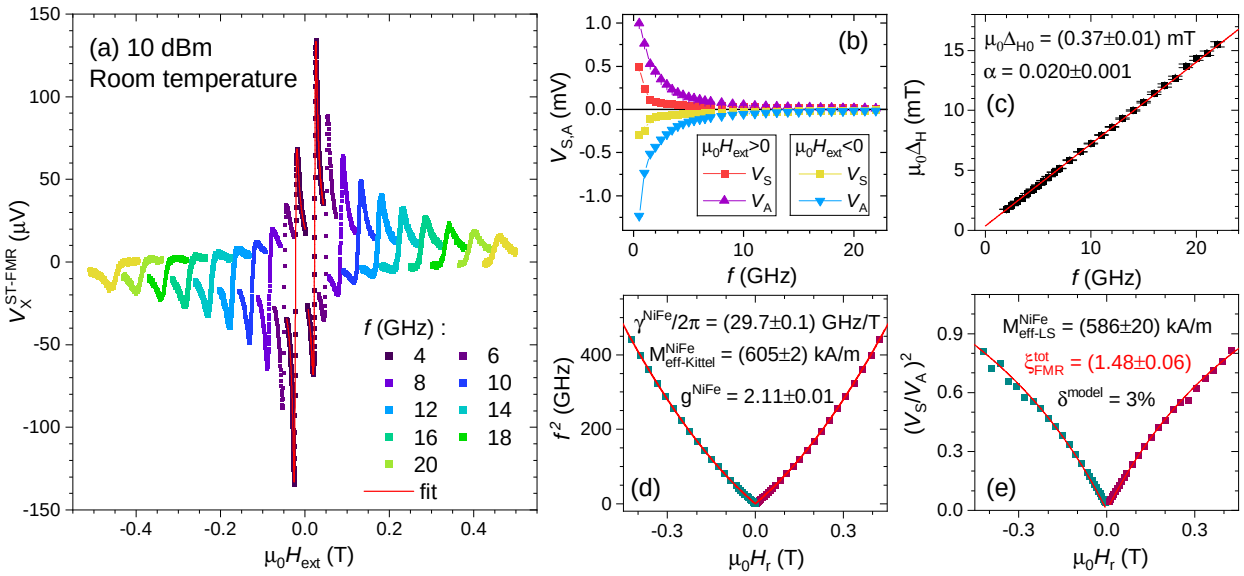

Figure 5.3: Lineshape analysis at room temperature for Pt(5)/NiFe(4). (a) ST-FMR voltage as a function of the external magnetic field for different frequencies. (b) Evolution of the symmetric and antisymmetric voltages V_S and V_A as a function of the frequency. From their signs, we can evaluate the sign of the effective field $h_{DL} < 0$ and $h'_{FL} < 0$. (c) Linear evolution of the linewidth with the frequency, from which we can extract the damping $\alpha^{NiFe} = 0.020 \pm 0.001$. (d) Estimation of the gyromagnetic ratio $\gamma^{NiFe} = 2\pi(29.7 \pm 0.1)$ GHz/T, of the Landé factor $g^{NiFe} = 2.11 \pm 0.01$ and of the effective magnetization $M_{eff-Kittel}^{NiFe} = (605 \pm 2)$kA/m from the evolution of the square of the frequency with the resonance field. (e) Estimation of the effective magnetization $M_{eff-LS}^{NiFe} = (586 \pm 20)$kA/m from the evolution of the square of the ratio of V_S and V_A as a function of the resonance field, which corresponds to a deviation of the model $\delta^{model} = 3\%$. The total FMR efficiency $\xi_{FMR}^{tot-Pt} = 1.48 \pm 0.06$.

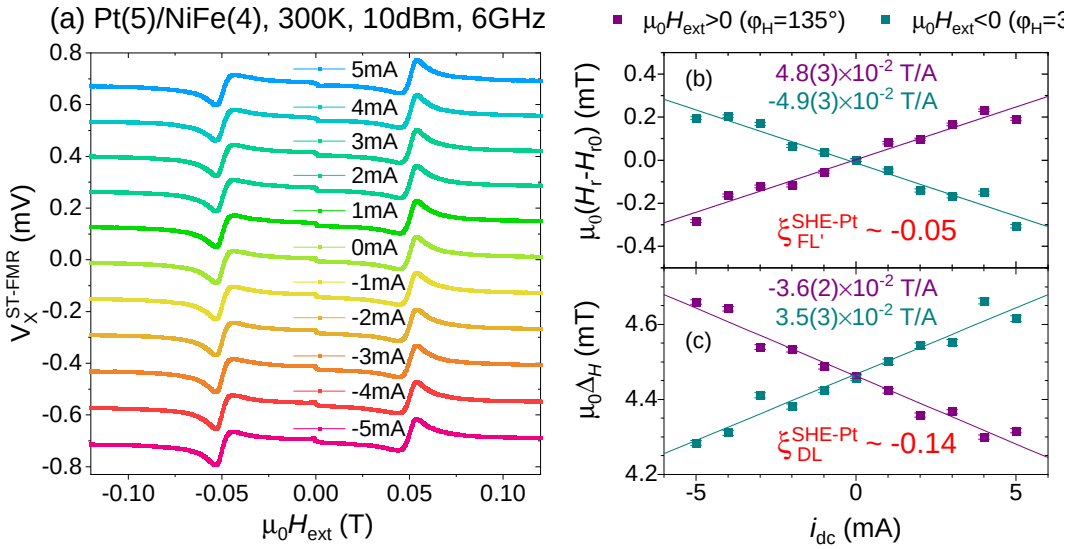

Figure 5.4: DC bias technique at room temperature for Pt(5)/NiFe(4). (a) ST-FMR voltage as a function of the external magnetic field for a power of 10dBm, a frequency of 6GHz and different DC currents. (b) Evolution of the resonance field shift as a function of the DC current. The slopes for the linear fit are shown. The slopes indicate that $\xi_{FL'} < 0$. The efficiency considering the field-like and Oersted field is estimated $\xi_{FL'}^{SHE-Pt} \sim -0.05$. (c) Evolution of the modulation of the linewidth with the DC current. It shows a linear evolution with the current. The slopes indicate that $\xi_{DL} < 0$, with an efficiency $\xi_{DL}^{SHE-Pt} \sim -0.14$.

with the frequency (see Figure 5.3(c)) and follows the expression [132]:

$$\mu_0\Delta_H = \mu_0\Delta_{H0} + \frac{2\pi\alpha^{NiFe}}{\gamma} f, \tag{5.15}$$

where Δ_{H0} is the inhomogeneous broadening related to the frequency independent contribution of the sample defects. We can extract $\mu_0\Delta_H = 0.37$mT and the damping of NiFe $\alpha^{NiFe} = 0.020 \pm 0.001$. Considering the relationship between the resonance field H_r and the frequency:

$$f^2 = \frac{\gamma_0^2}{4\pi^2}\left(H_r^2 + H_r M_{eff}^{NiFe}\right), \tag{5.16}$$

we can evaluate the gyromagnetic ratio of NiFe $\gamma/2\pi = (29.7 \pm 0.1)$ GHz/T and the effective magnetization $M_{eff-Kittel}^{NiFe} = (605 \pm 2)$ kA/m (see Figure 5.3(d)). We can also extract the Landé factor of NiFe from γ^{NiFe} considering that:

$$g^{NiFe} = \frac{\gamma^{NiFe}\hbar}{\mu_B}, \tag{5.17}$$

with $\hbar = 1.054 \times 10^{-34}$ J.s and the Bohr magneton $\mu_B = 9.274 \times 10^{-24}$ J/T. This gives $g^{NiFe} = 2.11 \pm 0.01$. We also extracted $M_{eff-LS}^{NiFe} = (586 \pm 20)$ kA/m from the evolution of the ST-FMR ratio with the resonant field (see Figure 5.3(e)) and found a relative error of 3% between the effective magnetizations extracted from the Kittel law and the lineshape analysis. This suggests a good agreement between the analytical model and the experiment. We estimate the total FMR efficiency $\xi_{FMR}^{tot-Pt} = 1.48 \pm 0.06$. The quantities related to the

magnetic properties of NiFe extracted from the lineshape analysis are in agreement with the literature [123, 130, 131]. The sign of the spin torque quantities extracted by the lineshape analysis (LS) are summarized in Table 5.1.

The DC bias analysis of Pt(5)/NiFe(4) is shown in Figure 5.4. The ST-FMR signals are measured for a frequency of 6 GHz and for different applied DC currents (Figure 5.3(a)) and both resonance peaks are fitted using Eq.(5.4). The linear evolution of the resonance field with the DC current (Figure 5.3(b)) indicates that $\xi_{FL'} < 0$, with an efficiency for the field-like and Oersted fields $\xi_{FL'}^{SHE-Pt} \sim -0.05$. The linear evolution of the linewidth with the current indicates that $\xi_{DL} < 0$. The corresponding efficiency is $\xi_{DL}^{SHE-Pt} \sim -0.14$. Thus, the signs of the torque are in agreement between the lineshape analysis and the DC bias technique. We calculate the total efficiency according to Eq.(5.11) and find $\xi_{FMR}^{tot-DC} = +2.8$, which is about twice the value found with the lineshape analysis. This factor of two can be explained by the fact that considering a noncolinear DC torque with respect to the magnetic equilibrium position changes the latter with a contribution proportional to a_j. The signs of the spin torque quantities extracted by the DC bias technique (DC) are summarized in Table 5.1 and are consistent with the literature [123, 130, 131].

Technique	LS	LS	LS	LS		DC	DC	DC
	V_S/V_A	h_{DL}	h'_{FL}	ξ_{FMR}^{tot-LS}	δ^{model}	ξ_{DL}	$\xi_{FL'}$	ξ_{FMR}^{tot-DC}
Pt(5)/NiFe(4)	+	-	-	+1.48	3%	-0.14	-0.05	+2.8

Table 5.1: Sign of the spin torque related quantities in the Pt(5)/NiFe(4) system extracted by the lineshape analysis (LS) or by the DC biased technique (DC).

In conclusion, in this section we have seen how ST-FMR and DC bias analysis are performed on an archetypal Pt/NiFe system. We have extracted the signs of the spin torques, evaluated the overall efficiency considering each technique, and evaluated the spin torque efficiency from the DC bias technique. We estimate a 3% deviation in the model, suggesting that the analytical model accurately describes the experiments.

In the following we discuss the case of GdFeCo/Cu/NiFe, which is more complex than Pt/NiFe due to the presence of spin currents with SHE symmetry, but also with SAHE symmetry.

5.2 Spin current generated by GdFeCo and absorbed by NiFe

5.2.1 Spin current symmetries and associated spin torque symmetries

Let us consider now a GdFeCo/Cu/NiFe trilayer, where GdFeCo emits spin currents and NiFe absorbs the spin currents. As discussed in section 2.4, GdFeCo generates spin currents with different symmetries: the SHE and SAHE symmetries. Both spin current symmetries

can induce a torque on the NiFe magnetization when they are absorbed, so they contribute to the total torque $\vec{\Gamma}_{tot}$:

$$\vec{\Gamma}_{tot} = \vec{\Gamma}_{SHE} + \vec{\Gamma}_{SAHE}. \tag{5.18}$$

We assume that the SHE spin current has a spin polarization $\hat{\sigma}_{SHE}$ along the $\hat{y}$ axis, similar to the usual SHE in HM, and that its direction is independent of the direction of $\hat{m}_{GdFeCo}$. The spin polarization of the SAHE spin current $\hat{\sigma}_{SAHE}$ is given by the orientation of the GdFeCo magnetization $\hat{m}_{GdFeCo}$. The torques can be expressed by the SOT fields:

$$\frac{\vec{\Gamma}_{SHE}}{\gamma M_S^{NiFe}} = h_{DL}^{SHE}\hat{m}_{NiFe} \times \left(\underbrace{\hat{\sigma}_{SHE}}_{\hat{y}} \times \hat{m}_{NiFe} \right) + h_{FL}^{SHE}\hat{m}_{NiFe} \times \underbrace{\hat{\sigma}_{SHE}}_{\hat{y}}, \tag{5.19}$$

and

$$\frac{\vec{\Gamma}_{SAHE}}{\gamma M_S^{NiFe}} = h_{DL}^{SAHE}\hat{m}_{NiFe} \times \left(\underbrace{\hat{\sigma}_{SAHE}}_{\hat{m}_{GdFeCo}} \times \hat{m}_{NiFe} \right) + h_{FL}^{SAHE}\hat{m}_{NiFe} \times \underbrace{\hat{\sigma}_{SAHE}}_{\hat{m}_{GdFeCo}}. \tag{5.20}$$

The efficiencies associated with each torque are then expressed as:

$$\xi_{DL(FL)}^{SHE} = \frac{2|e|}{\hbar}\mu_0 M_S^{NiFe} t_{NiFe} \frac{h_{DL(FL)}^{SHE}}{J_c^{GdFeCo}}, \tag{5.21}$$

and

$$\xi_{DL(FL)}^{SAHE} = \frac{2|e|}{\hbar}\mu_0 M_S^{NiFe} t_{NiFe} \frac{h_{DL(FL)}^{SAHE}}{(\hat{m}_{GdFeCo} \times J_c^{GdFeCo}).\hat{z}}, \tag{5.22}$$

It can be seen that the SAHE spin current (and thus the torque) vanishes when the magnetization of GdFeCo is perfectly along the $\hat{z}$ axis, i.e. along its easy axis. This feature is very interesting and allows to perform the ST-FMR measurement of the SHE symmetry without perturbing the SAHE symmetry when the GdFeCo magnetization is out of plane. Different measurement configurations will be discussed in Section 5.2.4.

5.2.2 Lineshape analysis

In the lineshape analysis experiment, the NiFe magnetization dynamics are driven by the RF Oersted field and SOT. The magnetization advances in the plane transverse to its equilibrium position. As a consequence, the NiFe magnetization is only sensitive to the polar and azimuthal components of the SOT fields. Therefore, the SAHE spin polarization does not contribute to the magnetization dynamics and only the SHE contributes. We recover the expressions for the voltages as derived in Eq.(5.23):

$$\boxed{\begin{aligned} V_S &= -\frac{i_{rf}R_{NiFe}^{AMR}}{2}\frac{\sin(2\varphi_H)\cos(\varphi_H)}{\mu_0(2H_{ext}+M_{eff}^{NiFe})}\frac{2\pi f}{\gamma}\frac{h_{DL}^{SHE}}{\Delta_H}, \\ V_A &= -\frac{i_{rf}R_{NiFe}^{AMR}}{2}\frac{\sin(2\varphi_H)\cos(\varphi_H)}{\mu_0(2H_{ext}+M_{eff}^{NiFe})}\frac{2\pi f}{\gamma}\sqrt{1+\frac{M_{eff}}{H_r}}\frac{h_{FL}^{SHE}}{\Delta_H}. \end{aligned}} \tag{5.23}$$

It turns out that the symmetric signal depends only on h_{DL}^{SHE} and the antisymmetric signal depends only on $h_{FL'}^{SHE}$. As mentioned above, the evaluation of the RF current flowing in the device is challenging, making it difficult to accurately quantify the effective fields from these expressions. Nevertheless, it is possible to discuss the sign of the torques in a certain extend.

5.2.3 DC bias

The addition of a DC current while performing the ST-FMR technique induces a DC torque on the oscillatory magnetization of NiFe, resulting in a change in the expression of its dynamic susceptibility matrix. The susceptibility is derived from the magnetic energy density of the magnetic material and is therefore related to the effective field $\mu_0\vec{H}_{eff}$ along which the magnetization lies. Consequently, a spin polarization with a projection aligned with this effective field can induce a change in the magnetization dynamics. Both the SHE and SAHE spin currents then participate in the magnetization dynamics of NiFe in DC biased measurements. We extend the expressions used for magnetic tunnel junctions [52, 128] and it comes for the change in linewidth:

$$\frac{\partial\mu_0\Delta_H^{NiFe}}{\partial i_{DC}} = -\frac{f}{\gamma_{NiFe}}\frac{2}{(2H_r^{NiFe}+M_{eff}^{NiFe})}\frac{S_{GdFeCo}}{wt_{GdFeCo}} \times\left(\hat{\sigma}_{SAHE}.\hat{m}_{NiFe}\frac{\partial h_{DL}^{SAHE}}{\partial J_c^{GdFeCo}}+\hat{\sigma}_{SHE}.\hat{m}_{NiFe}\frac{\partial h_{DL}^{SHE}}{\partial J_c^{GdFeCo}}\right), \tag{5.24}$$

where $S_{GdFeCo} = J_c^{GdFeCo}wt_{GdFeCo}/i_{DC}$ accounts for the shunting of the GdFeCo layer. Considering that both the GdFeCo and the NiFe magnetizations are aligned along the magnetic field, we can simplify to $\hat{\sigma}_{SAHE}.\hat{m}_{NiFe} = 1$. The equation can then be written in terms of the spin torque efficiencies:

$$\boxed{\frac{\partial\mu_0\Delta_H^{NiFe}}{\partial i_{DC}} = -\frac{f}{\gamma_{NiFe}}\frac{2}{(2H_r^{NiFe}+M_{eff}^{NiFe})}\frac{S_{GdFeCo}}{wt_{GdFeCo}}\times\frac{\hbar}{2|e|}\sin(\varphi_H)\frac{\xi_{DL}^{SAHE}+\xi_{DL}^{SHE}}{\mu_0 M_S^{NiFe}t_{NiFe}}} \tag{5.25}$$

. Concerning the shift of the resonance field, we obtain:

$$\frac{\partial\mu_0 H_{res}^{NiFe}}{\partial i_{DC}} = \frac{S_{GdFeCo}}{wt_{GdFeCo}}\left(\hat{\sigma}_{SAHE}.\hat{m}_{NiFe}\frac{\partial h_{FL}^{SAHE}}{\partial J_c^{GdFeCo}}+\hat{\sigma}_{SHE}.\hat{m}_{NiFe}\frac{\partial h_{FL}^{SHE}}{\partial J_c^{GdFeCo}}\right)-\hat{\sigma}_{SHE}.\hat{m}_{NiFe}\frac{\partial h_{Oe}}{\partial i_{DC}}, \tag{5.26}$$

and considering the alignment between the magnetizations of NiFe and GdFeCo, we can write the resonance field shift in terms of the efficiencies:

$$\boxed{\frac{\partial\mu_0 H_r^{NiFe}}{\partial i_{DC}} = \sin(\varphi_H)\left[\frac{S_{GdFeCo}}{wt_{GdFeCo}}\left(\frac{\hbar}{2|e|}\frac{\xi_{FL}^{SAHE}+\xi_{FL}^{SHE}}{\mu_0 M_S^{NiFe}t_{NiFe}}\right)-\frac{\partial h_{Oe}}{\partial i_{DC}}\right].} \tag{5.27}$$

Finally, the difference between the lineshape analysis and the DC bias technique in the case of GdFeCo can be highlighted. In the configuration of the lineshape analysis, only the spin torque induced by the SHE symmetry is detected. However, the DC bias technique allows to capture both the SHE and SAHE induced spin torque. For the latter case, the model

assumes that both magnetizations of GdFeCo and NiFe are aligned along the magnetic field to obtain Eq.(5.25) and Eq.(5.27). If this alignment is not ensured and maintained during the measurement, it can lead to an unknown SAHE contribution and a misleading interpretation. In the following section we discuss different measurement configurations where the SHE and SAHE contributions are perfectly known and described by the above equations.

5.2.4 Different configurations for the measurements

Since GdFeCo has a perpendicular magnetic anisotropy, the external magnetic field provided by our setup may not be sufficient to saturate the magnetization position in the plane. This is even more true as the temperature approaches magnetization compensation, where the field needed to saturate the magnetization in the plane, the anisotropic field, diverges. To avoid any possible misinterpretation of the data, we propose two measurement configurations for both the lineshape analysis and the DC bias experiments, where the position for GdFeCo is known or controlled:

- Parallel configuration $\parallel$, with $\hat{m}_{GdFeCo} \parallel \hat{m}_{NiFe} \parallel \mu_0\vec{H}_{ext}$:
  Far from the compensation temperature, the anisotropic field can usually be achieved by our experimental setup, which is limited to 0.6T. Therefore, at this limit, both magnetizations are aligned in the plane along the magnetic field, and the spin current emitted by GdFeCo is the sum of both SHE and SAHE symmetries, as shown in Figure 5.5(a), and the analytical expressions for the voltage are given by the equations of sections 5.2.2 and 5.2.3.

- Transverse configuration $\perp$, with $\hat{m}_{GdFeCo} \perp \hat{m}_{NiFe}$, $\hat{m}_{GdFeCo} \parallel \hat{z}$ and $\hat{m}_{NiFe} \parallel \mu_0\vec{H}_{ext}$:
  Near the compensation temperature of GdFeCo, the anisotropic field diverges and our experimental setup cannot control the magnetization. In this case, the magnetization of GdFeCo lies along the $\hat{z}$ axis and the SAHE spin current vanishes. Therefore, only a SHE spin current acts on the NiFe layer as shown in Figure 5.5(b). The analytical expressions are the same as in section 5.2.3, without the SAHE contribution.

5.2.5 Contribution of the GMR

In GdFeCo/Cu/NiFe, the presence of the two magnetic layers can be the origin of a GMR effect that can contribute to the ST-FMR signal. In the parallel configuration, where the GdFeCo and NiFe magnetizations are aligned, the GMR is a second-order effect in the signal and can then be neglected. In the transverse configuration, however, the GMR contribution is maximal. The result is (the full calculation is not presented in this work):

$$V_{DC}^{GMR,\perp} = -\frac{I_X}{2}\Delta R^{GMR}\left[\chi'_{\theta\theta}\frac{\delta h_\theta}{M_S} + \chi'_{\theta\varphi}\frac{\delta h_\varphi}{M_S}\right], \tag{5.28}$$

and this contribution adds up to the AMR signal as derived in Eq.(5.1), it then comes for the DC voltage:

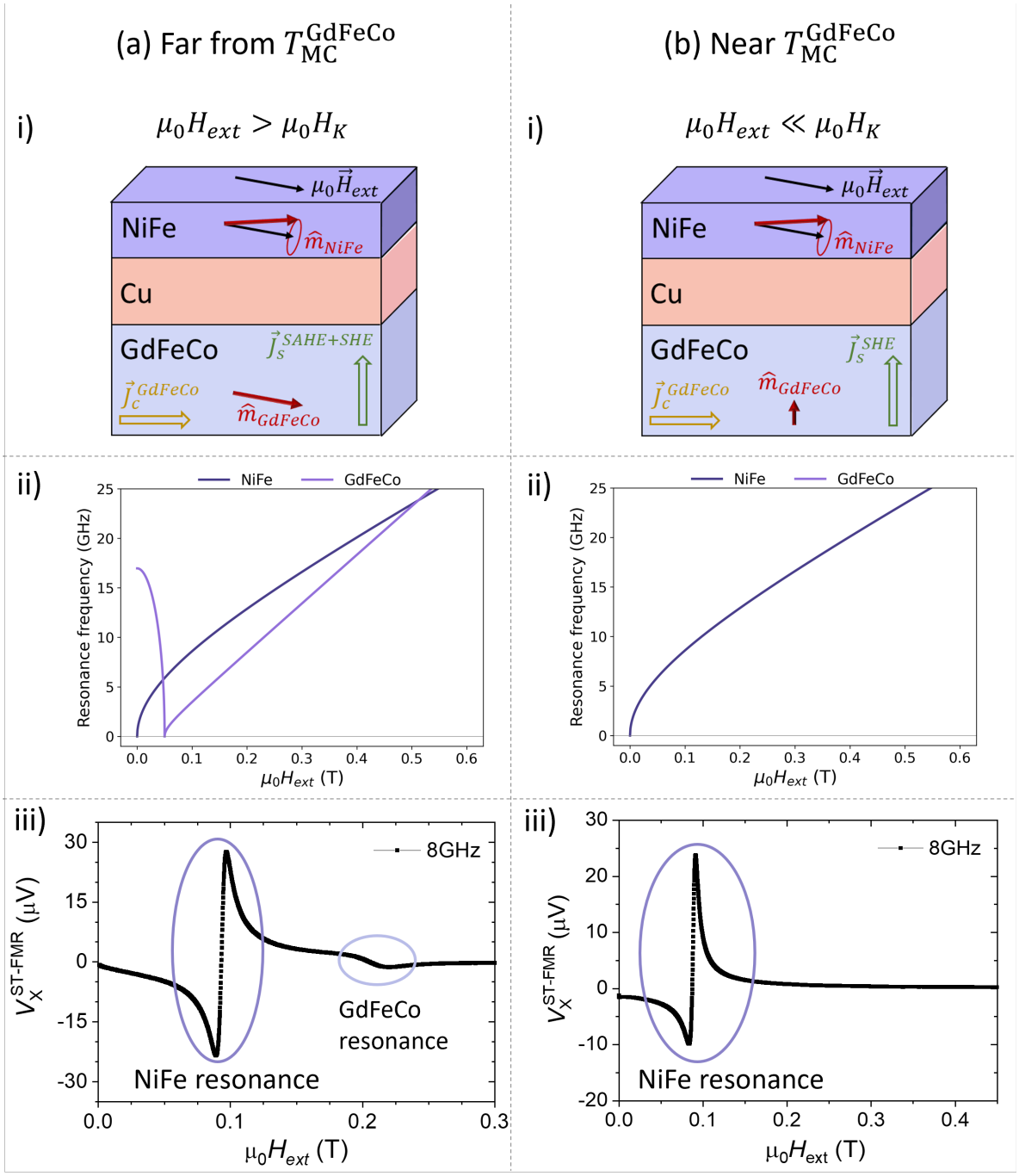

Figure 5.5: Schematic of the different measurement configurations. (a) Far from the magnetic compensation, the external magnetic field is strong enough to align the GdFeCo magnetization in the plane. In this case i) the spin current emitted by GdFeCo is the sum of the SHE and SAHE symmetries. ii) Schematic of the evolution of the resonance frequencies of NiFe and GdFeCo as a function of an external magnetic field. The resonances of both magnetic materials can be observed as shown in measurements iii). (b) Near the compensation, the anisotropic field of GdFeCo diverges, and the external magnetic field is not strong enough to manipulate the GdFeCo magnetization. Therefore, the latter magnetization remains out of the plane for the whole range of the magnetic field, and it emits a spin current with only the SHE symmetry i). In this scenario, only the resonance of NiFe can be observed in our range of magnetic field and frequencies used, as shown in the evolution of frequencies of NiFe with magnetic field ii), and as shown in our measurement iii).

$$V_{DC}^{\perp} = -\frac{I_X}{2M_S}\left[\left(\Delta R^{GMR}\chi'_{\theta\theta} + \Delta R^{AMR}\sin(2\varphi_H)\chi'_{\varphi\theta}\right)\delta h_\theta + \left(\Delta R^{GMR}\chi'_{\theta\varphi} + \Delta R^{AMR}\sin(2\varphi_H)\chi'_{\varphi\varphi}\right)\delta h_\varphi\right]. \quad (5.29)$$

We recall that the diagonal components of the real part of the susceptibility matrix are antisymmetric with respect to the resonance frequency, while the off-diagonal components are symmetric. We can therefore describe the signal as the sum of a symmetric and an antisymmetric part. It comes:

$$\begin{aligned} V_S &\propto \chi'_{\varphi\theta}\left(-\Delta R^{GMR}\delta h_\varphi + \Delta R^{AMR}\sin(2\varphi_H)\delta h_\theta\right) \\ V_A &\propto \Delta R^{GMR}\chi'_{\theta\theta}\delta h_\varphi + \Delta R^{AMR}\sin(2\varphi_H)\chi'_{\varphi\varphi}\delta h_\varphi, \end{aligned} \quad (5.30)$$

where $h_\theta \propto h_{DL}$ and $h_\varphi \propto h_{FL'}$ in the geometry of the ST-FMR technique.

Therefore, when the GMR and AMR contribute to the ST-FMR signal, the damping-like and field-like effective fields appear in both the symmetric and antisymmetric parts. As a consequence, the lineshape analysis and the method of considering the ratio between V_S and V_A are not relevant in the case of non-negligible GMR amplitude.

In our case, we have not estimated the GMR in our samples. Work in the literature shows that the change in resistance induced by the GMR in NiFe(10)/Cu(2)/GdCo(15) is about 1-3% [99], which dominates the 0.4% change induced by the AMR of NiFe(4) estimated in our sample. Since we have not verified that the GMR contributes in our structure, we will perform the lineshape analysis as if only the AMR contributes. The estimation of the deviation δ^{model} can further indicate the presence of an additional magnetoresistive effect.

5.3 Spin current generation of GdFeCo across the magnetization compensation temperature

We present the study of SiO_2//$Gd_{25}Fe_{65.6}Co_{9.4}$(10)/Cu(4)/$Ni_{81}Fe_{19}$(4)/Al(3). The Cu layer allows the decoupling between the two magnetic layers, and the long spin diffusion length of this material allows the spin currents to be transferred from GdFeCo to NiFe without loss.

5.3.1 Magnetic compensation temperature and anisotropic field of GdFeCo

To determine the magnetic compensation temperature of GdFeCo T_M, we performed magnetotransport measurements in a Hall cross. A single lithography mask provides both the ST-FMR and Hall cross devices, so the different devices studied in this chapter went through the same patterning process. We selected a Hall cross with the same current line width as the ST-FMR device (10μm) and located close to the ST-FMR device to avoid a possible change in the magnetic properties of the film along the wafer. The measurements were performed with a DC current $i_{DC} = 1$mA, and the transverse DC voltage was measured.

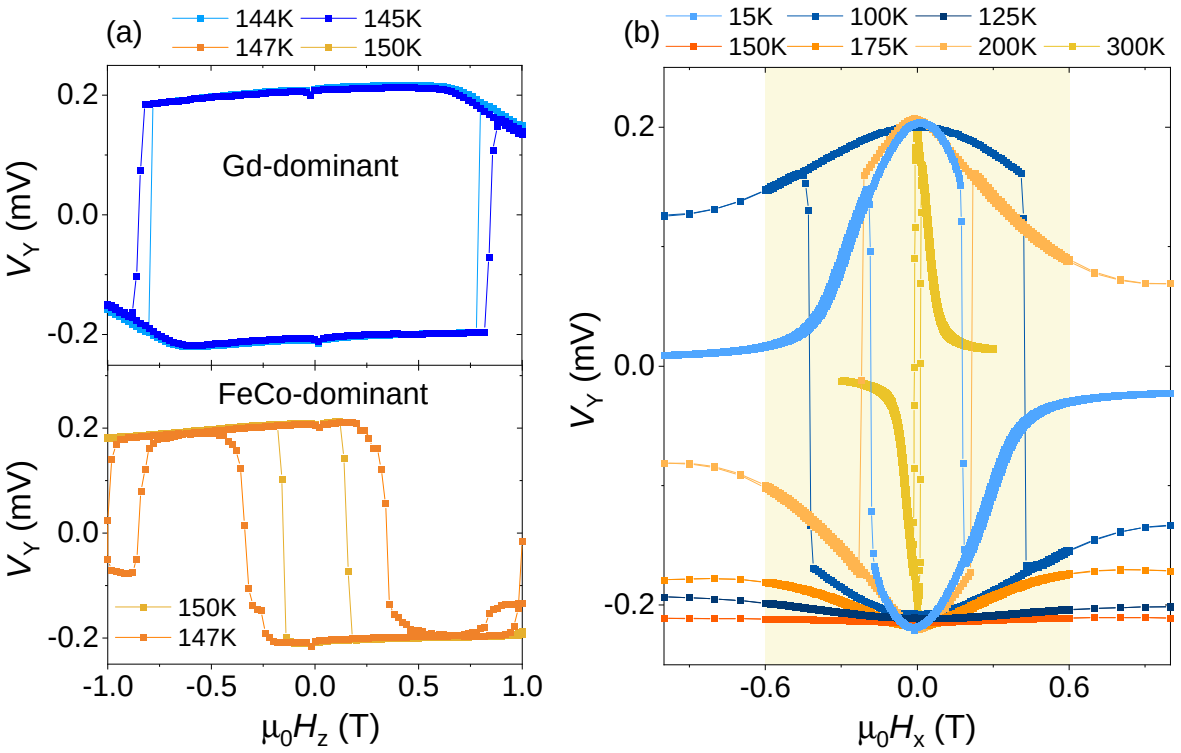

Figure 5.6: (a) Hall voltage as a function of the amplitude of the magnetic field applied along $\hat{z}$. The sign reversal of the AHE amplitude between 145K and 147K indicates that the magnetization compensation temperature of GdFeCo has been crossed. (b) Hall voltage as a function of the amplitude of the magnetic field applied along the current. The yellow background represents the range of the magnetic field provided by the ST-FMR setup. It turns out that we can perform the ST-FMR measurement in the transverse configuration for temperatures between 125K and 175K, since the magnetic field amplitude is not sufficient to reverse the magnetization.

The Hall voltage V_Y is measured at different temperatures as a function of the amplitude of the external magnetic field. First, with a field applied along $\hat{z}$, we can deduce $T_M \approx 146$K from the sign change of the anomalous Hall effect (AHE) shown in Figure 5.6(a). Then, by applying the magnetic field in the plane along $\hat{x}$, we can see magnetic field amplitude needed to fully saturate the magnetization of GdFeCo in the plane. The measurements are shown in Figure 5.6(b), where the yellow background represents the range of field provided for the ST-FMR measurements (about $\pm$0.6T). Let us discuss two cases:

- Far from T_M:
  At 20K we can see in Figure 5.6(b) that 0.40T is enough to saturate $\hat{m}_{GdFeCo}$ in the plane. Therefore, the ST-FMR measurements must be performed at high frequency to ensure a high resonance field of NiFe. Similarly, 0.1T is sufficient to saturate $\hat{m}_{GdFeCo}$ in the plane at 300K and ST-FMR measurements must be performed so that the resonance field of NiFe is above this value. Under these conditions, both the lineshape analysis and the DC bias technique can be measured and interpreted according to the model developed in Section 5.2.1. Therefore, the measurements can be performed in the parallel configuration for temperatures $T \notin]120\text{K},175\text{K}[$.

- Near T_M:
  At 100K and 200K, $\hat{m}_{GdFeCo}$ can be reversed from one state to the other with a field less than 0.6T, as shown by the coexistence of two voltage states. Therefore, these temperatures are not suitable for ST-FMR measurements. Between 125K and 175K the anisotropic field is much larger than 0.6T and the magnetization position is mostly along the $\pm\hat{z}$ direction. Therefore, measurements in the transverse configuration can only be performed for temperatures $T \in$ [120K,175K].

In the following subsection, we will present the lineshape analysis and DC bias experiments near the compensation in the transverse configuration at 140K, when the ferrimagnet is Gd-dominant, and at 160K, when the material is FeCo-dominant. Then we present the DC bias results far from the compensation at 15K and 300K, in the parallel configuration. The results are then summarized in the next section. The data for all temperatures and the corresponding analysis can be found in Appendix B.

5.3.2 Study of the SHE spin current across T_M in the transverse configuration

At 140K, Gd-dominant

At 140K, the measurement is performed in the transvserse configuration because the magnetic field is not strong enough to manipulate the GdFeCo magnetization. Therefore, only spin torques resulting from the SHE spin current are probed. Figure 5.7(a) shows the evolution of the longitudinal voltage as a function of the external magnetic field, for a power of 14dBm and for different frequencies. The measurements can be fitted by a sum of Lorentzian and anti-Lorentzian functions as expressed in Eq.(5.4), and the values for the symmetric and antisymmetric voltages V_S and V_A are plotted as a function of the frequency in Figure 5.7(b). The symmetric and antisymmetric parts are positive (negative) for a positive (negative) magnetic field. These signs are the same as in the case of Pt/NiFe presented in section 5.1.5, therefore the signs for the spin torque in the lineshape analysis are $h_{DL}^{SHE} < 0$ and $h_{FL'}^{SHE} < 0$ with a negative Oersted field. We can further estimate the total FMR efficiency from the square of the ratio of the symmetric and antisymmetric parts, it comes $\xi_{FMR}^{tot-LS-GdFeCo} \sim +0.68 \pm 0.02$ (Figure 5.7(c)) with a deviation of about 85%. The high deviation suggests that the analytical model used for the analysis is incomplete.

DC bias measurements are shown in Figure 5.8(a) with a power of 14dBm and a frequency of 6GHz. From these measurements, we report the current-induced shift of the resonance field in Figure 5.8(b). It describes a linear evolution with DC current, with a positive slope for positive magnetic field. It shows that $\xi_{FL'}^{SHE} < 0$ in the same way as Pt. We estimate $\xi_{FL'}^{SHE-GdFeCo} \sim -0.14$, which is about 2.5 times higher than for Pt/NiFe. Since the Oersted fields in both GdFeCo/Cu/NiFe and Pt/NiFe are estimated to be the same, the high increase of $\xi_{FL'}^{SHE-GdFeCo}$ can be attributed to a higher field-like torque in GdFeCo than in Pt. The modulation of the linewidth with the DC current is shown in Figure 5.8(c), with a negative linear behavior for positive magnetic field. It results in $\xi_{DL}^{SHE-GdFeCo} < 0$ and $\xi_{DL}^{SHE-GdFeCo} \sim -0.41$. This value is about 3 times the value obtained with Pt.

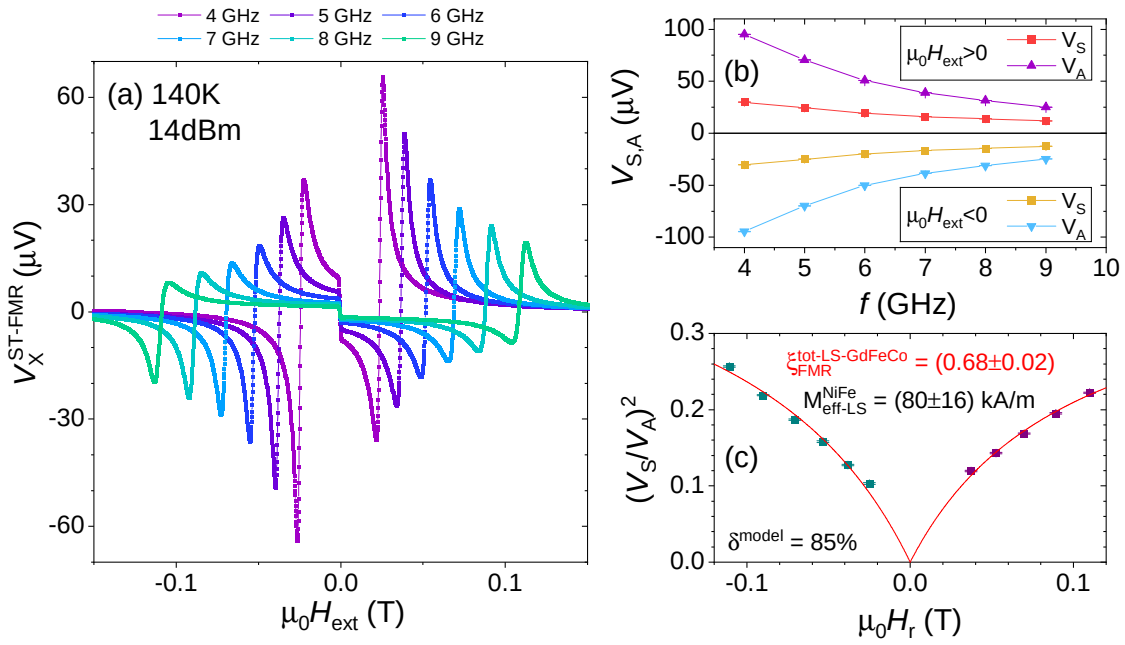

Figure 5.7: ST-FMR without DC bias at 140K, when the material is Gd-dominant. (a) ST-FMR voltage as a function of the external magnetic field for different frequencies. (b) Evolution of the symmetric and antisymmetric voltages V_S and V_A as a function of the frequency. For their signs, we have $h_{DL}^{SHE} < 0$ and $h_{FL'}^{SHE} < 0$. (c) Estimation of the positive FMR efficiency $\xi_{FMR}^{tot-LS-GdFeCo} \sim 0.68 \pm 0.02$ with a high deviation for the model $\delta^{model} = 85\%$.

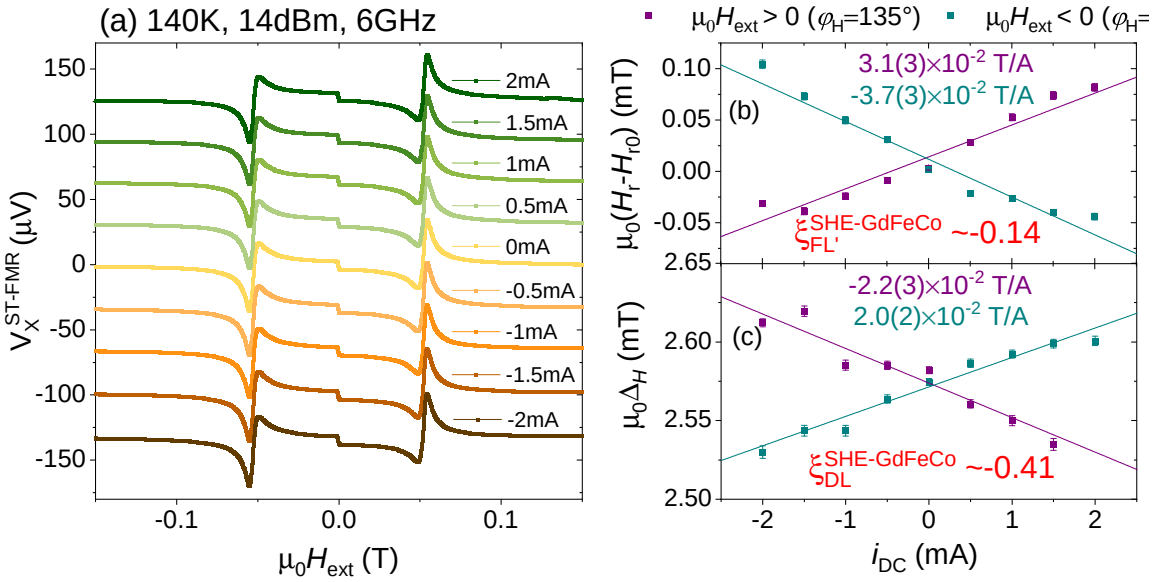

Figure 5.8: DC bias ST-FMR at 140K, when the material is Gd-dominant. (a) ST-FMR voltage as a function of the external magnetic field for a power of 14dBm, a frequency of 6GHz and different DC currents. (b) Evolution of the resonance field shift as a function of the DC current. It follows from the linear slopes that $\xi_{FL'}^{SHE-GdFeCo} \sim -0.14$. (c) Evolution of the modulation of the linewidth with the DC current. It results from the linear slopes that $\xi_{DL}^{SHE-GdFeCo} \sim -0.41$.

Thus, at 140K in the transverse configuration, we show that the torque extracted by the lineshape analysis and the DC bias technique have the same sign as Pt. We further show that GdFeCo is about 3 times more effective than Pt for the generation of spin torques with the SHE symmetry.

At 160K, FeCo-dominant

We now present the measurements at 160K when the ferrimagnet is FeCo-dominant. The external magnetic field is not strong enough to manipulate the magnetization, so the measurements are performed in the transverse configuration and only the SHE contributes to the spin torque on NiFe.

Figure 5.9(a) shows the evolution of the ST-FMR signal without DC bias as a function of the external magnetic field for a power of 14dBm and different frequencies. The associated symmetric and antisymmetric voltages are shown in Figure 5.9(b). Their signs are the same as in the lineshape analysis performed at 140K when GdFeCo is Gd-dominant. It is also the same as for Pt/NiFe. The FMR efficiency is positive and evaluated as $\xi_{FMR}^{tot-LS} = 0.88\ pm0.03$ (see Figure 5.9(c)), which is about the same amplitude as at 140K and with Pt.

DC bias measurements are shown in Figure 5.10(a) with a power of 14dBm and a frequency of 6GHz. From these measurements, we report the current-induced shift of the resonance field in Figure 5.10(b) and evaluate $\xi_{FL'}^{SHE-GdFeCo} = -0.17$, which has the same sign as at 140K, and which as the same sign as Pt/NiFe, but is about 3.5 times more effective than Pt. The modulation of the linewidth with the DC current is shown in Figure 5.10(c) and we evaluate $\xi_{DL}^{SHE-GdFeCo} = -0.37$, which sign agrees with the lineshape analysis and the DC technique performed at 140K. The sign is also the same as for Pt/NiFe, but the efficiency of GdFeCo is about 2.5 times more important than Pt.

Thus, at 160K in the transverse configuration, we show that the torques extracted by the lineshape analysis have the same sign as in Pt. Similarly, using the DC bias technique, we found that the torques generated by GdFeCo have the same sign as the torques generated by Pt. We also show that GdFeCo is about 3 times more effective than Pt in generating spin torques with the SHE symmetry.

In conclusion, we have shown that **in the temperature range $\boldsymbol{T \in [140K, 160K]}$, which includes the magnetization compensation temperature of GdFeCo, the spin torques acting on NiFe have the same sign over $\boldsymbol{T_M}$ and the same sign as the spin torque generated by Pt**. Therefore we can assign a positive spin Hall angle to GdFeCo $\theta_{SHE}^{GdFeCo} > 0$.

5.3.3 Study of the SHE+SAHE spin current across T_M in the parallel configuration

At 15K, Gd-dominant

At 15K, the ferrimagnet is Gd-dominant, and both the NiFe and GdFeCo magnetizations are aligned in the plane along the magnetic field in the parallel configuration. The lineshape analysis can be seen in Appendix B and shows that the SHE torques at 15K have the same

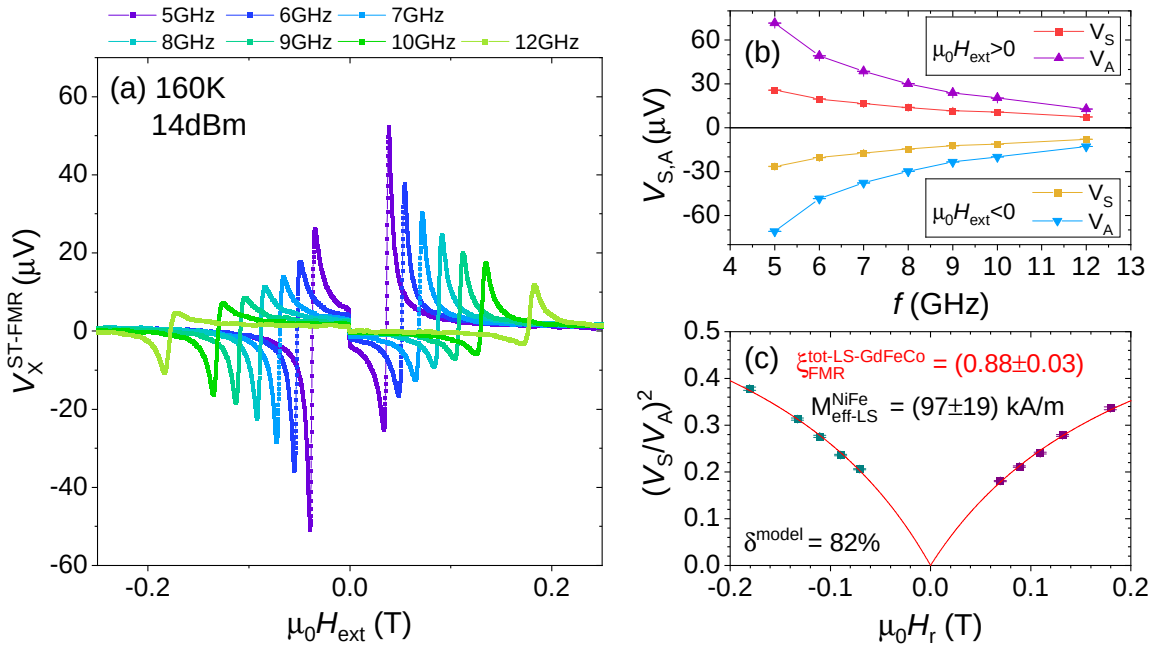

Figure 5.9: ST-FMR without DC bias at 160K, when the material is FeCo-dominant. (a) ST-FMR voltage as a function of the external magnetic field for different frequencies. (b) Evolution of the symmetric and antisymmetric voltages V_S and V_A as a function of the frequency. For their signs, we have $h_{DL}^{SHE} < 0$ and $h_{FL'}^{SHE} < 0$. (c) Estimation of the positive FMR efficiency $\xi_{FMR}^{tot-LS-GdFeCo} = 0.88 \pm 0.03$ with a deviation of the model estimated $\delta^{model} = 82\%$.

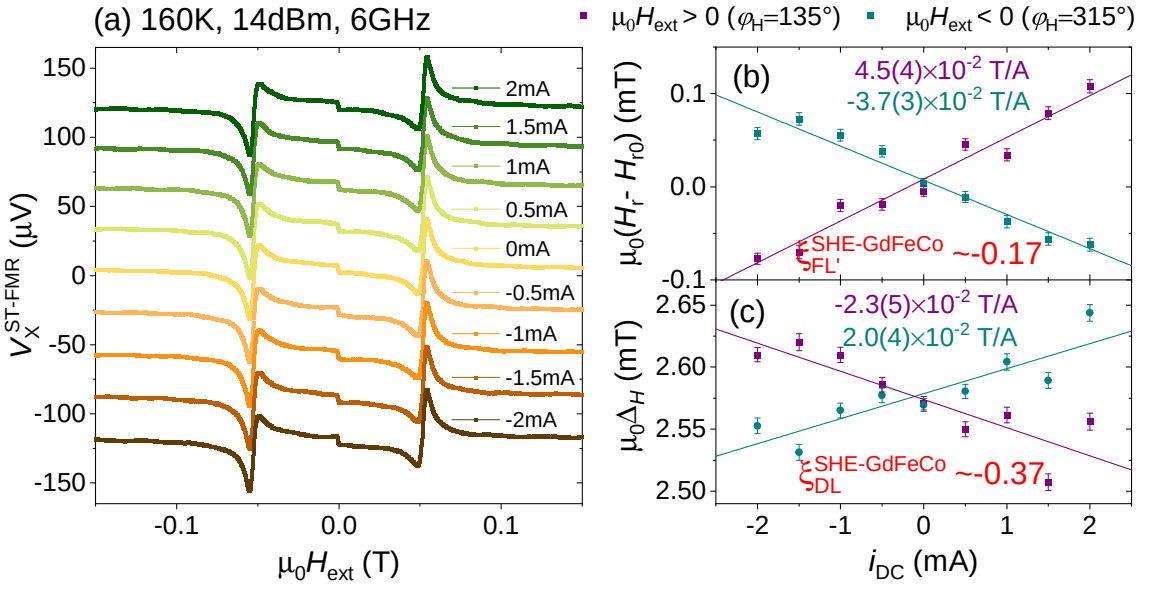

Figure 5.10: DC bias ST-FMR at 160K, when the material is FeCo-dominant. (a) ST-FMR voltage as a function of the external magnetic field for a power of 14dBm, a frequency of 6GHz and different DC currents. (b) Evolution of the resonance field shift as a function of the DC current. It results from the slopes that $\xi_{FL'}^{SHE-GdFeCo} = -0.17$. (c) Evolution of the modulation of the linewidth with the DC current. It comes from the slopes that $\xi_{DL}^{SHE-GdFeCo} = -0.37$.

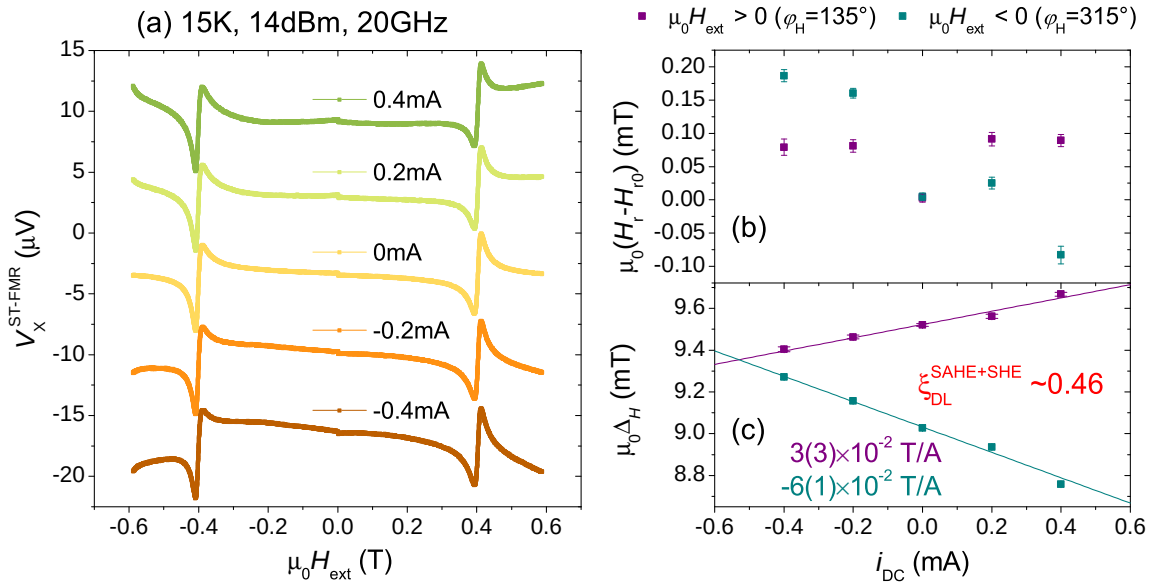

Figure 5.11: DC bias ST-FMR at 15K, when the material is Gd-dominant. (a) ST-FMR voltage as a function of the external magnetic field for a power of 14dBm, a frequency of 20GHz and different DC currents. (b) Evolution of the resonance field shift as a function of the DC current. For a positive magnetic field, the slope seems to be positive, indicating that $\xi_{FL}^{SAHE+SHE} < 0$, but the amplitude of the efficiency cannot be estimated. (c) Evolution of the modulation of the linewidth with the DC current. It follows from the slopes that $\xi_{DL}^{SAHE+SHE} = +0.46$.

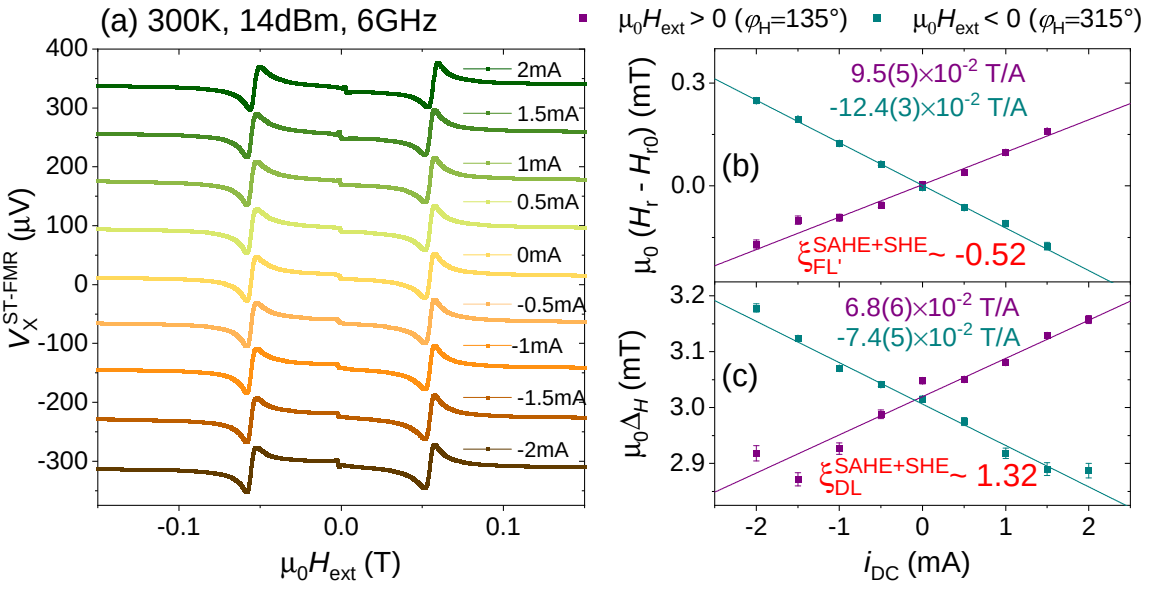

Figure 5.12: DC bias ST-FMR at 300K, when the material is FeCo-dominant. (a) ST-FMR voltage as a function of the external magnetic field for a power of 14dBm, a frequency of 6GHz and different DC currents. (b) Evolution of the resonance field shift as a function of the DC current. It results from the slopes that $\xi_{FL'}^{SAHE+SHE} \sim -0.52$ (c) Evolution of the modulation of the linewidth with the DC current. The slopes allow to evaluate $\xi_{DL}^{SAHE+SHE} \sim 1.32$.

sign as at 140K and 150K, i.e. $\xi_{DL}^{SHE} < 0$ and $\xi_{FL'}^{SHE} < 0$. The data in Figure 5.11(a) show the evolution of the longitudinal voltage with the external magnetic field for different DC currents. We can see that with the addition of current, a strong contribution in square of the magnetic field appears, leading to a difficult fit. The shift of the resonance field is shown in Figure 5.11(b) and we have estimated $\xi_{FL'}^{SAHE+SHE} < 0$, while the modulation of damping in Figure 5.11(c) shows that $\xi_{DL}^{SAHE+SHE} \sim 0.46$.

Thus, at 15K, when the material is Gd-dominant, the spin torques extracted from the lineshape analysis, which has only the SHE symmetry, have the same sign as the sample at 140K and 160K and as for Pt. The DC bias analysis, which probes the SHE and SAHE symmetries, shows that the damping-like torque has a sign opposite than that of Pt and to the SHE damping-like torque estimated at 140K and 160K. It suggests that the SAHE symmetry dominates over the SHE symmetry and that their sign is opposite.

At 300K, FeCo-dominant

At 300K, the ferrimagnet is FeCo-dominant, and the magnetic field provided by the setup allows the measurements to be performed in the parallel configuration. The lineshape analysis can be seen in Appendix B and shows that the SHE torques at 300K have the same sign as at 15K, 140K and 150K, i.e. $\xi_{DL}^{SHE} < 0$ and $\xi_{FL'}^{SHE} < 0$. Let us now focus on the DC bias technique. Figure 5.12(a) shows the longitudinal voltages as a function of the external magnetic field and for different DC currents. The shift of the resonance field is shown in Figure 5.12(b) and we evaluate $\xi_{FL'}^{SAHE+SHE} \sim -0.52$. For the modulation of damping shown in Figure 5.12(c), we evaluate $\xi_{DL}^{SAHE+SHE} \sim 1.32$.

Thus, at 300K when the material is FeCo-dominant, the spin torques extracted from the lineshape analysis, which has only the SHE symmetry, have the same sign as the sample at 15K, 140K, and 160K and as for Pt. The DC bias analysis, which probes the SHE and SAHE symmetries, shows that the damping-like torque has a sign opposite to that of Pt and to the SHE damping-like torque estimated at 140K and 160K. It suggests that the SAHE symmetry dominates over the SHE symmetry and that their sign is opposite.

In conclusion, we have shown that **far from the compensation temperature, the spin torques with the SHE symmetry acting on NiFe have the same sign over T_M and have the same sign as the spin torque generated by Pt**. Therefore **we can assign a positive spin Hall angle to GdFeCo $\theta_{SHE}^{GdFeCo} > 0$ for the whole temperature range $T \in [15K, 300K]$**. We also show that **the damping-like torque of the SAHE symmetry dominates and is opposite in sign compared to the SHE symmetry**.

The lineshape analysis and DC bias technique were also performed at other temperatures. The analysis and raw data can be found in Appendix B. Table 5.2 summarizes the sign and amplitude of the various spin torque related quantities for the lineshape and DC techniques.

			LS	LS	LS	deviation	DC	DC	DC	DC	DC
T	-rich	config.	h_{DL}^{SHE}	$h_{FL'}^{SHE}$	ξ_{FMR}^{tot-LS}	δ^{model}	ξ_{DL}^{SHE}	$\xi_{FL'}^{SHE}$	$\xi_{DL}^{SAHE+SHE}$	$\xi_{FL}^{SAHE+SHE}$	ξ_{FMR}^{tot-DC}
15K	Gd	$\parallel$	-	-	unclear	unclear	$\emptyset$	$\emptyset$	+0.46	unclear	$\emptyset$
120K	Gd	$\perp$	-	-	$+0.66 \pm 0.06$	90%	-0.150	- 0.133	$\emptyset$	$\emptyset$	+1.13
130K	Gd	$\perp$	-	-	$+0.93 \pm 0.04$	69%	-0.378	~ 0	$\emptyset$	$\emptyset$	$\emptyset$
140K	Gd	$\perp$	-	-	0.68 ± 0.02	85%	-0.408	-0.144	$\emptyset$	$\emptyset$	+2.83
150K	FeCo	$\perp$	-	-	unclear	55%	unclear	unclear	unclear	unclear	unclear
160K	FeCo	$\perp$	-	-	$+0.88 \pm 0.03$	82%	-0.37	-0.174	$\emptyset$	$\emptyset$	+2.11
300K	FeCo	$\parallel$	-	-	unclear	unclear	$\emptyset$	$\emptyset$	+1.32	-0.519	$\emptyset$
300K	Pt		-	-	$+1.48 \pm 0.06$	3%	-0.14	-0.05	$\emptyset$	$\emptyset$	+2.8

Table 5.2: Sign of the spin torque related quantities in GdFeCo(10)/Cu(4)/NiFe(4) extracted by the lineshape analysis (LS) or by the DC biased technique (DC).

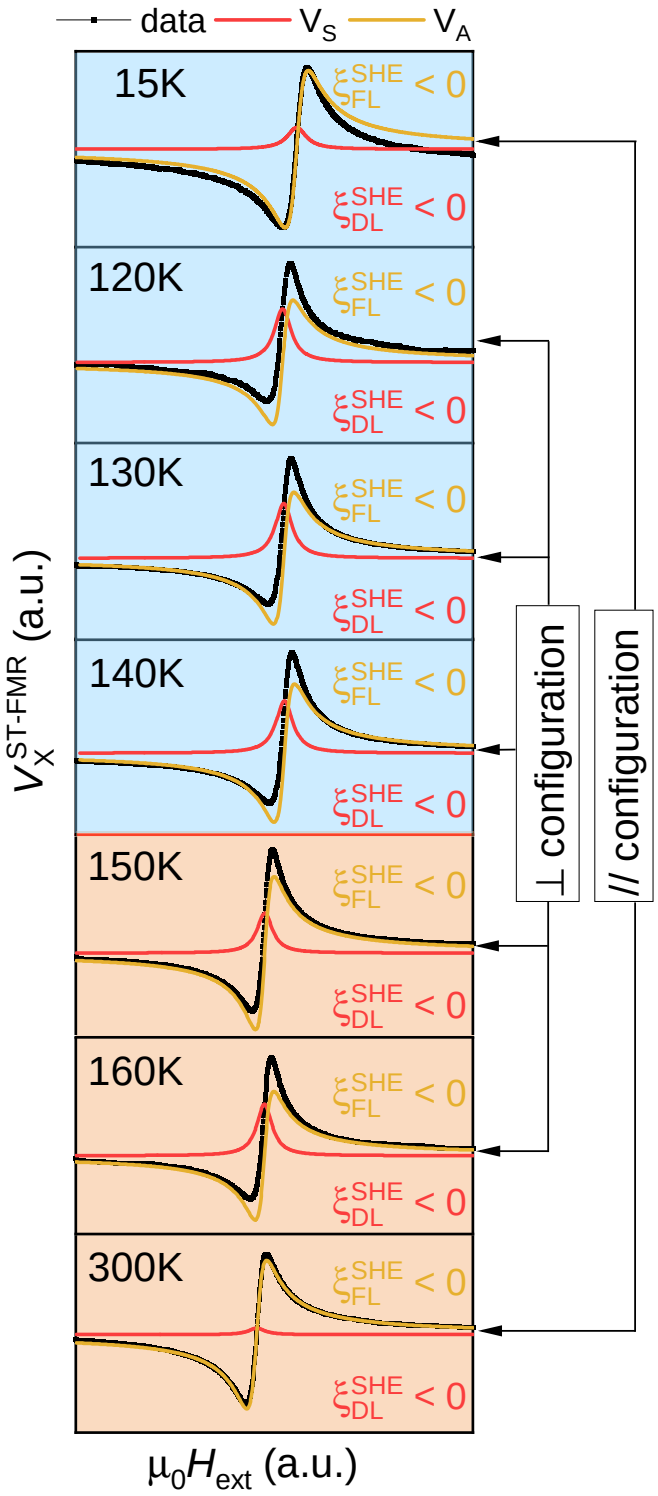

Figure 5.13: Summary of the lineshape analysis for temperatures from 15K to 300K. The blue background corresponds to the temperatures where the ferrimagnet is Gd-dominant, and the orange background corresponds to the temperatures where the ferrimagnet is FeCo-dominant. At all temperatures the symmetric and antisymmetric parts are positive, i.e. $\theta_{DL}^{SHE} > 0$ and $\theta_{FL}^{SHE} > 0$. The corresponding FMR efficiency is positive for all temperatures.

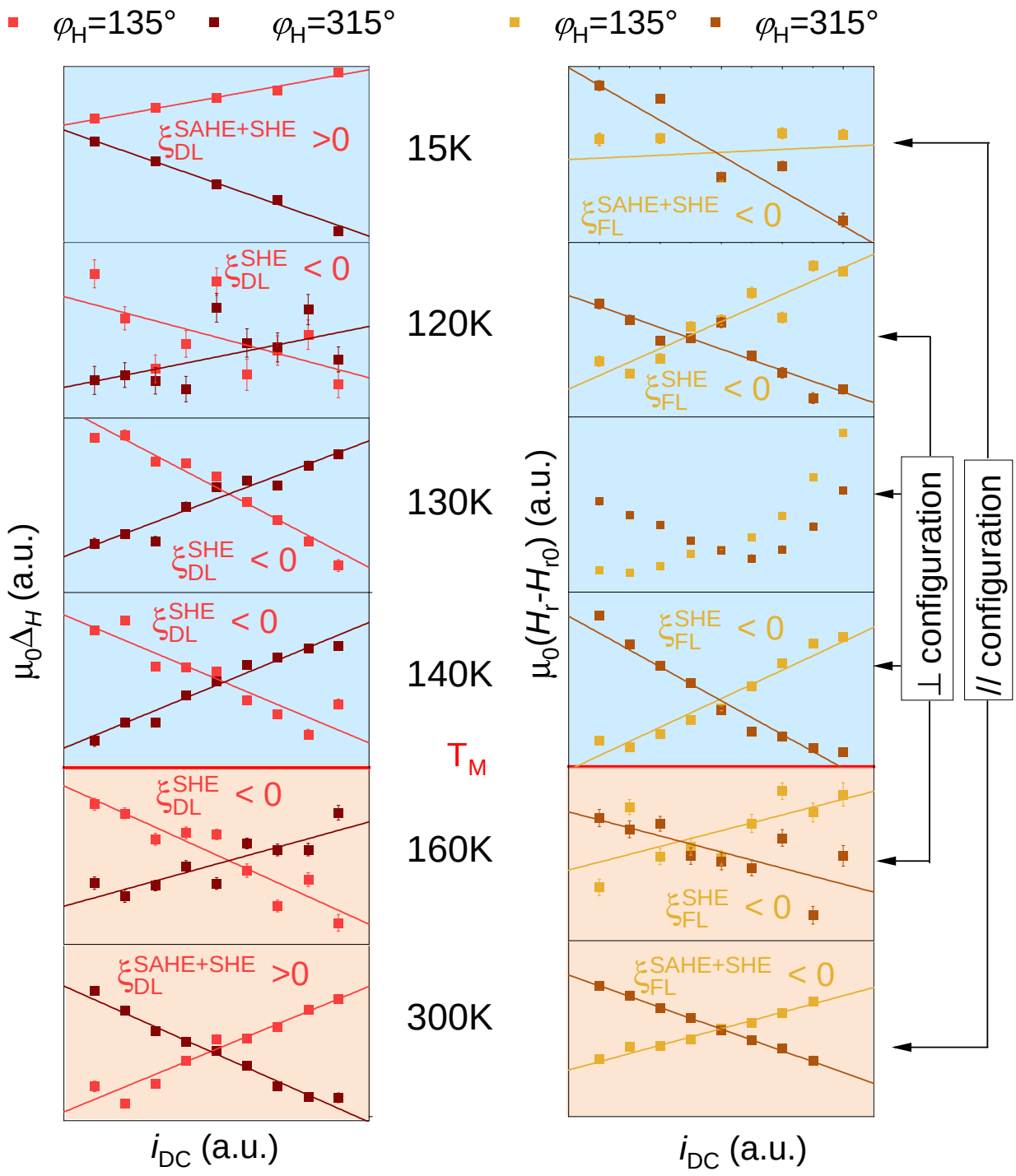

Figure 5.14: Summary of the DC bias analysis for temperatures from 15K to 300K. The blue background corresponds to the temperatures where the ferrimagnet is Gd-dominant, and the orange background corresponds to the temperatures where the ferrimagnet is FeCo-dominant. The positive evolution of the resonance field with the current for all temperatures shows that $\theta_{FL}^{SHE} > 0$ and $\theta_{FL}^{SAHE} > 0$ for all temperature ranges. Near the magnetization compensation temperature, in the transverse configuration, we have $\theta_{DL}^{SHE} < 0$ over T_M. At 15K and 300K we see that $\theta_{DL}^{SAHE+SHE} > 0$, indicating that the SAHE is opposite and stronger than the SHE.

5.4 Summary and interpretation

Figure 5.13 summarizes the lineshape analysis for all temperatures measured between 15K and 300K. The ST-FMR signals are plotted in arbitrary units because we want to focus on the shape of the peaks first (the amplitude will be discussed later), and only the peaks obtained at a positive magnetic field are shown. For the whole temperature range, above $T_M \approx 147$K, the signs of the symmetric and antisymmetric parts are preserved, and the FMR efficiency is always positive. The signs of the contributions are related to the sign of the spin torque with the SHE symmetry as derived in Eq.(5.2.2). Our measurements show that the sign of the DL torque is unchanged in the temperature range. The case of the FL torque is more uncertain because it is associated with a negative Oersted field that can dominate over the FL torque, so a sign change of the FL torque may not be visible. **Thus, our measurements using the lineshape analysis show that the sign of the damping-like spin torque with the SHE symmetry acting on NiFe is unchanged over the compensation temperatures of GdFeCo. In other words, the polarization of the SHE spin current is unchanged and seems to be independent of the magnetic state of GdFeCo**. The evolution of the total efficiency obtained by the lineshape analysis is shown as a function of the temperature in Figure 5.15(a). We can see a significant increase in the amplitude near the magnetic compensation temperature of GdFeCo, which can be associated with a higher value of the damping-like torque. However, we recall that the deviation of the model estimated near the compensation is stronger than far from the compensation.

Figure 5.14 summarizes the DC bias analysis for temperatures from 15K to 300K. The left panel shows the electrical modulation of the linewidth associated with the DL torque, and the right panel shows the shift of the resonance peak associated with the FL torque and the Oersted field. Again, the data are plotted in arbitrary units because we want to focus first on the signs of the slopes. We can see that between 120K and 160K, in the transvserve configuration for the measurement, the signs of ξ_{DL} and $\xi_{FL'}$ are the same. In this configuration, only the SHE spin current is generated and sensed, and so its sign is consistent with the lineshape analysis. In the parallel configuration at 15K and at 300K, both the SHE and SAHE spin currents are emitted, and our results show that the SAHE spin contribution to the DL torque is opposite to and dominant over the SHE DL torque. Figure 5.15(b) and (c) shows the evolution of the efficiency of the DL torque and the FL' torque obtained from the DC bias technique as a function of the temperature. **The results obtained with the DC bias technique are congruent with the results obtained with the lineshape analysis and show that the damping-like torque with the SHE symmetry is unchanged over T_M. Therefore the generation of the associated spin current is not related to the magnetic state of GdFeCo. In addition, the DL torque with SAHE symmetry has an opposite sign to and dominates the DL torque with SHE symmetry. The SAHE DL torque has the same sign over T_M, emphasizing that the SAHE spin current generation is related to the magnetization of GdFeCo and not to a specific sublattice**.

Looking at the evolution of the SHE damping-like torque as a function of the temperature (Figure 5.15(b)), we can see that the efficiency is maximum near the compensation

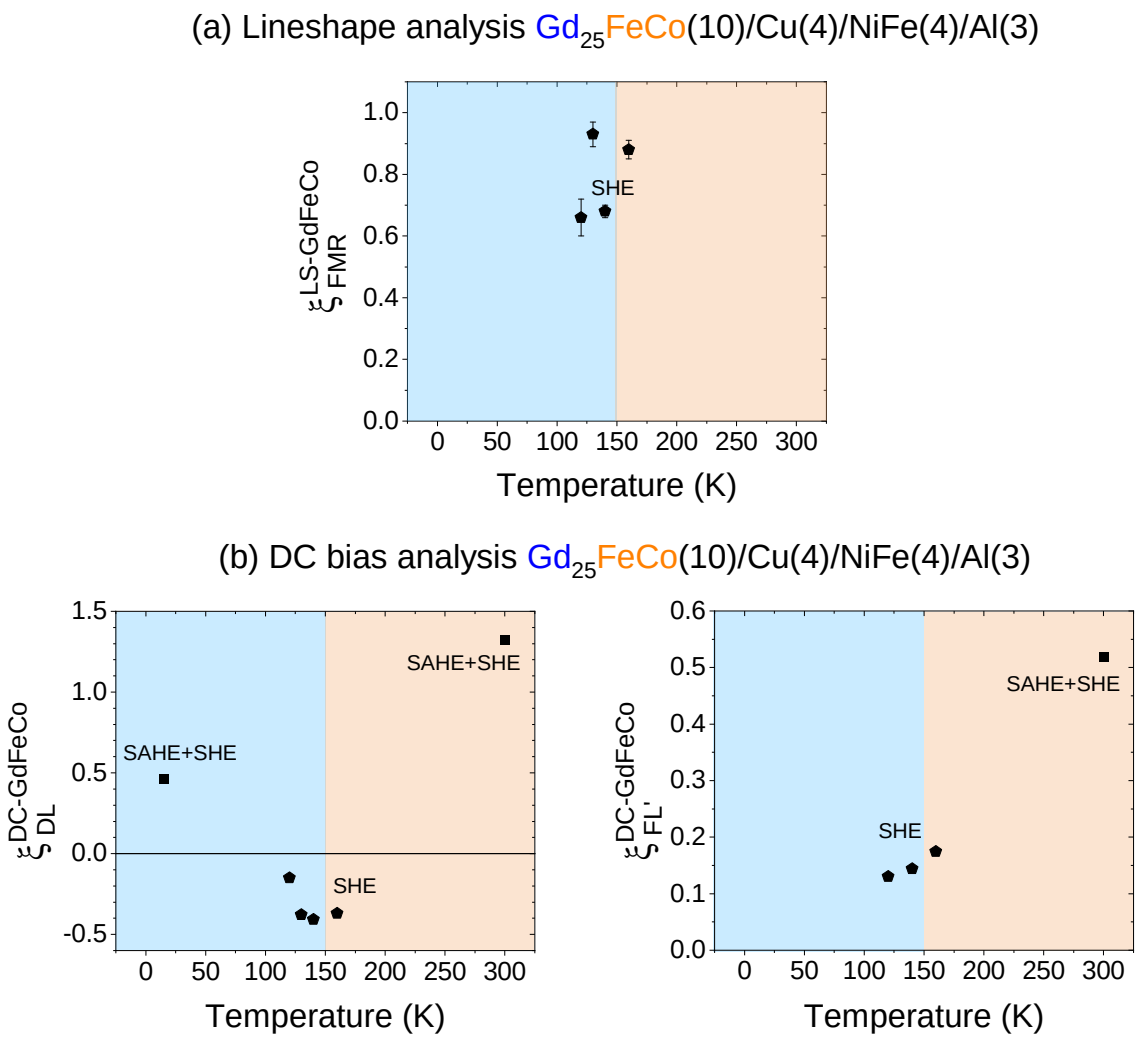

Figure 5.15: (a) Evolution of the total efficiency extracted from the lineshape analysis ξ_{FMR}^{tot-LS} as a function of the temperature. (b) Evolution of the damping-like efficiency extracted from the modulation of the linewidth $\xi_{DL}^{DC-GdFeCo}$ as a function of the temperature. (c) Evolution of the field-like efficiency evaluated from the shift of the resonance field $\xi_{FL'}^{DC-GdFeCo}$ as a function of the temperature.

temperature. The damping-like torque results specifically from the absorption of the SHE and SAHE spin currents emitted by GdFeCo in the NiFe layer. Since both the SAHE and SHE spin currents have a projection along the equilibrium position of the magnetization, the associated spin torque can change the damping of NiFe. In Figure 5.16 we show the evolution of the damping-like torque and the damping of NiFe as a function of the temperature. This figure highlights a clear correlation between the damping of NiFe and the damping-like torque efficiency. **The increase of the damping-like torque originating from the SHE spin current generated by GdFeCo can be explained by the longer spin dephasing length in GdFeCo at the compensation. This result is consistent with the observed increase in the spin dephasing length near the compensation composition of GdCo [91]. More spin current can travel outside the ferrimagnet without being absorbed, therefore more spin current can travel towards NiFe and more spin current can be absorbed by NiFe, resulting in a stronger spin torque.**

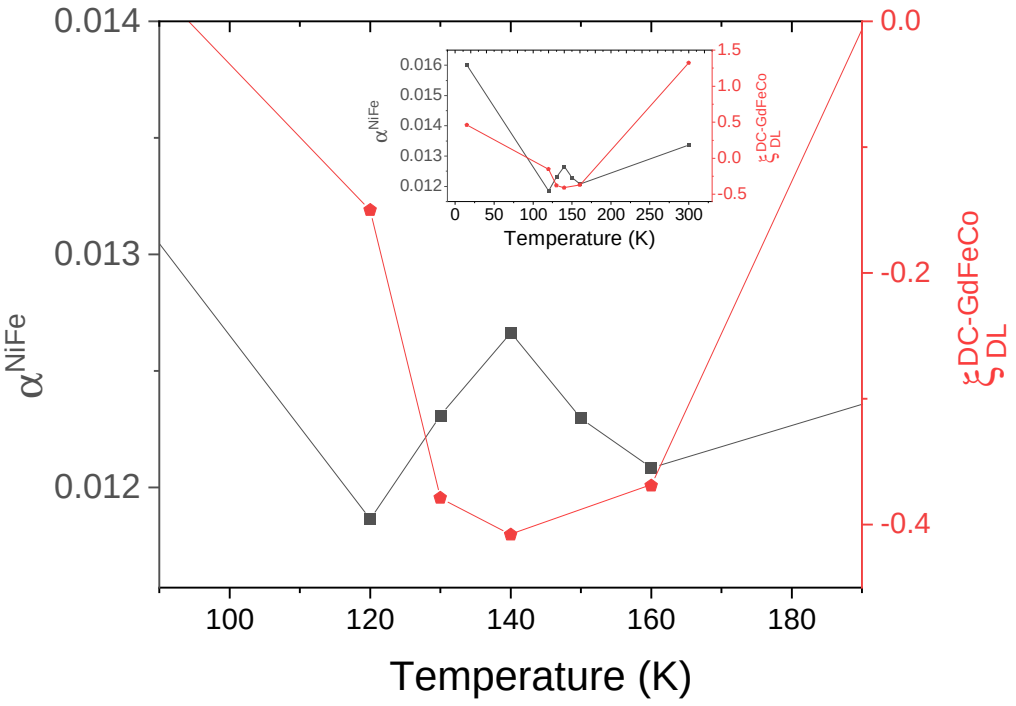

Figure 5.16: Evolution of the damping of NiFe, α^{NiFe}, as a function of the temperature, and evolution of the damping-like efficiency with the SHE symmetry, $\xi_{DL}^{DC-GdFeCo}$, as a function of the temperature. We focus on the temperature range near the compensation $T_M \sim 150K$, and the evolution of both quantities over the full temperature range is shown in the inset.

5.5 Limitations of the experimental study

This experimental study presents limitations that we have already discussed throughout this chapter. Here, we summarize the limiting effects specific to our system and discuss them in more detail.

- Uncertainty on T_M and T_A:
  In this study, T_M is determined in a Hall cross using a weak DC current. Using a 14dBm power in the ST-FMR measurement, the Joule heating can be strong enough to heat the sample above T_M for a lower cryostat temperature. Therefore, for the temperatures of the study around T_M (120K-160K), there is a non-zero possibility that the ferrimagnet is always FeCo-dominant. If we assume that the ferrimagnet is Gd-dominant at 15K with the 14dBm power, then our conclusions still hold because the lineshape analysis shows that the SHE spin current is the same at 15K and 300K. We have highlighted in Chapter 3 that the AMR of GdFeCo is unchanged over its magnetization compensation temperature. Therefore, it is impossible to measure T_M with the ST-FMR device as it is. Another possibility is to design a ST-FMR device where both the longitudinal and transverse voltage can be measured [127], allowing to measure the AHE of GdFeCo which changes its sign over the compensation. The angular compensation T_A is also unknown. It is usually 30 to 50K above T_M, but this temperature can be shifted due to the Joule heating we mentioned above. As a

result, we don't know for sure if the spin current generation has been studied in the temperature range between T_M and T_A.

- Spin-pumping of NiFe:
  In this study, we only considered the spin current emitted by GdFeCo and absorbed by NiFe. However, since the magnetization of NiFe is precessing, it can generate a spin current by spin pumping effect. This spin current can be injected and absorbed into the GdFeCo layer by various effects, resulting in an increase in the damping of NiFe. The spin current can be converted into a charge current in the GdFeCo by an inverse spin Hall effect and contribute to the measured DC voltage. This effect can be corrected using values for the spin diffusion length and spin Hall angle of GdFeCo [133], but is not done in the case of this study.

- Giant Magnetoresistance (GMR):
  As discussed in section 5.2.5, the potential GMR associated with the trilayer would be maximum in the transverse configuration. In this case, the symmetric and antisymmetric parts include both the damping-like and the field-like torques. In Chapter 3, we showed that the sign of the GMR changes over the magnetization compensation of the ferrimagnet. Therefore, if the GMR dominated the signal in our case, we would observe a sign change of the signal over the compensation. In our lineshape analysis, such sign reversal is not observed, but it could also be compensated by a simultaneous sign change of the spin torque. The DC bias technique allows us to address this issue as it allows us to extract the spin torque without relying on magnetoresistive effects. Our results show no sign reversal of the spin torque over the magnetic compensation, and the lineshape analysis is consistent with these results. Therefore, it seems that the GMR does not dominate in our case.

- Thermal effects:
  The anomalous Nernst effect can also contribute to the signals. It can be evaluated from the jump in voltage observed at zero magnetic field. Since this jump is small compared to the resonance peak, we decided to neglect this effect. If this effect were non negligible, it would result in a symmetric contribution to the signal for positive and negative magnetic fields.

5.6 Conclusion

In this chapter, we have applied our model to derive the analytical expressions for the voltage in the case of the lineshape analysis and the DC bias technique. We considered a typical spin current source such as Pt, which generates only a spin current with the SHE symmetry. We presented the corresponding study on an archetypal Pt/NiFe using these techniques.

We then adapted our model to the system of interest: GdFeCo/Cu/NiFe, where the spin current generated by GdFeCo is the sum of the SHE and SAHE symmetries. It follows from our model that the lineshape analysis technique is sensitive only to the SHE spin current, while the DC bias technique is sensitive to the sum of the SAHE and SHE symmetries. We

proposed two measurement configurations: the parallel configuration, where the magnetizations of GdFeCo and NiFe are aligned in the plane and where the spin current generated by GdFeCo is the sum of the SHE and SAHE symmetries, and the transverse configuration where the magnetization of GdFeCo remains out of the plane while the NiFe magnetization is in the plane and where the spin current generated by GdFeCo is only of the SHE symmetry. The transverse configuration allows us to perform the ST-FMR measurements near the magnetization compensation temperature of GdFeCo where the magnetic field provided by our setup is not strong enough to manipulate the magnetization.

The lineshape analysis for the temperatures between 15K and 300K shows that the sign of the DL torque is unchanged over the whole temperature range. In other words, **the SHE spin current generated by GdFeCo is independent of the magnetic state of GdFeCo** and the mechanism at the origin of the generation of the SHE spin current is not related to the magnetization. Indeed, theoritical work suggests that the generation of SHE spin currents in magnetic materials with strong spin-orbit coupling is completely independent of magnetization [114].

The DC bias technique allows to extract either the SHE spin current or the sum of the SHE and SAHE spin currents depending on the orientation of the GdFeCo magnetization. In the transverse configuration, this technique confirms that the SHE spin current is independent of GdFeCo magnetization. At 15K and 300K, **the DL torque with the SAHE symmetry is opposite and dominates over the DL torque with the SHE symmetry. No sign change of the SAHE is observed over the magnetic compensation temperature of GdFeCo, indicating that the SAHE contribution depends on the net magnetization of GdFeCo rather than on a specific sublattice.**

The observed increase in damping-like torque efficiency with the SHE symmetry near the magnetization compensation temperature of GdFeCo is a signature of the larger spin dephasing length of GdFeCo at this point. As a result, more spin current can be ejected from GdFeCo without being absorbed, and more spin current is absorbed by NiFe. We can use this result to tune the efficiency of the spin torque for applications.

As a complement to this study, the same study could be performed on the inverted stack, i.e. SiO_2//$Ni_{81}Fe_{19}(4)$/Cu(4)/$Gd_{25}Fe_{65.6}Co_{9.4}(10)$/Al(3) to verify that the SHE spin current emitted by GdFeCo is a pure spin current. In this case, the torque acting on the NiFe layer should be opposite in sign.

In the next chapter we will focus on the study of self-torque in a quasi-isolated layer of GdFeCo. The self-torque results from the generation of the SHE spin current and its absorption in the layer. Knowing that the generated SHE spin current is unchanged over the magnetization compensation is a first step in understanding the process behind the generation of self-torque.

CHAPTER 6

Spin-orbit torque and self-torque in GdFeCo

The samples were deposited by Prof. Michel Hehn. The TEM characterizations were performed at IJL by Jaafar Ghanbaja, and the samples for TEM were prepared by either Sylvie Migot or myself. The patterning of the devices was mainly done by myself, using CC Minalor facilities at IJL. All electrical measurements and data analysis were done by myself. The interpretation was discussed with Dr. Sébastien Petit-Watelot, Dr. Juan-Carlos Rojas-Sanchez and myself. The results on the self-torque in GdFeCo/Cu have been published in Advanced Materials in 2021 [74].

Spin-polarized currents and pure spin currents can be used to generate a spin torque on a magnetic layer. For the purposes of this chapter, we will distinguish between two types of spin torque: external spin-orbit torque (SOT), when the spin current is generated outside the magnetic layer -for example in a heavy metal (HM)-, and self-torque, when the spin current is generated and absorbed in the same layer. The main idea of this chapter is to report the behavior of external SOT and self-torque over the magnetic and angular compensation temperatures of GdFeCo ferrimagnet. For this purpose, we will study a GdFeCo/Pt bilayer, where the torque source is external, and a GdFeCo/Cu bilayer, where the torque source is internal.

We first introduce the second harmonic technique, which allows to determine the sign and intensity of the spin torques acting on a magnetization. We extend the model derived in Chapter 4 to obtain the analytical expressions for the voltage in our measurement configuration. The measurements are performed over a wide temperature range so that we can discuss the evolution of the external SOT and the self-torque over the magnetization compensation temperature. We will see that the results raise some questions and contradictions that we will try to resolve by studying the dynamics of the two magnetic sublattices of GdFeCo under the action of a torque.

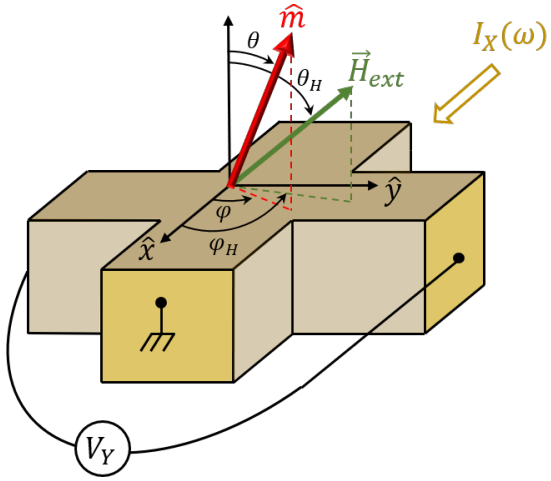

Figure 6.1: Illustration of a Hall cross for the second harmonic technique. An AC current $I_X(\omega)$ is applied along $\hat{x}$ and the Hall voltage V_Y is measured along $\hat{y}$. The magnetization and the external magnetic field positions are described by the angles (θ,φ) and (θ_H,φ_H) respectively.

6.1 Second harmonic technique for spin torque characterization

The second harmonic technique consists of recording the first and second harmonics of the Hall voltage while a harmonic current-induced spin-orbit torque acts on the magnetization. As we derived in Chapter 4, the first harmonic senses the equilibrium position of the magnetization (see Eq.(4.20b)), while the second harmonic contains its dynamics induced by the spin torque (see Eq.(4.21b)). The idea of the technique is to compare the two harmonics to determine the extent to which the magnetization dynamics are affected, thereby quantifying the spin torque.

The second harmonic technique is fully equivalent to the ST-FMR technique in the sense that both techniques measure the magnetization dynamics induced by a spin torque by means of magnetoresistive effects. The main difference lies in the frequency used for the electrical excitation ω compared to the resonance frequency of the material ω_0: tens of Hz for the second harmonic technique, i.e. $\omega \ll \omega_0$, and tens of GHz for the ST-FMR technique, i.e. $\omega \approx \omega_0$, which require different electronic equipment and different patterns for the device. In this sense, the second harmonic technique is more popular and used to characterize SOT because it requires more common equipment.

A typical Hall cross is illustrated in Figure 6.1, where the alternating current $I_X(\omega)$ is applied along $\hat{x}$ and the transverse voltage V_Y is measured along $\hat{y}$. The magnetization position is defined by the angles (θ,φ) and is controlled by an external magnetic field. To characterize the DL and FL contributions to the spin torque, the magnetic field position can be fixed in the plane of the sample and its amplitude swept, or the field can be rotated in certain planes of the sample with a fixed amplitude. The latter configuration has the great advantage of distinguishing more precisely between spin torque and thermal effects, since their contributions to the voltage have different angular dependencies. At the beginning of my thesis work, we did not have the equipment to rotate the sample or the field for different temperatures, so most of the measurements shown in this thesis were performed with a sweeping magnetic field applied in the plane of the sample.

In the following sections, we will derive the analytical expressions for the Hall voltage

when the magnetic field is applied in the plane of the sample.

6.1.1 Measurements configurations and geometry of the exciting field

Let us first consider different configurations for the measurements related to the different projections of the magnetic field in the plane, as shown in Figure 6.2. We define:

$$\begin{cases} H_x = H_{ext}\cos(\varphi_H) & \text{when} \quad \varphi_H = 0[\pi], \\ H_y = H_{ext}\sin(\varphi_H) & \text{when} \quad \varphi_H = \dfrac{\pi}{2}[\pi], \end{cases} \tag{6.1}$$

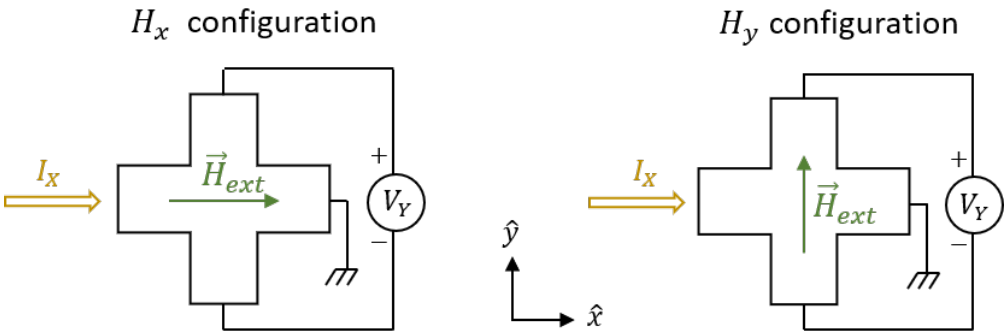

Figure 6.2: Illustration of the H_x and H_y configurations. In the H_x configuration, the magnetic field and current are along $\hat{x}$, while in the H_y configuration, the magnetic field is transverse to the current along $\hat{y}$.

The geometry of the excitation field was derived in Chapter 4 in section 4.4.2. Considering that the magnetic field can be applied along the $\hat{x}$ axis ($\varphi_H = 0[\pi]$) or along the $\hat{y}$ axis ($\varphi_H = \dfrac{\pi}{2}[\pi]$):

- For $\varphi_H = 0[\pi]$:

$$\delta h_\theta = -h_{DL}\cos(\varphi_H), \tag{6.2a}$$
$$\delta h_\varphi = h'_{FL}\cos(\varphi_H). \tag{6.2b}$$

- For $\varphi_H = \dfrac{\pi}{2}[\pi]$:

$$\delta h_\theta = h'_{FL}\cos(\theta_0)\sin(\varphi_H), \tag{6.3a}$$
$$\delta h_\varphi = h_{DL}\cos(\theta_0)\sin(\varphi_H). \tag{6.3b}$$

6.1.2 Analytical expression for the Hall voltage

The second harmonic technique is performed by applying an external magnetic field in the plane of the sample, i.e. $\theta_H = \dfrac{\pi}{2}$. The excitation frequency is much lower than the resonance frequency, i.e. $\omega \ll \omega_0$, and the Gilbert damping can be neglected, i.e. $\alpha \ll 1$. The expression of the susceptibility matrix is therefore simplified and has been derived in Chapter 4 in Section 4.2.

Considering the expressions for the equilibrium position of the magnetization Eq.(4.39), we can derive the first harmonic of the Hall voltage from Eq.(4.20b):

$$\begin{cases} V_Y^{1\omega} = I_X \left[\text{sign}(\cos(\theta_0)) \Delta R^{AHE} \sqrt{1 - \left(\frac{H_{ext}}{H_K}\right)^2} + \Delta R^{PHE} \left(\frac{H_{ext}}{H_K}\right)^2 \sin(2\varphi_H) \right] & \text{if } |H_{ext}| \leq H_K, \\ V_Y^{1\omega} = I_X \left[\Delta R^{PHE} \sin(2\varphi_H) \right] & \text{if } |H_{ext}| \geq H_K, \end{cases}$$

where

$$\begin{cases} \text{sign}(\cos(\theta)) = +1 \quad \text{if} \quad \theta \in [0, \frac{\pi}{2}[\quad \text{i.e for the} + M_z \text{ state.} \\ \text{sign}(\cos(\theta)) = -1 \quad \text{if} \quad \theta \in]\frac{\pi}{2}, \pi] \quad \text{i.e for the} - M_z \text{ state.} \end{cases} \tag{6.4}$$

The expression reduces to the same expression in the H_x and H_y configurations:

$$\begin{cases} V_Y^{1\omega} = I_X \left[\text{sign}(\cos(\theta_0)) \Delta R^{AHE} \sqrt{1 - \left(\frac{H_{ext}}{H_K}\right)^2} \right] & \text{if } |H_{ext}| \leq H_K, \\ V_Y^{1\omega} = 0 & \text{if } |H_{ext}| \geq H_K, \end{cases} \tag{6.5}$$

Considering the expressions for the derivatives of the magnetic energy density Eq.(4.40), the expression for the susceptibility matrix Eq.(4.46) and (4.47), and the expression for the excitation fields Eq.(6.2) and (6.3), we can derive the second harmonic from Eq.(4.23):

- In H_x configuration:

$$\begin{cases} V_Y^{2\omega} = \frac{I_X}{2} \left[\Delta R^{AHE} \frac{H_x}{H_K^2 - H_x^2} h_{DL} + 2\Delta R^{PHE} \frac{H_x}{H_K^2} h'_{FL} \right] & \text{if } |H_x| \leq H_K, \\ V_Y^{2\omega} = \frac{I_X}{2} \left[\Delta R^{AHE} h_{DL} \frac{1}{H_x \left(1 - \frac{H_K}{|H_x|}\right)} + 2\Delta R^{PHE} \frac{1}{H_x} h'_{FL} \right] & \text{if } |H_x| \geq H_K, \end{cases}$$

- In H_y configuration:

$$\begin{cases} V_Y^{2\omega} = \frac{-I_X}{2} \text{sign}(\cos(\theta_0)) \left[\Delta R^{AHE} \sqrt{\frac{1}{H_K^2 - H_y^2}} \frac{H_y}{H_K} h'_{FL} \right. \\ \qquad \left. + 2\Delta R^{PHE} \sqrt{1 - \left(\frac{H_y}{H_K}\right)^2} \frac{H_y}{H_K^2} h_{DL} \right] & \text{if } |H_y| \leq H_K, \\ V_Y^{2\omega} = 0 & \text{if } |H_y| \geq H_K. \end{cases}$$

It can be seen that at low magnetic fields, the second harmonic of the Hall voltages is linear. This can be emphasized by a linearization. We obtain that:

- In H_x configuration:

$$V_Y^{2\omega} = \frac{I_X}{2}\left[h_{DL}\Delta R^{AHE}\frac{H_x}{H_K^2}\left(1+\frac{H_x^2}{H_K^2}\right) + 2h'_{FL}\Delta R^{PHE}\frac{H_x}{H_K^2}\right] \tag{6.6}$$

- In H_y configuration:

$$V_Y^{2\omega} = \frac{I_X \text{sign}(\cos(\theta_0))}{2}\left[-h'_{FL}\Delta R^{AHE}\frac{H_y}{H_K^2}\left(1+\frac{1}{2}\frac{H_y^2}{H_K^2}\right) - 2h_{DL}\Delta R^{PHE}\frac{H_y}{H_K^2}\left(1-\frac{1}{2}\frac{H_y^2}{H_K^2}\right)\right] \tag{6.7}$$

Let us derive the above expressions:

$$\partial_{H_x} V_Y^{2\omega} = \frac{I_X}{2H_K^2}\left[\Delta R^{AHE}h_{DL} + 2\Delta R^{PHE}h'_{FL}\right] \qquad \text{in the } H_x \text{ configuration,}$$

$$\partial_{H_y} V_Y^{2\omega} = -\frac{I_X}{2H_K^2}\text{sign}(\cos(\theta_0))\left[\Delta R^{AHE}h'_{FL} + 2\Delta R^{PHE}h_{DL}\right] \qquad \text{in the } H_y \text{ configuration.}$$

It can be seen that the contribution from the DL effective field also gives a cubic contribution. Doing the same process for the first harmonic, it comes:

$$V_Y^{1\omega} = I_X \text{sign}(\cos(\theta_0))\Delta R^{AHE}\left(1-\frac{1}{2}\frac{H_{x,y}^2}{H_K^2}\right) \tag{6.8}$$

and the second derivative of the latter expression is:

$$\partial^2_{H_{x,y}} V_Y^{1\omega} = -I_X \text{sign}(\cos(\theta_0))\Delta R^{AHE}\frac{1}{H_K^2} \tag{6.9}$$

It is obtained by taking the ratio between the first and second derivatives of the various harmonics that:

$$\begin{aligned} h_{DL} &= -\frac{2}{1-4\xi^2}\left(\text{sign}(\cos(\theta_0))\frac{\partial_{H_x}V_Y^{2\omega}}{\partial^2_{H_x}V_Y^{1\omega}} + 2\xi\frac{\partial_{H_Y}V_{XY}^{2\omega}}{\partial^2_{H_x}V_{XY}^{1\omega}}\right), \\ h'_{FL} &= \frac{2}{1-4\xi^2}\left(\frac{\partial_{H_y}V_Y^{2\omega}}{\partial^2_{H_y}V_Y^{1\omega}} + \text{sign}(\cos(\theta_0))2\xi\frac{\partial_{H_x}V_y^{2\omega}}{\partial^2_{H_x}V_Y^{1\omega}}\right), \end{aligned} \tag{6.10}$$

with $\xi = \dfrac{\Delta R^{PHE}}{\Delta R^{AHE}}$. If $\xi << 1$ and if $\Delta R^{PHE}h'_{FL}$ is not too large compared to $\Delta R^{AHE}h_{DL}$, then we can directly write:

$$\begin{aligned} h_{DL} &= 2\text{sign}(\cos(\theta_0))\frac{\partial_{H_x}V_Y^{2\omega}}{\partial^2_{H_x}V_Y^{1\omega}} \qquad \text{en configuration } H_x, \\ h'_{FL} &= 2\frac{\partial_{H_y}V_Y^{2\omega}}{\partial^2_{H_y}V_Y^{1\omega}} \qquad \text{en configuration } H_y. \end{aligned} \tag{6.11}$$

Therefore, the intensity of the effective fields can be directly extracted from the measurements of the first and second harmonics of the Hall voltage. We only need to extract the linear part of the second harmonic signal and divide it by the quadratic coefficient of the first harmonic. In other words, this process consists of comparing the strength of the dynamics with

respect to the equilibrium position. The simplicity with which the torque can be extracted is the great strength of this technique, making it a popular choice for torque extraction. It should be noted, however, that this relationship is only valid if $\Delta R^{PHE} h'_{FL} \ll \Delta R^{AHE} h_{DL}$, but especially when thermal effects are negligible. In fact, as we will discuss in the next subsection, one of the thermal contributions has the same field dependence as the effective fields, so the extraction of the effective field by the ratio will inevitably be incorrect.

6.1.3 Thermal contribution in the Hall voltage

We consider the expression of the transverse voltage induced by thermal effects as derived in Chapter 4 (see Eq.(4.28)).

- In configuration H_x:

  The thermal contribution to the Hall voltage $V_{Y_{th}}^{2\omega}$ in the limit of a weak external magnetic field:

$$V_{Y_{th}}^{2\omega} = R_{th} I_X^2 + R_{ARLth} I_X^2 \left[\text{sign}(\cos(\theta)) \left(1 - \frac{1}{2} \frac{H_x^2}{H_K^2} \right) - \frac{H_x}{H_K} \right]. \tag{6.12}$$

- In configuration H_y: The thermal contribution to the Hall voltage $V_{Y_{th}}^{2\omega}$ in the low-field approximation is given by:

$$\begin{aligned} V_{Y_{th}}^{2\omega} = R_{th} I_X^2 + \Delta R_{\parallel th} I_X^2 \left[\frac{H_y^2}{H_K^2} + \text{sign}(\cos(\theta)) \left(\frac{H_y}{H_K} - \frac{1}{2} \frac{H_y^3}{H_K^3} \right) \right] \\ + R_{ARLth} I_X^2 \left[\text{sign}(\cos(\theta)) \left(1 - \frac{1}{2} \frac{H_y^2}{H_K^2} \right) \right] \end{aligned} \tag{6.13}$$

6.1.4 Full analytical expression for the Hall voltage

- In H_x configuration:

$$\boxed{\begin{aligned} V_Y^{2\omega} = \frac{I_X}{2} \left[h_{DL} \Delta R^{AHE} \frac{H_x}{H_K^2} \left(1 + \frac{H_x^2}{H_K^2} \right) + 2 h'_{FL} \Delta R^{PHE} \frac{H_x}{H_K^2} \right] \\ + \frac{C I_X}{2} + \frac{I_X}{2} \left[\text{sign}(\cos(\theta)) \, C_{ip} \left(1 - \frac{1}{2} \frac{H_x^2}{H_K^2} \right) - C_{oop} \frac{H_x}{H_K} \right], \end{aligned}} \tag{6.14}$$

  with $C = R_{th} I_X$, $C_{ip} = R_{ARLth} I_X$ and $C_{oop} = R_{ARLth} I_X$. We can see that in the presence of thermal effects the signal has a magnetization dependent offset C_{ip}, which also contributes to the signal with the square of the magnetic field. This effect can be easily corrected by the offset in the limit where both $+M_z$ and $-M_z$ states are detected during the measurement. However, the thermal effect associated with the out-of-plane thermal gradient C_{oop} contributes linearly with the magnetic field, in the same way as

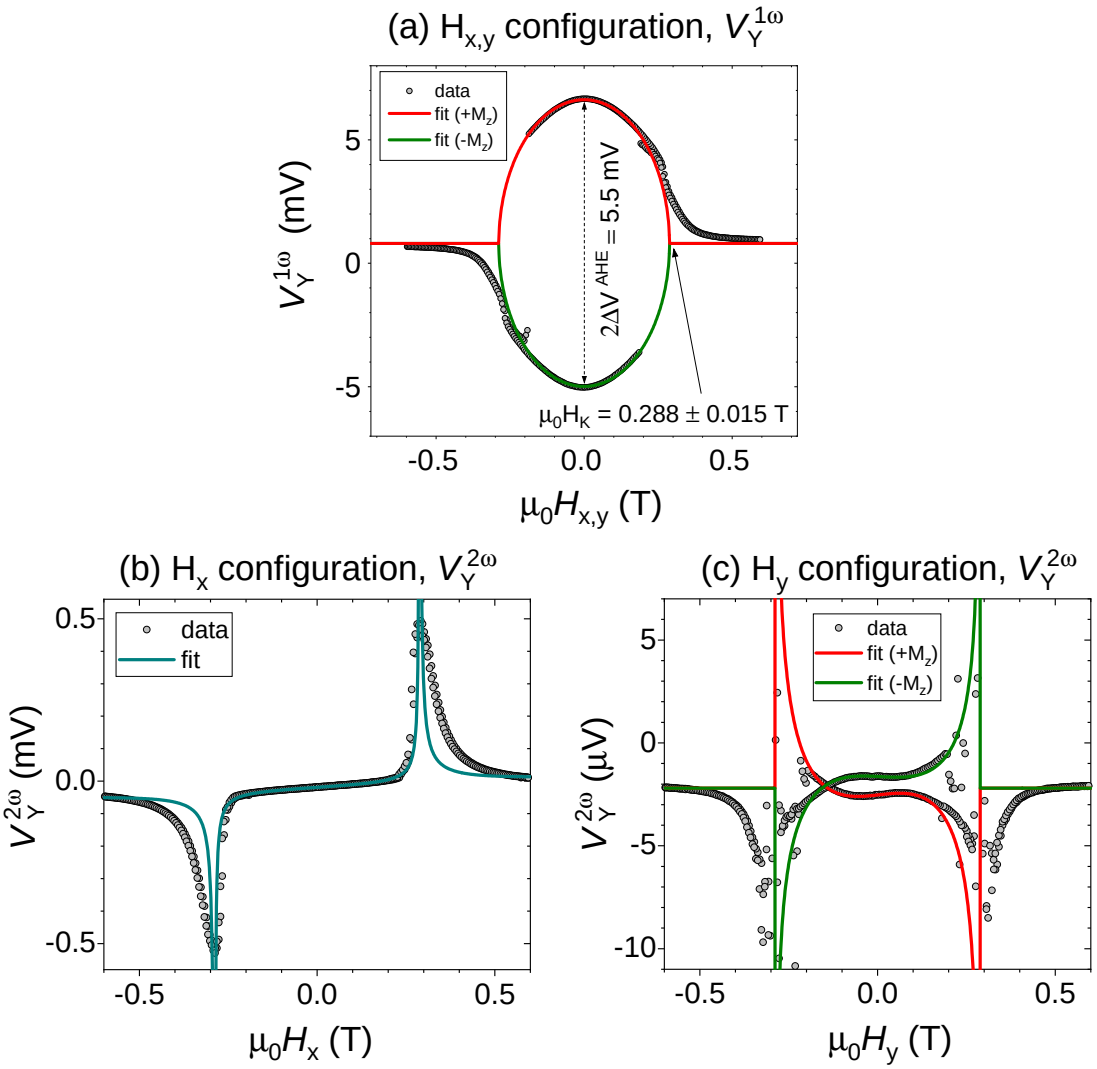

Figure 6.3: (a) Experimental data $V_Y^{2\omega}$ in the H_x configuration and analytical fit. We fix the parameters $\Delta V^{AHE} = -5.5$ mV and $\mu_0 H_K = 0.2882$ T. The fit describes the overall shape of the signal well and is particularly good for the low-field experimental data. (b) Experimental data $V_Y^{2\omega}$ in the H_y configuration and analytical fit using $\Delta V^{AHE} = -5.5$ mV, $\mu_0 H_K = 0.2882$ T. The analytical curve describes the overall shape of the signal well and is particularly good at matching the low-field experimental data.

the effective fields. In the case of $\Delta R^{PHE} h'_{FL} \ll \Delta R^{AHE} h_{DL}$, which is our case, we fit our data by Eq.(6.14) and include the cubic behavior of h_{DL} at higher magnetic fields. This fit is done for data far from the compensation temperature. The value for the thermal effect is then fixed constant with the temperature. In fact, if this parameter is left free, the fit leads to an incorrect value for the torque.

- In H_y configuration:

$$
\begin{aligned}
V_Y^{2\omega} = & \frac{I_X \cos(\theta_0)}{2}\left[-h'_{FL}\Delta R^{AHE}\frac{H_y}{H_K^2}\left(1+\frac{1}{2}\frac{H_y^2}{H_K^2}\right) - 2h_{DL}\Delta R^{PHE}\frac{H_y}{H_K^2}\left(1-\frac{1}{2}\frac{H_y^2}{H_K^2}\right)\right] \\
& + \frac{CI_X}{2} + \frac{I_X}{2}\left[D_{ip}\frac{H_y^2}{H_K^2} + \text{sign}(\cos(\theta))\, D_{oop}\left(\frac{H_y}{H_K} - \frac{1}{2}\frac{H_y^3}{H_K^3}\right)\right] \\
& + \left[\text{sign}(\cos(\theta))\, C_{ip}\left(1-\frac{1}{2}\frac{H_y^2}{H_K^2}\right)\right],
\end{aligned}
\tag{6.15}
$$

with $C = R_{th}I_X$, $C_{ip} = R_{ARLth}I_X$, $C_{oop} = R_{ARLth}I_X$, $D_{ip} = \Delta R_{\parallel th}I_X$ and $D_{oop} = \Delta R_{\parallel th}I_X$. Similar to the previous configuration, C_{ip} can be easily extracted from the magnetization dependent offset of the signal. D_{ip} is the only parameter that is even with the magnetic field, so it can be extracted by decomposing the signal into an even and an odd signal. Otherwise, separating the thermal effects from the effective fields is very difficult.

6.2 Spin-orbit torque in GdFeCo/Pt bilayer

SOT are studied in a $Gd_{24.8}$FeCo(10)/Pt(2)/Al(3) bilayer. We assume that the self-torque contribution in the ferrimagnet is negligible compared to the SOT induced by the SHE in Pt.

6.2.1 Characterization of the GdFeCo/Pt bilayer

The magnetization compensation temperature of GdFeCo in this sample was determined by measuring the first harmonic of the Hall voltage while applying a magnetic field along $\hat{z}$ for different temperatures. An AC current $i_{AC} = 4$mA was applied for these measurements, and the same current value is used for the SOT measurements to avoid any shift in the compensation temperature due to Joule heating. Figure 6.4(a) shows the resulting evolution of the transversal resistance. We estimate $T_M \in 200K - 210$K, as indicated by the polarity reversal of the hysteresis loop. T_M is further confirmed by the divergence of the coercive field shown in Figure 6.4(b). The amplitude of the AHE is estimated to be $\Delta R^{AHE} \approx \pm 6\Omega$ for the entire temperature range. We can see that between 208K and 212K the magnetization along the easy axis is not fully saturated. This may be due to the gradient of the composition along the thickness, which leads to a gradient of the magnetization and thus a distribution of the compensation temperature.

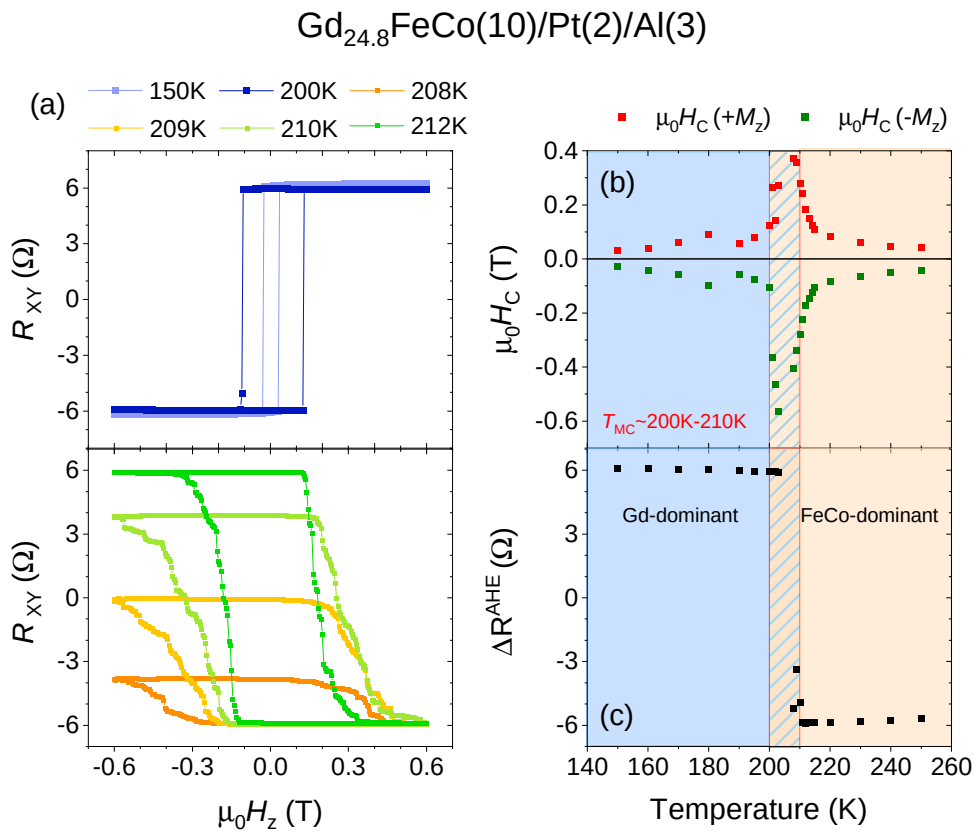

Figure 6.4: Characterization of the $Gd_{24.9}FeCo(10)/Pt(2)$ bilayer for spin-orbit torque measurements. (a) Evolution of the transverse resistance with the external magnetic field applied along $\hat{z}$ for different temperatures. The two resistance states at low magnetic field and the square shape of the hysteresis cycles show that the magnetization is spontaneously out-of-plane. The sign change of the AHE cycle indicates that $T_M \in 200 - 208K$. (b) Evolution of the coercive field H_C with the temperature. H_C diverges near T_M. (c) Evolution of the AHE amplitude ΔR^{AHE} at different temperatures.

6.2.2 Raw data over the magnetization compensation

The measurements of the different harmonics of the Hall voltage are shown in Figure 6.5. The amplitude of the current used is $i_{AC} = 4$mA, and is the same as the current used to determine T_M. Consequently, we can expect $T_M \approx 200 - 208$K.

Magnetization dependent offsets are observed for the different configurations, indicating the presence of thermoelectric contributions. However, from the intensity of the voltages we can see that the thermal effects in the DL configuration can be neglected compared to the SOT contribution. The first harmonic fit allows the extraction of ΔR^{AHE} and H_K, which are needed for the second harmonic fit. Using Eq.(6.14) to extract the damping effective field taking into account the thermal effects, we find that the damping effective field $h_{DL} < 0$ is negative at 160K and 300K. Performing the measurements for a wide range of temperatures, we find that h_{DL} is always negative, regardless of the magnetic state of GdFeCo. The complete evolution of h_{DL} for a wide range of temperatures is summarized in Figure 6.9(a). The sum of the field-like and Oersted fields is determined taking into account the thermal effects

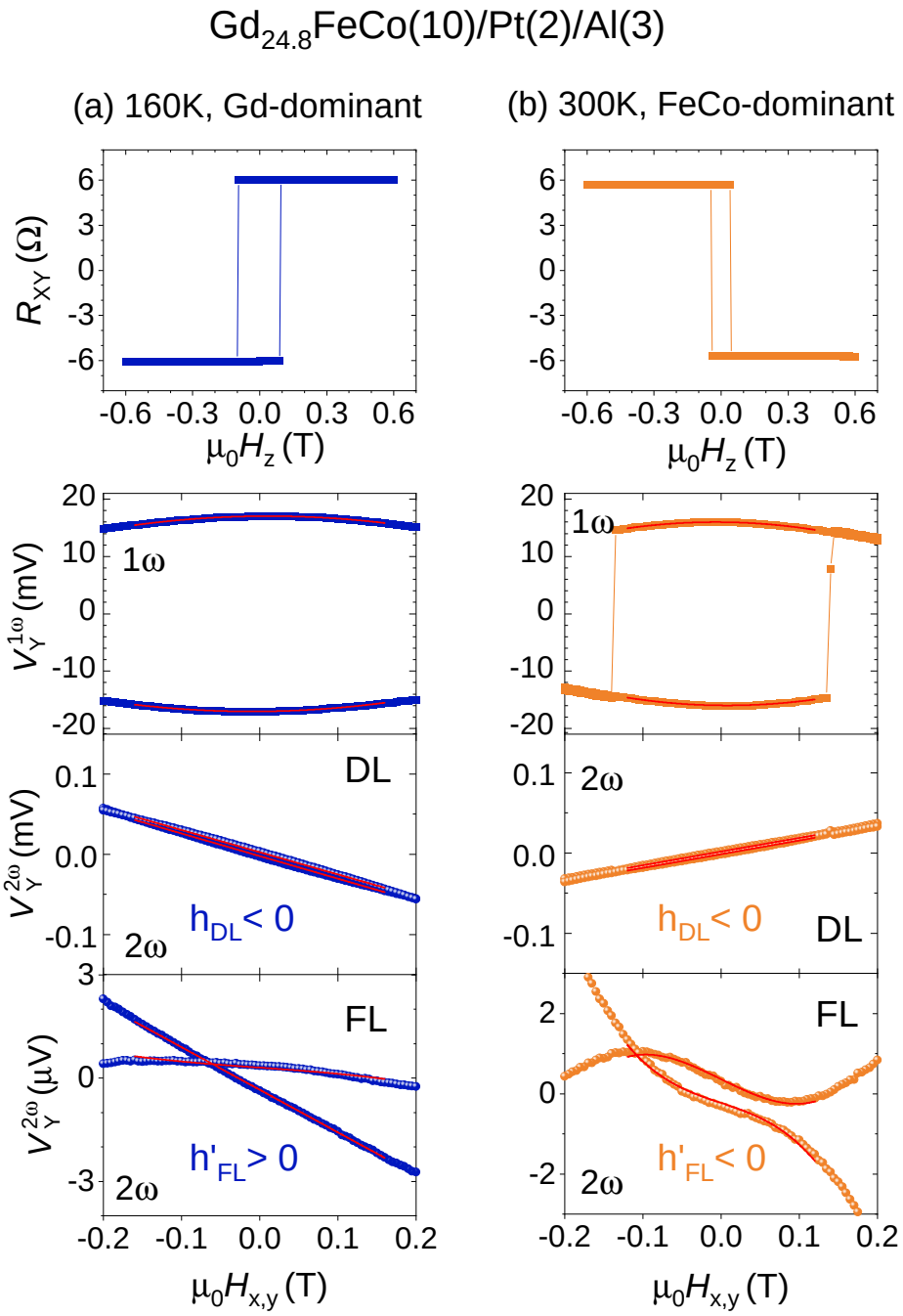

Figure 6.5: Characterization of the spin-orbit torque in $Gd_{24.8}FeCo(10)/Pt(2)/Al(3)$.(a) At 160K, the sign of the hysteresis loop indicates that the ferrimagnet is Gd-dominant. Evolution of the first and second harmonics as a function of the magnetic field in the H_x and H_y configurations. After correcting for thermal effects, $h_{DL} < 0$ and $h'_{FL} > 0$. (b) At 300K, the sign of the hysteresis loop indicates that the ferrimagnet is FeCo-dominant. Evolution of the first and second harmonics as a function of the magnetic field in the H_x and H_y configurations. After correcting for thermal effects, we find that $h_{DL} < 0$ and $h'_{FL} < 0$. Thus, the sign of the DL effective field seems to be unchanged over the magnetic compensation temperature of GdFeCo, while the sign of h'_{FL} is reversed.

using Eq.(6.15). It turns out that $h'_{FL} > 0$ at 160K when the material is Gd-dominant, and

$h'_{FL} < 0$ at 300K when the material is FeCo-dominant. The evolution of h'_{FL} is shown for the full temperature range in figure 6.9(a). In this system, the Oersted field is positive and aligned along $\hat{y}$, so the negative sign for h'_{FL} indicates that the FL effective field dominates over the Oersted field.

A similar evolution of the DL effective field over the magnetic compensation has been reported several times in the literature. For example, N. Roshewsky *et al.* reported in a similar GdFeCo/HM bilayer that the DL effective field maintains its sign over the magnetization compensation concentration of GdFeCo [65, 134]. The case of the FL effective field is more difficult to interpret, because the correction of the Oersted field can artificially lead to a sign change of the field-like effective field. In the literature, some groups reported that the field-like effective field has the same sign over the magnetic compensation [65, 134], while others reported a sign change of the field-like effective field [135].

6.3 Self-torque in GdFeCo/Cu bilayer

The self-torque is studied in a Gd_{26}FeCo(10)/Cu(2)/Al(3) bilayer. The Cu layer is used to enhance the perpendicular magnetic anisotropy of GdFeCo. Due to the weak spin-orbit coupling, no spin current generation is expected from Cu. Nevertheless, it cannot be excluded that the GdFeCo/Cu interface, together with a bulk contribution, contributes to the SHE spin current and the resulting self-torque. The idea of this study is to characterize the self-torque over T_M.

6.3.1 Characterization of the GdFeCo/Cu bilayer

The magnetization compensation temperature of GdFeCo, T_M, was determined by measuring the first harmonic of the Hall voltage while applying a magnetic field along $\hat{z}$ for different temperatures. An AC current $i_{AC} = 4$mA was applied for these measurements, and the same current value was used for the self-torque measurements. This ensures that T_M is not shifted by Joule heating. Figure 6.6(a) shows the resulting evolution of the transverse resistance with the magnetic field. We estimate $T_M \approx 204 - 205K$, as indicated by the sign reversal of the hysteresis loop. This value is confirmed by the divergence of the coercive field shown in Figure 6.6(b). The anomalous Hall amplitude of the bilayer is estimated for the whole temperature range.

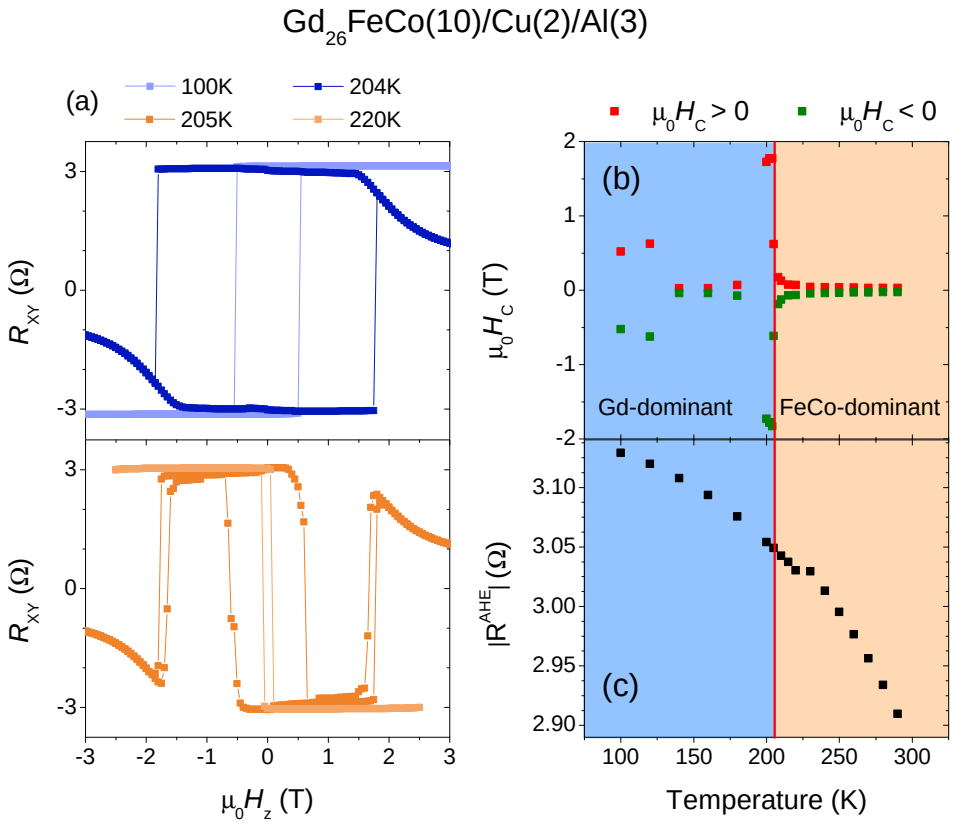

Figure 6.6: Characterization of the $Gd_{26}FeCo(10)/Cu(2)$ bilayer for self-torque measurements. (a) Evolution of the transverse resistance with the external magnetic field applied along $\hat{z}$ for different temperatures. The two resistance states at low magnetic field and the square shape of the hysteresis cycle show that the magnetization is spontaneously out-of-plane. The decrease of the resistance at higher field is the signature of the spin-flop, which was discussed in Chapter 3. The sign change of the AHE cycle indicates that $T_M \approx 204 - 205K$. (b) Evolution of the coercive field H_C with the temperature. H_C diverges near T_M. (c) Estimation of the anomalous Hall angle θ_{AHE} for the bilayer at different temperatures. It comes $\theta_{AHE}^{GdFeCo/Cu} \approx 0.022$.

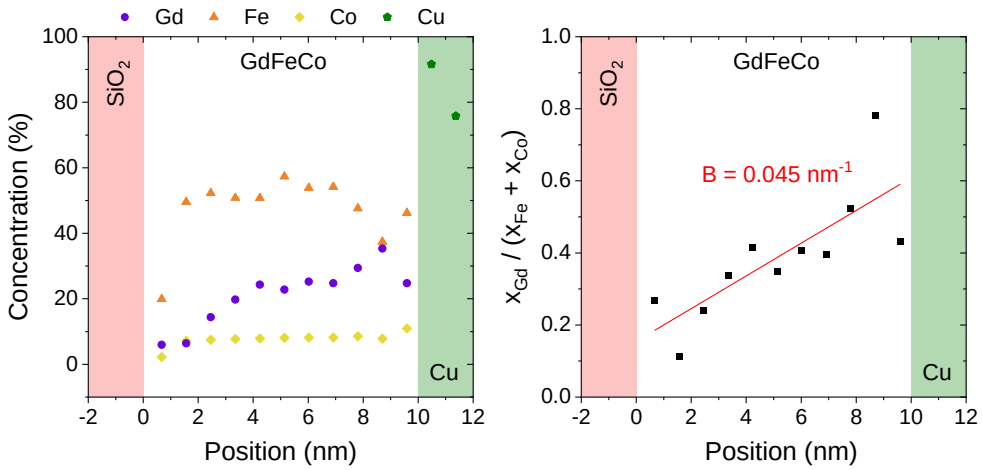

Figure 6.7: Element concentration along the sample thickness obtained by EDS. We estimate the gradient of Gd concentration $B = 0.045$ nm^{-1}.

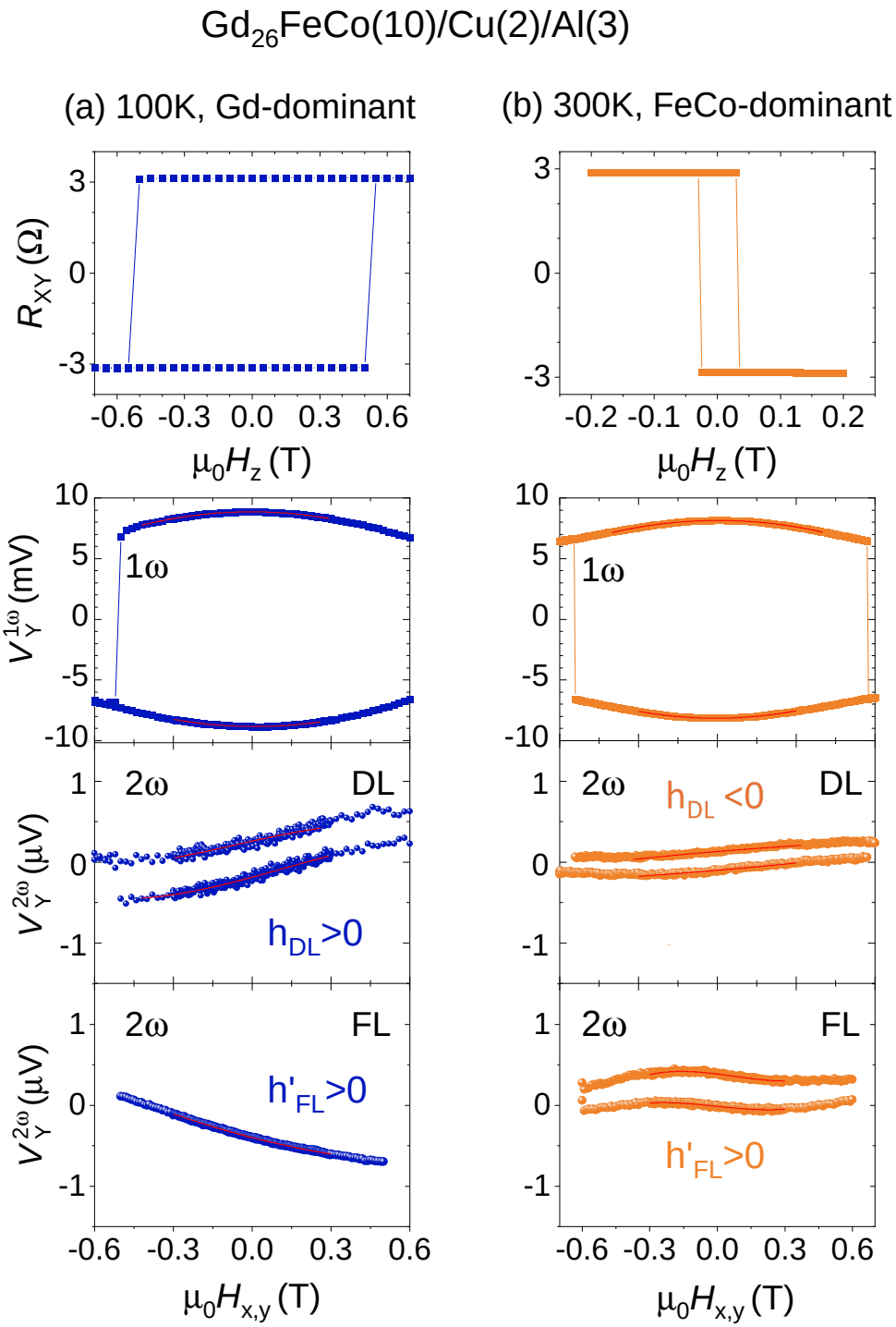

Figure 6.8: Characterization of the self-torque in $Gd_{26}FeCo(10)/Cu(2)/Al(3)$.(a) At 100K, the sign of the hysteresis loop indicates that the ferrimagnet is Gd-dominant. Evolution of the first and second harmonics as a function of the magnetic field in the H_x and H_y configurations. After correcting for thermal effects, $h_{DL} > 0$ and $h'_{FL} > 0$. (b) At 300K, the sign of the hysteresis loop indicates that the ferrimagnet is FeCo-dominant. Evolution of the first and second harmonics as a function of the magnetic field in the H_x and H_y configurations. After correcting for thermal effects, we find that $h_{DL} < 0$ and $h'_{FL} > 0$. Thus, the sign of the DL effective field changes over the magnetization compensation temperature of GdFeCo.

For self-torque to be generated, there should be an imbalance between the spin current generated and the one absorbed, as discussed in Chapter 2. Here we attribute the self-torque to the gradient of Gd concentration along the thickness of the material as determined by EDS characterization. The analysis confirms the inhomogeneous distribution of Gd, Fe and Co along the thickness of the ferrimagnet (see Figure 6.7). We estimate the gradient of Gd concentration to be $B = 0.045$ nm^{-1}.

6.3.2 Raw data over the magnetization compensation

The first and second harmonics of the Hall voltage are plotted as a function of the applied magnetic field amplitude for different temperatures. We chose to work with a rather low magnetic field amplitude (± 0.65 T) because we wanted to focus on the low-field approximation for extracting the torque, but also to avoid spin-flop, which can be obtained with less than 2T near T_M. The amplitude of the current is $i_{AC} = 4$mA, and is the same as the current used to determine T_M in the previous subsection. Consequently, we can expect $T_M \approx 204 - 205$K.

We show measurements at 100K when the material is Gd-dominant (see Figure 6.8(a)) and at 300K when the ferrimagnet is FeCo-dominant (see Figure 6.8(b)). We can see offsets in the second harmonic signals in the different configurations, indicating a non-negligible thermal contribution to the signal. These effects are carefully taken into account in the extraction of the effective fields. The first harmonic is fitted by a parabola and allows the extraction of the amplitudes of ΔR^{AHE} and H_K needed to fit the second harmonic. **From our analysis we see that the damping-like effective field changes sign over T_M, and the sum of the field-like and Oersted fields changes sign twice, first at the magnetization compensation temperature and then at 205K.** The complete evolution of h_{DL} and h'_{FL} in the case of self-torque is summarized in Figure 6.9(b).

We first reported the sign reversal of h_{DL} over the magnetic compensation of GdFeCo in 2021 [74], and we reported this sign change as a specific signature of self-torque.

Shortly after our publication, a study of the self-torque in GdFeCo(5)/Al at different temperatures was published by S. Krishnia *et al.*. [136]. In the study, h_{DL} was not extracted at low field, but at the anisotropic field H_K, where only the torque contribution diverges. This method for extracting the torque, or discussing the sign of the torque, seems more robust than the fit at low field where thermal effects can dominate. Their results show that h_{DL} is unchanged over $T - T_{MC} = \pm\,[20 - 60]$K. Unfortunately, we cannot apply this method of extracting the torque to our data, since we applied the magnetic field only up to ± 0.67 T, and H_K is estimated to be at least 0.9 T even far from T_M. Two hypotheses arise from this study: 1) our data analysis at low magnetic fields leads to incorrect results, or 2) the sign change of h_{DL} is missed near T_M, but since H_K diverges at this point, it seems difficult to extract the torques.

In 2022, Q. Liu *et al.* reported a concentration study of the self-torque in FeTb by angular dependence measurements [137]. They show that h_{DL} encounters two signal reversals,

first at the angular compensation concentration and then at the magnetization compensation concentration. Their explanation for the double sign reversal of h_{DL} is based on the double sign reversal of the effective gyromagnetic ratio of ferrimagnets. Before attempting to compare our results with theirs, we must ask whether a concentration study is equivalent to a temperature study. In the case of a concentration study, each sample has different magnetic properties and the spin current generation and absorption may differ from one sample to another. In fact, we have shown in GdFeCo that the anomalous Hall effect generation can be dominated by the Gd sublattice for a concentration of 30% (section 3.4.2), while FeCo dominates the generation of the AHE for lower concentrations of Gd. The generation of the AHE and the generation of the SHE are actually described by the same microscopic mechanisms (section 1.2.2), so by doing a concentration study, the spin current generation can be drastically different from one sample to another because of the change in the relative concentrations of Gd and FeCo. In addition, we have shown that the sublattice that dominates the AHE is unchanged by temperature. Therefore, by performing a temperature study, we can assume that the spin current generation mechanism is unchanged over the entire temperature range, and that changing the temperature only allows for a change in the magnetization and dynamics of the magnetization.

6.4 A fundamental difference between self-torque and SOT ?

Figures 6.9(a) and (b) summarize the evolution of the damping-like and total field-like effective fields as a function of the temperature for the case of GdFeCo/Pt and for the case of GdFeCo/Cu. We recall that in the case of GdFeCo/Pt the spin-orbit torque is attributed to the spin current from Pt, while in the case of GdFeCo/Cu we assume that the spin current is generated in GdFeCo and absorbed in the same layer. Therefore, we can draw the following conclusion from our results: **the spin torque effective fields acting on GdFeCo magnetization seem to have a different signature over magnetization compensation temperature depending on the source of the spin current. If it is external (case of SOT), then the sign of h_{DL} is the same over the whole temperature range of GdFeCo. If it is internal (case of self-torque), then h_{DL} changes its sign at the magnetization compensation temperature**. For the case of the field-like effective field no clear conclusion can be drawn because of the contribution of the Oersted field in h'_{FL}.

From the evolution of the effective fields with the temperature, we can approximate the evolution of the associated torques by defining $\tau_{DL,FL'} \propto h_{DL,FL'}/H_K$. These torques are represented in Figure 6.10.

Let us recall the results obtained with the ST-FMR technique. We have shown that the SHE spin current generated by GdFeCo is independent of the magnetic state of GdFeCo over a wide temperature range that includes the magnetization compensation temperature T_M and usually the angular compensation temperature T_A, which is about 50K to 100K above T_M. Thus, **our results suggest that the sign reversal of the damping-like self-torque is not related to a change in the SHE spin current generation, but rather to the dynamics of the ferrimagnet during the spin current absorption process**. Our first intuition was

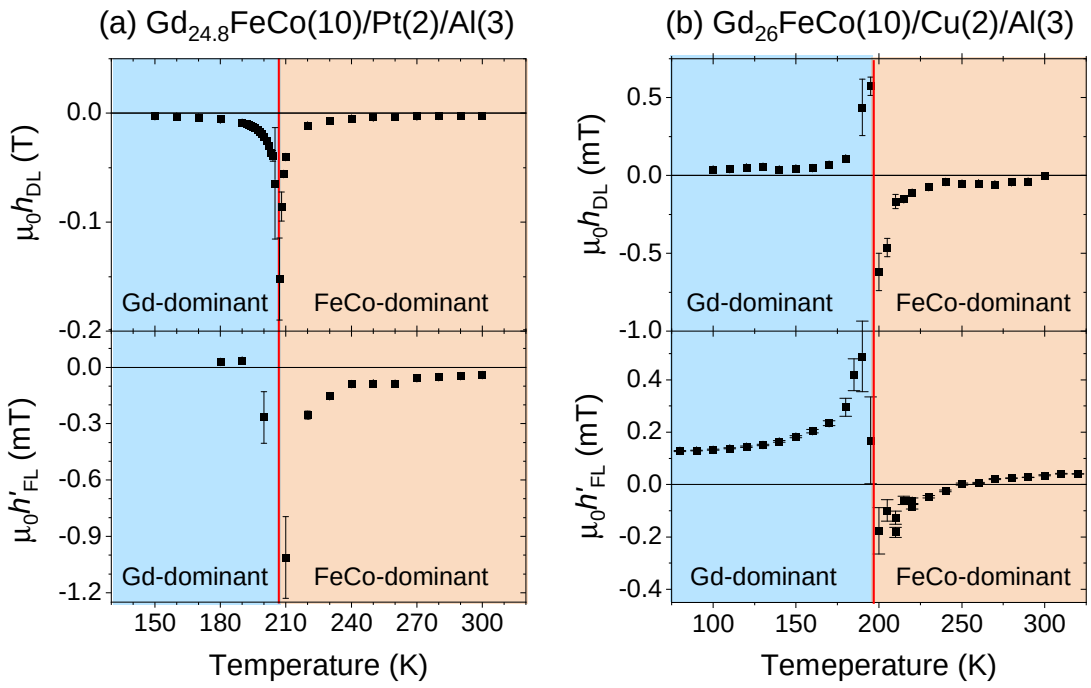

Figure 6.9: Evolution of SOT (a) and self-torque (b) as a function of temperature, where the background color change corresponds to the magnetization compensation temperature of GdFeCo. (a) For $Gd_{24.8}FeCo(10)/Pt(2)/Al(3)$. It turns out that h_{DL} has the same sign over T_M and h'_{FL} has the opposite sign over T_M. (b) For $Gd_{26}FeCo(10)/Cu(2)/Al(3)$. It turns out that h_{DL} has a sign reversal over T_M. h'_{FL} shows two sign reversals, first at T_M and then at 250K. We can see that the amplitude of the damping-like self-torque is 100 less than the damping-like SOT with Pt.

that the sign change of the effective gyromagnetic ratio could explain the sign change of the damping-like effective field in the case of self-torque. However, this hypothesis raised an important contradiction: if the sign of the effective field is related to the effective gyromagnetic ratio of GdFeCo, then the effective fields in the case of GdFeCo/Pt should also depend on the effective gyromagnetic ratio, since in fact, regardless of the source of the spin current -internal or external-, the absorption process seems to be the same. Thus, we need to go further in modeling the torque acting on the magnetization of a ferrimagnet to understand the different mechanisms behind the self-torque and SOT signatures. For this purpose, we will derive the Landau-Lifshitz-Gilbert-Slonczewski (LLGS) equation considering both the Gd and FeCo sublattices.

In Chapter 4 section 4.1.1, we showed that the dynamics of the net magnetization of a ferrimagnet is equivalent to the dynamics of the magnetization of a ferromagnet, provided that effective quantities are introduced which can change their sign over the compensation points of the ferrimagnet. These effective quantities are indicated in Figure **??** for the different temperature ranges defined by the magnetic and angular compensation temperatures of GdFeCo. By considering a_j and b_j for both the Gd and FeCo sublattices in the expression of the effective quantities and for the LLGS equation, we imply that a torque can act on both

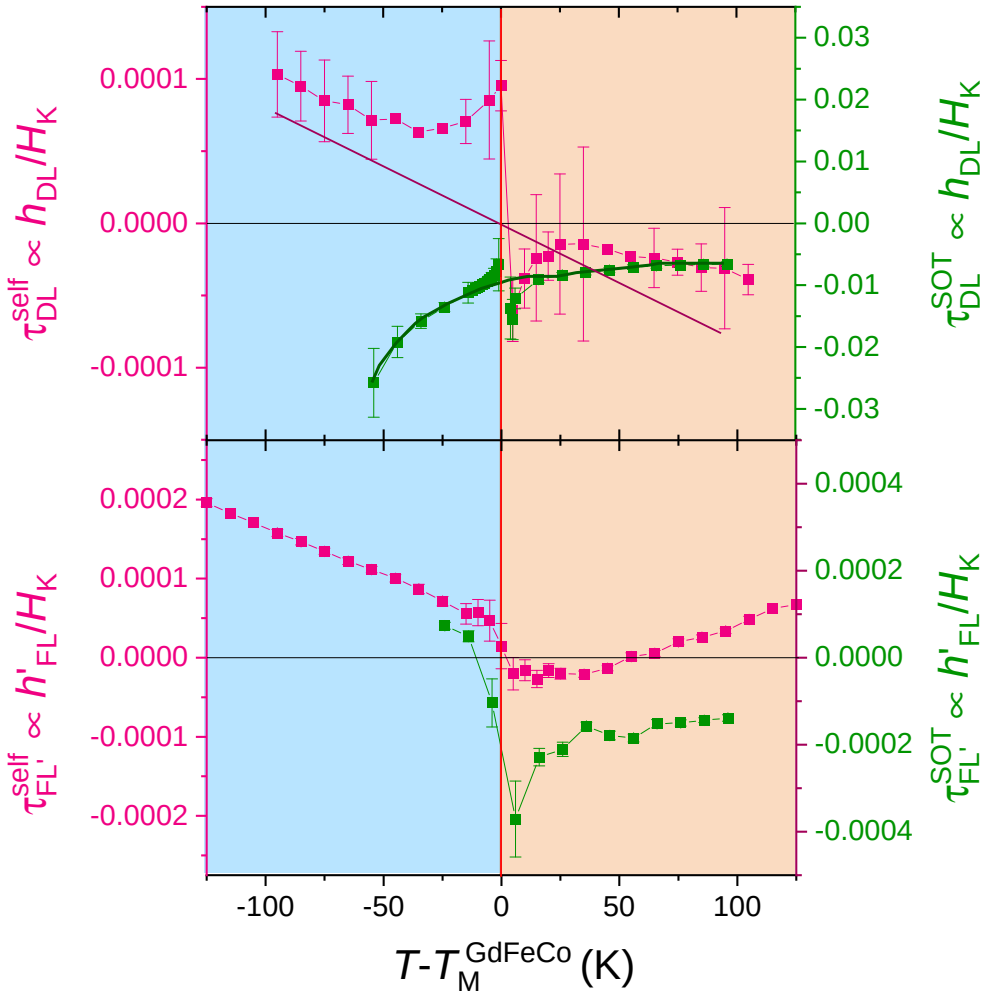

Figure 6.10: Estimation of a damping-like torque $\tau_{DL} = h_{DL}/H_K$ and of a total field-like torque $\tau_{FL'} = h'_{FL}/H_K$ in $Gd_{24.8}FeCo(10)/Pt(2)/Al(3)$ as a function of the temperature. Estimation of the torque in $Gd_{26}FeCo(10)/Cu(2)/Al(3)$ as a function of the temperature.

sublattices.

The idea now is to compare the expressions of the effective torques defined in Figure **??** and to compare them with the torques we have estimated experimentaly in Figure 6.10. The field-like torque is not considered in our model because the mechanism that generates such a torque is more complex than in the case of the damping-like torque. We will consider the case of GdFeCo/Pt and GdFeCo/Cu, where in the first case the spin current comes from outside the ferrimagnet, and in the second case the spin current generation is inside to the ferrimagnet.

6.4.1 Case of the damping-like effective field in GdFeCo/Pt

Let us discuss the case of the damping-like effective field resulting from the absorption of the transverse component of the spin current in a magnetic material. In GdFeCo/Pt, the spin

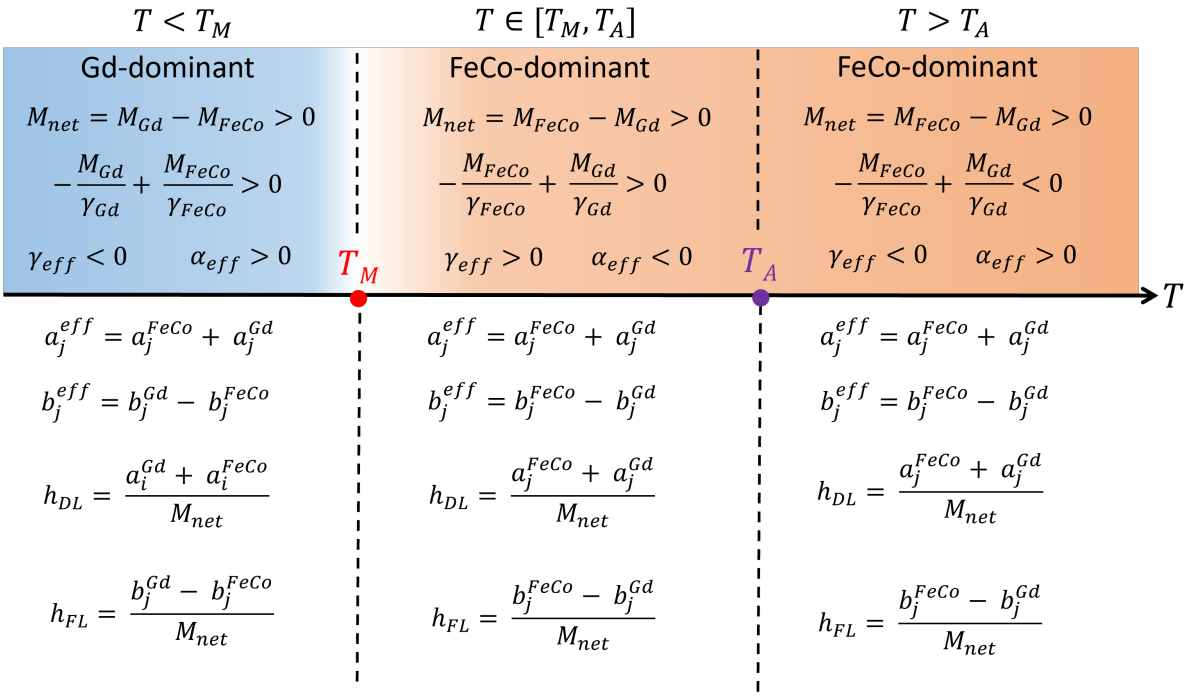

Figure 6.11: Expression of the effective quantities in the LLGS equation for GdFeCo ferrimagnet. It turns out that the effective gyromagnetic ratio and the effective damping reverse their sign at the magnetic and angular compensation temperatures.

current comes from outside the ferrimagnet. As a result, an excess of angular momentum is introduced by the external spin current. This angular momentum excess results in a torque on both magnetic sublattices and we can consider a_j^{Gd} and a_j^{FeCo} to have the same sign given by the spin polarization of the spin current and to be constant with temperature. Considering the expression of the effective damping-like torque a_j^{eff} and that the sign of $a_j^{Gd} + a_j^{FeCo}$ does not change with temperature, it follows that a_j^{eff} has the same sign over the compensation temperatures. If we then look at the DL effective field h_{DL}, which is defined as the ratio between the effective damping-like torque and the net magnetization, we see that the sign of h_{DL} is unchanged over the compensation temperatures of GdFeCo. This is indeed what we observe for GdFeCo(10)/Pt(2). We further verify that a_j^{Gd} and a_j^{FeCo} have the same sign by the finite torque obtained experimentally at the magnetization compensation temperature (see Figure 6.10).

Thus, our model shows that in the case of an external spin current source, the resulting damping-like effective field has the same sign over the magnetization compensation temperatures. This model is in perfect agreement with the behavior of the damping-like effective field in the case of GdFeCo/Pt.

6.4.2 Case of the damping-like effective field in GdFeCo/Cu

In GdFeCo/Cu, the source of the spin current is internal. The ferrimagnet has generated a spin current whose partial absorption is at the origin of a self-torque. In this process the system has lost spin angular momentum and at the same time has regained spin angular

momentum. In this case the amplitudes and signs of a_j^{Gd} and a_j^{FeCo} can be different, and all this can evolve with temperature. As a consequence, we cannot consider a specific action of a sublattice, and we consider instead the sum $a_j^{Gd} + a_j^{FeCo}$. Looking at the evolution of the DL torque as a function of temperature in Figure 6.10, we can see that the DL torque vanishes at the magnetization compensation temperature. This suggests that $a_j^{eff} \propto M_{Gd} - M_{FeCo}$.

In the case where the spin current is internal to the ferrimagnet, our experimental data suggest that the damping-like torque vanishes at the magnetization compensation temperature. This particular behavior suggests that $\boldsymbol{a_j^{eff} \propto M_{Gd} - M_{FeCo}}$.

6.5 Conclusion

The aim of this chapter was to study spin-orbit torques and self-torques in GdFeCo using the second harmonic technique. For this purpose, we derived the analytical expressions for the Hall voltage and thermal contributions, taking into account the specific parameters used for the technique.

We show that the spin torque effective fields behave differently over the magnetization compensation temperature of GdFeCo in the case of GdFeCo/Pt and GdFeCo/Cu. On the one hand, it is found that the damping-like effective field is always negative with Pt, while the damping-like self-torque in GdFeCo/Cu changes sign over the magnetization compensation temperature.

Considering our experimental results explained in Chapter 5, it follows that **the sign change of the self-torque cannot be attributed to a spin change of the spin current generated in GdFeCo, but rather to the dynamics of the magnetization**.

Considering the dynamical equation of a ferrimagnet, we can express the spin torque in terms of the contributions of each magnetic sublattice. **We were able to show with our model that in the case of an external spin current generating a spin torque on the magnetization of a ferrimagnet, the damping-like effective field has the same sign. Therefore, our model is in agreement with our experimental results in GdFeCo/Pt**.

The torque in GdFeCo/Cu results from the generation and partial absorption of a spin current in the GdFeCo layer. **Our experimental results show that the damping-like self-torque vanishes at the magnetization compensation temperature of GdFeCo. Therefore the self-torque is related the net magnetization of GdFeCo**.

In the following chapter, we discuss ways to improve the efficiency of self-torque for applications.

CHAPTER 7

Tunability of self-torque

Samples were grown by Prof. Michel Hehn. The TEM characterizations were performed at IJL by Jaafar Ghanbaja, and the samples for TEM were prepared by either Sylvie Migot or myself. The patterning of the devices was mainly done by myself using CC Minalor facilities at IJL. All electrical measurements and data analysis were done by myself. The interpretation was discussed with Dr. Sébastien Petit-Watelot, Dr. Juan-Carlos Rojas-Sanchez, Prof. Michel Hehn and myself. The Kerr images of the switching without an external magnetic field were made by Emeric Robinet and Arthur Hellé as part of their master internship under my supervision.

The self-induced spin-orbit torque has the potential to be used in applications to manipulate the magnetization of a single magnetic layer without the use of an external heavy metal. In the case of GdFeCo(10)/Cu(2), we have shown in Chapter 6 that the torque has a very low intensity and no electrical switching of the magnetization is observed. Therefore, the material or stack must be optimized to make the self-torque useful in applications. The idea of this chapter is to present some hints for a more intense self-torque. In a first study, we show the effect of adding a buffer layer. Then we show the effect of adding a magnetic spin sink.

7.1 Enhanced self-torque using different buffer layers

For GdFeCo/Cu, we assume that the torque comes from the bulk of the GdFeCo, but we cannot exclude an interfacial effect. For this study, we keep the upper interface and add a light metal layer between the substrate and the FiM (a buffer layer). The addition of a light metal eliminates the possibility of generating an external spin current by the spin Hall effect, but it may lead to two effects: 1) a change in the properties of GdFeCo, especially its concentration gradient 2) an additional interfacial effect. We will focus on the DL effective field, which is responsible for the switching of the magnetization. In the following we present

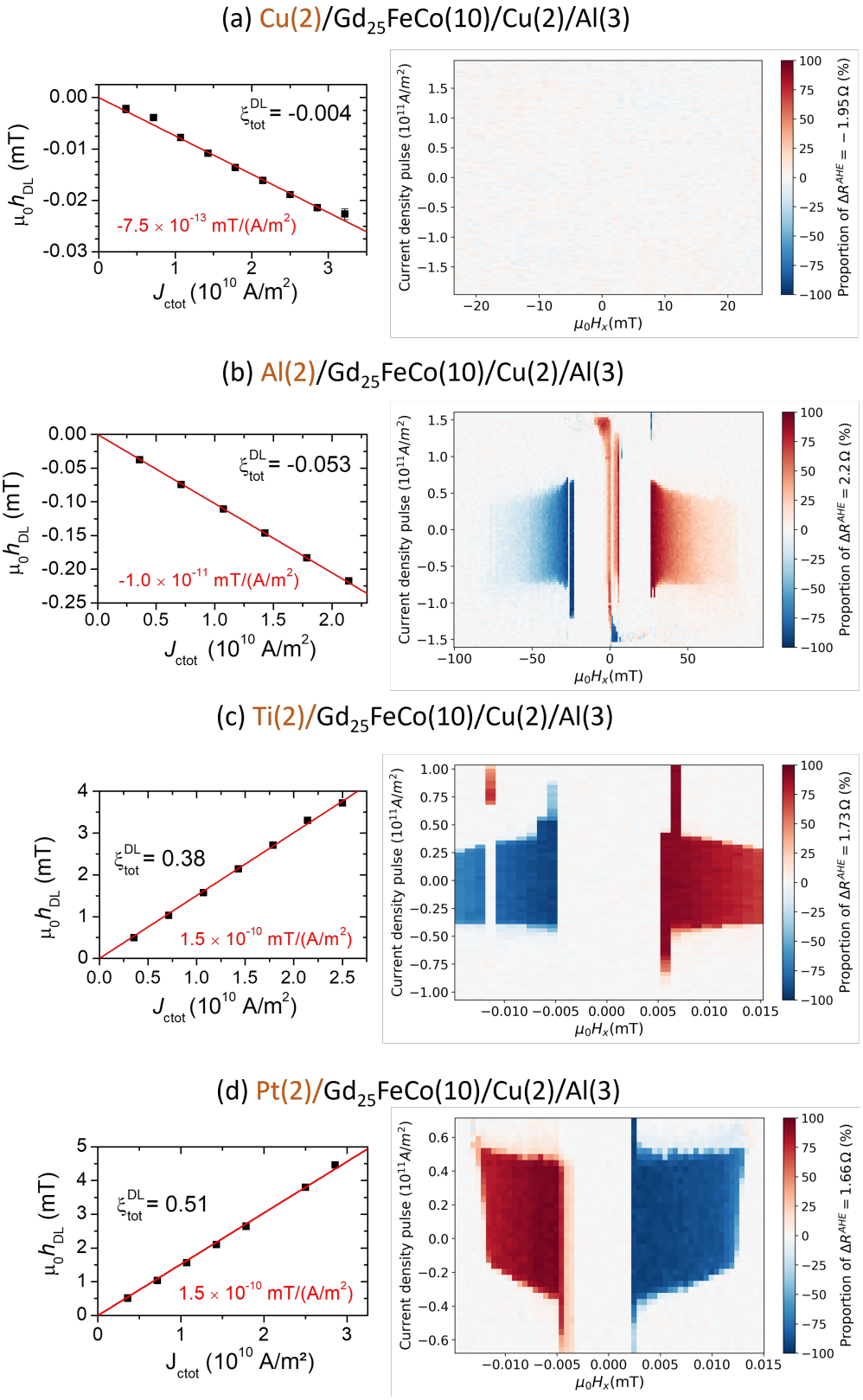

Figure 7.1: Evalution of the efficiency of self-torque and electrical switching of the magnetization in (a) Cu(2)/GdFeCo(10)/Cu(2)/Al(3), (b) Al(2)/GdFeCo(10)/Cu(2)/Al(3), (c) Ti(2)/GdFeCo(10)/Cu(2)/Al(3) and (d) Pt(2)/Gd_{25}FeCo(10)/Cu(2)/Al(3).

the study of the DL self-torque:

- Cu(2)/Gd_{25}FeCo(10)/Cu(2)/Al(3)
- Al(2)/Gd_{25}FeCo(10)/Cu(2)/Al(3)
- Ti(2)/Gd_{25}FeCo(10)/Cu(2)/Al(3)

and we will consider for each sample its overall efficiency defined as:

$$\xi_{tot}^{DL} = \frac{2|e|}{\hbar} M_S t_{tot} \frac{h_{DL}}{J_{ctot}}, \tag{7.1}$$

where M_S is determined for each sample by SQUID VSM measurements.

We will compare the efficiencies associated with the different light metal buffer layers with the case of a heavy metal buffer layer:

- Pt(2)/Gd_{25}FeCo(10)/Cu(2)/Al(3)

where Pt is an external source of spin current but also a spin-sink. The idea is to compare the efficiencies of the DL torque to see if tuned self-torque can be as effective as a structure with Pt.

7.1.1 Self-torque efficiencies and switching

Figure 7.1 shows the evolution of h_{DL} with the total current density J_{ctot} obtained using the second harmonic technique for (a) Cu buffer layer, (b) Al buffer layer and (c) Ti buffer layer. The linear slope corresponding to the efficiency and the spin Hall angle are given and also summarized in Table 7.1. In addition, the electrical switching of the magnetization was tested for each sample. Switching measurements consist of applying 100 μs current pulses of different amplitude and measuring the transverse voltage with a low DC current after each pulse to determine the equilibrium position of the magnetization. These measurements are performed under an in-plane magnetic field aligned with the current to allow deterministic switching of the magnetization [138]. The corresponding switching maps are shown in the same Figure 7.1. The colored areas in the map indicate the current density at which an opening of the resistance cycle is observed for different in-plane magnetic field intensities. The intensity of the color is related to the percentage of cycle opening compared to the AHE amplitude obtained with an out-of-plane magnetic field. We see that for opposite magnetic field intensities, the polarity of the cycle (described by the blue or red) is also reversed. This is the signature of the spin-orbit torque. We can also see that the critical current density required to switch the magnetization decreases with higher magnetic fields as the magnetization is tilted toward the plane, requiring less energy to switch to the other magnetic state. The switching point decreases with increasing magnetic field because the magnetic field tilts the magnetization and the maximum resistance state is lower than when we use an out-of-plane magnetic field.

It turns out that the overall efficiency of the DL effective field is highly dependent on the different interfaces. Without the buffer layer, the efficiency is estimated to be -2.63×10^{-11} mT/A/m^2 and no switching of the magnetization is reported. In the case of the Cu buffer layer, the DL efficiency is even lower and no electrical switching of the magnetization is obtained. However, the DL efficiency reaches 10^{-11} and 10^{-10} mT/(A/m^2) for the case of Al and Ti buffer layers, respectively. The switching map associated with the Al buffer layer (see figure 7.1) shows that 100% switching of the magnetization can be achieved for a critical current density of 0.5×10^{11} A/m^2 and an external magnetic field of about ± 30 mT. The polarity reversal of the resistive loop is a signature of the electrical switching induced by SOT. Ppening of the loop is observed at zero external magnetic field, but is more likely induced by the Oersted field (this will be discussed in more detail in the subsection 7.2.4). In the case of the Ti buffer layer, 100% switching of the magnetization is observed at even lower current densities (about 0.35×10^{11} A/m^2).

To compare the different values obtained, we discuss the case of the Pt(2) buffer layer. The effect of Pt is twofold: it generates SOT on GdFeCo, which can add to or counteract the self-torque, and Pt can also act as a spin sink, which increases the efficiency of the self-torque. The different effects are indistinguishable and we look at the overall effect. We can see that the DL effect is positive and opposite in sign to the DL effect in GdFeCo/Pt, which is consistent with the symmetry of the SHE. Surprisingly, the amplitude of the DL effect is about the same for Pt and for the Ti buffer layer, their efficiencies being different because the sample with Pt has a higher magnetization at saturation.

Buffer	-dominant	ρ_{XX}^{tot} ($\mu\Omega$.cm)	Δ (nm^{-1})	h_{DL}/J_{ctot} mT/(A/m^2)	ξ_{SHE}^{DL}
$\emptyset$	FeCo	101	+0.045	-2.63×10^{-12}	-0.004
Cu	FeCo	92	-0.044	-7.4×10^{-13}	-0.003
Al	Gd	93	+0.008	-1.0×10^{-11}	-0.053
Ti	Gd	74	-0.031	$+1.5 \times 10^{-10}$	0.38
Pt	Gd	75	-0.035	$+1.5 \times 10^{-10}$	0.51

Table 7.1: Table showing the total resistivity of the layers (ρ_{XX}^{tot}), the concentration gradient (Δ), the slope h_{DL}/J_{ctot} and the DL efficiency ξ_{tot}^{DL} for the different buffer layers.

7.1.2 Discussion on the effect of the buffer layer

Two main sources of self-torque are discussed: the concentration gradient in the bulk and the interfaces.

For the Cu, Al, Ti and Pt buffer layer samples, TEM characterization was performed and the evolution of the Gd concentration compared to the sum of the Fe and Co concentrations along the ferrimagnet thickness was estimated by EDS. The corresponding analysis is shown in Figure 7.2. First note that the sign of the concentration gradients depends on the bottom interface: it is negative in the case of Cu, Ti and Pt, while it is positive for Al. We also

recall that it was positive for //GdFeCo/Cu (see figure 6.7). The mechanism leading to the different signs of the gradient is not fully understood. It is suggested that in //GdFeCo/Cu the oxidation of Gd comes mainly from the substrate which is in direct contact with GdFeCo. Similarly, we can assume that the 2 nm of Al between the substrate and GdFeCo is not thick enough to prevent the oxidation of Gd from the substrate, resulting in an excess of oxygen at the lower interface and a positive concentration gradient. On the other hand, Pt is not oxidized and Ti is known to passivate. We can see that the resistivities in the samples with the Pt and Ti buffer layers are about the same, indicating that the layers are indeed not oxidized. The protection against oxidation of GdFeCo provided by Pt and Ti can explain the negative gradient. However, in the case of Cu/GdFeCo/Cu, both the bottom and top layers can be oxidized, and the sign of the gradient cannot really be explained. Performing the EDS chemical characterization taking into account the oxygen in the layer would allow a better understanding of the relationship between the sign of the gradient and the material used for the buffer layer.

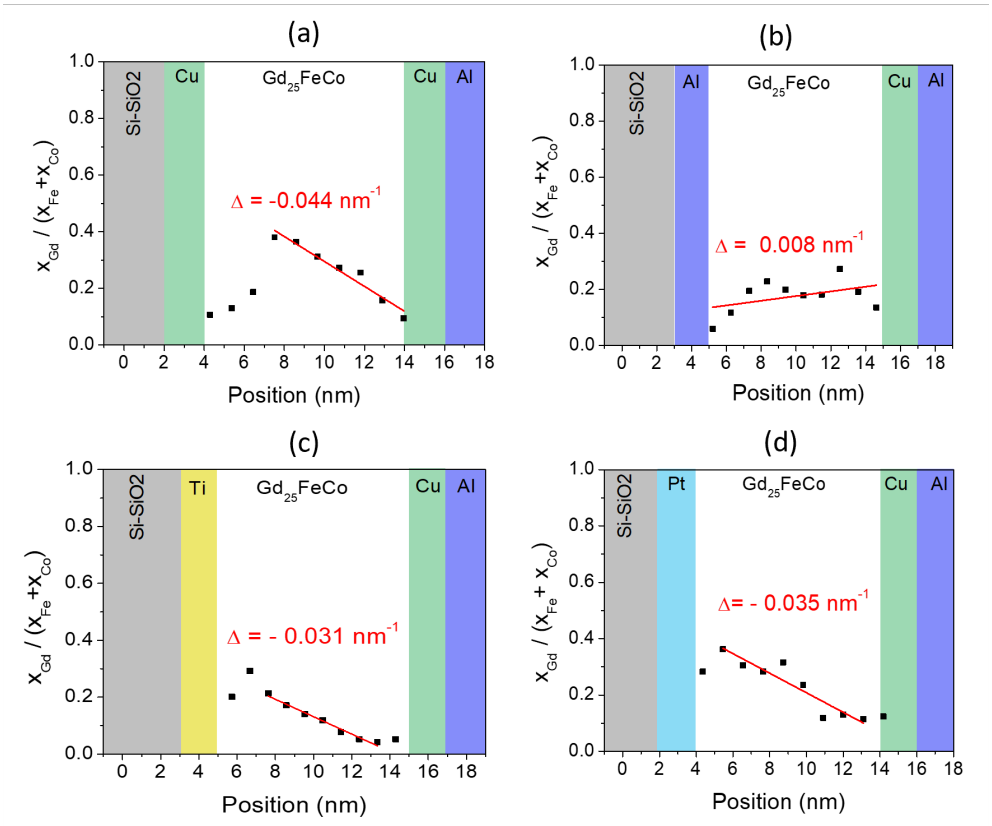

Figure 7.2: Estimation of the concentration gradient of Gd by EDS in (a) Cu(2)/Gd_{25}FeCo(10)/Cu(2)/Al(3), (b) Al(2)/Gd_{25}FeCo(10)/Cu(2)/Al(3), (c) Ti(2)/Gd_{25}FeCo(10)/Cu(2)/Al(3) and (d) Pt(2)/Gd_{25}FeCo(10)/Cu(2)/Al(3).

In the set of samples shown here, there is no consistent correlation between the strength of the gradient and the strength of the DL torque. Consider the case of the Cu buffer layer: the gradient is the strongest, but its DL efficiency is the lowest. This low DL torque can also be explained by the shunting of the current in the Cu layers, but the drop in resistivity induced by the Cu buffer layer is not significant (see Table 7.1). If we do not consider the

case of Cu buffer, we do indeed have an increase in torque with stronger gradients (regardless of sign) for the case of Al and Ti. There is also no consistent correlation between the sign of the torque and the sign of the gradient. For Al and Ti buffer layers, the sign of the gradient is opposite and their torque is opposite, and we note that both samples are Gd-dominant. However, comparing //GdFeCo/Cu and Cu/GdFeCo/Cu, their gradients have opposite signs, but their DL torques are opposite when the FiM is FeCo dominant.

Let us now discuss results from the literature regarding the role of the bulk in the generation of self-torque. In 2021, an amorphous FePt single layer with an artificially tuned concentration gradient [92] was studied. They show that a uniform $Fe_{50}Pt_{50}$ does not produce a significant self-torque. However, Fe_xPt_{1-x} with an intentional positive composition gradient of Pt ($x = 25 \rightarrow 75$) shows a significant negative DL torque efficiency of about $\xi_{J_c}^{DL} = -0.077$. The conclusion of this study is that the composition gradient allows an inversion asymmetry through a strain gradient, which allows the generation of self-torque.

In conclusion, the use of a buffer layer allows the tuning of the self-torque. By using an Al and Ti buffer layer, we have demonstrated the switching of the magnetization, which is the first step for the implementation of the material for applications. The origin of the self-torque enhancement is not fully understood. Two main clues are highlighted: interfacial effects and bulk effects due to the gradient of Gd concentration. Future studies should be conducted to clarify the origin.

7.2 Enhanced self-torque using a spin-sink

Self-torque in GdFeCo results from the generation and absorption of the SHE spin current in the single layer. In Chapter 2 we discussed the concept of spin dephasing, which is the process by which a spin current loses its coherence when flowing in a ferromagnet due to the interaction with the magentization. In ferrimagnets it is shown that spin dephasing takes place at a longer distance (about 4 nm for GdCo, while it is about 1 nm in a ferromagnet) as a result of the two antiferromagnetically coupled sublattices. In other words, in a simple picture, the spin current can travel a longer distance before being absorbed in a FiM than in a FM, and this is especially true when the FiM is at its magnetization compensation where the dephasing length diverges as in antiferromagnets. This effect is an obstacle to the generation of self-torque, as it allows the spin current to flow outside the ferrimagnet without being absorbed. To overcome this problem we can use a spin sink, which is an additional layer designed to absorb the spin current. We can use different types of materials for this purpose:

- heavy metals, where the spin relaxation can be induced by Elliott-Yafet spin scattering or Dyakonov-Perel relaxation [139] at a distance of about 3-6 nm [140].

- magnetic layer, where the spin current is absorbed by the combination of the spin dephasing process and spin dependent scattering effects. This effect occurs at about 1 nm in FM.

- resistive layer, with a high scattering and more likely spin-flip events such as the Elliott-Yafet mechanism.

We will discuss two types of spin-sinks, first the case of a heavy metal, and then the case of a magnetic layer.

7.2.1 Using heavy metals as a spin-sink

Heavy metals can be used to improve the overall effect of a GdFeCo structrue. On the one hand, the SHE spin current can induce a torque on the magnetization of GdFeCo. On the other hand, the SHE spin current generated by GdFeCo can be absorbed by the heavy metal, leading to a self-torque. The two effects can compete or enhance the overall effect, depending on the sign of the spin polarization emitted by each material. We can discuss two cases:

- If θ_{DL}^{GdFeCo} has the same sign as θ_{DL}^{HM}.
  In this case the spin polarizations sent to the other layer are opposite to each other (see Figure 7.3(a)). The spin polarization sent by GdFeCo is absorbed in the HM, resulting in a loss of angular momentum. This loss of angular momentum is described by a self-torque acting on the magnetization of GdFeCo, which is opposite to the direction of the absorbed spin polarization. The HM emits a spin polarization in the same direction as the self-torque on GdFeCo. As a result, the overall effect is enhanced in this case.

- If θ_{DL}^{GdFeCo} has the opposite sign of θ_{DL}^{HM}.
  In this case the spin polarizations sent to the other layer are in the same direction (see Figure 7.3(b)). The spin polarization sent by GdFeCo is absorbed in the HM, resulting in a loss of angular momentum. This loss of angular momentum is described by a self-torque acting on the magnetization of GdFeCo, which is opposite to the direction of the absorbed spin polarization. The HM emits a spin polarization in the opposite direction of the self-torque on GdFeCo. As a result, in this case, the effect of the spin-sink and the effect of the SHE spin current from the HM on GdFeCo compete, and the overall effect is small.

A study using different spin-sinks with GdFeCo was performed at IJL and published in 2021 [74]. The idea was to compare the effect of an additional Pt spin-sink, an additional Ta spin-sink, and to compare with a reference layer without spin-sink. The damping-like effective field for the different stacks was measured using the second harmonic technique. The results are shown in Figure 7.3(c). Pt and GdFeCo have the same sign of the spin Hall angle, and the experimental results confirm the overall enhancement of the damping-like torque in this case compared to the case without spin-sink. Using Ta spin-sink, we can see an enhancement of the overall damping-like effective field compared to the case without spin-sink, but the enhancement is smaller than in the case of Pt.

Let us now discuss the case of a magnetic material used as a spin-sink.

7.2.2 CoAl spin-sink

In this study, we used a polycrystalline CoAl alloy as a spin-sink. This particular material, with 50 percent Co and 50 percent Al, has a Curie temperature close to room temperature.

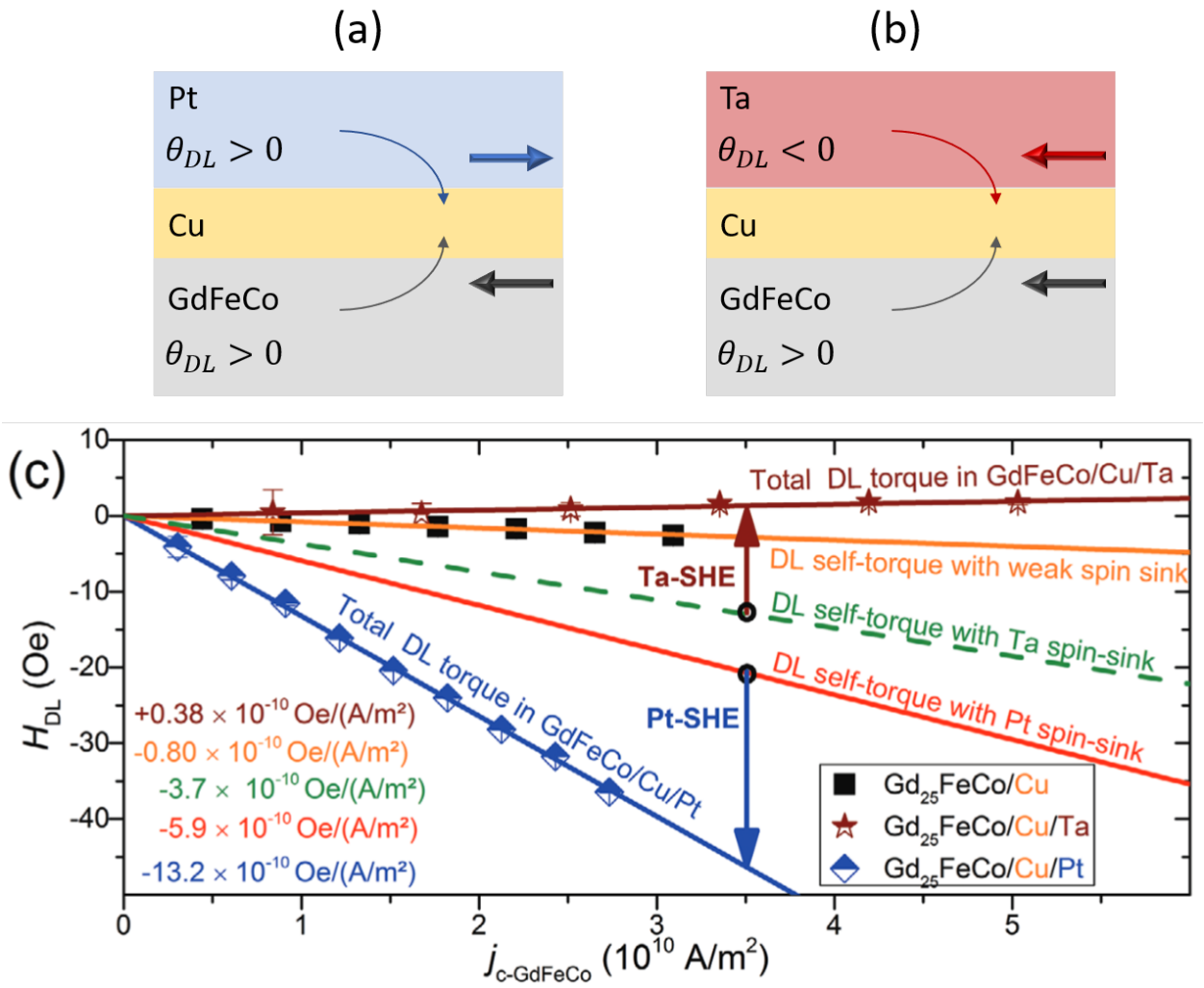

Figure 7.3: Use of a heavy metal to improve the overall efficiency of a structure containing GdFeCo. (a) The overall effect is enhanced when the HM and GdFeCo have the same sign of the spin Hall angle. (b) The overall effect is small when the HM and GdFeCo have opposite signs of the spin Hall angle. (c) Evolution of the damping-like effective field as a function of the charge current density in GdFeCo for different stacks. The orange line corresponds to the case without spin-sink. We can see that the overall damping-like effective field is more enhanced in the case of additional Pt spin-sink (blue line) compared to the case of Ta spin-sink (brown line).

The idea was to see if an increase in self-torque was observed when the spin-sink was magnetic, compared to when it was paramagnetic. The characterization of the sample after the lithography process shows us that the spin-sink has a strong magnetization at saturation equivalent to that of pure Co. It suggests that the polycrystalline CoAl segregates into Co rich and Al rich regions due to annealing. Therefore, the influence of the magnetic properties of CoAl on the self-torque could not be investigated. Nevertheless, we have tried to see if the use of this spin-sink allows the electrical switching of GdFeCo magnetization.

In the GdFeCo/Cu bilayer presented in Chapter 6, no electrical switching of the magnetization is observed. In the CoAl spin-sink we observed switching and tried different temperatures to cross the magnetization compensation temperature of the ferrimagnet.

7.2.3 Switching over the compensation temperature

In GdFeCo/HM, it has been observed in the literature that the switching cycle polarity is reversed over the magnetization compensation of GdFeCo [65]. This is well explained by the sign reversal of the AHE which is used to probe the magnetization state. For the self-torque, we can wonder if due to the sign reversal of the AHE, and the possible sign reversal of h_{DL} observed in Chapter 6 the cycle polarity is the same over the magnetic compensation.

We performed switching measurements in $Gd_{24}FeCo(10)/Cu(3)/Co_{55}Al_{45}(5)/Al(3)$. The magnetization compensation temperature was estimated to be $T_M = 150$K, as suggested by the sign change of the transverse resistance. The switching measurement consists in sending a 100 μs wide pulse of different intensities and to measure the transverse resistance after the pulse when the magnetization has returned to an equilibrium position. We performed the switching measurements at different temperatures, and show the results at 90K, when the ferrimagnet is Gd-dominant, and at 300K, when the ferrimagnet is FeCo-dominant. Figure 7.4 shows the 2D switching maps for the two temperatures, as well as the raw data for two opposing magnetic fields. We can see that at 90K and at 300K, for a positive field, the polarity of the cycle is the same. Similarly, the polarity of the cycle is the same at 300K. We can discuss two scenarios: 1) the cycle polarities are the same over T_M due to the sign reversal of both h_{DL} and AHE or 2) Joule heating due to the rather high current density flowing in the ferrimagnet shifts the magnetization compensation of GdFeCo. The latter hypothesis has been mentioned in the literature in TbFeCo ferrimagnet [141].

7.2.4 Field-free switching, or Oersted field reversal ?

A large number of articles report zero-field switching, i.e. the electrical reversal of the magnetization without the assistance of an in-plane magnetic field. Achieving the switching without magnetic field is indeed of great interest, as it would allow the fabrication of magnetic memories without downscalling problem of the external magnetic field. However, free field switching is very often supported only by the opening of the resistance cycle with the current pulses. In this section we want to emphasize that the opening of the resistance cycle can be induced by the Oersted field generated by the current pulse and has nothing to do

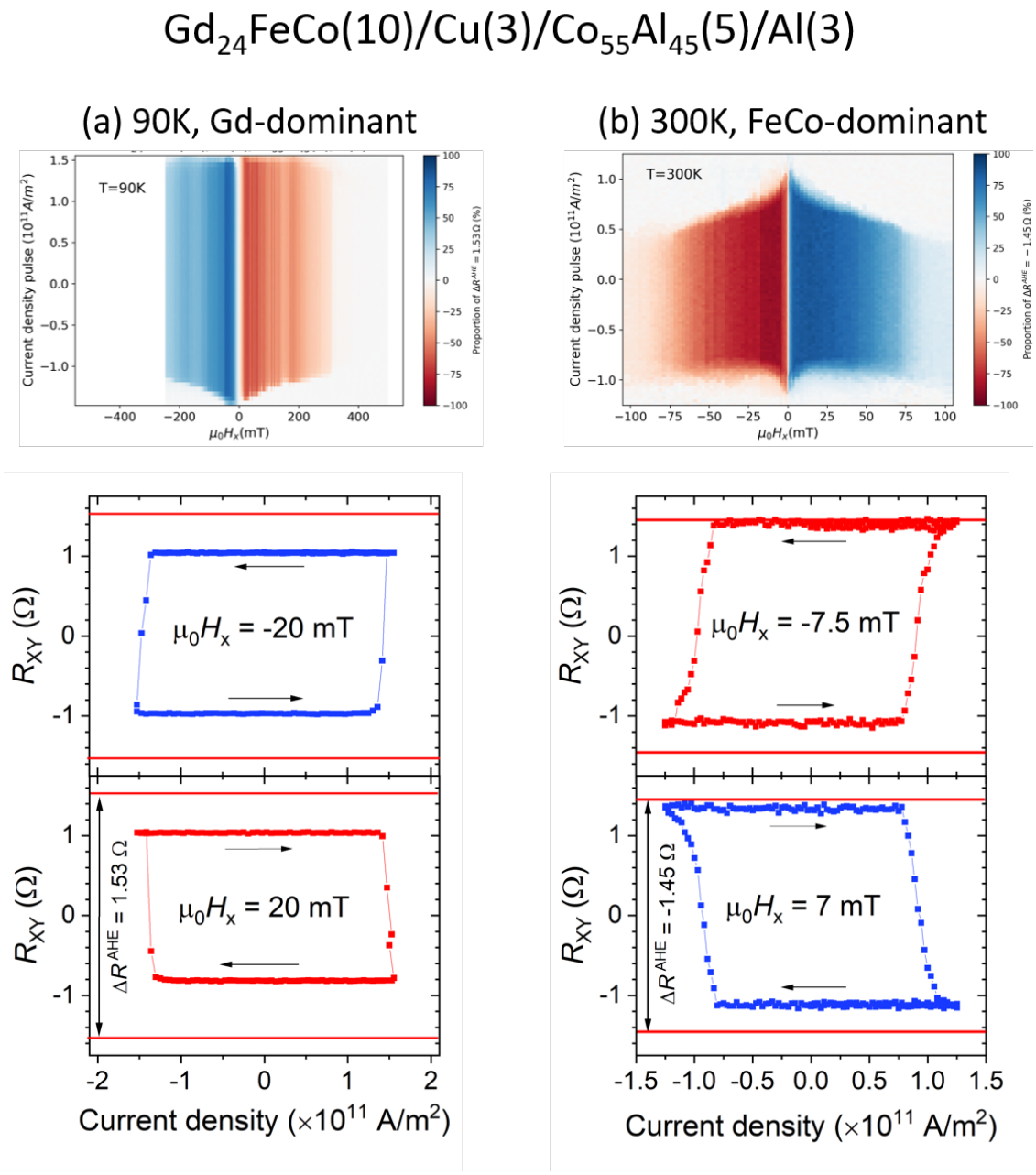

Figure 7.4: Electrical switching of the magnetization in $Gd_{24}FeCo(10)/Cu(3)/Co_{55}Al_{45}/Al(3)$. (a) Switching measurements at 90K when the material is Gd-dominant. 2D map of the current density of the pulse for which switching of the magnetization is observed at a given in-plane magnetic field intensity. The intensity of the color corresponds to the percentage of switching compared to the full AHE amplitude $\Delta R_{AHE} = 1.53$. It shows that at this temperature the switching is incomplete and about 25-70 percent. We show the raw data for two opposing magnetic field amplitudes, showing opposite loop polarity. (b) Switching measurements at 300K when the material is FeCo-dominant. 2D map of the current density of the pulse for which switching of the magnetization is observed at a given in-plane magnetic field intensity. The intensity of the color corresponds to the percentage of the switching compared to the full AHE amplitude $\Delta R_{AHE} = -1.45$. It shows that at this temperature the switching is almost complete up to a magnetic field of 50 mT. We show the raw data for two opposing magnetic fields, showing opposite polarity of the loop.

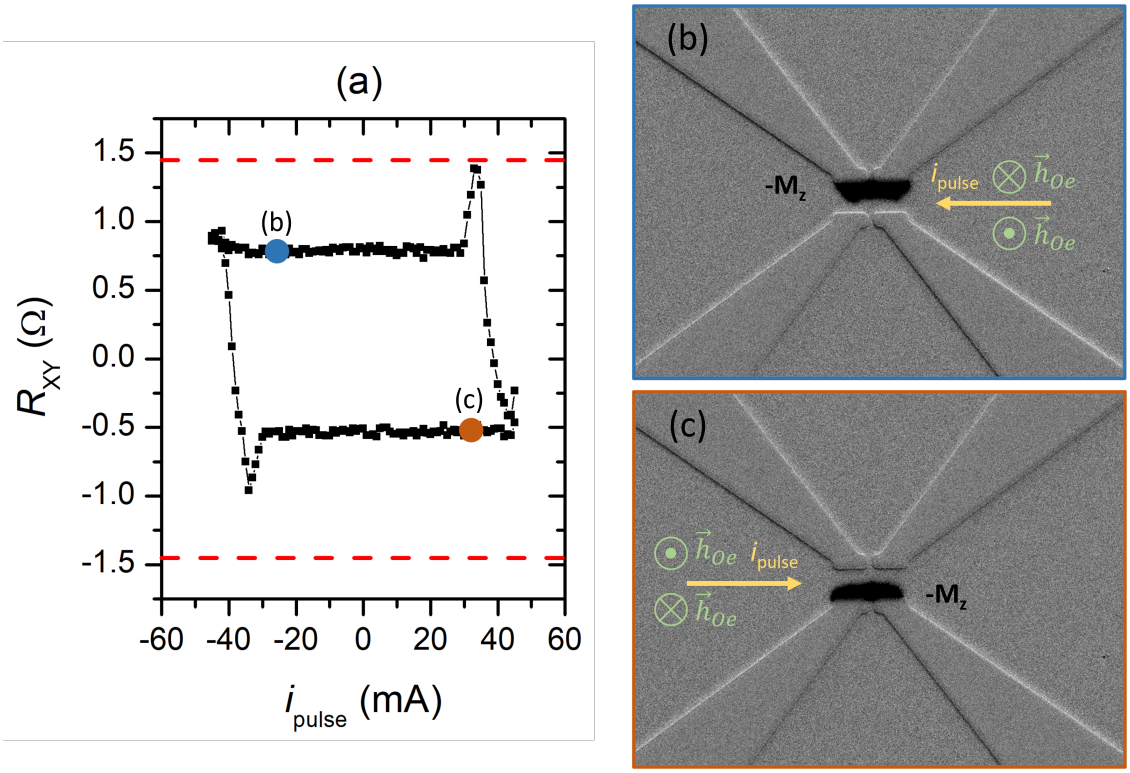

Figure 7.5: Free-field switching in GdFeCo(10)/Cu(3)/CoAl(5)/Al(3). (a) Hall resistance as a function of the current pulse intensity. (b) Switching image obtained with a magneto-optical Kerr effect microscope. The magnetization was first saturated in the $+M_z$ state. The black contrast corresponds to the part that is switched to the opposite state -M_z. We can see that only the upper half of the cross is switched. This suggests that the Oersted field created by the current is able to nucleate.

with spin-orbit torque [84].

We show in Figure 7.5(a) we show the Hall resistance signal as a function of the current pulse intensity. We can see that the amplitude of the cycle is about half of the full cycle, suggesting that the magnetization reversal is not complete and that the current pulses are nucleating magnetic domains in the device. To further understand these measurements, we performed the same measurements with the same parameters (100 μs pulse) under a Kerr microscope. There was no coil in the setup, so there is no residual field. Before applying the current pulses, the magnetic state was saturated using a magnet along the $+\hat{z}$ axis. We can see that the application of current leads to the nucleation of a domain wall located in the upper half of the device. When the polarity of the current is reversed, the domain is displaced along the lower part of the device. This type of domain nucleation at the edges is associated with the Oersted field generated by the pulse, which is strong enough to nucleate domain wall, especially at the edges of the device.

By applying an external magnetic field as shown in the previous section, the complete reversal of the magnetization can be obtained. The cycle polarity is reversed with an opposite magnetic field, respecting the symmetry of the SOT switching. However, knowing that the Oersted field can be large in our samples, we can attribute the switching not only to the self-torque, but also to the Oersted field. This cooperation can explain the asymmetries in the switching cycles, where for one magnetic field the positive and negative critical current densities are not the same to switch from one state to the other.

7.3 Different leads to increase the effect of self-torque

To summarize and conclude, we have exploited different ways to increase the self-torque in GdFeCo to achieve the electrical switching of the magnetization.

By addying a light metal buffer layer, such as Al and Ti, we observed a significant increase in the DL torque, which allows the electrical switching of the magnetization. This enhancement can be related to the concentration gradient in the bulk or to interfacial effects.

The addition of a heavy metal can improve the overall effect of a structure. **We show that the overall effect is enhanced by using Pt with GdFeCo. This enhancement is explained by the positive spin Hall angle of both Pt and GdFeCo, which allows to maximize the torque on GdFeCo. On the contrary, the enhancement of the overall effect using Ta is reduced due to the opposite spin Hall angles of GdFeCo and Ta.**

The use of a magnetic layer acting as a spin-sink also allowed the enhancement of the self-torque in GdFeCo and electrical switching of the magnetization was observed.

Therefore, we were able to tune the intensity of the self-torque by these different means. Further studies are possible:

- Artificial gradient of Gd concentration. In the same essence as reference [92], we could see how the strength of the gradient affects the strength of the torque. We could also see if the sign of the torque is determined by the sign of the gradient. By doing this in a single layer with no surrounding layer, we can avoid shunting the current and avoid interfacial effects.

- Higher thickness of GdFeCo. In this thesis, only 10 nm has been studied. Studying the intensity of the self-torque as a function of the thickness of the GdFeCo single layer would allow to optimize the layer to keep the PMA without the use of Cu, and would determine the optimal thickness for the best absorption of the SHE spin current. If other layers surround the ferrimagnet, a thickness study would also allow to distinguish bulk effects from interface effects.

- Light metal spin-sink. It has been shown that self-torque can be increased by a heavy metal [74] or a magnetic spin-sink. Finding a light metal that is resistive enough to absorb the spin current emitted by GdFeCo could be of great interest as it would increase the self-torque without shunting the current in this light metal due to its high resistivity. During my PhD work, we investigated the AlTi alloy as a spin-sink, but no significant increase in self-torque was observed. To continue this study, spin pumping measurements can be used to determine the light metal thickness at which the spin current is absorbed.

Thus, thanks to the inherent properties of GdFeCo, such as the gradient of the Gd concentration and the large spin dephasing length, the material and the structure can be tuned in a variety of ways to achieve the electrical reversal of the magnetization of GdFeCo by self-torque. These preliminary results pave the way for the use of GdFeCo in applications.

Conclusion

The aim of this thesis manuscript was to present the main results of my research on the generation of spin current and self-induced spin torque in quasi-isolated GdFeCo.

To this end, in Chapter 1 I first introduced the main mechanisms we consider for spin current generation and for its absorption, which can lead to spin torque. At the beginning of my PhD work, the idea of self-torque was quite new, so I provided the state of the art on self-torque.

Then in Chapter 2, I introduced the magnetic properties of GdFeCo ferrimagnet. I highlighted its interesting properties in the context of self-torque generation. This material presents a rich physics due to the presence of two magnetic sublattices and their specific temperature dependence, making GdFeCo and RE-TM FiM interesting platforms to understand the mechanism behind self-torque. Two main features are highlightes: its large spin dephasing length, which allows the spin current to be emitted outside the FiM and harvested in a spin-sink, and its natural composition gradient, which allows the inversion symmetry to be broken and can lead to a net torque in a single layer.

In Chapter 3, I presented the spin-polarized transport of Gd-based ferrimagnets from results in the literature. It is shown that the transition metal sublattice dominates the spin-polarized transport. I then presented a primary study of magnetotransport in GdFeCo. By studying the magnetoresistance of Gd and FeCo, I showed that the anisotropic magnetoresistance and the anomalous Hall effect in GdFeCo can be described phenomenologically by the sum of the Gd and FeCo contributions. Due to the antiferromagnetic coupling between the Gd and FeCo sublattices, a measurement of the anomalous Hall effect does not allow to determine the dominant sublattice for the effect. Therefore, I proposed to use a high magnetic field to break the antiferromagnetic coupling and measure the anomalous Hall effect when both Gd and FeCo are parallel to the field. **This study allows to determine the sublattice that dominates the anomalous Hall effect transport, and I also presented the case of a sample where the Gd sublattice dominates the transport**.

In Chapter 4 I presented a general model that allows to derive the analytical expressions of the voltage of a magnetic material whose dynamics is driven by an oscillating spin-orbit torque. The basis of this model has been used in the rest of the thesis to derive the analytical expression of the voltages in the specific configurations of the spin-torque ferromagnetic resonance technique and the second harmonic technique.

Chapter 5 presents our results on the spin current generation of GdFeCo by the ST-FMR technique. By studying the effect of the spin current of GdFeCo on the resonance peak of a NiFe spin sink, and this for different temperatures, **we demonstrated that the SHE spin current is independent of the magnetic state of the ferrimagnet**. As for the SAHE spin current, it seems to dominate over the SHE spin current and is opposite to it. It has the same sign at 15K and 300K suggesting that **the SAHE spin current is related to the net magnetization of the ferrimagnet rather than to a specific sublattice.**

In Chapter 6, I presented the study of the self-torque in GdFeCo/Cu induced by a SHE spin current in GdFeCo and the spin-orbit torque in GdFeCo/Pt induced by the SHE in Pt. **It turns out that the spin-orbit torque and the self-torque have a different behavior over the magnetization compensation temperature. Namely, the sign of the spin-orbit torque is always the same, while the sign of the damping-like self-torque is reversed over the magnetization compensation temperature. By deriving the dynamical equation of the magnetization of a ferrimagnet, we were able to show that in the case of a torque generated by an external spin current, the resulting damping-like torque has the same sign over the compensation points of GdFeCo.** Finally, we proposed that the damping-like self-torque is related to the net magnetization of the ferrimagnet, since the torque vanishes at the magnetization compensation temperature.

In Chapter 7, we discussed ways to increase the self-torque using different types of buffer layers, and using a spin-sink. We show that it is possible to electrically manipulate the magnetization, which opens the way to using self-torque for applications.

Introduction étendue

Avec la prolifération des appareils connectés, la croissance exponentielle d'Internet et le développement rapide de diverses technologies, notre monde est témoin d'un déluge de données numériques qui doivent être manipulées et stockées. A titre d'exemple, en une minute en 2021, 200 millions de mails sont envoyés et simultanément 500 heures de contenu sont mises en ligne sur YouTube (voir Figure 1), ce qui exerce une pression immense sur les infrastructures de stockage de données existantes. On estime que la consommation mondiale du stockage, qui était de 286 Thw en 2016, pourrait atteindre 321 Thw en 2030 [1], ce qui équivaut à 1,15 fois l'énergie produite par l'ensemble du parc nucléaire français lors de l'année 2022 [2]. En réponse au défi croissant des données, les efforts de recherche doivent se concentrer sur le développement de solutions efficaces et durables. Dans ce contexte, l'électronique d'aujourd'hui est confrontée à certaines contraintes: la miniaturisation des éléments électroniques approche de ses limites physiques, et le besoin correspondant de dissipation de la chaleur entraîne une consommation d'énergie supplémentaire pour les systèmes de refroidissement [3]. Par exemple, la mémoire vive (RAM) dans les ordinateurs ou téléphones nécessite une alimentation électrique continue pour éviter la perte de données. Contrairement à l'électronique, qui repose uniquement sur le mouvement des charges portées par les électrons, la spintronique exploite l'interaction entre une propriété quantique des électrons, le spin, et le magnétisme. Dans ce cadre, le spin peut être vu comme un petit aimant porté par chacun des électrons. Un courant de spin, composé d'électrons aux spins identiques, devient un outil permettant de manipuler l'orientation de l'aimantation d'un matériau magnétique. En effet, comme illustré sur la Figure 2, un courant de spin porte un moment cinétique qu'il peut transférer à l'aimantation. Ce transfert résulte en un couple (comme un couple mécanique) qui change la direction de l'aimantation et peut la renverser. Ainsi, un matériau magnétique peut être vu comme une mémoire, où un état de l'aimantation est associé au bit 0, et l'autre état est associé au bit 1. Les données étant encodées dans un état magnétique, les dispositifs de mémoire basés sur la spintronique offrent des capacités de stockage non volatiles, ce qui signifie que l'information persiste même en l'absence d'alimentation électrique. Grâce à ce changement fondamental, la spintronique s'est imposée au cours des dernières décennies comme une discipline clé pour le développement de technologies innovantes en matière de traitement et de stockage de l'information.

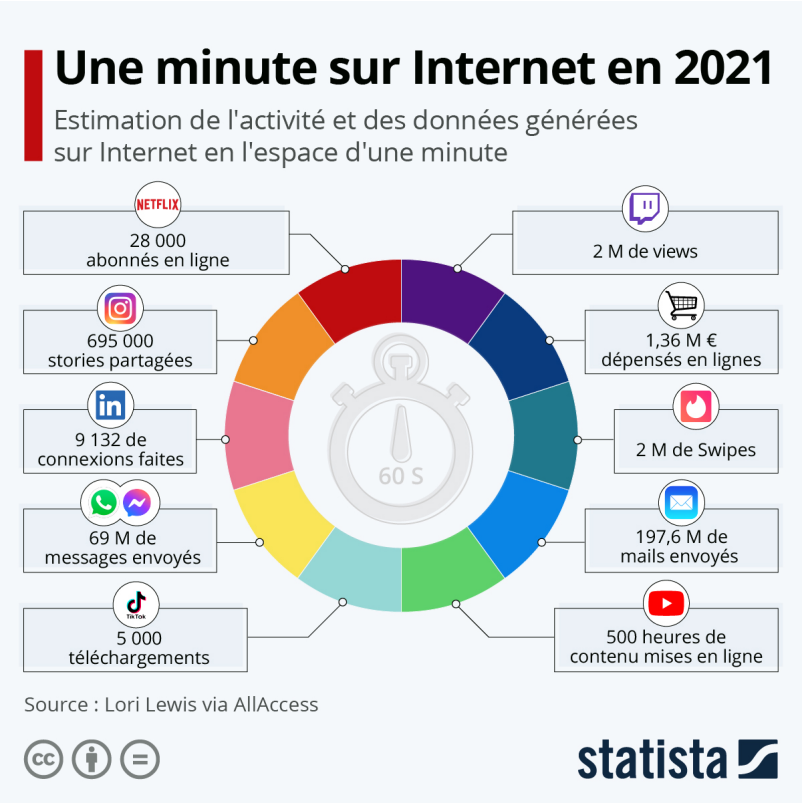

Figure 7.6: Schéma représentant l'activité et les données génerées sur Internet en une minute.

La naissance de la spintronique remonte à la découverte de la magnétorésistance géante (GMR) en 1988 par A. Fert [4] et un an plus tard par P. Grünberg [5], qui leur a valu le prix Nobel en 2007. Cette découverte a contribué de manière significative au développement de têtes de lecture plus efficaces et plus compactes dans les disques durs (HDD) [6], ce qui a permis d'augmenter considérablement la capacité de stockage. Le transfert du moment cinétique entre un courant de spin et une aimantation a ensuite été prédit par J.C. Slonczewski [7] et L. Berger [8] en 1996 et a conduit à la manipulation électrique de l'aimantation. Ces révolutions majeures ont ouvert la voie à la création de dispositifs de mémoire magnétique à accès aléatoire (MRAM), qui combinent les avantages de la mémoire traditionnelle avec un stockage magnétique non volatil. Poursuivant cette trajectoire, la découverte du couple spin-orbite (SOT) en 2010 [9] a introduit une méthode alternative pour générer des courants de spin et écrire l'information d'une manière économe en énergie, attirant une attention considérable pour son potentiel à stimuler le développement de dispositifs logiques et de mémoire à haute densité.

La SOT-MRAM conventionnelle repose sur une configuration multicouche qui comprend des couches magnétiques et des métaux lourds non magnétiques. Ces éléments ont des fonctions différentes: les couches magnétiques stockent l'information, tandis que les métaux lourds sont responsables de l'écriture de l'information. Cependant, en raison de cette structure complexe, l'évolutivité de ces dispositifs présente des défis, tels que le maintien d'une manipulation efficace du spin, ce qui nécessite des techniques de fabrication innovantes. C'est pourquoi de nouveaux matériaux, de nouvelles structures et de nouveaux mécanismes

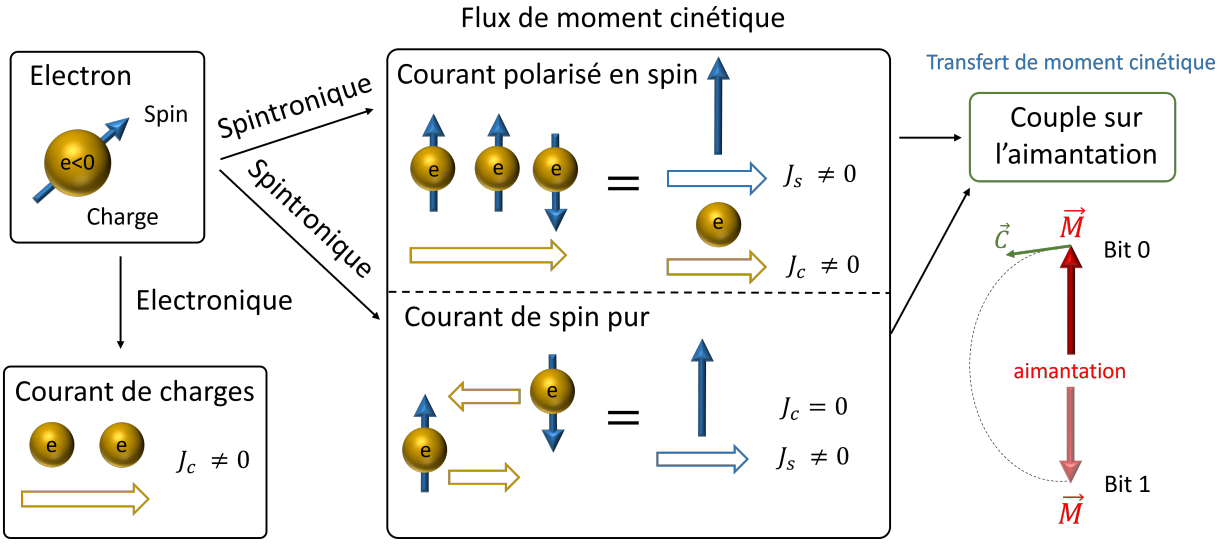

Figure 7.7: Illustration du courant polarisé en spin et du courant de spin pur. Ces courants de spin portent du moment angulaire qui peut être transferé à une aimantation d'un matériau magnétique. En réponse au transfert de moment cinétique, un couple (équivalent à un couple mécanique) agit sur l'aimantation et peut la faire basculer. On a alors un système binaire où une direction de l'aimantation correspond au bit 0, et l'autre direction correspond au bit 1.

de génération de courant de spin sont à l'étude. Dans ce contexte, le SOT à l'intérieur d'une seule couche (appelé couple auto-induit dans cette thèse) est apparu comme une approche prometteuse pour simplifier les architectures des dispositifs.

Le couple auto-induit a été observé pour la première fois dans des matériaux cristallins en 2014 [10] et 2016 [11]. Cependant, la première observation du couple auto-induit dans un matériau ferromagnétique polycristallin - préféré pour les applications pratiques - n'a eu lieu qu'en 2019 [12]. Mon parcours de recherche a commencé en 2020, en me concentrant sur le matériau ferrimagnétique amorphe GdFeCo en tant que matériau principal pour la génération efficace d'un couple auto-induit. Au cours de mes recherches, il s'est avéré que GdFeCo est également une plateforme unique pour étudier les mécanismes à l'origine des couples auto-induits, en particulier grâce aux propriétés magnétiques du matériau qui dépendent de la température.

L'objectif principal de cette thèse est de présenter les principaux résultats de mes recherches sur le couple auto-induit dans une couche quasi-isolée de GdFeCo sans dépendre de métaux lourds externes connus pour générer des courants de spin. Ma thèse met également en évidence les moyens d'améliorer le couple auto-induit en vue de son intégration potentielle dans des applications spintroniques pratiques.

Dans le premier chapitre, nous définissons les quantités et mécanismes importantes pour la compréhension de cette thèse. L'idée de ce chapitre est de décrire le cycle de vie d'un courant de spin. Nous commençons par cela par décrire les mécanismes de conversion de courant de charge en courant de spin qui résulte du couplage spin-orbite. Un courant de spin

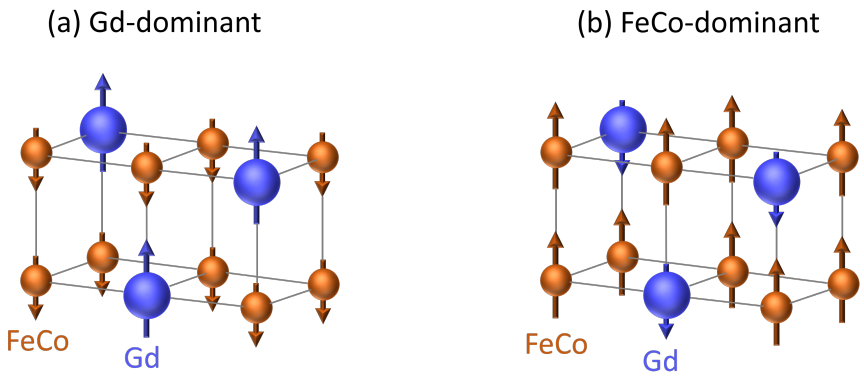

Figure 7.8: Schéma de l'ordre ferrimagétique de GdFeCo. Le magnétisme résulte de la contribution des deux sous-réseaux de Gd and FeCo. Le matériau peut-être Gd-dominant (à basse température), ou FeCo-dominant (à une température plus grande que la température de compensation magnétique.)

peut se propager dans différent types de matériaux, mais celui-ci subit des effets de relaxation qui tendent à détruire le courant de spin. La destruction de ce courant de spin dans une couche magnétique résulte en un transfert du moment cinétique en réponse à la conservation du moment cinétique. Ce processus entraîne un couple qui agit sur l'aimantation. En particulier, si ce couple est suffisamment intense, il peut renverser l'aimantation. Nous introduisons ensuite la notion de couple auto-induit et décrivons l'état de l'art à ce sujet au commencement de ma thèse.

Dans le chapitre 2, nous introduisons le matériau d'intérêt dans la thèse: GdFeCo, qui est un matériau ferrimagnétique. Les matériaux ferrimagnétiques ont la particularité de posséder deux sous-réseaux magnétiques de signe opposé, mais d'intensité différentes qui résultent en une aimantation faible comme illustré sur la Figure 3. Nous présentons des images effectuées à l'aide d'un microscope électronique à transmission pour présenter une spécificité importante de GdFeCo: son absence d'ordre cristallin à longue distance, c'est à dire le fait qu'il est amorphe. Nous présentons une analyse de la composition du matériau afin de mettre en évidence l'inhomogénéité dans la distribution des éléments dans l'épaisseur d'une couche mince de GdFeCo. Nous discutons ensuite des propriétés magnétiques de GdFeCo. Du fait de l'ordre ferrimagnétique, le matériau présente une unique dépendance de son aimantation et de son moment cinétique avec la température. Finalement, nous discutons des propriétés du matériau qui en font un matériau de choix pour l'étude des couples auto-induits, et expliquons les types de structures dans lesquelles un couple auto-induit peut être observé.

Dans le chapitre 3, nous présentons le transport électrique dépendant de l'aimantation dans GdFeCo. L'idée est de discuter le rôle des sous-réseau dans la génération de ces effets magnétoélectriques. Dans le cas du transport polarisé en spin, comme la magnétorésistance géante, il a été montré que le réseau du FeCo domine le transport. Pour l'effet Hall anomal cependant, sa génération est souvent systématiquement attribué au sous-réseau du FeCo seul comme pour le cas de la GMR. Cette dernière idée a été récemment contredite, suggérant plutôt que les deux sous-réseaux contribuent. Dans ce chapitre, nous montront des

mesures de transport dans du Gd pur, du FeCo pur puis dans GdFeCo pour dissocier les deux sous-réseaux. Avec des mesures à très fort champ magnétique lorsque les deux sous-réseaux tendent à s'aligner, nous arrivons à montrer dans un échantillon spécifique que le transport est dominé par le sous-réseau de Gd.

Le chapitre 4 présente un modèle qui décrit la dynamique de l'aimantation sous l'action d'un couple. Ce modèle est le point de départ pour calculter les expressions analytiques des signaux électriques que nous allons mesurer dans les chapitres suivants. Dans un premier temps, nous montrons que la dynamique d'un matériau ferrimagnétique (dont l'aimantation résulte de la contribution de deux sous-réseaux) peut être approximée par la dynamique d'un matériau ne comportant qu'une seule aimantation. Nous dérivons ensuite les équation de la dynamique de l'aimantation lorsque agit un couple périodique. Dans le cadre de la réponse linéaire, la réponse de l'aimantation à une excitation est directement proportionnelle à cette excitation, le facteur de proportionnalité étant la susceptibilté du matériau. Cela nous permet de lier directement la position de l'aimantation à l'excitation. Nous considerons dans le modèle les effets magnétoélectriques et magnétothermiques qui dépendent de la position de l'aimantation et qui nous permettent de sonder l'aimantation dans le cadre de nos mesures. Ainsi, les tensions électriques générées dans ce cadre reflètent directement la position de l'aimantation, qui est elle-même le reflet de l'action de l'excitation, c'est à dire du couple. En exprimant la susceptibilité grâce aux densités d'énergie magnétique, nous pouvons exprimer analytiquement les tensions en fonction du couples agissant sur l'aimantataion, ce qui nous permet par les mesures électriques d'extraire le sens et l'intensité du couple.

Dans le chapitre 5, nous présentons nos résultats sur la génération des courants de spin par GdFeCo obtenus par une technique exploitant la résonance d'un matériau ferromagnétique. Avant de présenter l'étude sur GdFeCo, nous calculons les expressions analytiques associées à la technique en utilisant le modèle développé dans le chapitre 4. Nous présentons un cas de réference Pt/NiFe, où le courant de spin et les couples ont été garbdement étudiés dans la littérature. Le cas de GdFeCo est plus complexe, puisque le matériau génère des courants de spin avec plusieurs symétries qui peuvent tout deux induire des couples. Nous adaptions alors le modèle pour prendre en compte ces deux symétries dans les expressions analytiques des tensions mesurées. Nous présentons les mesures à plusieurs températures et plus spécifiquement avant et après la compensation magnétique. Nos mesures suggèrent que le courant de spin qui peut générer des couples auto-induits est inchangé même en passant la compensation magnétique, ce qui suggère que la génération du courant de spin n'est pas associée à un courant de spin en particulier.

Dans le chapitre 6, nous présentons les mesures des couples par la technique de la seconde harmonique. Après avoir calculé les expressions analytiques pour les tensions dans le cadre de cette technique, nous comparons deux systèmes. D'abord, le cas de référence GdFeCo/Pt, où Pt est connu pour être la source d'un courant de spin. Dans ce sytème où le courant de spin à l'origine du couple est principalement externe, nous observons que les couples ne change pas de signe lorsque du passage à travers la compensation magnétique. Dans le cas de GdFeCo/Cu, où nous avons des couples auto-induits, nous observons que le signe du couple

auto-induit change à travers la compensation magnétique. Ce changement de signe ne peut pas être attribué à un changement de signe dans la génération du courant de spin d'après les résultats du chaputre 5. Il semble donc être expliqué par la dynamique de l'aimantation de GdFeCo. Pour apporter des pistes de réflexion sur ce changement de signe, nous exprimons la dynamique de chaque sous-réseaux sous l'action de couples.

Dans le chapitre 7, nous présentons des structures qui montrent une efficacité plus importante pour le couple auto-induit que dans le cas de GdFeCo/Cu. D'abord en ajoutant une couche supplémentaire entre le substrat et GdFeCo, nous pouvons obtenir le renversement électrique de l'aimantation. L'origine de cette plus grande efficacité du couple auto-induit ne peut pas être précisment identifiée, puisque l'ajout d'une interface change les propriétés en volume de GdFeCo, notamment son gradient de concentration, mais peut aussi induire des effets d'interface. Nous discutons donc ici que de l'effet complet de la structure. Nous montrons notament que le switching peut être obtenu pour une valeur de courant électrique plus faible qu'avec l'utilisation d'un métal lourd comme le platine. Nous présentons ensuite l'ajout d'une couche de CoAl dont le but est d'améliorer l'absorption du courant de spin généré par GdFeCo. Pour cette structure, nous observons également le renversement de l'aimantation pour une faible intensité de courant électrique. Nous mentionnons ensuite d'autres structures et matériaux qui pourraient être utilisés pour un travail futur.

Nous finissons cette thèse par une conclusion de nos résultats les plus importants et proposons des perspectives pour ce matériau.

Bibliography

[1] M. Koot and F. Wijnhoven. Usage impact on data center electricity needs: A system dynamic forecasting model. Applied Energy, 291:116798, 2021.

[2] Réseau de transport d'électricité de France. Bilan électrique. https://analysesetdonnees.rte-france.com/bilan-electrique-production, 2022.

[3] R. W. Keyes. Physical limits of silicon transistors and circuits. Reports on Progress in Physics, 68(12):2701, 2005.

[4] M. N. Baibich, J-M. Broto, A. Fert, F. N. Van Dau, F. Petroff, P. Etienne, G. Creuzet, A. Friederich, and J. Chazelas. Giant magnetoresistance of (001) Fe/(001) Cr magnetic superlattices. Physical review letters, 61(21):2472, 1988.

[5] G. Binasch, P. Grünberg, F. Saurenbach, and W. Zinn. Enhanced magnetoresistance in layered magnetic structures with antiferromagnetic interlayer exchange. Physical review B, 39(7):4828, 1989.

[6] E. Grochowski. Emerging trends in data storage on magnetic hard disk drives. Datatech (September 1998), ICG Publishing, pages 11–16, 1998.

[7] J. C. Slonczewski et al. Current-driven excitation of magnetic multilayers. Journal of Magnetism and Magnetic Materials, 159(1):L1, 1996.

[8] L. Berger. Emission of spin waves by a magnetic multilayer traversed by a current. Physical review. B, Condensed matter, 54(13):9353–9358, 1996.

[9] I. M. Miron, G. Gaudin, S. Auffret, B. Rodmacq, A. Schuhl, S. Pizzini, J. Vogel, and P. Gambardella. Current-driven spin torque induced by the Rashba effect in a ferromagnetic metal layer. Nature materials, 9(3):230–234, 2010.

[10] H. Kurebayashi, J. Sinova, D. Fang, A. C. Irvine, T. D. Skinner, J. Wunderlich, V. Novák, R. P. Campion, B. L. Gallagher, E. K. Vehstedt, et al. An antidamping spin–orbit torque originating from the Berry curvature. Nature nanotechnology, 9(3):211–217, 2014.

[11] C. Ciccarelli, L. Anderson, V. Tshitoyan, A. J. Ferguson, F. Gerhard, C. Gould, L. W. Molenkamp, J. Gayles, J. Železnỳ, L. Šmejkal, et al. Room-temperature spin-orbit torque in NiMnSb. Nature physics, 12(9):855–860, 2016.

[12] W. Wang, T. Wang, V. P. Amin, Y. Wang, A. Radhakrishnan, A. Davidson, S. R. Allen, T. J. Silva, H. Ohldag, D. Balzar, et al. Anomalous spin–orbit torques in magnetic single-layer films. Nature nanotechnology, 14(9):819–824, 2019.

[13] M. D. Stiles and A. Zangwill. Anatomy of spin-transfer torque. Physical Review B, 66(1):014407, 2002.

[14] D. C. Ralph and M. D. Stiles. Spin transfer torques. Journal of Magnetism and Magnetic Materials, 320(7):1190–1216, 2008.

[15] N. W. Ashcroft and N. D. Mermin. Physique des solides, ch. 1.3. Les Ulis Bagneux: EDP sciences, pages 13–18, 2002.

[16] C. Kittel. Introduction to solid state physics eighth edition. 2021.

[17] E. Du Trémolet de Lacheisserie. Magnétisme-tome i. In Magnétisme-Tome I. EDP Sciences, 2022.

[18] N. F. Mott. Electrons in transition metals. Advances in Physics, 13(51):325–422, 1964.

[19] S. Maekawa, S. O. Valenzuela, E. Saitoh, and T. Kimura. Spin current, volume 22. Oxford University Press, 2017.

[20] K. Uchida, S. Takahashi, K. Harii, J. Ieda, W. Koshibae, K. Ando, S. Maekawa, and E. Saitoh. Observation of the spin Seebeck effect. Nature, 455(7214):778–781, 2008.

[21] Y. Tserkovnyak, A. Brataas, and G. E. W. Bauer. Spin pumping and magnetization dynamics in metallic multilayers. Physical Review B, 66(22):224403, 2002.

[22] K. Ando, S. Takahashi, J. Ieda, Y. Kajiwara, H. Nakayama, T. Yoshino, K. Harii, Y. Fujikawa, M. Matsuo, S. Maekawa, and E. Saitoh. Inverse spin-Hall effect induced by spin pumping in metallic system. Journal of applied physics, 109(10):103913, 2011.

[23] M. Matsuo, J. Ieda, and S. Maekawa. Mechanical generation of spin current. Frontiers in Physics, 3:54, 2015.

[24] M. I. Dyakonov and V. I. Perel. Current-induced spin orientation of electrons in semiconductors. Physics Letters A, 35(6):459–460, 1971.

[25] P. Gambardella and I. M. Miron. Current-induced spin–orbit torques. Philosophical Transactions of the Royal Society A: Mathematical, Physical and Engineering Sciences, 369(1948):3175–3197, 2011.

[26] S. Maekawa, T. Kikkawa, H. Chudo, J. Ieda, and E. Saitoh. Spin and spin current—from fundamentals to recent progress. Journal of Applied Physics, 133(2):020902, 2023.

[27] C. Cohen-Tannoudji, B. Diu, and F. Laloe. Quantum mechanics, volume 1. Quantum Mechanics, 1:898, 1986.

[28] E. H. Hall. On a new action of the magnet on electric currents. American Journal of Mathematics, 2(3):287–292, 1879.

[29] E. H. Hall. Xviii. on the "rotational coefficient" in nickel and cobalt. The London, Edinburgh, and Dublin Philosophical Magazine and Journal of Science, 12(74):157–172, 1881.

[30] N. Nagaosa, J. Sinova, S. Onoda, A. H. MacDonald, and N. P. Ong. Anomalous Hall effect. Reviews of modern physics, 82(2):1539, 2010.

[31] T. Taniguchi, J. Grollier, and M. D. Stiles. Spin-transfer torques generated by the anomalous Hall effect and anisotropic magnetoresistance. Physical Review Applied, 3(4):044001, 2015.

[32] S. Iihama, T. Taniguchi, K. Yakushiji, A. Fukushima, Y. Shiota, S. Tsunegi, R. Hiramatsu, S. Yuasa, Y. Suzuki, and H. Kubota. Spin-transfer torque induced by the spin anomalous Hall effect. Nature electronics, 1(2):120–123, 2018.

[33] M. I. Dyakonov and V. I. Perel. Possibility of orienting electron spins with current. Soviet Journal of Experimental and Theoretical Physics Letters, 13:467, 1971.

[34] A. Hoffmann. Spin Hall effects in metals. IEEE transactions on magnetics, 49(10):5172–5193, 2013.

[35] J. Sinova, D. Culcer, Q. Niu, N. A. Sinitsyn, T. Jungwirth, and A. H. MacDonald. Universal intrinsic spin Hall effect. Physical review letters, 92(12):126603, 2004.

[36] S. Murakami and N. Nagaosa. Berry phase in magnetic superconductors. Physical review letters, 90(5):057002, 2003.

[37] O. P. Sushkov, A. I. Milstein, M. Mori, and S. Maekawa. Does the side jump effect exist? arXiv preprint arXiv:1211.2372, 2012.

[38] O. P. Sushkov, A. I. Milstein, M. Mori, and S. Maekawa. Relativistic effects in scattering of polarized electrons. Europhysics Letters, 103(4):47003, 2013.

[39] M. B. Lifshits and M. I. Dyakonov. Swapping spin currents: Interchanging spin and flow directions. Physical review letters, 103(18):186601, 2009.

[40] V. P. Amin, J. Zemen, and M. D. Stiles. Interface-generated spin currents. Physical review letters, 121(13):136805, 2018.

[41] R. J. Elliott. Theory of the effect of spin-orbit coupling on magnetic resonance in some semiconductors. Physical Review, 96(2):266, 1954.

[42] Y. Yafet. g factors and spin-lattice relaxation of conduction electrons. In Solid state physics, volume 14, pages 1–98. Elsevier, 1963.

[43] M. I. Dyakonov and V. I. Perel. Spin orientation of electrons associated with the interband absorption of light in semiconductors. Soviet Journal of Experimental and Theoretical Physics, 33:1053, 1971.

[44] M. I. Dyakonov and V. I. Perel. Spin relaxation of conduction electrons in noncentrosymmetric semiconductors. Soviet Physics Solid State, Ussr, 13(12):3023–3026, 1972.

[45] A. Einstein and W. J. De Haas. Experimental proof of the existence of Ampere's molecular currents. In Proc. KNAW, volume 181, page 696, 1915.

[46] L. D. Landau and E. M. Lifshitz. On the theory of the dispersion of magnetic permeability in ferromagnetic bodies. Sov. Phys, 8:153–166, 1935.

[47] T. L. Gilbert. [abstract only; full report, armor research foundation project no. a059, supplementary report, may 1, 1956] (unpublished). Phys. Rev., 100:1243, 1955.

[48] T. L. Gilbert. A phenomenological theory of damping in ferromagnetic materials. IEEE transactions on magnetics, 40(6):3443–3449, 2004.

[49] M. D. Stiles and J. Miltat. Spin-transfer torque and dynamics. Spin dynamics in confined magnetic structures III, pages 225–308, 2006.

[50] A. Manchon and S. Zhang. Theory of spin torque due to spin-orbit coupling. Physical Review B, 79(9):094422, 2009.

[51] S. Zhang, P. M. Levy, and A. Fert. Mechanisms of spin-polarized current-driven magnetization switching. Physical review letters, 88(23):236601, 2002.

[52] S. Petit, C. Baraduc, C. Thirion, U. Ebels, Y. Liu, M. Li, P. Wang, and B. Dieny. Spin-torque influence on the high-frequency magnetization fluctuations in magnetic tunnel junctions. Physical review letters, 98(7):077203, 2007.

[53] T. Chen, R. K. Dumas, A. Eklund, P. K. Muduli, A. Houshang, A. A. Awad, P. Dürrenfeld, B. G. Malm, A. Rusu, and J. Åkerman. Spin-torque and spin-hall nano-oscillators. Proceedings of the IEEE, 104(10):1919–1945, 2016.

[54] A. D. Kent and D. C. Worledge. A new spin on magnetic memories. Nature nanotechnology, 10(3):187–191, 2015.

[55] W. Zhang, W. Han, X. Jiang, S-H. Yang, and S. Parkin. Role of transparency of platinum–ferromagnet interfaces in determining the intrinsic magnitude of the spin Hall effect. Nature physics, 11(6):496–502, 2015.

[56] L. Zhu, D. C. Ralph, and R. A. Buhrman. Maximizing spin-orbit torque generated by the spin Hall effect of Pt. Applied Physics Reviews, 8(3), 2021.

[57] M-H. Nguyen, D. C. Ralph, and R. A. Buhrman. Spin torque study of the spin Hall conductivity and spin diffusion length in platinum thin films with varying resistivity. Physical review letters, 116(12):126601, 2016.

[58] C-F. Pai, Y. Ou, L. H. Vilela-Leão, D. C. Ralph, and R. A. Buhrman. Dependence of the efficiency of spin Hall torque on the transparency of Pt/ferromagnetic layer interfaces. Physical Review B, 92(6):064426, 2015.

[59] L. Zhu, D. C. Ralph, and R. A. Buhrman. Effective spin-mixing conductance of heavy-metal–ferromagnet interfaces. Physical Review Letters, 123(5):057203, 2019.

[60] C. O. Pauyac, M. Chshiev, A. Manchon, and S. A. Nikolaev. Spin Hall and spin swapping torques in diffusive ferromagnets. Physical Review Letters, 120(17):176802, 2018.

[61] M. H. Kryder. Magneto-optic recording technology. Journal of Applied Physics, 57(8):3913–3918, 1985.

[62] R. Carey, D. M. Newman, and B. W. JJ Thomas. Magneto-optic recording. Journal of Physics D: Applied Physics, 28(11):2207, 1995.

[63] J. Hohlfeld, T. Gerrits, M. Bilderbeek, T. Rasing, H. Awano, and N. Ohta. Fast magnetization reversal of GdFeCo induced by femtosecond laser pulses. Physical Review B, 65(1):012413, 2001.

[64] C. D. Stanciu, A. V. Kimel, F. Hansteen, A. Tsukamoto, A. Itoh, A. Kirilyuk, and T. Rasing. Ultrafast spin dynamics across compensation points in ferrimagnetic GdFeCo: The role of angular momentum compensation. Physical Review B, 73(22):220402, 2006.

[65] N. Roschewsky, T. Matsumura, S. Cheema, F. Hellman, T. Kato, S. Iwata, and S. Salahuddin. Spin-orbit torques in ferrimagnetic GdFeCo alloys. Applied Physics Letters, 109(11):112403, 2016.

[66] K-J. Kim, S. K. Kim, Y. Hirata, S-H. Oh, T. Tono, D-H. Kim, T. Okuno, W. S. Ham, S. Kim, Y. Go, G. Tserkovnyak, A. Tsukamoto, T. Moriyama, K-J. Lee, and T. Ono. Fast domain wall motion in the vicinity of the angular momentum compensation temperature of ferrimagnets. Nature materials, 16(12):1187–1192, 2017.

[67] Y. Hirata, D-H. Kim, S. K. Kim, D-K. Lee, S-H. Oh, D-Y. Kim, T. Nishimura, T. Okuno, Y. Futakawa, H. Yoshikawa, A. Tsukamoto, Y. Tserkovnyak, Y. Siota, T. Moriyama, S-B. Choe, K-J. Lee, and T. Ono. Vanishing skyrmion Hall effect at the angular momentum compensation temperature of a ferrimagnet. Nature nanotechnology, 14(3):232–236, 2019.

[68] M. Ding and S. J. Poon. Tunable perpendicular magnetic anisotropy in GdFeCo amorphous films. Journal of magnetism and magnetic materials, 339:51–55, 2013.

[69] A. Frisk, F. Magnus, S. George, U. B. Arnalds, and G. Andersson. Tailoring anisotropy and domain structure in amorphous TbCo thin films through combinatorial methods. Journal of Physics D: Applied Physics, 49(3):035005, 2015.

[70] T. Lee, M. K. Panduranga, C. W. Han, V. Ortalan, and G. P. Carman. Strain-modulated exchange-spring magnetic behavior in amorphous Tb-Fe thin films. Physical Review Applied, 8(2):024024, 2017.

[71] K. A. Thórarinsdóttir, B. R. Thorbjarnardóttir, U. B. Arnalds, and F. Magnus. Competing interface and bulk anisotropies in Co-rich TbCo amorphous thin films. Journal of Physics: Condensed Matter, 35(20):205802, 2023.

[72] D-H. Kim, M. Haruta, H-W. Ko, G. Go, H-J. Park, T. Nishimura, D-Y. Kim, T. Okuno, Y. Hirata, and Y. et al. Futakawa. Bulk Dzyaloshinskii–Moriya interaction in amorphous ferrimagnetic alloys. Nature materials, 18(7):685, 2019.

[73] J. Wang, C. Li, F. Liu, and C. Jiang. Characterization of spin-orbit torque in a single ferrimagnetic GdFeCo film by oblique sputtering. SSRN 3982086.

[74] D. Céspedes-Berrocal, H. Damas, S. Petit-Watelot, D. Maccariello, P. Tang, A. Arriola-Córdova, P. Vallobra, Y. Xu, J-L. Bello, E. Martin, S. Migot, J. Ghanbaja, S. Zhang, M. Hehn, S. Mangin, C. Panagopoulos, V. Cros, A. Fert, and J-C. Rojas-Sanchez. Current-induced spin torques on single GdFeCo magnetic layers. Advanced Materials, 33(12):2007047, 2021.

[75] S. S. Deodhar and P. J. Ficalora. A study of the reaction kinetics for the formation of rare earth-transition metal laves compounds. Metallurgical Transactions A, 6:1909–1914, 1975.

[76] A. V. Ruban, H. L. Skriver, and J. K. Nørskov. Surface segregation energies in transition-metal alloys. Physical review B, 59(24):15990, 1999.

[77] E. Kirk, C. Bull, S. Finizio, H. Sepehri-Amin, S. Wintz, A. K. Suszka, N. S. Bingham, P. Warnicke, K. Hono, P. W. Nutter, J Raabe, G. Hrkac, T. Thomson, and L. J. Heyderman. Anisotropy-induced spin reorientation in chemically modulated amorphous ferrimagnetic films. Physical Review Materials, 4(7):074403, 2020.

[78] P. Hansen. Chapter 4 : Magnetic amorphous alloys. Handbook of magnetic materials, 6:289–452, 1991.

[79] G. Sala. Magnetization dynamics induced by spin and orbital currents in ferro-and ferrimagnets. PhD thesis, ETH Zurich, 2022.

[80] I. A. Campbell. Indirect exchange for rare earths in metals. Journal of Physics F: Metal Physics, 2(3):L47, 1972.

[81] K. H. J. Buschow. Intermetallic compounds of rare-earth and 3d transition metals. Reports on Progress in Physics, 40(10):1179, 1977.

[82] E. Haltz. Domain wall dynamics driven by spin-current in ferrimagnetic alloys. PhD thesis, Université Paris Saclay (COmUE), 2019.

[83] H. J. Leamy and A. G. Dirks. The microstructure of amorphous rare-earth/transition-metal thin films. Journal of Physics D: Applied Physics, 10(8):L95, 1977.

[84] J-L Bello, Y. Quessab, J-W Xu, M. Vergès, H. Damas, S. Petit-Watelot, J-C. Rojas Sánchez, M. Hehn, A. D. Kent, and S. Mangin. Field-free current-induced magnetization switching in GdFeCo: A competition between spin–orbit torques and Oersted fields. Journal of Applied Physics, 132(8), 2022.

[85] R. Harris, M. Plischke, and M. J. Zuckermann. New model for amorphous magnetism. Physical Review Letters, 31(3):160, 1973.

[86] T. M. Danh, N. H. Duc, and N. P. Thuy. Exchange interactions in amorphous Gd–Fe alloys. Journal of magnetism and magnetic materials, 185(1):105–108, 1998.

[87] J. Park, Y. Hirata, J-H. Kang, S. Lee, S. Kim, C. Van Phuoc, J-R. Jeong, J. Park, S-Y. Park, Y. Jo, A. Tsukamoto, T. Ono, Kim S. K., and K-J. Kim. Unconventional magnetoresistance induced by sperimagnetism in GdFeCo. Physical Review B, 103(1):014421, 2021.

[88] J. M. D. Coey. Amorphous magnetic order. Journal of Applied Physics, 49(3):1646–1652, 1978.

[89] R. C. Taylor and A. Gangulee. Magnetic properties of the 3 d transition metals in the amorphous ternary alloys: Gd 0.2 (Fe x Co 1- x) 0.8, Gd 0.2 (Co x Ni 1- x) 0.8, and Gd 0.2 (Fe x Ni 1- x) 0.8. Physical Review B, 22(3):1320, 1980.

[90] O. Krupin, G. Bihlmayer, K. Starke, S. Gorovikov, J. E. Prieto, K. Döbrich, S. Blügel, and G. Kaindl. Rashba effect at magnetic metal surfaces. Physical Review B, 71(20):201403, 2005.

[91] Y. Lim, B. Khodadadi, J-F. Li, D. Viehland, A. Manchon, and S. Emori. Dephasing of transverse spin current in ferrimagnetic alloys. Physical Review B, 103(2):024443, 2021.

[92] L. Zhu, D. C. Ralph, and R. A. Buhrman. Unveiling the mechanism of bulk spin-orbit torques within chemically disordered FexPt1-x single layers. Advanced Functional Materials, 31(36):2103898, 2021.

[93] A. Ogawa, T. Katayama, M. Hirano, and T. Tsushima. Reversal of Hall effect and Kerr rotation in ferrimagnetic rare earth-cobalt systems. 24(1):575–576, 1975.

[94] Y. Mimura, N. Imamura, and Y. Kushiro. Hall effect in rare-earth–transition-metal amorphous alloy films. Journal of Applied Physics, 47(7):3371–3373, 1976.

[95] R. Asomoza, I. A. Campbell, H. Jouve, and R. Meyer. Extraordinary Hall effect in rare-earth–cobalt amorphous films. Journal of Applied Physics, 48(9):3829–3831, 1977.

[96] R. Malmhäll. Extraordinary Hall resistivity in amorphous terbium–iron thin films and its temperature dependence. Journal of applied physics, 54(9):5128–5131, 1983.

[97] T. R. McGuire, R. J. Gambino, and R. C. Taylor. Hall effect in amorphous thin-film magnetic alloys. Journal of Applied Physics, 48(7):2965–2970, 1977.

[98] C-H. Lai, C-C. Lin, B. M. Chen, H-P. D. Shieh, and C-R. Chang. Positive giant magnetoresistance in ferrimagnetic/Cu/ferrimagnetic films. Journal of Applied Physics, 89(11):7124–7126, 2001.

[99] N. T. Nam and L. Ranno. Unconventional GMR angular dependence using a compensated ferrimagnet. Journal of magnetism and magnetic materials, 322(9-12):1428–1430, 2010.

[100] N. T. Hai, J-C. Wu, J-P. Chou, and J. Pothan. Novel anomalous Hall effect mechanism in ferrimagnetic GdCo alloy. Journal of Applied Physics, 133(23), 2023.

[101] R. Meservey and P. M. Tedrow. Spin-polarized electron tunneling. Physics reports, 238(4):173–243, 1994.

[102] P. M. Tedrow and R. Meservey. Spin polarization of electrons tunneling from films of Fe, Co, Ni, and Gd. Physical Review B, 7(1):318, 1973.

[103] G. Chrobok, M. Hofmann, G. Regenfus, and R. Sizmann. Spin polarization of field-emitted electrons from Fe, Co, Ni, and rare-earth metals. Physical Review B, 15(1):429, 1977.

[104] J. M. Valentine and C. L. Chien. Determination of spin polarization of Gd and Dy by point-contact Andreev reflection. Journal of applied physics, 99(8), 2006.

[105] C. Kaiser, A. F. Panchula, and S. Parkin. Finite tunneling spin polarization at the compensation point of rare-earth-metal–transition-metal alloys. Physical review letters, 95(4):047202, 2005.

[106] A. D. Naylor, G. Burnell, and B. J. Hickey. Transport spin polarization of the rare-earth transition-metal alloy co 1- x gd x. Physical Review B, 85(6):064410, 2012.

[107] I. A. Campbell and A. Fert. Transport properties of ferromagnets. Handbook of Ferromagnetic Materials, 3:747–804, 1982.

[108] Y-Y. Chen and J-Y. Juang. Finite element analysis and equivalent parallel-resistance model for conductive multilayer thin films. Measurement Science and Technology, 27(7):074006, 2016.

[109] R. Asomoza, I. A. Campbell, and A. Fert. Transport properties of amorphous rare-earth alloys. Le Journal de Physique Colloques, 40(C5):C5–225, 1979.

[110] A. Fert and R. Asomoza. Transport properties of magnetic amorphous alloys. Journal of Applied Physics, 50(B3):1886–1891, 1979.

[111] R. Asomoza, A. Fert, and R. Reich. Gadolinium-heavy rare earth alloys: preparation, metallographic study and extraordinary Hall effect. Journal of the Less Common Metals, 90(2):177–201, 1983.

[112] K. Chadova, S. Mankovsky, J. Minár, and H. Ebert. Impact of finite temperatures on the transport properties of Gd from first principles. Physical Review B, 95(12):125109, 2017.

[113] M-H. Nguyen and C-F. Pai. Spin-orbit torque characterization in a nutshell. APL Materials, 9(3):030902, 2021.

[114] A. Manchon, J. Železnỳ, I. M. Miron, T. Jungwirth, J. Sinova, A. Thiaville, K. Garello, and P. Gambardella. Current-induced spin-orbit torques in ferromagnetic and antiferromagnetic systems. Reviews of Modern Physics, 91(3):035004, 2019.

[115] A. Leduc. Modifications de la conductibilité calorifique du bismuth dans un champ magnétique. Journal de Physique Théorique et Appliquée, 7(1):519–525, 1888.

[116] J-E. Wegrowe, H-J. Drouhin, and D. Lacour. Anisotropic magnetothermal transport and spin Seebeck effect. Physical Review B, 89(9):094409, 2014.

[117] B. Madon, D. C. Pham, J-E. Wegrowe, D. Lacour, M. Hehn, V. Polewczyk, A. Anane, and V. Cros. Anomalous and planar Righi-Leduc effects in Ni 80 Fe 20 ferromagnets. Physical Review B, 94(14):144423, 2016.

[118] D-K. Zhou, Q-L. Xu, X-Q. Yu, Z-G. Zhu, and G. Su. Identification of spin effects in the anomalous Righi–Leduc effect in ferromagnetic metals. Scientific Reports, 10(1):1–11, 2020.

[119] T. Fache. Iridium-based synthetic ferrimagnets for spintronics. PhD thesis, 2020.

[120] H. Damas, A. Anadon, D. Céspedes-Berrocal, J. Alegre-Saenz, J-L. Bello, A. Arriola-Córdova, S. Migot, J. Ghanbaja, O. Copie, M. Hehn, V. Cros, S. Petit-Watelot, and J-C. Rojas-Sanchez. Ferrimagnet GdFeCo characterization for spin-orbitronics: Large field-like and damping-like torques. physica status solidi (RRL)–Rapid Research Letters, 16(6):2200035, 2022.

[121] O. Yalçın. Ferromagnetic Resonance: Theory and Applications. InTech, 2013.

[122] M. Farle. Ferromagnetic resonance of ultrathin metallic layers. Reports on progress in physics, 61(7):755, 1998.

[123] L. Liu, T. Moriyama, D. C. Ralph, and R. A. Buhrman. Spin-torque ferromagnetic resonance induced by the spin Hall effect. Physical review letters, 106(3):036601, 2011.

[124] C. Wang, H. Seinige, and M. Tsoi. Ferromagnetic resonance driven by an AC current: A brief review. Low Temperature Physics, 39(3):247–251, 2013.

[125] G. D. H. Wong. Spin-torque ferromagnetic resonance investigation for enhancement of spin-orbit torque efficiency. 2021.

[126] A. V. Khvalkovskiy, V. Cros, D. Apalkov, V. Nikitin, M. Krounbi, K. A. Zvezdin, A. Anane, J. Grollier, and A. Fert. Matching domain-wall configuration and spin-orbit torques for efficient domain-wall motion. Physical Review B, 87(2):020402, 2013.

[127] S. Karimeddiny, J. A. Mittelstaedt, R. A. Buhrman, and D. C. Ralph. Transverse and longitudinal spin-torque ferromagnetic resonance for improved measurement of spin-orbit torque. Physical Review Applied, 14(2):024024, 2020.

[128] S. Petit, N. De Mestier, C. Baraduc, C. Thirion, Y. Liu, M. Li, P. Wang, and B. Dieny. Influence of spin-transfer torque on thermally activated ferromagnetic resonance excitations in magnetic tunnel junctions. Physical Review B, 78(18):184420, 2008.

[129] K. Ando, S. Takahashi, K. Harii, K. Sasage, J. Ieda, S. Maekawa, and E. Saitoh. Electric manipulation of spin relaxation using the spin Hall effect. Physical review letters, 101(3):036601, 2008.

[130] Y. Wang, P. Deorani, X. Qiu, J. H. Kwon, and H. Yang. Determination of intrinsic spin hall angle in Pt. Applied Physics Letters, 105(15), 2014.

[131] T. Nan, S. Emori, C. T. Boone, X. Wang, T. M. Oxholm, J. G. Jones, B. M. Howe, G. J. Brown, and N. X. Sun. Comparison of spin-orbit torques and spin pumping across NiFe/Pt and NiFe/Cu/Pt interfaces. Physical Review B, 91(21):214416, 2015.

[132] T. Fache, J. C. Rojas-Sanchez, L. Badie, S. Mangin, and S. Petit-Watelot. Determination of spin hall angle, spin mixing conductance, and spin diffusion length in CoFeB/Ir for spin-orbitronic devices. Physical Review B, 102(6):064425, 2020.

[133] A. Kumar, S. Akansel, H. Stopfel, M. Fazlali, J. Åkerman, R. Brucas, and P. Svedlindh. Spin transfer torque ferromagnetic resonance induced spin pumping in the Fe/Pd bilayer system. Physical Review B, 95(6):064406, 2017.

[134] N. Roschewsky, C-H. Lambert, and S. Salahuddin. Spin-orbit torque switching of ultralarge-thickness ferrimagnetic GdFeCo. Physical Review B, 96(6):064406, 2017.

[135] K. Kawakami, T. Kato, D. Oshima, and S. Iwata. Spin orbit torques in ferrimagnetic GdFeCo with various compositions. Japanese Journal of Applied Physics, 59(SE):SEEF01, 2019.

[136] S. Krishnia, E. Haltz, L. Berges, L. Aballe, M. Foerster, L. Bocher, R. Weil, A. Thiaville, J. Sampaio, and A. Mougin. Spin-orbit coupling in single-layer ferrimagnets: direct observation of spin-orbit torques and chiral spin textures. Physical Review Applied, 16(2):024040, 2021.

[137] Q. Liu, L. Zhu, X. S. Zhang, D. A. Muller, and D. C. Ralph. Giant bulk spin–orbit torque and efficient electrical switching in single ferrimagnetic FeTb layers with strong perpendicular magnetic anisotropy. Applied Physics Reviews, 9(2), 2022.

[138] G. Yu, P. Upadhyaya, Y. Fan, J. G. Alzate, W. Jiang, K. L. Wong, S. Takei, S. A. Bender, L-T. Chang, Y. Jiang, et al. Switching of perpendicular magnetization by spin–orbit torques in the absence of external magnetic fields. Nature nanotechnology, 9(7):548, 2014.

[139] R. Freeman, A. Zholud, Z. Dun, H. Zhou, and S. Urazhdin. Evidence for Dyakonov-Perel-like spin relaxation in Pt. Physical review letters, 120(6):067204, 2018.

[140] A. J. Berger, E. R. J. Edwards, H. T. Nembach, O. Karis, M. Weiler, and T. J. Silva. Determination of the spin Hall effect and the spin diffusion length of Pt from self-consistent fitting of damping enhancement and inverse spin-orbit torque measurements. Physical Review B, 98(2):024402, 2018.

[141] T. H. Pham, S-G. Je, P. Vallobra, T. Fache, D. Lacour, G. Malinowski, M-C. Cyrille, G. Gaudin, O. Boulle, M. Hehn, J-C. Rojas-Sanchez, and S. Mangin. Thermal contribution to the spin-orbit torque in metallic-ferrimagnetic systems. Physical Review Applied, 9(6):064032, 2018.

APPENDIX A

Symbols, units and geometry reminders

A.1 Physical quantities

Magnetic field	H_{eff}, $h_{DL,FL}$	$\mathrm{A \cdot m^{-1}}$ ou[1] Oe
Magnetic induction	$\mu_0 H$	T
Vacuum permeability	μ_0	$\mathrm{T \cdot m \cdot A^{-1}}$
Magnetic energy density	ε	$\mathrm{J \cdot m^{-3} = T \cdot A \cdot m^{-1}}$
Gyromagnetic ratio	γ	$\mathrm{rad.s^{-1}.T^{-1}}$
$\mu_0\gamma$	γ_0	$\mathrm{rad.s^{-1} \cdot m \cdot A^{-1}}$
Magnetization	M	$\mathrm{A \cdot m^{-1}}$
Gilbert damping	α	S.U.
Torque	T	$\mathrm{T \cdot A \cdot m^{-1}}$
Magnetocristaline anisotropy constant	K	$\mathrm{J \cdot m^{-3}}$
Pulsation	ω	$\mathrm{rad \cdot s^{-1}}$
Frequency	f	Hz
Electric field	E	$\mathrm{V.m^{-1}}$
Electrical resistivity	ρ	Ω.m
Electrical current density	J^e,J_c	$\mathrm{A.m^{-2}}$
Thermal coefficient	r_{th}	$\mathrm{K.W^{-1}}$
Thermal current	J^Q	W
Thermal gradient, difference	$\vec{\nabla T}, \Delta T$	K

A.2 Geometrical quantities

Vectors :	$\vec{v}$
Unitary vectors :	$\hat{v}$
Vector projection $\vec{v}$ or $\hat{v}$ on a k axis :	v_k
Complex number :	$\underline{c}$
Vectors with complex coordinates :	$\underline{\vec{v}}$
Vectors with complex coordinates projection $\underline{\vec{v}}$ on k axis :	$\underline{v_k}$
Matrix :	$\underline{\underline{M}}$
Real matrix coefficients :	M_{kl}
Imaginary matrix coefficients :	$\underline{M_{kl}}$
Temporal derivative of $a(t)$:	$\dot{a}$, $\frac{da}{dt}$
First derivative of a functional $f(k,l,...)$:	$\frac{\partial f}{\partial k,l,...} = f_{k,l,...}$
Second derivative of a functional $f(k,l,...)$:	$\frac{\partial f}{\partial kk,ll,kl,...} = f_{kk,ll,kl,...}$

A.3 Geometry reminders

- Spherical coordinates of a point P on a sphere centered in O : (r,θ,φ) so that r is the radius of the sphere, $\theta = (\hat{z},\overrightarrow{OP})$ and $\varphi = (\hat{x},\overrightarrow{OP'})$ where P' is the projection of P in the plane xOy

- Vector $\vec{M}(r,\theta,\varphi)$ in an orthonormal coordinate system $(\hat{e}_r, \hat{e}_\theta, \hat{e}_\varphi)$: $\vec{M}(r,\theta,\varphi) = M_r\hat{e}_r + M_\theta\hat{e}_\theta + M_\varphi\hat{e}_\varphi$

- Conversion from cartesian coordinates to spherical coordinates :

$$\begin{pmatrix}\hat{x}\\ \hat{y}\\ \hat{z}\end{pmatrix} = \begin{pmatrix}\sin(\theta)\cos(\varphi) & \cos(\theta)\cos(\varphi) & -\sin(\varphi)\\ \sin(\theta)\sin(\varphi) & \cos(\theta)\sin(\varphi) & \cos(\varphi)\\ \cos(\theta) & -\sin(\theta) & 0\end{pmatrix}\begin{pmatrix}\hat{e}_r\\ \hat{e}_\theta\\ \hat{e}_\varphi\end{pmatrix}$$

- Gradient in spherical coordinates

$$\vec{\nabla}_{r,\theta,\varphi} f = \begin{bmatrix} f_r \\ \frac{1}{r} f_\theta \\ \frac{1}{r\sin\theta} f_\varphi \end{bmatrix}$$

On a unit sphere, the gradient is defined as :

$$\vec{\nabla}_{r,\theta,\varphi} f = \begin{bmatrix} 0 \\ f_\theta \\ \dfrac{1}{\sin\theta} f_\varphi \end{bmatrix}$$

- Temporal derivative in spherical coordinates :

$$\dot{\hat{e}}_r = \dot{r}\ \hat{e}_r + r\dot{\theta}\ \hat{e}_\theta + r\sin(\theta)\dot{\varphi}\ \hat{e}_\varphi$$

i.e, on the unit sphere:

$$\dot{\hat{e}}_r = \dot{\theta}\ \hat{e}_\theta + \sin(\theta)\dot{\varphi}\ \hat{e}_\varphi$$

- Weak angular displacements ($\delta\theta$, $\delta\varphi$) around the equilibrium (θ_0, φ_0) :

$$\theta \to \theta_0 + \delta\theta \quad \text{with} \quad \delta\theta \ll \pi$$
$$\varphi \to \varphi_0 + \delta\varphi \quad \text{with} \quad \delta\varphi \ll \pi,$$

which gives for the evolution of the position vector :

$$\delta\hat{e}_r = \delta\theta\ \hat{e}_\theta + \sin(\theta_0)\delta\varphi\ \hat{e}_\varphi$$

This allows to linearize the functions sin and cos around the average value of the considered angle, which gives for instance for oscillations of $\delta\theta$ around its average position θ_0 :

$$\sin(\theta_0 + \delta\theta) = \sin(\theta_0)\cos(\delta\theta) + \cos(\theta_0)\sin(\delta\theta) \approx \sin(\theta_0) + \delta\phi\cos(\theta_0)$$
$$\cos(\theta_0 + \delta\theta) = \cos(\theta_0)\cos(\delta\theta) - \sin(\theta_0)\sin(\delta\theta) \approx \cos(\theta_0) - \delta\theta\sin(\theta_0)$$

- Transition to complex notations for an harmonic object :

$$\delta\theta(\omega) \to \underline{\delta\theta} e^{i\omega t} \quad \text{with} \quad \underline{\delta\theta} = \delta\theta e^{i\phi_\theta},$$

where $\delta\theta$ is the modulus of the complex quantity and ϕ_θ its phase compared to the reference phase given by the injected current.

- Explicit definition of the susceptibility in spherical coordinates

$$M_s\left(\begin{bmatrix} \underline{\delta\theta(\omega)} \\ \sin(\theta_0)\underline{\delta\varphi(\omega)} \end{bmatrix} e^{i\omega t}\right) = \begin{bmatrix} \underline{\chi_{\theta\theta}}(\omega) & \underline{\chi_{\theta\varphi}}(\omega) \\ \underline{\chi_{\varphi\theta}}(\omega) & \underline{\chi_{\varphi\varphi}}(\omega) \end{bmatrix} \cdot \left(\begin{bmatrix} \underline{\delta h_\theta} \\ \underline{\delta h_\varphi} \end{bmatrix} e^{i\omega t}\right)$$

APPENDIX B

Spin current generation of GdFeCo : raw data of ST-FMR technique

B.1 Summary for all temperatures

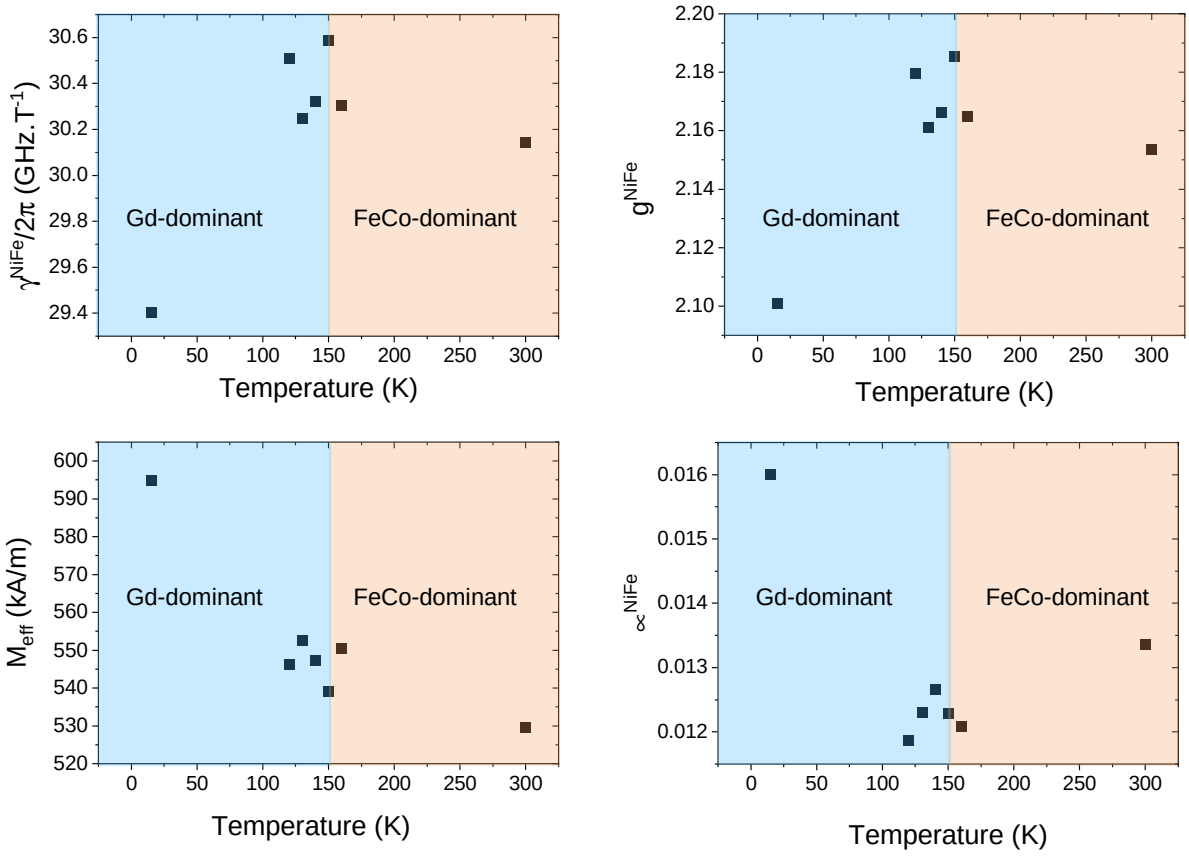

B.2 15K, Gd-dominant, lineshape analysis and DC bias

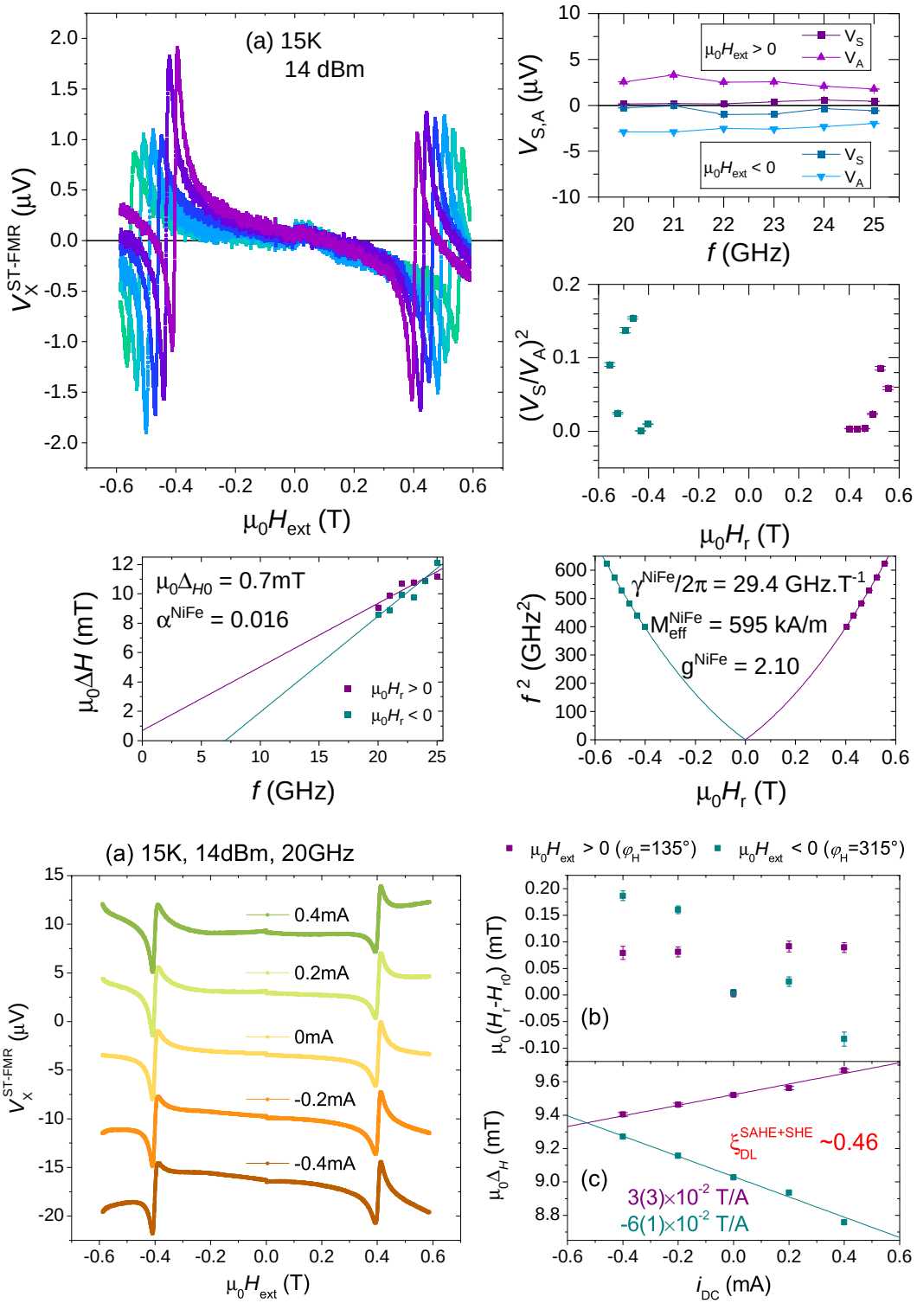

B.3 120K, Gd-dominant, lineshape analysis and DC bias

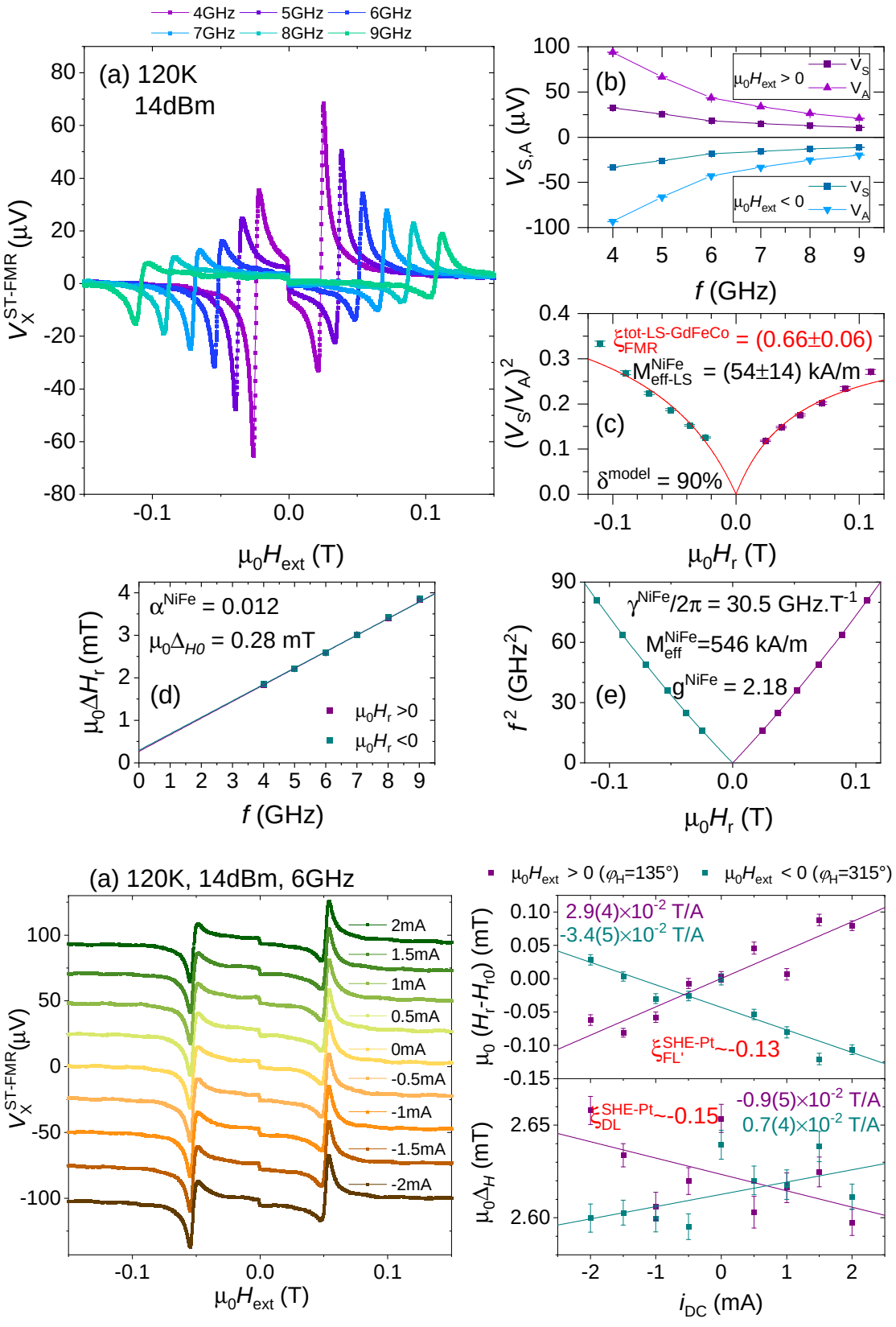

B.4 130K, Gd-dominant, lineshape analysis and DC bias

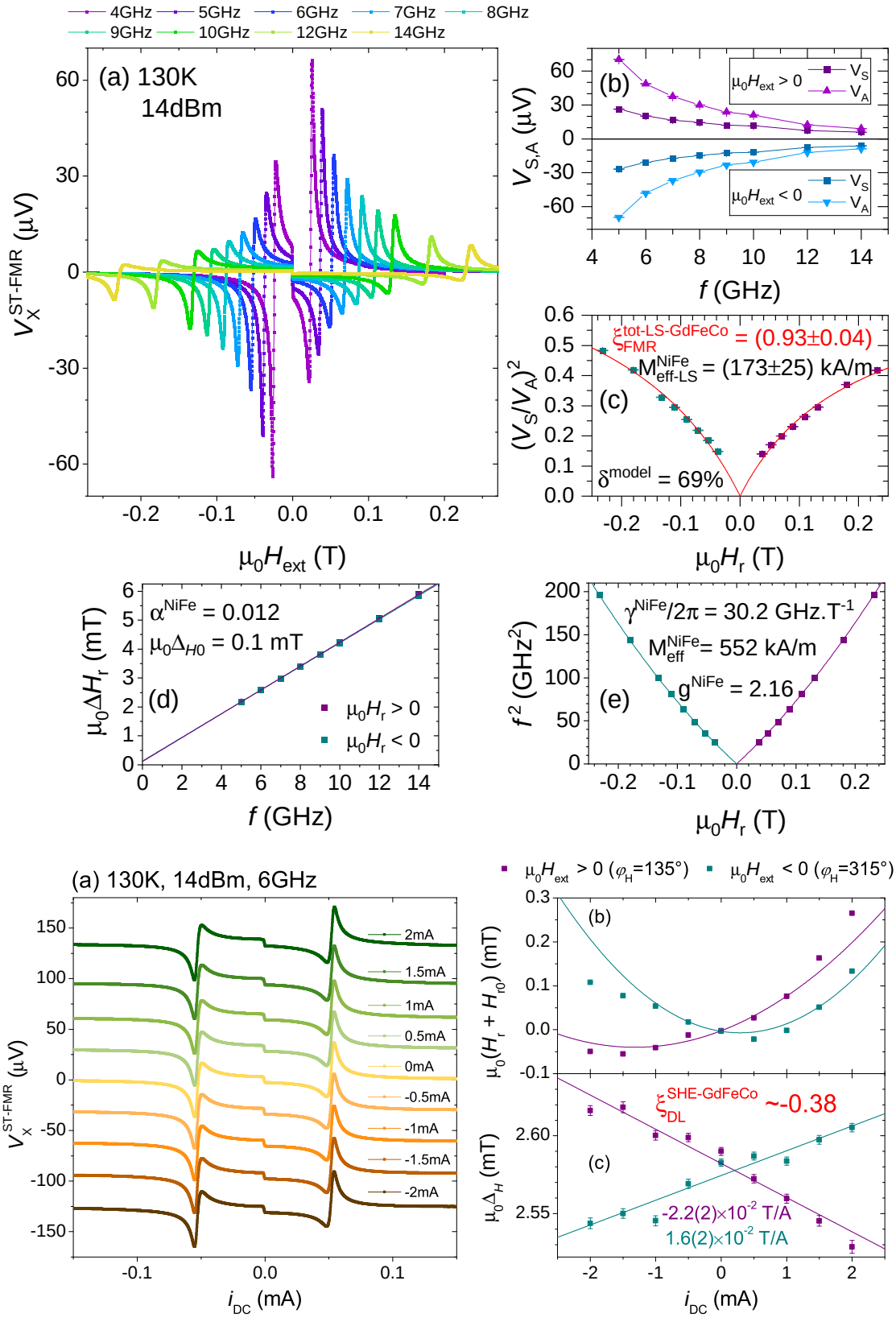

B.5 140K, Gd-dominant, lineshape analysis and DC bias

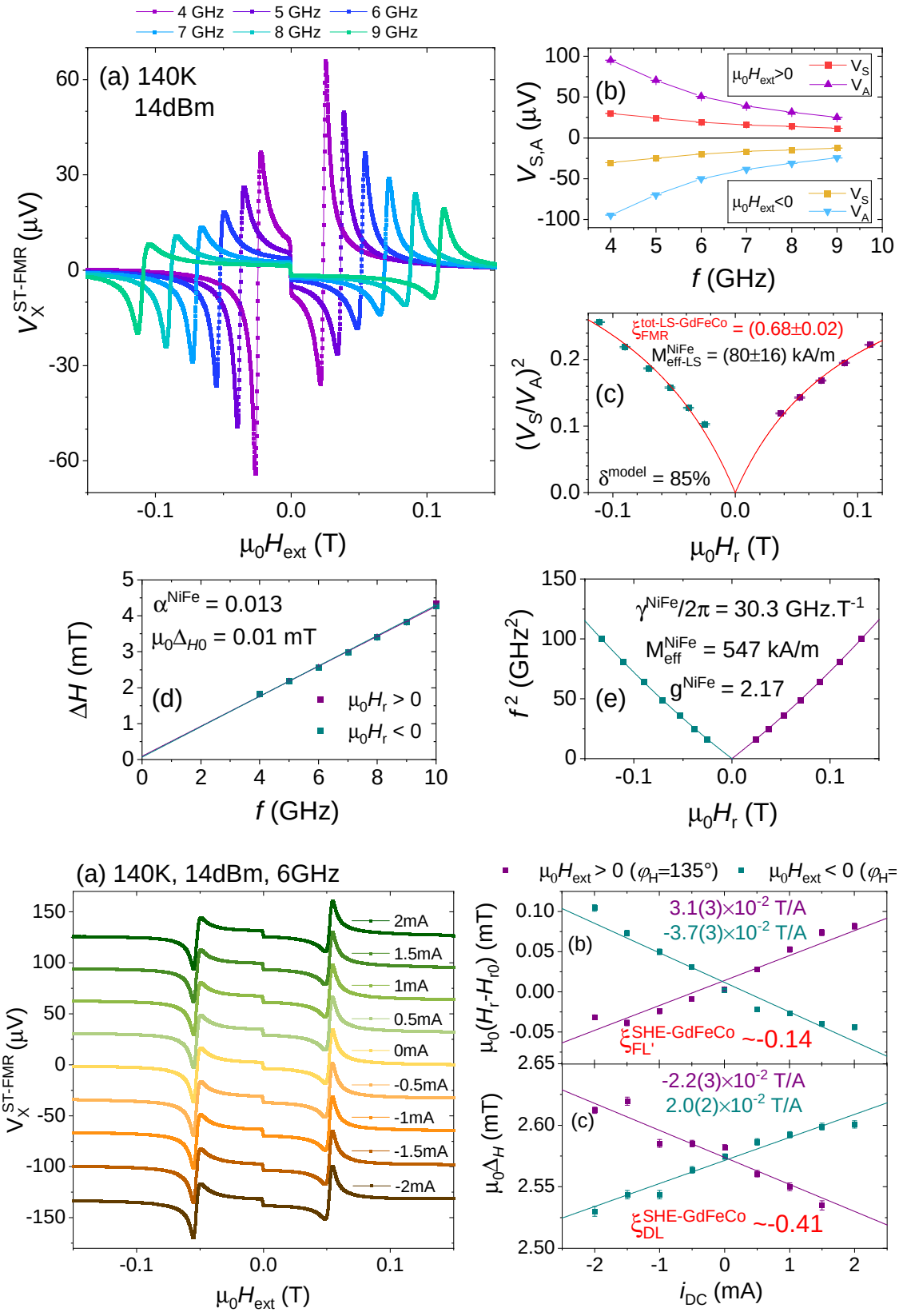

B.6 150K, FeCo-dominant, lineshape analysis

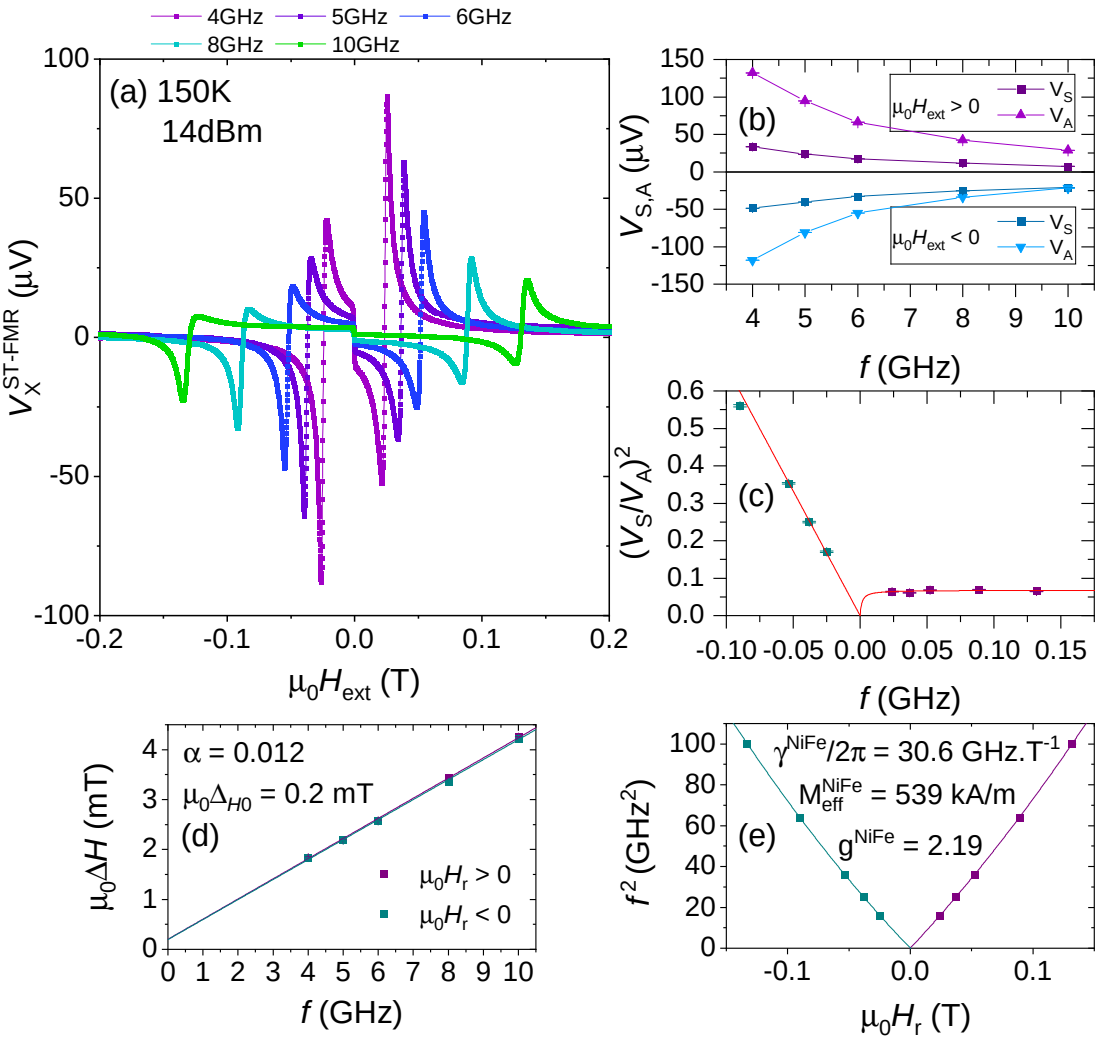

B.7 160K, FeCo-dominant, lineshape analysis and DC bias

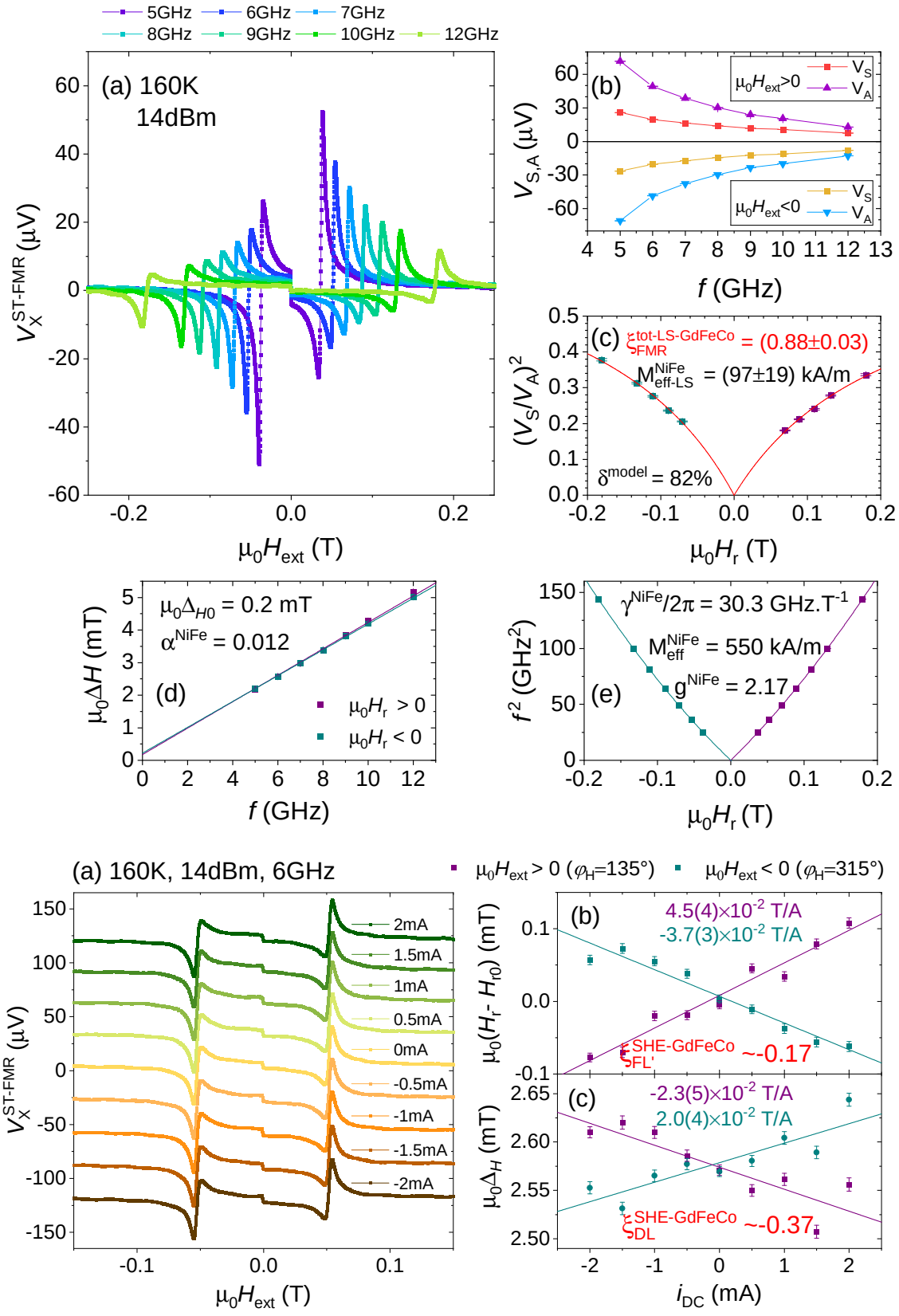

B.8 300K, FeCo-dominant, lineshape analysis and DC bias

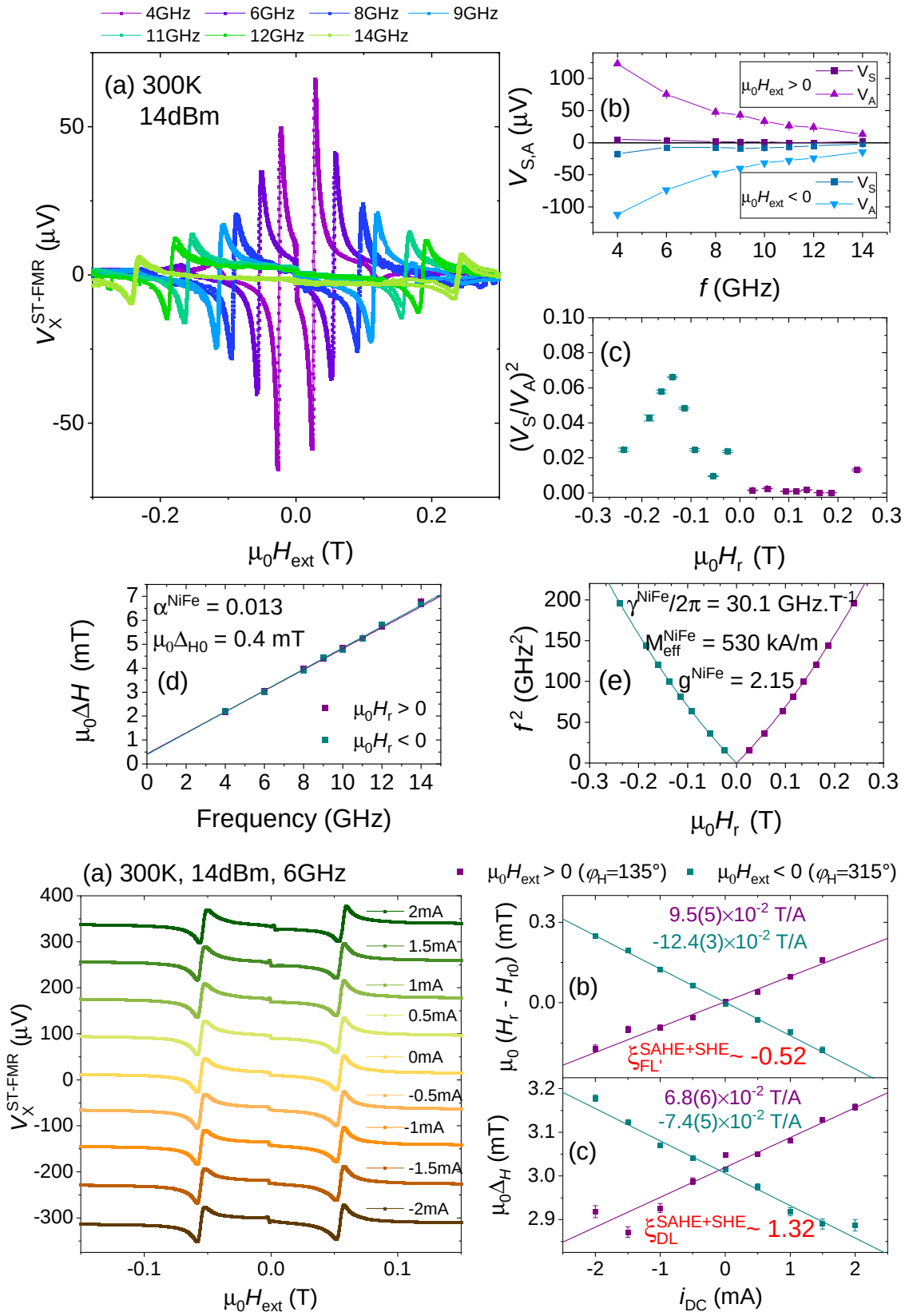

APPENDIX C

Self-torque in GdFeCo/Cu

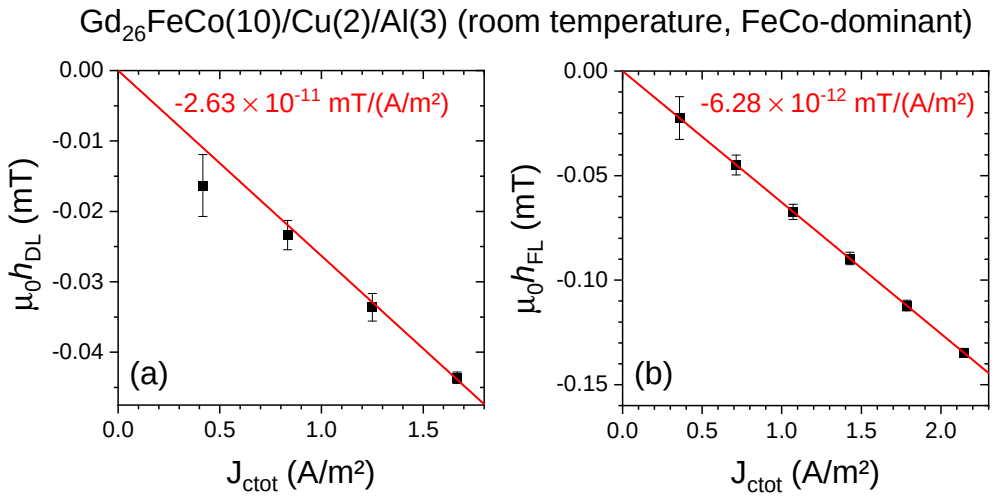

Figure C.1: Evolution of the effective fields with the total currrent density. (a) h_{DL} as a function of J_{ctot}. It shows a linear dependence with the current, and the slope is estimated $\mu_0 h_{DL}/J_{ctot} = -2.63 \times 10^{11}$ mT/(A/m^2). (b) h_{FL} as a function of J_{ctot}. It shows a linear dependence with the current, and the slope is estimated $\mu_0 h_{FL}/J_{ctot} = -6.28 \times 10^{12}$ mT/(A/m^2).

APPENDIX D

Spin-orbit torque in GdFeCo/Pt

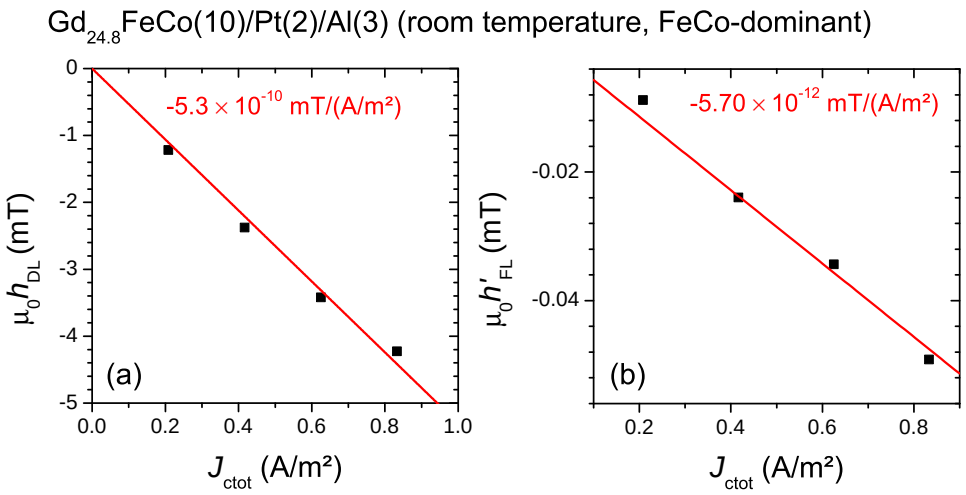

Figure D.1: Evolution of the effective fields with the total currrent density. (a) h_{DL} as a function of J_{ctot}. It shows a linear dependence with the current, and the slope is estimated $\mu_0 h_{DL}/J_{ctot} = -5.3 \times 10^{10}$ mT/(A/m^2). (b) h_{FL} as a function of J_{ctot}. It shows a linear dependence with the current, and the slope is estimated $\mu_0 h'_{FL}/J_{ctot} = -5.70 \times 10^{12}$ mT/(A/m^2).

APPENDIX E

Change of the buffer layer : chemical characterization

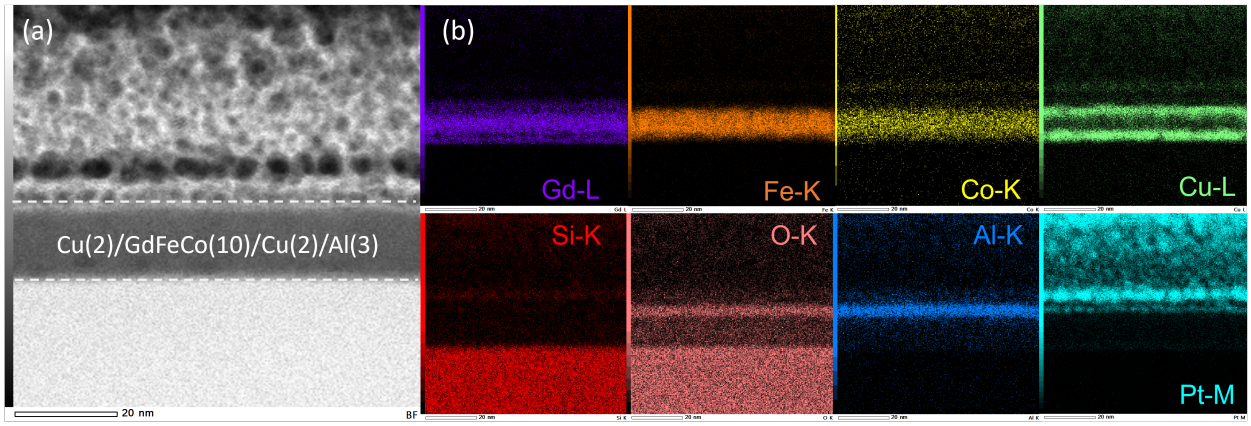

Figure E.1: (a) Micrograph of SiO_2//Cu(2)/Gd_{25}FeCo(10)/Cu(2)/Al(3) with the associated chemical analysis in (b) performed by EDS.

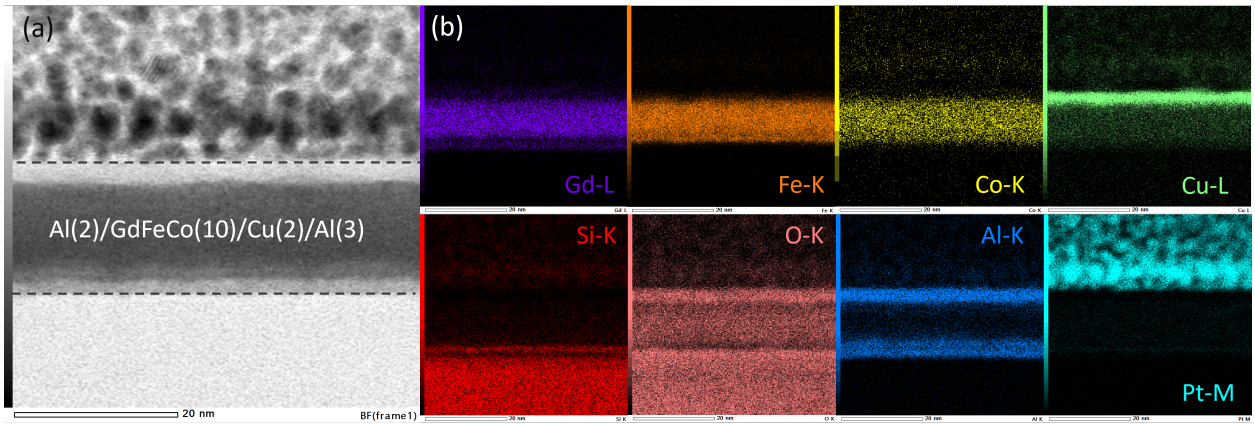

Figure E.2: (a) Micrograph of SiO_2//Al(2)/Gd_{25}FeCo(10)/Cu(2)/Al(3) with the associated chemical analysis in (b) performed by EDS.

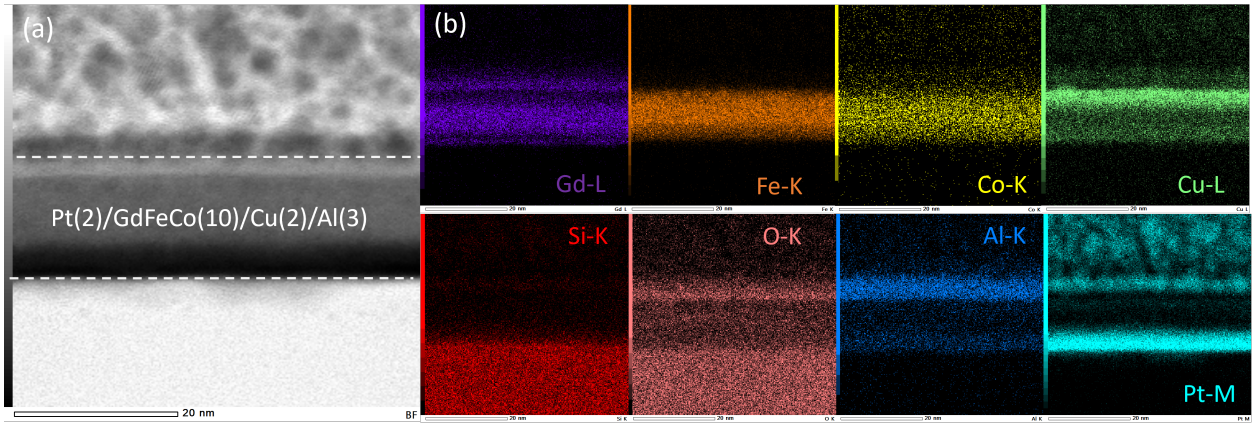

Figure E.3: (a) Micrograph of SiO_2//Pt(2)/Gd_{25}FeCo(10)/Cu(2)/Al(3) with the associated chemical analysis in (b) performed by EDS.

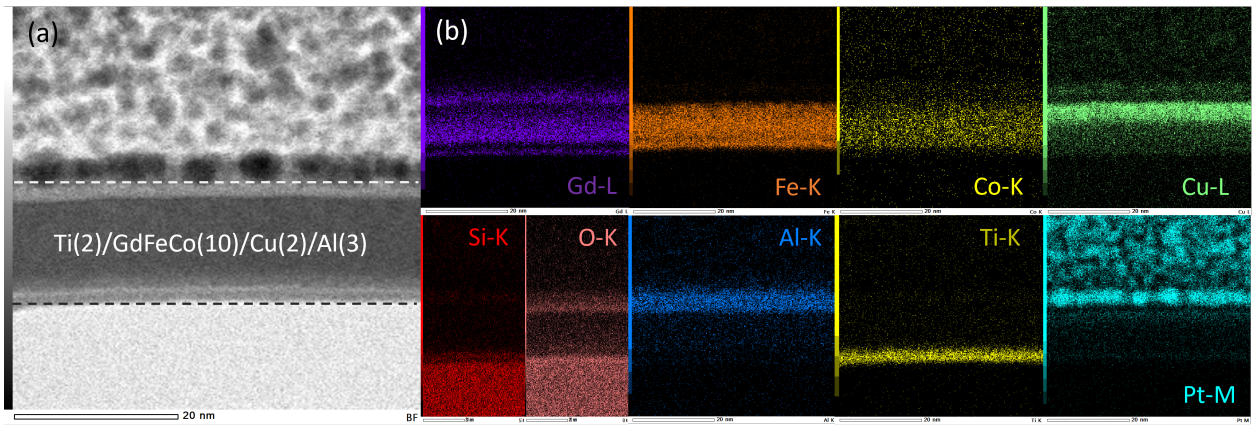

Figure E.4: (a) Micrograph of SiO_2//Ti(2)/Gd_{25}FeCo(10)/Cu(2)/Al(3) with the associated chemical analysis in (b) performed by EDS.